Optimisation and comparison of dSTORM and DNA-PAINT super-resolution for quantitative cardiac protein imaging.

Submitted by

Alexander Harrington Clowsley

to the University of Exeter as a thesis for the degree of Doctor of Philosophy in Physics

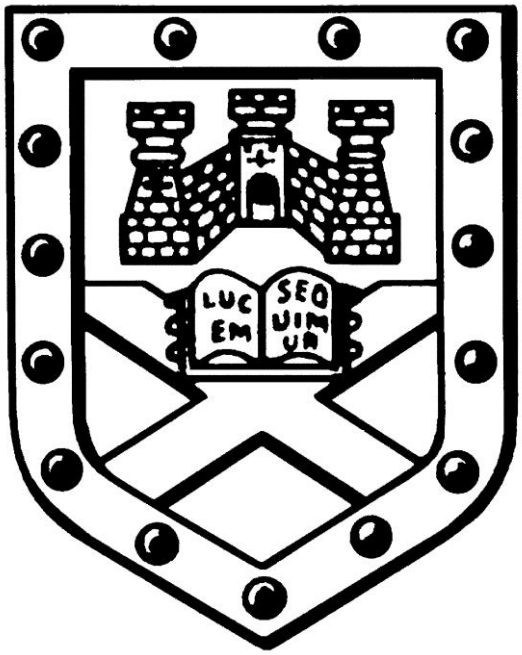

I certify that all the material in this thesis which is not my own work has been identified and that no material has previously been submitted and approved for the award of a degree by this or any other University.

October, 2017

Abstract

Fluorescence microscopy techniques, restricted by the diffraction limit of light, have seen a remarkable advancement in recent years. An approach called dSTORM (direct stochastic optical reconstruction microscopy) utilises the photoswitching capabilities of organic fluorophores when in the presence of special mounting media, the solution within which the sample is placed, to detect single molecule fluorescing events over time. The image that can be reconstructed from these events is not diffraction limited, but instead is limited by how well each event can be precisely localised. In **Chapter 3** the importance of using a suitable mounting buffer in order to achieve super-resolution dSTORM is discussed in detail. A quantitative method for determining the reactivity of thiol dSTORM switching mountants was developed for use within the lab. Every fluorescent probe has different photophysical-properties which can be manipulated by varying the composition of the switching buffer to enhance desirable qualities, such as; increased photon counts, faster switching rates, and longer survivability. In addition to investigating the effects of buffer composition the use of a near UV light-source was also explored as a means of manipulating the same properties to improve overall resolution and quality of the resulting images. A range of photoswitchable fluorescent dyes were tested including Alexa Fluor 660 which is a dye that to my knowledge has not been greatly tested for use in single molecule localisation microscopy by others to date. This dye performed strongly alongside the traditional Alexa Fluor 647 used for dSTORM imaging in optimal conditions.

A relatively new approach to single molecule imaging which does not require the fluorophore to photoswitch, called DNA-PAINT (point accumulation for imaging in nanoscale topography), has been investigated throughout this thesis. This approach relies on the transient binding of small oligonucleotide sequences, called “Imagers”, to target docking strands anchored in positions of interest. These imagers have a photostable and bright fluorophore conjugated to the oligonucleotide. It is the transient immobilisation of the

imager strand, as it binds to a fixed docking strand, which appears as stochastic blinks. The duration of these events, which can be extended by increasing the number of overlapping base pairs, is primarily responsible for improved localisation precision and therefore potentially overall resolution. At the end of **Chapter 3** I compare this new pointillism microscopy approach, DNA-PAINT, with dSTORM using a set of custom-designed oligonucleotide sequences that allow both formats to be employed on the same target.

The transient binding of small strands of oligonucleotides offers a far more controllable system for stochastic imaging. In **Chapter 4** I use this superior approach to achieve greater resolution than other fluorescence techniques in biological samples, sufficient to visualise single ryanodine receptors (RyR). The RyR are extremely important in the contraction of muscle cells as they are capable of detecting transient changes to calcium concentration and are responsible for releasing large stores of calcium from the sarcoplasmic reticulum. With DNA-PAINT I observed that RyRs cluster into irregular arrays which contain significant gaps that are occupied by other proteins, including junctophilin (JPH). The stoichiometry of JPH with RyR varied cluster to cluster, exposing a new complexity in the regulation of RyRs.

In **Chapter 5**, quantitative super-resolution is reliably achieved through the implementation of quantitative DNA-PAINT (qPAINT) within the Python Microscopy Environment (PYME) software. Quantitative measurements are possible because of the statistical predictability of DNA hybridisation and the near constant influx of fresh imager strands by diffusion. This results in limited photobleaching, a permanent dark state. The frequency with which a region of interest blinks is proportional to the number of binding sites available, and therefore the mean dark time between detected events is also inversely proportional. I validate my approach to qPAINT, which maintains the spatial information of individual structures, by using a DNA-origami test slide. Two distinguishable structures were present and an estimate for the ratio of available docking sites between them was satisfactorily established. I conclude that with this tool, molecule densities can be inferred and information about biological samples can be probed to new levels.

The results of the full methodological approach to accomplish dual-colour super-resolution imaging of optically thick cardiac tissue, using both dSTORM and DNA-PAINT techniques, is discussed in detail in **Chapter 6**. The current range of photoswitchable fluorophores limits the possible combination of molecular dyes for use with dSTORM and some compromise is made in their selection. For DNA-PAINT, the prospect of chromatic aberration is removed by imaging the same dye in subsequent rounds of imaging. The process, called Exchange-PAINT, allows the user to remove previously imaged imager strands, through a series of washes, and replace them with a complementary sequence for another target. I introduce the concept of using quencher strands to eliminate signal from unwanted imager sequences, accelerating their removal in samples of reduced diffusion and decreasing the risk of sample disturbance, in a process we termed Quencher-Exchange-PAINT. Using this technique, I achieve superior super-resolution results in optically thick samples.

The results presented in this thesis are expected to (1) lead to a better understanding of the variables associated with single molecule localisation microscopy, (2) further reveal the complexity in cardiac protein distribution, (3) quantify relationships between co-localising proteins and other targets, and (4) apply DNA-PAINT to imaging in optically thick biological samples. This study shows promise for the future applications of the DNA-PAINT pointillism super-resolution method and its ability to investigate a multitude of biological questions.

Acknowledgements

To my incredible parents, you fed my curiosity for science and nature and never stopped me from asking why. Thank you.

To Sam, who came up with two Nobel prize ideas… several years too late. I look forward to the third! Thank you.

To Nic, who regularly heard from me late at night when walking home. Thank you.

Thank you to Nikki who has put up with the late nights, and occasional weekends without me, because she knows for how long I have wanted to do this.

Stuart Brown, Laura Innes, Hannah Johnson and James Ward, you will never read this and you are all hundreds of miles away but, in your own way, each of you still has the power to drive me forwards.

Thank you to those who successfully defended their work during my time here. Dr. Sahand Zanjani-Pumpkin-pour, Dr. Laureline Mahe, Dr. Martha Vardaki, and Dr. Kelly Curtis. Your advice and friendship has been invaluable to me.

Ryan Edginton, my old lab partner. I got you into this and perhaps once you hand in, you will forgive me…

Thank you to Dr. Izzy Jayasinghe, a fantastic scientist who has taught me a great deal. I still think you are on holiday.

Thank you Dr. Ruisheng Lin for the times you have helped me with python and optics. Always question whether the lamb can be served raw.

Prof. Christian Soeller, thank you for a project that has enabled me to do something interesting and different nearly every day. It has been incredibly enjoyable.

Prof. Peter Winlove, thank you for your enthusiasm. A wealth of knowledge and friendly counsel, I have appreciated every meeting.

Tobius Lutz, an engineer and a physicist play with DNA, imagine the consequences. If you do not say "oops" in your thesis, I will be disappointed.

Anna Meletiou, thank you for all of your questions over your first year, you have been excellent viva preparation.

Thank you to the whole of the Biomedical Physics group. It is an excellent interdisciplinary department and I have enjoyed my time with you all immensely.

“ It is not what we believe to be impossible that holds us back, but merely the limit to our imagination ”

AHC iGEM, 2012

Contents

Author's Declaration

Chapter 4 is the combined effort of Dr. I.D Jayasinghe and myself. The Chapter, in an edited form, is in the process of being submitted to a journal for scientific review as equal co-authors. I would like to thank Izzy for running the simulations present within and for the many discussions we have had on the topic.

Cultured cells were kindly provided by Rikke Morrish, whose expertise yielded excellent samples for use in super-resolution experimentation. Thank you Rikke for your time and skill.

List of Abbreviations

2D – Two-Dimensional

ATP – Adenosine Triphosphate

AU – Airy Unit

AV – Atrioventricular

BME – 2-Mercaptoethanol

BP – Bandpass

BSA – Bovine Serum Albumin

Ca^{2+} - Calcium

CICR – Calcium-Induced Calcium-Release

CLS - Collagenase

CSQ – Calsequestrin

DHPRs – Dihydropyridine Receptors

DM – Dichroic Mirror

DS – Docking Strand

dSTORM – Direct Stochastic Optical Reconstruction Microscopy

DTNB – Ellman's Reagent

E – Emission Filter

EC – Excitation-Contraction

EDTA – Ethylenediaminetetraacetic acid

EM – Electron Microscopy

FI – Fixed Imager

fPALM – Fluorescence Photoactivated Localisation Microscopy

FS – Field Stop

FW – Neutral density filter wheel

FWHM – Full-Width at Half-Maximum

HILO – Highly Inclined and Laminated Optical Sheet

I – Imager

JPH – Junctophilin

LLG – Liquid Light Guide

MEA – 2-Mercaptoethylamine / Cysteamine

NA – Numerical Aperture

Na_2SO_3 – Sodium Sulphite

$NaBH_4$ – Sodium Borohydride

NADH – Nicotinamide Adenine Dinucleotide

NaN_3 – Sodium Azide

NCX – Sodium-Calcium Exchangers

ND – Neutral Density

NGS – Normal Goat Serum

NIR – Near Infra-Red

OCT – Optical Cutting Temperature Compound

OL – Objective Lens

OTC – Oxygen Tight Chambers

P – Photobleaching

PA - Photoactivated

PAINT – Point Accumulation for Imaging in Nanoscale Topography

PALM – Photoactivated Localisation Microscopy

PBS – Phosphate Buffered Saline

PFA – Paraformaldehyde

PLN – Phospholamban

PSF – Point Spread Function

PYME – Python Microscopy Environment

qPAINT – Quantitative Point Accumulation for Imaging in Nanoscale Topography

ROI – Region of Interest

ROS – Reactive Oxygen Species

RT – Room Temperature

RyR – Ryanodine Receptor

S_0 – Singlet Ground State

S_1 – Excited Singlet State

SA – Sinoatrial

SD – Splitter Device

SEM – Scanning Electron Microscopy

SIM – Structured Illumination Microscopy

SMLM – Single Molecule Localisation Microscopy

SP – Short Pass Filter

SR – Sarcoplasmic Reticulum

STED – Stimulated Emission Depletion

STORM – Stochastic Optical Reconstruction Microscopy

T_1 – Triplet State

TCEP - Tris 2-Carboxyethly Phosphine

TEM – Transmission Electron Microscopy

TIFF – Tagged Image File Format

TIRF – Total Internal Reflection Fluorescence

TL – Transmitted Light Source

t-system – Transverse Tubules

T-tubules – Transverse Tubules

UV – Ultraviolet

Chapter 1

A brief history

This thesis is concerned with new techniques of high resolution optical microscopy and their application to research on myocardial proteins. In this Chapter, I introduce the key concepts important to optical microscopy. I look at a range of experimental techniques and technologies and how they are implemented. Later I discuss the physiology of the heart and the intricate structures present within cardiomyocytes. Existing problems in super-resolution microscopy and imaging cardiac tissue are deliberated and I set out how some of these issues can be addressed in later Chapters.

1.1. Resolution

Since its inception, optical light microscopy has been limited to the diffraction limit of light, first realised by Abbe in 1873[1]. He concluded that two illuminated objects could only be resolved if they are separated by a minimum distance *d*, which is approximately greater than half the wavelength of visible light being used to probe the sample, as described by equation (1.1).

$$d = {}^{\lambda}/_{(2\,NA)} \tag{1.1}$$

where *λ* is the wavelength and the numerical aperture of the objective lens, $NA = n \sin(\Theta)$ defined by the refractive index, *n*, and the aperture angle, $\sin(\Theta)$.

When a single point source emits light, the observer will always see a spot with a blurry outline, where at the centre of this object the light is actually emitted. When a second point source is introduced, the two are easily resolved, for as long as their emissions do not overlap, Figure 1.1. The closer the two point sources are, the more difficult it becomes to ascertain their exact position and distinguish separate sources within the point spread function.

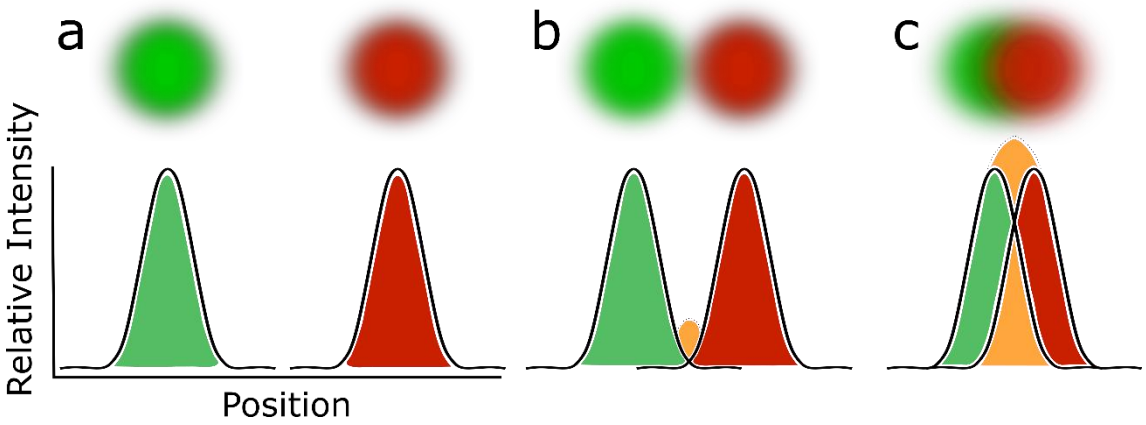

Figure 1.1. (Top) *Two single fluorophores, point sources, and* ***(below)*** *their respective point spread functions (PSF). Whilst the emission of the two probes are separated* ***(a)****, by a distance greater than d they can each be completely disassociated from one another and therefore are fully resolved. As the fluorophores are brought closer together* ***(b)****, the ability to separately resolve them becomes increasingly more difficult until* ***(c)****, they interfere with one another so greatly, due to their close proximity, that neither can be independently resolved.*

This problem increases with the number of light sources, as present in a well labelled fluorescent sample. The relative flatness, ability to grow onto and adhere to glass coverslips and the controllable nature of cultured cells makes them an ideal biological sample to use for optical experiments. Microtubules, formed of globular proteins alpha (α) and beta (β) tubulin, are involved in the transport of material within cells and have complicated networks of interlacing tubule filaments, Figure 1.2. These structures, which are prolific in COS-7 cells, when imaged with any normal wide-field fluorescence microscopy approach, appear blurred along their peripheries and merge into one complex where any overlap. This is caused by the diffraction limit of light which fundamentally is what limits the resolution of a given microscope.

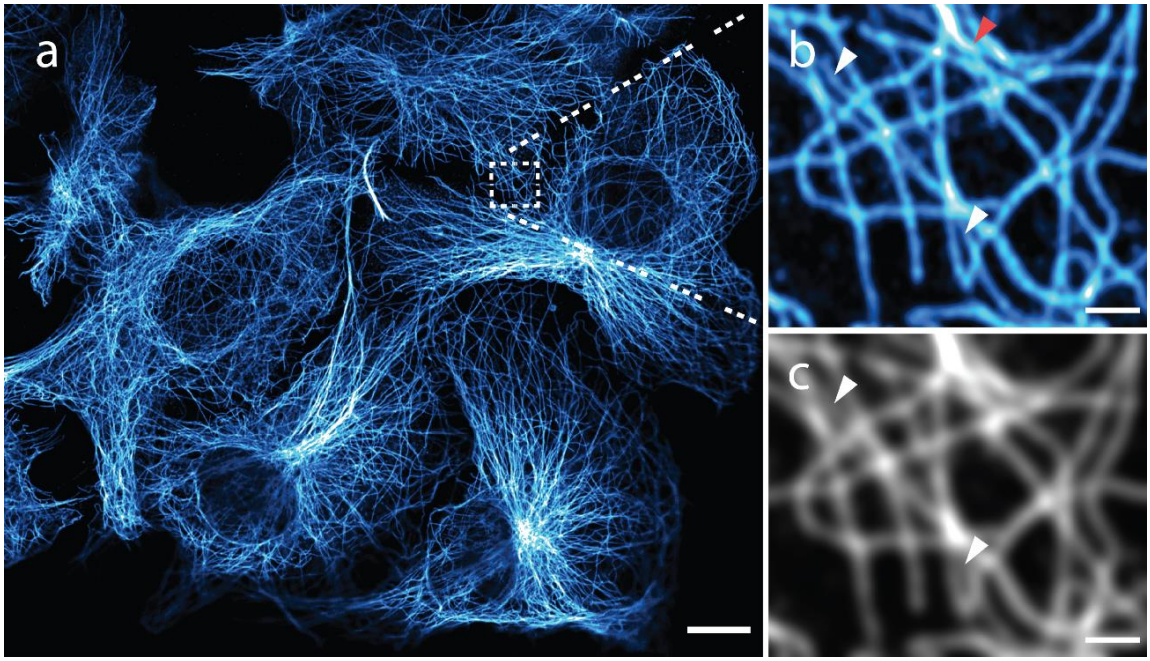

Figure 1.2. *An overview image* ***(a)*** *of COS-7 cultured cells, labelled to show the intricate structure of microtubules, taken with a Zeiss Airyscan system. The Airyscan system achieves the performance of a confocal microscope with a tightly closed pinhole* ***(a & b)****, whilst it can also be used to obtain conventional confocal microscopy images* ***(c)****, with a much larger pinhole diameter. The Airyscan region of interest image* ***(b)*** *has many overlapping microtubules, and in comparison to the simulated confocal microscopy image* ***(c)****, is able to differentiate between a greater number of these complexes (white arrows). There are examples in* ***(b)*** *however, that show the optical technique is still diffraction limited (red arrow), and does not allow all structures to be resolved.* ***Scale bars: (a)*** *1 µm,* ***(b&c)*** *100 nm.*

The resolution can be quantified by measuring a point like object, such as fluorescent beads of known size, to determine how ‘blurry’ they appear, Figure 1.3. Due to the diffraction limit this point source will appear larger than it really is, and the minimal size and shape observed is the system’s point-spread function (PSF), which fully quantifies the system resolution. Stepping through the sample axially will produce several concentric rings of decreasing intensity, light and dark, spreading away from a central bright disc-like object, caused by the diffraction of light, Figure 1.3b. It is the size of this central bright spot, called the “Airy disk”, which provides a measure when two points

will be resolvable. Known as Rayleigh's criterion their distance *d* must be at least the radius *r* of an Airy disk shaped PSF. The full width at half-maximum (FWHM) of a PSF will also give a reasonable measure of the obtainable resolution, Figure 1.3.

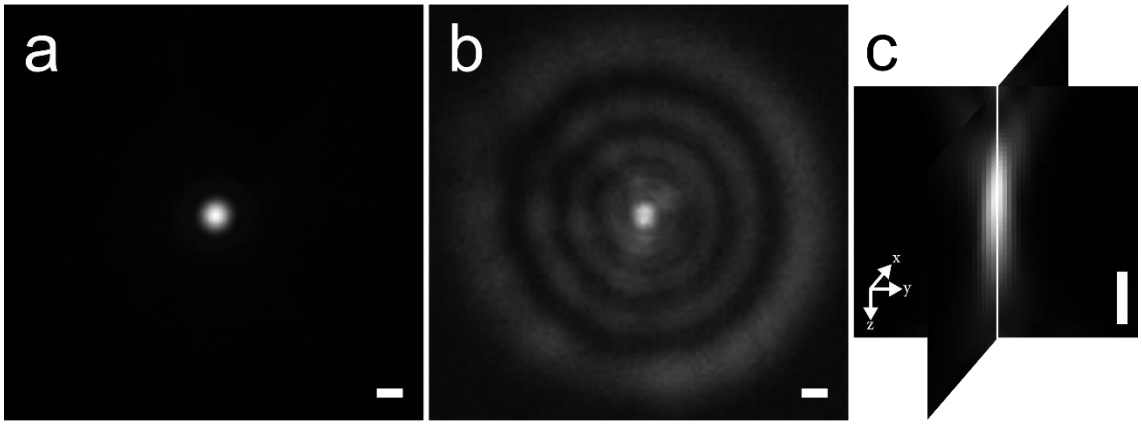

Figure 1.3. *Obtaining the point spread function of an optical experimental setup. A sub-diffraction 100 nm dark red fluorescent bead* ***(a)*** *acts as a single point source emitter. As the focal plane is moved, above and below the axial position of the bead, Airy disks are observed* ***(b)****. After a complete z-stack has been taken its three-dimensional profile* ***(c)****, can be visualised.* ***Scale bar:*** *200 nm.*

Another important constraint to consider when obtaining digital data is the Nyquist sampling theorem. It states that; in order to reconstruct the original input from the sampled data, the sampling frequency must be greater than twice the bandwidth of the input signal[2]. For imaging, this corresponds to the minimum size each pixel should represent when taking an image, and is approximately half the expected resolution of the system, Figure 1.4.

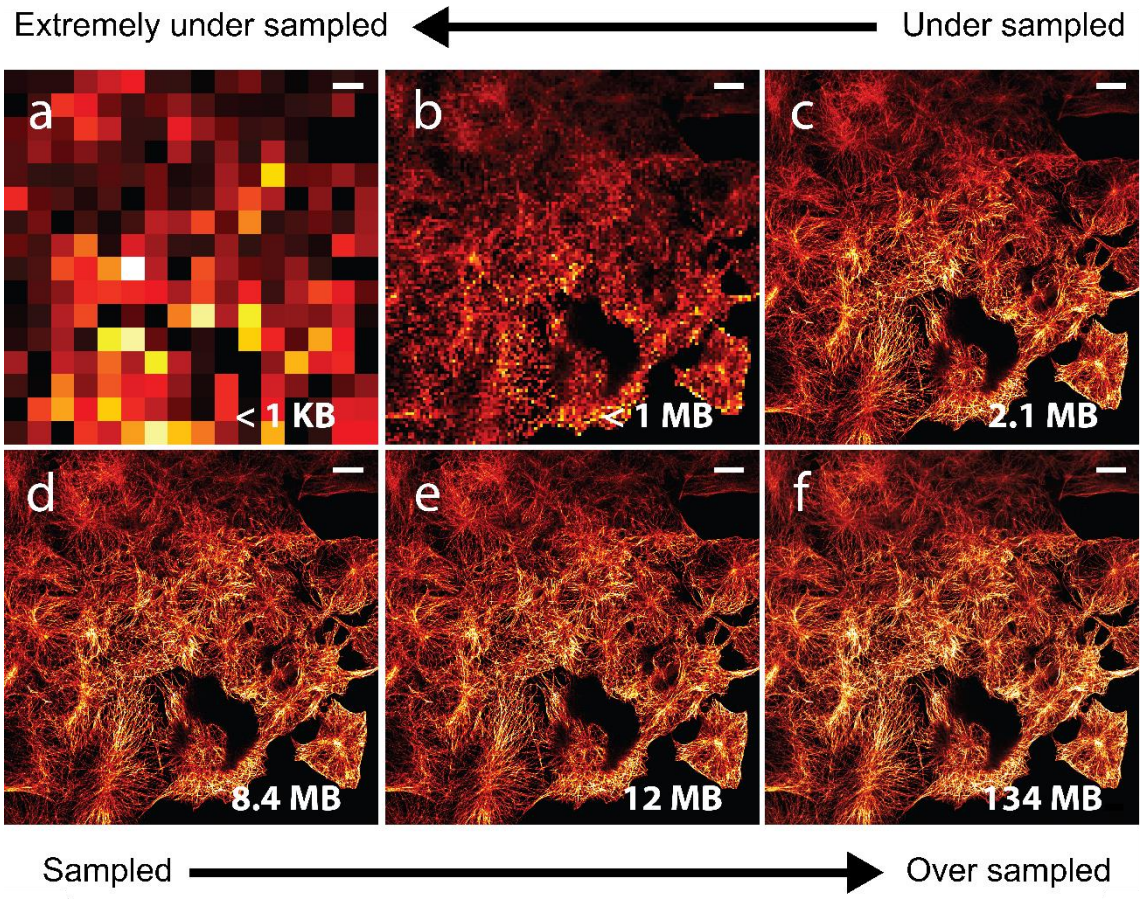

Figure 1.4. *Observed under different sampling conditions, a cultured COS-7 α-& β-tubulin labelled sample, imaged on a confocal microscope. Extreme under-sampling* ***(a)****, effectively making pixel sizes far larger than the intricate structures the experimentalist desires to image, produces unrecognisable data. As the pixel size is reduced the individual cells begin to be resolved* ***(b-c)*** *but still hide objects smaller than the pixel size. A correctly-sampled image* ***(d)*** *shows the complex windings of the microtubular structures. Slightly over-sampling during image acquisition* ***(e)*** *is an acceptable approach, as nothing is lost by this cautious methodology, as file size will only grow gradually. Extreme over-sampling* ***(f)*** *has two main points of concern. Firstly, the acquisition time required to generate such an image increases, exposing biological samples to longer than necessary irradiation and leads to photobleaching as the image is taken. The second important factor is the growth in file size, comparing* ***(e)*** *to* ***(f)****, no additional useful information has been uncovered and yet an additional 100 megabytes has been added to the file. Image file size* ***(bottom right)****.* ***Scale bar:*** *20 µm.*

From equation (1.1) it is clear that there are two ways to improve optical resolution; firstly to increase the numerical aperture and secondly to use shorter wavelengths. Numerical apertures are already at values that limit refractive index mismatching of oil/glass and imaging media with high refractive indices, such as glycerol are regularly used. Visible light is also clearly constrained to operating within 400 – 700 nm but obviously is not the only method to image. Electron microscopy (EM) techniques utilise wavelengths in the picometre scale, calculated from the electron's momentum, and can therefore achieve resolutions of sub-nanometre. The process requires an electron gun, with high voltage electromagnetic coils, to accelerate electrons towards the target and, in the case of transmission electron microscopy (TEM), straight through the sample, enabling the user to image inside at sub-nanometre resolution[3]. Scanning electron microscopes (SEM) use a series of electromagnetic coils to scan the electron beam across the surface of the sample. Here the electrons effectively "bounce" off of the surface, creating secondary electrons which are collected, generating a highly detailed image of the surface of the object[4]. Despite the clear resolution advantage of EM there are several drawbacks that include; cost, sample preparation, technical training, space, and the impossibility of imaging live samples. It is for these reasons that any improvement to resolution in fluorescent microscopy is greatly sought after[5].

1.2. The confocal microscope

Imaging thick samples, greater than several microns, that have been fluorescently labelled is difficult with conventional widefield microscopy. This is simply due to all light being collected from the sample at the same time, increasing the background levels. In 1955 Marvin Minsky invented the confocal microscope[6], which through the use of a pinhole rejects out of focus information, Figure 1.5. A scanning confocal microscope illuminates a single diffraction-limited area at a time with a focussed laser, so that detected intensity drops off rapidly above and below the plane of focus. More importantly a pinhole, which is conjugate to the focal point, passes all emitted fluorescence from that plane and very little out of focus information. This

significantly reduces the amount of out of focus background obtained during imaging and makes the confocal microscope an indispensable tool for microscopists. Further improvements to the confocal microscope have recently been made in the form of the Airyscan system[7] using the concept of pixel reassignment[8]. Here the single pinhole is replaced with a hexagonally-packed detector array in a conjugate focal plane to the excitation spot. This array of 32 detectors, each with an effective 0.2 airy unit (AU) sized pinhole and combined collection efficiency of 1.25 AU, has both the advantages of combining the resolution benefits of imaging with a small pinhole while achieving high signal with the use of large pinhole. An improved linear deconvolution can also be accomplished based on the higher signal to noise ratio achieved, resulting in ~1.7 times improved resolution in all spatial directions.

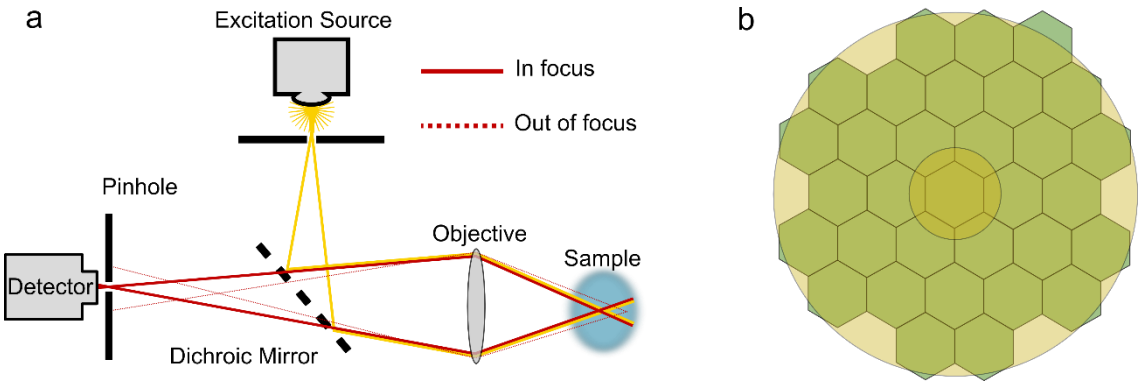

Figure 1.5. *A diagram depicting the confocal microscopy principle* ***(a)*** *shows that out of focus fluorescence, emitted from the sample, is attenuated through the use of a confocal pinhole. The Airyscan uses an array of 32 hexagonally-packed detectors,* ***(b)****, in place of the conventional confocal pinhole, improving resolution in x, y, and z by a factor of nearly two.*

1.3. TIRF and HILO

Total internal reflection fluorescence (TIRF) microscopy utilises an evanescent field, which is created when an incident laser beam totally internally reflects at the interface, that propagates parallel to the surface[9]. This limits the excitation volume in the sample to a region at the surface of

the coverslip. The angle at which total internal reflection (TIR) occurs is called the critical angle θ_c, Figure 1.6, and can be determined from using Snell's Law, equation (1.2).

$$\theta_c = sin^{-1}(n_2/n_1) \tag{1.2}$$

where n_2 is the refractive index of the sample and n_1 the refractive index of the coverslip.

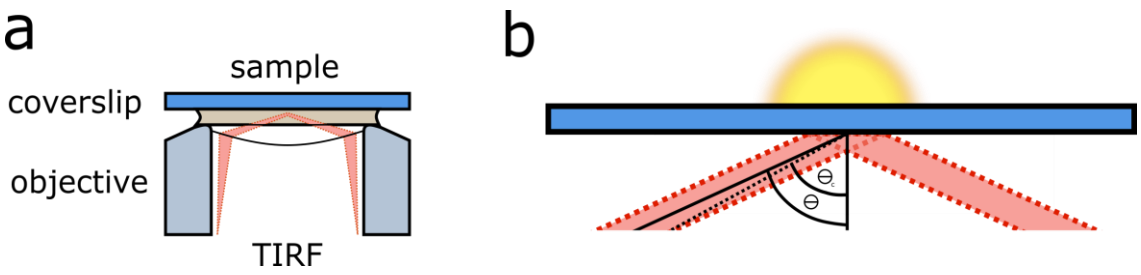

Figure 1.6. (a) *A laser beam is focussed onto the back focal plane of a TIRF objective lens. The incoming beam enters at an angle θ exceeding the critical angle* θ_c. ***(b)****. The evanescent field produced is restricted to a few hundred nanometres above the coverslip.*

The evanescent field intensity, *I(z)*, exponentially decays with perpendicular distance *z* from the interface, equation 1.3.

$$I(z) = I_0 e^{-z/d} \tag{1.3}$$

where *d* is the penetration depth found by equation 1.4.

$$d = \frac{\lambda}{4\pi\sqrt{n_1^2\, sin^2\, \theta - n_2^2}} \tag{1.4}$$

where λ is the wavelength of light used and *θ* is the angle of incidence greater than the critical angle. This improves the signal to noise by reducing the background fluorescence whilst only the labelling close to the surface are excited.

If the target structure to be imaged is deeper than the maximum depth achievable with TIRF, such as for sectioned tissue or suspended cells, another imaging mode called highly inclined and laminated optical sheet (HILO) microscopy[10] can be implemented. Here the incident angle is just less than the critical angle so that the laser beam is refracted into the sample, Figure 1.7. A signal to noise relationship suitable for single molecule is still produced and enable SMLM in optically thick samples.

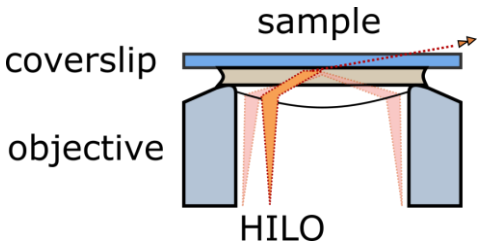

Figure 1.7. *The angle of incidence is such that the laser beam is highly inclined after refracting at the glass interface.*

1.4. Super-resolution microscopy

Clever workarounds have been developed over the last decade to beat the diffraction limit of visible light using far-field approaches[11]. Structured illumination microscopy (SIM) creates a series of Moiré patterns that are projected and rotated over the imaged sample. After processing, these structures are removed and result in high frequency information yielding a resolution of approximately 130 nm[12].

Stimulated emission depletion (STED) achieves super-resolution by narrowing the PSF of an ensemble image containing multiple fluorophores. As in confocal microscopy a laser is scanned across the sample, however before the sample can fluoresce, a second, red-shifted American doughnut shaped, laser also illuminates the region. This STED-beam forces the excited fluorophores back into their ground-state, within the beam, leaving only the centre to fluoresce thus manufacturing an improved PSF. A modified version of equation (1.1) describes the obtainable resolution of a STED system[13], equation (1.5).

$$d = \lambda \Big/ (2\,NA)\sqrt{1 + I_{STED} \Big/ I_{fSAT}} \tag{1.5}$$

where I_{STED} is the intensity of the STED-beam and I_{fSAT} is the intensity at which the fluorescence emission of the dye is reduced by half.

Theoretically this approach can routinely achieve single-nanometre resolution, however experimentally the complexity of the optics and the high intensity required for the STED-beam makes the process difficult in practice[14].

A relatively simple idea, that beats the diffraction limit of light and achieves super-resolution, relies on a pointillism approach where the fluorescent molecules are reversibly switched between light and dark states. In doing so, single probes are detected and, dependent on the number of collected photons, are localised with a high degree of accuracy. Three such pointillism techniques all surfaced independently in 2006 and revolve around the same principle of stochastically switching fluorescent probes on and off, these are; photoactivated localisation microscopy (PALM)[5], fluorescence photoactivated localisation microscopy (fPALM)[15] and stochastic optical reconstruction microscopy (STORM)[16]. The real difference between each of these papers is the photoswitchable probe used in their experiments and therefore, for the purpose of this thesis, only the STORM acronym will be carried forward.

1.5. direct Stochastic Optical Reconstruction Microscopy (dSTORM)

The ability to localise multiple fluorescent probes within a sample can be achieved with what now appears to be a straightforward idea. It is accomplished with the use of photoswitchable molecules[17] that can be switched between an “on” and “off” state by exposure to intense laser light, Figure 1.8. By keeping the majority of fluorophores in the off position, or dark state, at any one moment only a handful will be in a fluorescent state. This pointillism approach massively reduces the probability that any two probes’

fluorescence will be overlapping, enabling each to be imaged and localised with high precision[18]. The process is repeated until all emission has been exhausted and can no longer emit photons or until no new event gives the user any additional information towards the underlying structure. From the measured locations of each molecule, a super-resolution image can then be constructed, Figure 1.8.

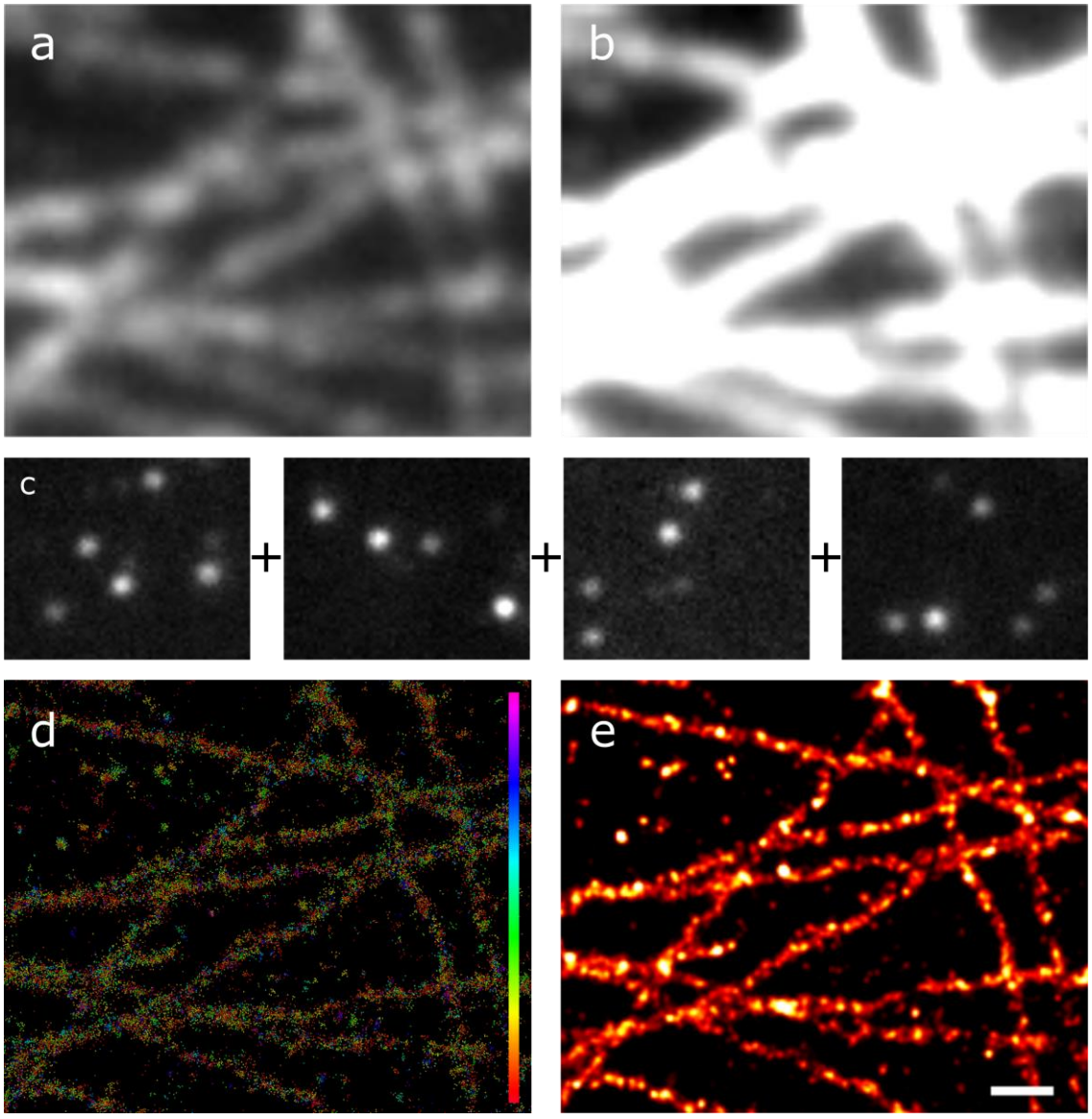

Figure 1.8. *The process of dSTORM. A fluorescently labelled microtubule sample* ***(a)****, imaged with a conventional widefield microscope, displays the diffraction limited resolution of the system. The sample is then strongly illuminated with laser light* ***(b)****, pushing the majority of the fluorescent probes into a dark state. Subsequently these markers stochastically recover and are able to fluoresce again at some future point in time* ***(c)****. Each detected event has their central position precisely localised by fitting a Gaussian profile to the individual event, colour coded for time* ***(d)****. These localisations, when combined together, beat the diffraction limit, to produce a super-resolution image* ***(e)****.* ***Scale bar:*** *100 nm.*

The resolution of this assembled picture is not limited by diffraction, but instead on the precision of localising each fluorophore and their density within the sample[19]. These conditions rely directly on the quantity of photons emitted (and collected) each time a probe fluoresces, and the ability to achieve a high labelling density of marker molecules with low background fluorescence.

1.6. Fluorescence and photoswitching

Normal fluorescence occurs when a photon gets absorbed, and in doing so stimulates a singlet ground state (S_0) molecule into an excited singlet state (S_1). As the molecule returns to the ground state, energy is released in the form of a photon having a longer wavelength than the one used to excite, Figure 1.9a. In this simplified model, when a sample is labelled with a fluorescent probe and is illuminated with appropriate excitation, the molecules get excited and photons are subsequently released in events lasting nanoseconds. This process repeats numerous times before photobleaching, an irreversible non-fluorescing state, inevitably occurs. The kinetics in a real fluorophore is more complex and several other states and processes exist, each with their own probabilities of occurring. After the molecule has been excited, there is a very low probability of decaying into an excited triplet state (T_1), Figure 1.9b. This transition, which competes with the fluorescence processes, is termed “intersystem crossing” and is allowed only through spin-orbit coupling[20]. Whilst in T_1 the fluorophore is unable to undergo fluorescence emission until relaxation to S_0 is achieved. In this position, relaxation lasts an order of magnitude longer than normal S_1 to S_0 fluorescence. Through chemical reduction, the triplet state can further enter more prolonged, meta-stable, dark radical anionic states.

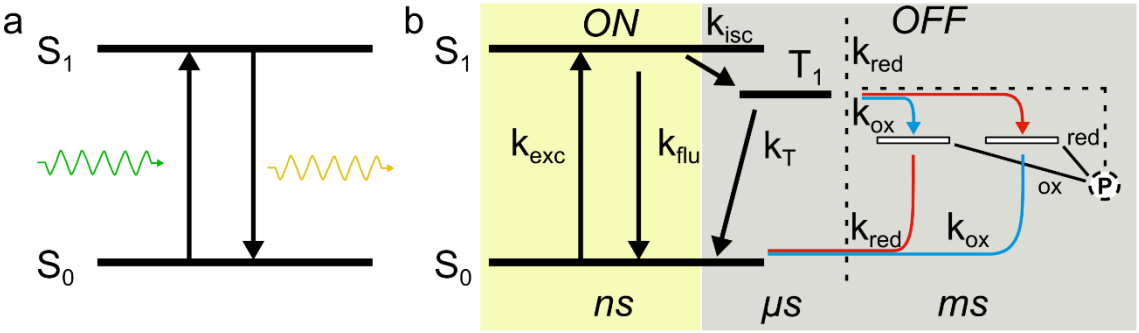

Figure 1.9. *A Jablonski diagram showing a simple fluorescing process* ***(a)*** *as a molecule is excited from its ground state, S_0, to the singlet excited state, S_1, and the subsequent emission of a photon as it returns to rest. The inclusion of more complex, additional possible transitions* ***(b)****, dependent on a probability factor k; most importantly, k_{isc} the intersystem-crossing rate, that leads to the triplet, T_1, state. Once in the T_1 state, redox reactions with oxidants* ***(ox)*** *or reducing agents* ***(red)****, present in dSTORM buffers, transition the fluorophore from the triplet state to a meta-stable, dark radical anionic/cationic state. Inevitably, any point of the fluorescence process can be subject to photobleaching* ***(P)****, an irreversible darkened state.*

The probe is more sensitive to entering an irreversible dark state if it reacts with molecular oxygen[21]. This results in the production of reactive oxygen species (ROS), which is a source of phototoxicity to cells. A singlet state is one where all electron spins are paired, thus the excited electron is still paired with the ground state electron. In contrast, a triplet state is no longer paired and will have the same spin as the ground state. Due to forbidden spin transitions, the probability of this occurring is approximately one in every thousand events. It is possible to increase the probability of intersystem crossing events when the fluorophores are in the presence of paramagnetic materials[22] or heavy atoms[23]. However an easier method to increase the number of molecules entering the triplet state is to raise the power of the laser used to probe the system. This generates far greater numbers of cycles between ground and excited states, pushing the majority of fluorophores into the triplet, and subsequently dark states.

1.7. Switching buffers

Several probes have now been shown to be effective at achieving semi-controllable photoswitching and have thus been used in numerous articles in which they were successfully used for super-resolution imaging. These include the carbocyanine fluorophores (e.g. Cy5)[24], oxazine fluorophores (e.g. ATTO655)[25], and rhodamine fluorophores (e.g. Alexa Fluor 647)[26]. The sensitivity of some synthetic organic fluorophores towards reducing agents enables them to be operated as photoswitchable molecules. This process is due to the formation of stable non-fluorescent states and can be achieved using thiol compounds. A thiol is an organic compound that contains a carbon bonded sulfhydryl group, and is readily oxidised. The triplet state dye is quenched upon reduction or oxidation by suitable electron donors or acceptors and a radical ion is formed. A second complementary redox reaction restores the probe to its singlet state[27].

Current dSTORM methodologies commonly use mounting, or switching, buffers that contain millimolar concentrations of 2-Mercaptoethylamine (MEA) or 2-Mercaptoethanol (BME), thiols that behave as reducing agents. An additional choice experimentalists have is the use of aqueous or glycerol based solutions both having their own merits. Aqueous mountants often require a system to scavenge the free oxygen, such as oxygen scavenging enzymes like glucose oxidase, to improve photoswitching. This process, however, leads to the production of hydrogen peroxide and increases the overall acidity of the solution, potentially harming living samples.

Due to the low diffusivity in glycerol, the removal of oxygen is not an immediate process. This consequently adds to the preparation time required, before it can become an effective and suitable switching buffer. Glycerol has the additional benefit of having a larger refractive index (~1.47) as compared to aqueous solutions (~1.33). As explained previously in equation (1.1), a larger refractive index will improve resolution but of greater importance is its closeness to that of the glass coverslip (~1.52). Refractive index mismatching increases the amount of spherical aberration observed with increasing depth[28] and should therefore be kept minimal.

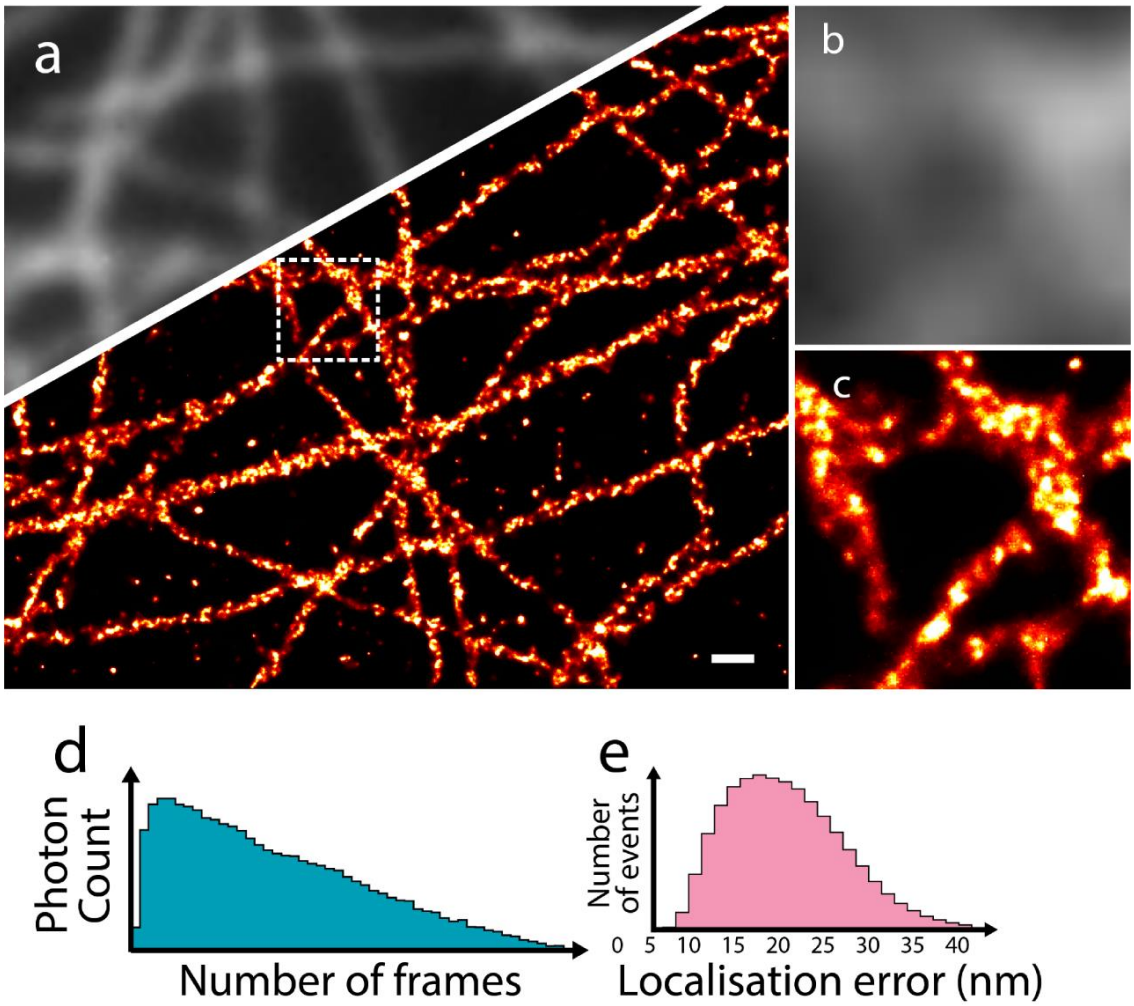

Figure 1.10. *A comparative widefield (top) and super-resolution image (bottom), acquired using the dSTORM approach, of α and β tubulin in COS-7 cultured cells* ***(a)****. A magnified view of the boxed region in* ***(a)*** *displays the obscured nature of the widefield* ***(b)*** *and the level of resolvable detail found using single molecule localisation microscopy (SMLM) techniques* ***(c)****. The process requires thousands of frames to reliably construct a well-labelled super-resolution image. Over the time it takes to acquire these frames, inevitably, the fluorescent probes become permanently photobleached, at this point the number of detected events depletes to near zero* ***(d)*** *bringing an end to the experiment. Largely dependent on the number of photons collected per event, the localisation precision can be measured* ***(e)****.* ***Scale bar:*** *100 nm.*

As one may expect, the dSTORM technique is disk-space hungry, with the final image being constructed from the localisations obtained across tens of thousands of camera frames. The colossal amount of information recorded quickly results in gigabytes of generated data, and both handling and storage of this will be a significant challenge to future researchers. An x-y spatial resolution of typically 20-60 nm is attainable, Figure 1.10, with acquisitions taking in excess of ten minutes. The duration makes drift, in both lateral and axial directions, a considerable adversary that is capable of producing imaging artefacts. The length of experiments, high laser powers, and the use of special mounting mediums required to construct a super-resolution image present considerable difficulties.

dSTORM is reliant on the ability of the fluorescent dye to switch between "on" and "off" states. Out of the many fluorophores that have been tested, there is only a subset that have the desirable qualities sought after for photoswitching probes[29,30]. These attributes include; high photon yields, sufficient "on" times, and resistance to photobleaching. Understanding dye behaviour and how these characteristics can be enhanced by experimental interaction is critical to obtaining high quality single molecule super-resolution data.

1.8. Point Accumulation for Imaging in Nanoscale Topography (PAINT)

A single molecule localisation microscopy (SMLM) method that avoids photoswitching of the fluorophores completely has recently been developed[31]. This approach, called DNA-PAINT[32], uses the predictable nature of DNA hybridisation to image the transient binding of oligonucleotides to target docking sites. Here the oligonucleotides, termed '*imagers'*, have a fluorophore modification and are introduced into the sample solution. They are free to diffuse through the media and bind to complementary sequences situated at desired marker locations. Controlling the concentration of the imager strand allows for single, non-overlapping, events to be recorded, in the same manner as dSTORM, indefinitely. The length of complementary base pairs, between imager and docking strands, regulates the duration of

these events. This controllable feature enables detectable events to emit greater photon numbers, improving localisation precision beyond those obtainable in most dSTORM experiments. The improved resolution can be used to further enhance our knowledge of diffraction-limited structures.

1.9. Camera technology

Single molecule localisation microscopy commonly use electron multiplying charge-coupled devices (EMCCDs) for their high sensitivity and low effective readout noise. However, they have relatively slow readout, small sensor areas and are costly in comparison to sCMOS camera technology, Table 1.1.

Specifications	EMCCD iXon 897U	sCMOS Zyla 4.2+
Sensor format	512x512	2048 x 2048
Pixel size (µm)	16	6.5
Sensor diagonal (mm)	11.6	18.8
Read noise	<1 e^- with EM Gain	0.9 e^-

Table 1.1. *Specifications of an iXon 897 Ultra EMCCD and Zyla 4.2+ sCMOS. Figures obtained from Andor, more information available at their website (www.andor.com).*

An EMCCD works by transferring the electron signal in a pixel along a many-stage multiplication register. Each pixel in an sCMOS camera has its own individual readout, rather than a single readout port in the case of CCDs. This results in non-uniform pixel characteristics and therefore a subset of pixels have significantly higher noise or offset values. When using standard SMLM algorithms, which assume uniform pixel properties, this may cause imprecise localisations near these pixels. Recently however, an sCMOS localisation algorithm which incorporates pixel specific properties based on a weighted least squared fitting method has been presented that removes the effect of sCMOS pixel non-uniformities[33]. This approach has been used in conjunction with the sCMOS camera used throughout this thesis.

Although the quantum efficiency (QE), Figure 1.11, is higher in an EMCCD (~90%) than that of our sCMOS (~60%) however, noise introduced during the amplification process results in a lower SNR by a factor of ~$\sqrt{2}$ and effectively halves the QE of EMCCD sensors to <45%[34]. This, alongside ongoing CMOS sensor development, means that sCMOS cameras now perform as well as, or better than, EMCCD for SMLM at a fraction of the cost and have the added bonus of larger chip sizes.

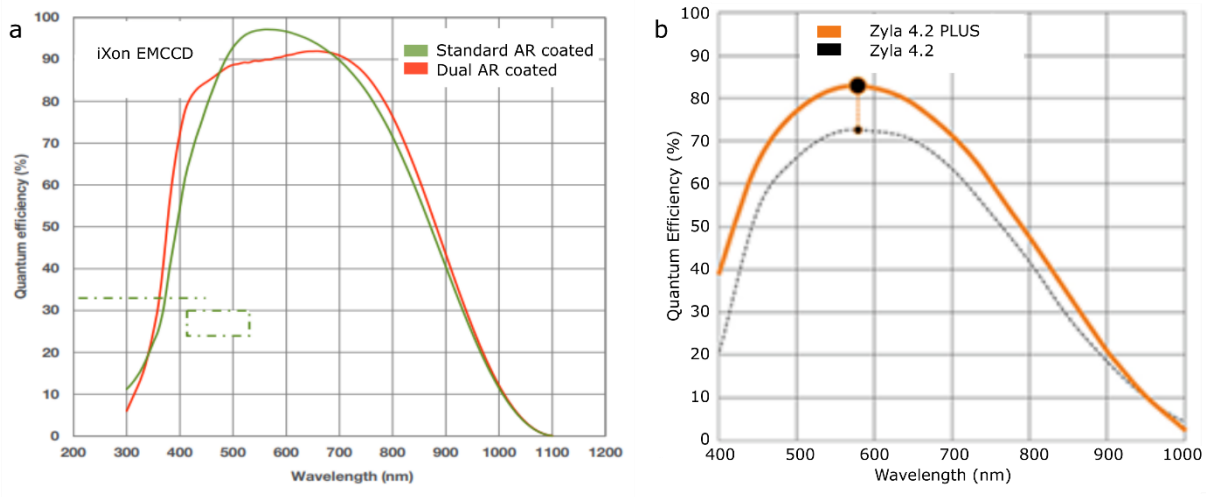

Figure 1.11. *Quantum efficiency profile across different wavelengths for iXon EMCCD* ***(a)*** *and Zyla 4.2 sCMOS* ***(b)*** *cameras, taken from www.andor.com.*

1.10. Cardiac physiology

The mammalian heart is constructed of four chambers; two atria, left and right, that receive blood; and two ventricles, left and right that pump the blood outwards, Figure 1.12. The right ventricle pumps deoxygenated blood out of the pulmonary artery towards the lungs for the pulmonary circuit. Using its thicker-chambered walls, the left ventricle pumps oxygenated blood out to the aorta to complete the systemic circuit. These pumping mechanisms occur synchronously with every heartbeat, without tiring, for a lifetime.

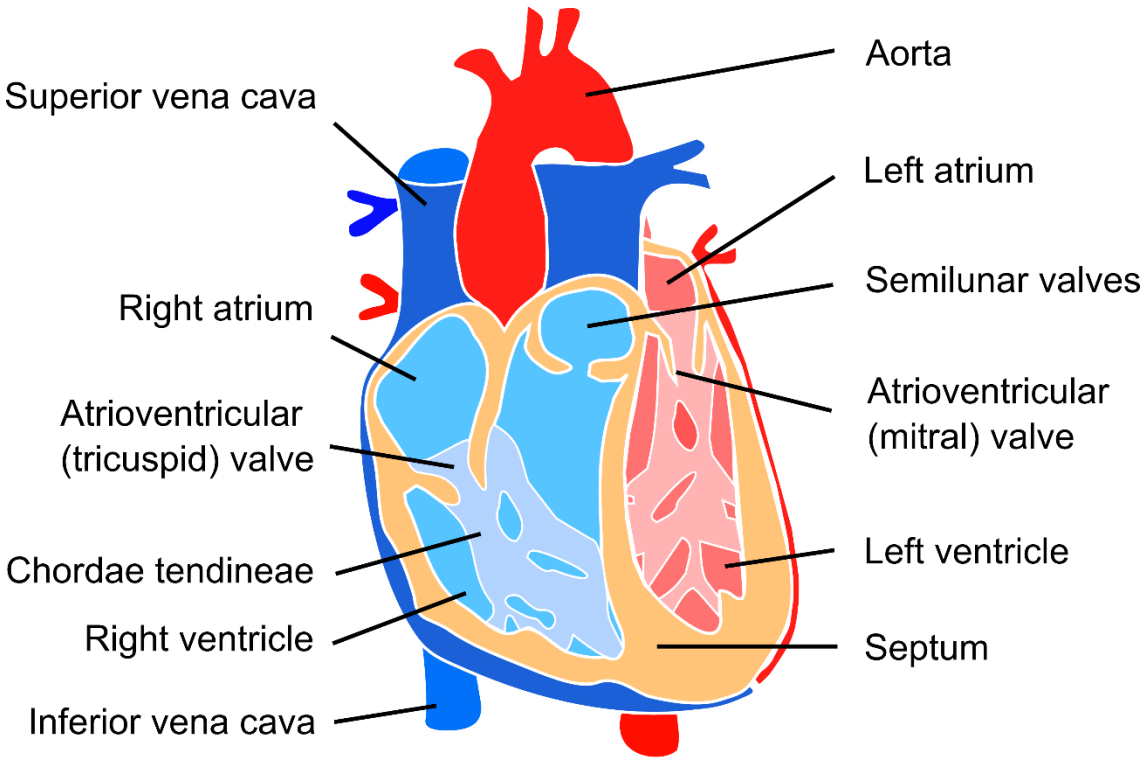

Figure 1.12. *A sectioned diagram of the human heart, labelling key anatomical features.*

1.11. Structure of the muscle cell

There are several morphological and functional differences between cardiomyocytes and skeletal muscle cells, however their contractile elements are quite similar[35]. Each cell is packed with long, contractile bundles termed

myofibrils, and each myofibril is composed of numerous basic contractile units called sarcomeres, Figure 1.13. These span from Z-line to Z-line and contain thick filaments made of myosin (in the A-band) and thin filaments containing actin. The thin filaments extend from their anchored position on the Z-line, through the isotropic I-band, and are free in the A-band interposed between the myosin filaments[36].

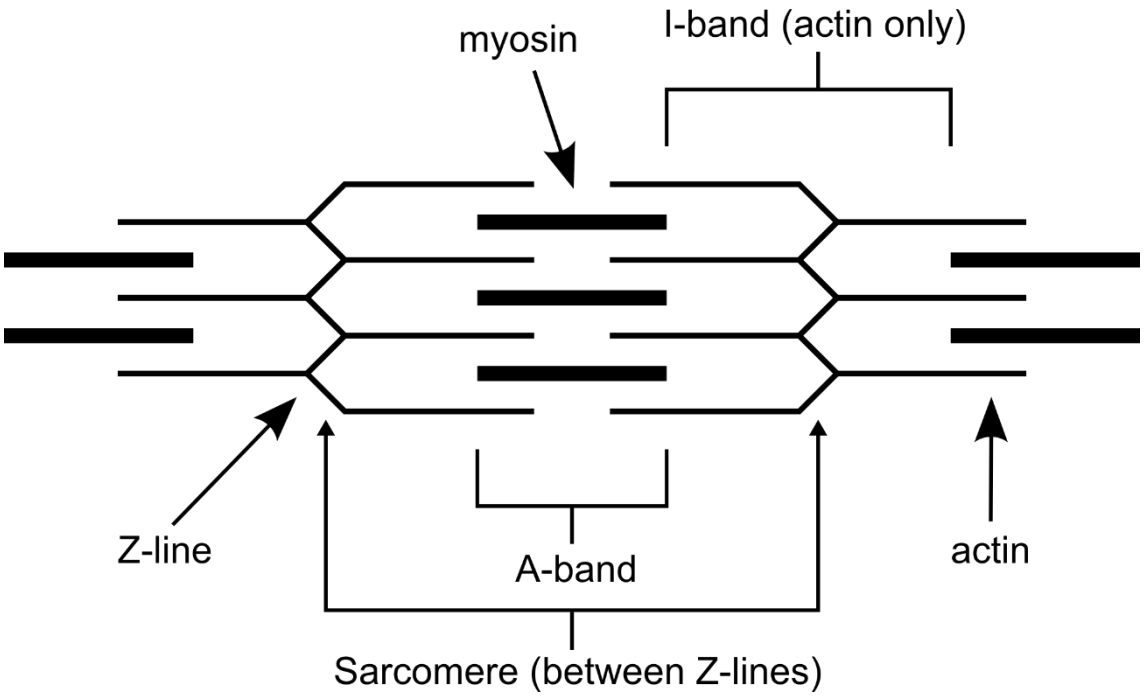

Figure 1.13. *The contractile elements in mammalian muscle. Myosin, the thick filaments, are confined to the A-band whilst the thin actin filaments extend from the Z-line and intertwine, as shown. Upon contraction, the myosin heads pull the actin filaments, bringing the Z-lines closer together.*

Mitochondria are organelles that convert energy stored in the chemical bonds of nutrients into adenosine triphosphate (ATP), the energy currency in biological systems, and are often referred to as the “power houses” of biological systems. The requirement for cardiac muscle to contract repetitively for a lifetime means they require a near-continuous energy supply[37]. This is achieved thanks to mitochondria occupying approximately 30-40% of each cells’ volume in the heart[38].

Transverse tubules, or T-tubules, are deep invaginations of the sarcolemma, the cell membrane of striated muscle cells into the fibre at the Z-lines, Figure 1.14, and play a key role in distributing the action potential across the cell[39]. Within the muscle cytoplasm there is a second set of tubules called the sarcoplasmic reticulum (SR). These are a closed set of anastomosing tubes that in places pass very closely to the T-tubules and sarcolemma[40].

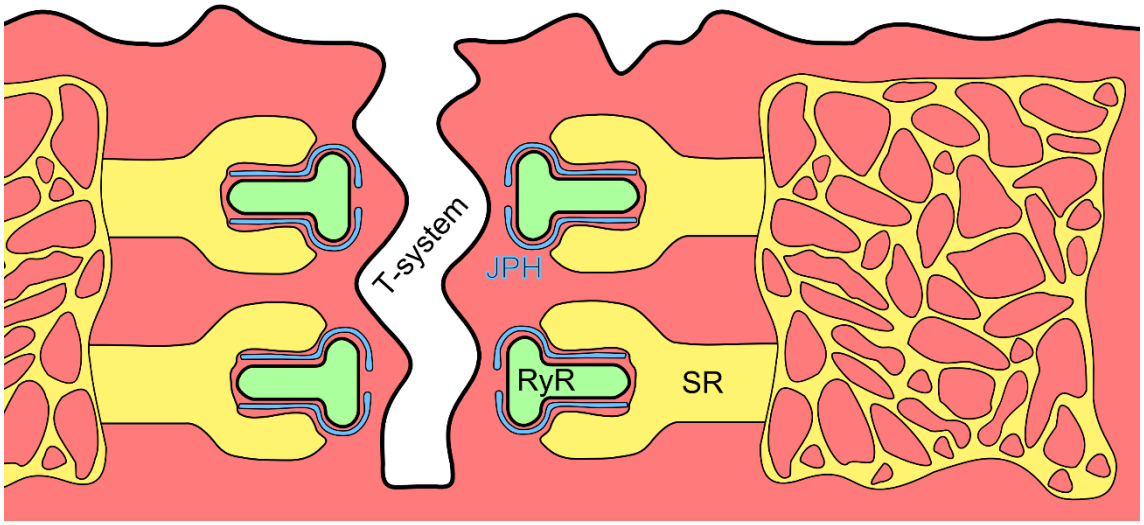

Figure 1.14. *A diagram depicting some of the important architecture present within cardiomyocytes. The transverse-tubules* ***(T-tubules/system)*** *are continuous from the outer membrane of the sarcomere, enabling a continuous propagation of electrical stimulus that quickly reaches inside the cell. The ryanodine receptors* ***(RyR)*** *are intracellular Ca^{2+} channels that form clusters in junctions between the T-system and the sarcoplasmic reticulum* ***(SR)*** *network. In these positions the RyR are capable of detecting transient increases to intracellular levels of calcium coming from outside of the cell and open up their gateway to the SR to release large stores of calcium present within, leading to contraction. Junctophilin* ***(JPH)*** *are membrane proteins of the SR and play a role in junction formation and maintenance[41].*

The SR has a large store of calcium ions which are partially released into the sarcoplasm when the cell is excited, leading to its contraction, and thus is of major importance[42]. There are two functionally-distinct regions of the SR that handle Ca^{2+} differently, namely the junctional SR which is involved in Ca^{2+}

release and network SR which is involved in Ca^{2+} uptake. The junctional SR approaches T-tubules to within 15 nm and the lumen contains a store of Ca^{2+} loosely-attached to the protein calsequestrin (CSQ), each molecule of which can bind approximately 40–50 Ca^{2+} ions[43]. Gigantic proteins extend from the junctional SR called Ryanodine receptors (RyRs); these are Ca^{2+} release channels and are activated once they detect an increase to free Ca^{2+} in their local periphery. The network SR comprises of a network of tubes that run over the myofibrils and actively take up sarcoplasmic Ca^{2+} through Ca^{2+} ATPase pumps (SERCA), which in turn are regulated by an inhibitory protein, phospholamban (PLN)[44].

1.12. How the heart beats

In order to beat, the heart is reliant on an electrical action potential[45], that originates in the sinoatrial (SA) node and is radially dispersed across the heart. Specialised myocytes called pacemaker cells have a membrane potential oscillator that spontaneously generates repetitive action potentials[46]. These travel across the wall of the atrium to the atrioventricular (AV) node, which traverse slowly in order to allow the atrium to contract prior to the ventricle. The signal then rapidly passes along the ventricular bundle to the septum and descends to the base of each ventricle, where Purkinje fibres from the bundle branch to the ventricular walls. This rapid conduction allows the ventricular muscle cells to contract in unison[47]. The action potential in human ventricles consists of a series of phases, Figure 1.15. Briefly, the rapid depolarisation is caused by a Na^+ influx which neutralises the negative charges inside the cell until an electrostatic force no longer pulls Na^+ in. Due to the large concentration gradient, Na^+ continues to enter the cell until the inactivation gate closes, creating the positive overshoot on the action potential. As the membrane potential becomes progressively less negative, the voltage regulated long lasting, or L-type, Ca^{2+} channels open. Ca^{2+} enters the cell throughout the plateau phase because the intracellular Ca^{2+} concentration is much lower than the extracellular concentration. It is this calcium that is involved with excitation-contraction (EC) coupling. Just before the plateau phase begins voltage gated K^+ channels open, allowing

the K^+ ions to leave the contractile fibre. Ca^{2+} inflow balances K^+ outflow, sustaining the depolarisation. As the L-type Ca^{2+} channels close, K^+ re-enters the cell exceeding the efflux of Ca^{2+}, causing the membrane potential to again become negative, resulting in the associated repolarisation. The resting membrane potential is dominated by K^+, to which the cells are most permeable at rest.

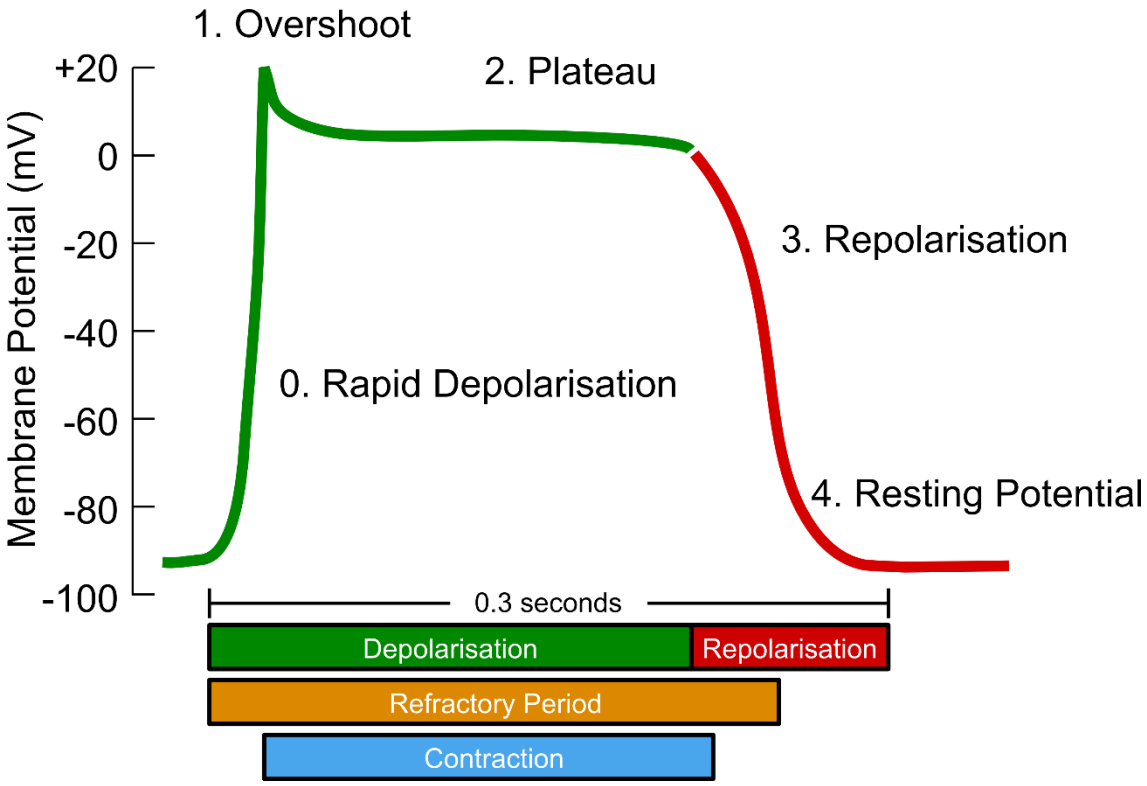

Figure 1.15. *The action potential, in healthy human ventricular myocytes, is the resultant of changes in ionic concentrations.* ***Phase 0:*** *rapid depolarisation occurs due to an increase in sodium and the expulsion of potassium ions.* ***Phase 1:*** *the overshoot and initial repolarisation.* ***Phase 2:*** *plateau stage caused by the steady inflow of calcium ions through L-type channels.* ***Phase 3:*** *repolarisation results from an increase in potassium and decrease in calcium.* ***Phase 4:*** *the resting potential, which is the resultant of a large potassium content.*

Throughout its prolonged depolarisation the myocyte is electrically inexcitable (refractory), meaning a second contraction cannot be triggered.

The refractory period of a cardiac muscle fibre lasts longer than the contraction itself and as a result another contraction cannot begin until relaxation is well underway. It is therefore impossible for a sustained contraction to occur within the heart, a very important development when considering the pumping function; dependent on alternating between contraction and relaxation.

Unsurprisingly the electrophysiology of cardiomyocytes varies between species. This is due to differences in the expression levels and subtypes of ion channels and transporters[48]. As such, the action potential of a rat is much shorter than that of a human, Figure 1.16. For cardiac research there is no ideal animal model available, as each is accompanied with their own advantages and disadvantages.

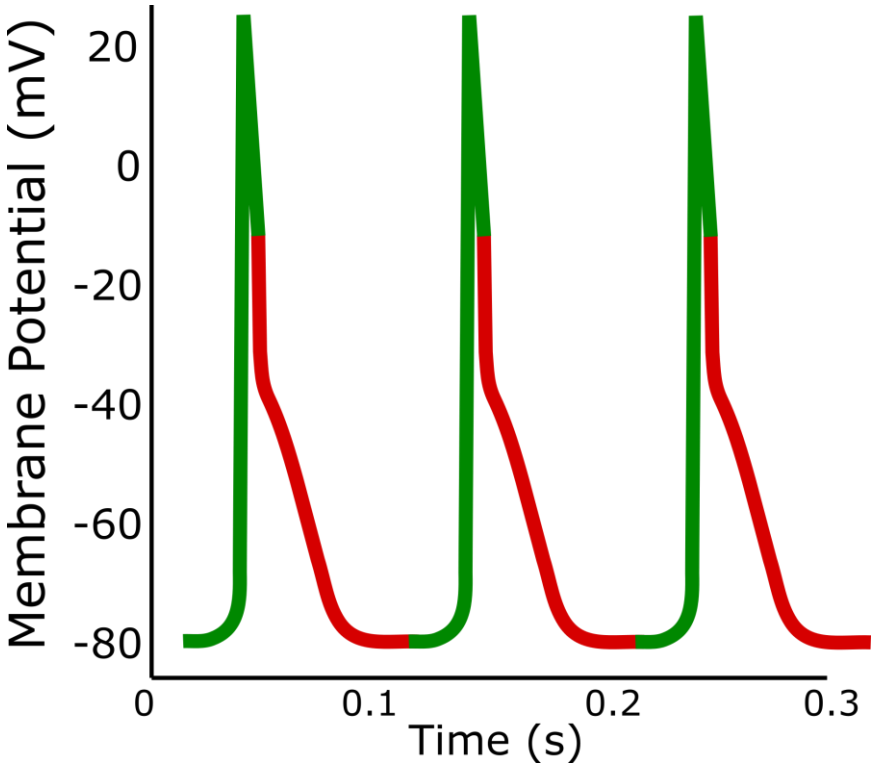

Figure 1.16. *The action potential of a rat, in ventricular myocytes. The striking difference is the absence of a plateau phase observed in humans. Rodent hearts therefore have rapid systolic contraction and diastolic filling.*

1.13. Excitation-Contraction (EC) coupling

The action potential propagates along the myocardial sarcolemma, from cell to cell, through gap junctions that are composed of proteins called connexons[49]. The excitation spreads to the cells' interior via the T-tubules that all contain L-type calcium channels called dihydropyridine receptors (DHPRs). During the plateau phase of the action potential Ca^{2+} enters the cell through the DHPRs. This calcium is not sufficient to induce a contraction but instead serves as a trigger to release more calcium. The RyRs in the membrane of the junctional SR detect the slight increase of Ca^{2+}, opening the channel. In a calcium-induced calcium-release (CICR) mechanism[50], a proportion of the intracellular stores of Ca^{2+} within the SR is released, triggering more RyRs to open[51,52]. An order of magnitude shift in cytosolic Ca^{2+} concentration occurs, typically from 0.1 µM – 1 µM[53], and binds to the protein, troponin C. The formed Ca^{2+} troponin complex interacts with tropomyosin to unblock actin binding sites. Myosin head groups on the thick filament can then bind, allowing ATP-hydrolysis to occur, where the myosin head pulls the actin filaments towards the centre of the sarcomere. After a contraction has finished the intracellular calcium must be reduced, to reset the system, and it is taken back into the SR via ATPase pumps (SERCA)[54] or ejected from the cytosol and back into the extracellular space mainly by sodium-calcium exchangers (NCX)[55]. The SERCA pump has dual purpose; to lower cytosolic calcium and thus cause muscle relaxation, and restore the SR calcium store, required for muscle contraction[56]. Clearance of calcium via membrane Ca^{2+} ATPase pumps and NCX, play minimal roles when compared to SERCA.

1.14. Ryanodine Receptors (RyRs)

Over the last decade the advent of single molecule switching and localisation-based PALM, STORM and related super-resolution microscopies[5,15,16] have greatly advanced insight into cell biology. Visualising nanostructures including optically resolved nuclear pore complexes[57], microtubules[58], actin-spectrin scaffolds for membranes[59], membrane compartments[60] and protein ensembles

in signalling nanodomains[61] have seen significant breakthroughs. This also includes the visualisation of the clusters of the giant (~ 2 MDa) ryanodine receptor-2 (RyR) Ca^{2+} release channels in cardiomyocytes to characterise the calcium signalling nanodomains which are the structural units of calcium signalling in cardiac myocytes[62] using dSTORM[63]. RyR2 is strongly expressed in both the heart and brain, and provides the molecular basis of CICR. Changes at the molecular scale, during pathology[64] or genetic manipulation[65], have been observed with super-resolution data of these ion channels. Computational models have been made to understand how adaptations in molecular cluster shapes underlie changes in microscopic calcium signalling[66,67]. These models used super-resolution data of RyR and was instrumental in their building.

Due to their vital role in physiology and pathology, RyRs present a key target for molecular investigations. Improved cryoelectron microscopy methods have recently revealed the 3D structure of RyRs[68,69]. The clustering of RyRs at the supra-molecular level is of major interest due to their general role in calcium signalling in both muscle[70,71] and neurons[72], and also because the clustering can dramatically modulate the excitability of RyRs[66,73].

RyR clusters are a prototypical system for which the biophysical cluster properties, e.g. cluster excitability, can be directly tied to the spatial arrangement of receptors within the cluster as recently shown by Walker et al[66] who made this relationship quantitative. The cytoplasmic and internal [Ca^{2+}] store acutely control the regulation of RyR channels, but the local configuration of other molecular components also contribute. These include JPH2, an accessory protein anchored in the intracellular store membrane, which can modulate the Ca^{2+} released by the cluster. JPH2 may also play a role in adjusting the physical size of clusters[65].

An effective lateral spatial resolution of 30-60 nm, limited in part by localisation precision, of RyR within cardiomyocytes was achieved in previous work with the application of dSTORM (or STED). At this resolution, only the outlines of the tightly-organised RyR clusters were consistently resolvable[62,74]. An assumption that RyRs are arranged on a regular 30 x 30 nm quasi-crystalline lattice, based on observations in skeletal muscle cells[75], was used in quantitative analysis of the clusters. This hypothesis has been challenged with recent electron tomography data which suggested that the arrangement might be more variable[76]. The complexities of this technique however, mean that this has yet to

be replicated in other laboratories. To resolve this and related open questions there is a growing need for super-resolution methods which can consistently and robustly achieve higher resolution in complex cells and quantify protein numbers. These are both elements which are tackled within this thesis and that I have achieved through the implementation of DNA-PAINT and related methodologies. Future investigations will be able to build on this foundation to answer important biological questions.

Chapter 2

Methodologies

This Chapter lists in detail all of methods used within this thesis and should be consulted when viewing later Chapters.

2.1. Cleaning coverslips

Number 1.5, 22x22 mm, glass coverslips (Menzel Gläser, ThermoFisher Scientific, Loughborough, UK) were cleaned in saturated NaOH in methanol. These coverslips were then thoroughly rinsed using freshly distilled water and left, under a dust protector, to dry.

2.2. Imaging chamber construction

Pre-cleaned coverslips were affixed to custom built Perspex slides with hollowed out regions, Figure 2.1. A 1:1 ratio of PINKYSIL (Barnes, Auckland, New Zealand) was applied to the perimeter of hollowed out segments on the chamber slide before it was quickly and firmly introduced to the coverslip. The newly made imaging chamber was then left to dry before transportation to a microscope.

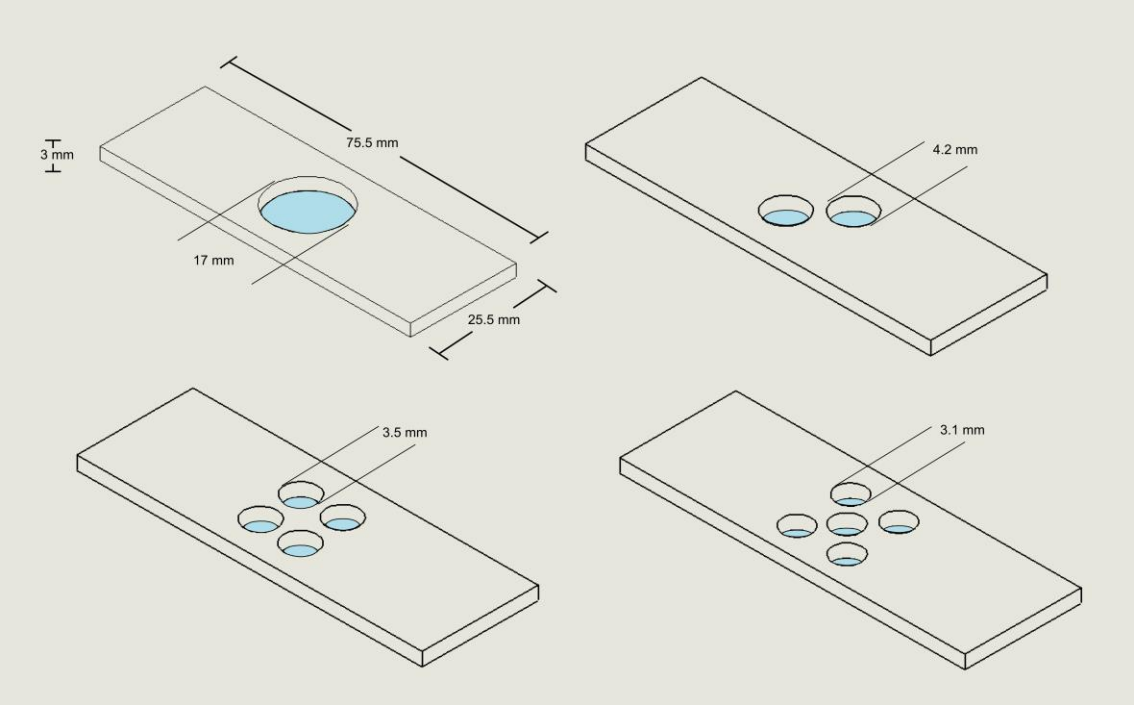

Figure 2.1. *Special, custom built, open-top imaging chambers made out of 3 mm thick Perspex were designed and used throughout this thesis. These chambers were ideal for an assortment of possible experiments enabling quick and easy access for solution changes.*

2.3. Coverslip treatment with poly-L-lysine

0.01 % poly-L-lysine (P8920, Sigma Aldrich, Gillingham, UK) was diluted with distilled water, to 0.005 %. 50 – 200 µL was applied to the centre of pre-cleaned and dry number 1.5 glass coverslips for 10 – 15 minutes. Remaining poly-L-lysine was aspirated and coverslips were left to dry overnight.

2.4. Coverslip treatment with laminin

Laminin solution (11.9 µg / mL, diluted from 23017-015, ThermoFisher Scientific, Loughborough, UK) was applied to pre-cleaned coverslips attached to imaging chambers. This coating was left at room temperature (RT) overnight to allow for strong attachment of cardiomyocytes.

2.5. Rodent euthanasia

Male Wistar rats weighing 250-350 g were euthanized humanely with lethal dose (100 mg per kg of body weight) of sodium pentobarbitone according to a Schedule 1 protocol in compliance with the 1986 Animals (Scientific Procedures) Act, approved by the Animal Ethics Approval Committee of the University of Exeter (ETH1418b_CEMPS to C.Soeller).

2.6. Rodent cell isolation

After animal euthanasia the hearts were quickly excised. The hearts were cannulated at the aorta and retrogradely perfused with calcium (Ca^{2+})-free Tyrode's solution using a Langendorff perfusion protocol, Figure 2.2, described previously[77]. The calcium free Tyrode's solution (40 mM NaCl (S7653, Sigma Aldrich, Gillingham, UK), 1mM MgCl (M8266, Sigma Aldrich, Gillingham, UK), 4 mM KCl (P9541, Sigma Aldrich, Gillingham, UK), 10 mM HEPES (H3375, Sigma Aldrich, Gillingham, UK), 10 mM Glucose (G7528, Sigma Aldrich, Gillingham, UK)), was made fresh and pH'd to 7.4. After 5 minutes, the perfusate was switched to a Tyrode's solution containing 200 µM $CaCl_2$, 1 mg/mL Collagenase-II (CLS2, Worthington Biochemical, Lakewood, USA) and 0.1 mg/mL Protease from bovine pancreas (P4630, Sigma Aldrich, Gillingham, UK). Following 10-15 minutes of perfusion, the ventricles were dissected into fresh Tyrode's solution containing 200 µM $CaCl_2$, diced with sharp scissors and gently triturated to liberate isolated ventricular myocytes. Successful cell liberation was determined via quick inspection using a simple light microscope.

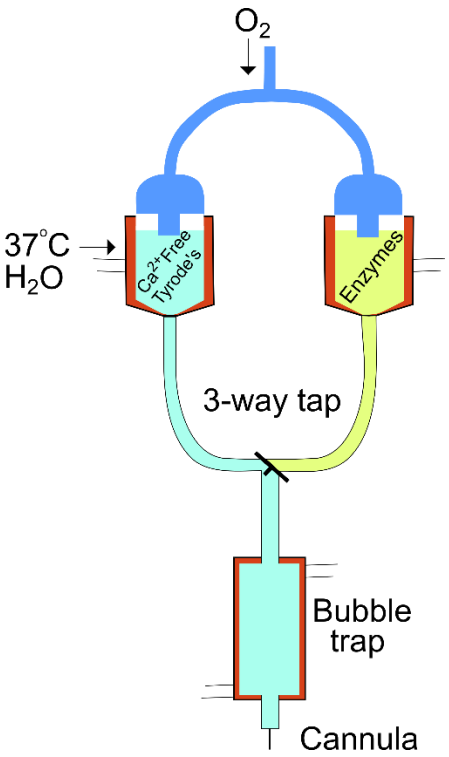

Figure 2.2. *The langendorff perfusion setup. The glass beakers and bubble trap have an outer glass jacket which constantly has water flowing through at approximately 37° C. Oxygen is bubbled into the solutions perfused through the heart.*

2.7. Paraformaldehyde (PFA)

Paraformaldehyde was freshly made to 10 % (w/v) concentration in phosphate buffered saline (PBS)(Gibco 10010-015, ThermoFisher Scientific, Loughborough, UK) with the following procedure. 80 mL of PBS was heated to between 55-58°C in a glass beaker. In a fume hood 10 g of PFA powder (Sigma Aldrich, Gillingham, UK) was added to the heated PBS whilst stirring. 1-2 drops of 10 M NaOH was added and the PFA stirred until the powder fully dissolved. Additional PBS was added to make the total volume 100 mL. The solution was filtered into a cooled Schott bottle and pH adjusted to 7.4 with HCl. Solutions were kept for a maximum of 2 weeks and stored at 4°C until used..

2.8. pH measurements

Stock solutions were pH'd using a Mettler Toledo (Mettler Toledo, Leicester, UK) pH meter. Prior to each measurement the probe was calibrated by two-point calibration using pH 4.0 (Sigma Aldrich, Gillingham, UK) and pH 7.0 (Sigma Aldrich, Gillingham, UK) standard solutions. Measurements were taken whilst the sample was under continual mixing using a magnetic stirrer on a spinning plate.

2.9. Isolated cardiomyocyte fixation

Pre-made PFA was diluted to 4 % in PBS and mixed 1:1 with the suspension of isolated cardiomyocytes in Tyrode's solution containing 200 μM $CaCl_2$. Cells were fixed for 10 minutes at RT. Samples were then spun at 1000 rpm for 2 minutes and its supernatant discarded and replaced with PBS for a further 10 minutes before repeating this washing step. Cell were re-suspended in a PBS storage buffer containing 0.5 % albumin from bovine serum (BSA) (A7906, Sigma Aldrich, Gillingham, UK), 0.1 % sodium azide (Sigma Aldrich, Gillingham, UK) and stored at 4 °C until used for immunocytochemistry.

2.10. Attachment of isolated cardiomyocytes to coverslips

Coverslips, treated the previous night with laminin solution, were rinsed with calcium-free Tyrode's solution. Cardiomyocyte suspensions were filtered and transferred in ~300 μL aliquots to imaging chambers with these pre-treated laminin coverslips. Cells were incubated in chambers for 90-120 minutes attaching time at 30 °C. Attached cells were fixed by the addition of equal volume 4 % paraformaldehyde in PBS at pH of 7.4 for 10 minutes at RT. The fixative was replaced with fresh PBS and allowed to wash for another 10 minutes. This washing was repeated twice more before storing the chambers in fresh PBS storage buffer.

2.11. Perfusion fixation

Two 50 mL syringes were first prepared; the first containing 1x PBS and the other freshly diluted 2% PFA (pH = 7.4) in PBS. These were attached to the inputs of a 3-way tap. Following euthanasia and excision of the rodent heart, as described in *2.5* and 2.6, using two sets of tweezers (one fine-toothed and one fine-tipped) the aorta was then cannulated on the remaining 3-way tap channel and secured into place with the use of surgical thread. PBS was flushed through the heart for 2-5 minutes. Once the flow ran continuously clear 2 % PFA was steadily perfused at a rate of approximately one drop per second for 10 minutes. The heart was then removed and dissected into desired tissue blocks and stored temporarily in PBS before cryoprotection steps enacted.

2.12. Chunk fixation

Excised cardiac tissue from horse hearts, obtained from a local abattoir, was cut into approximate 1 cm^3 chunks and submerged in fresh 2 % PFA for 1 hour at 4 °C. The fixative was replaced with PBS for one further hour at 4 °C. After this duration the samples were moved to fresh PBS prior to cryoprotection steps.

2.13. Cryoprotection of tissue samples

30% sucrose solutions were made by weighing out 18 g sucrose (S0389, Sigma Aldrich, Gillingham, UK) into 45 mL PBS whilst stirring. 600 µL 10% sodium azide (NaN_3) was added and the solution topped up with PBS to 60 mL. 10 and 20% sucrose solution were made by diluting the stock 1:2 or 2:1 respectively with PBS. Fixed tissue samples were transferred to 10% sucrose and kept at 4 °C for 1 hour or until the tissue sank, whichever took longer. This step was subsequently repeated with 20% sucrose and finally the 30% sucrose was kept overnight at 4°C

2.14. Freezing Tissue

Cryoprotected tissue had any remaining sucrose dabbed off and was transferred to uniquely labelled cryotubes, (V7884, Sigma Aldrich, Gillingham, UK). A metal dish containing 2-Methylbutane (M32631, Sigma Aldrich, Gillingham, UK) was lowered into a container holding liquid nitrogen for 5-10 minutes to equilibrate. Samples were then gently placed into the metal bowl for at least 10 minutes to freeze. For prolonged storage the samples were kept at -80 °C.

2.15. Cryosectioning

Frozen tissue blocks were affixed into optimal cutting temperature (OCT) (361603E, VWR, Lutterworth, UK) compound in the desired orientation on top of a chuck sitting in a fast-freeze block. The tissue chuck was fixed in front of the cutting stage and the cutting angle set. Cryostat chamber temperature was set to minus 24-28°C and allowed time to acclimatise. The tissue was slowly advanced towards the blade and the sample sectioned until the cut was even. A 30-40 µm test section slice was taken on a glass slide to confirm the orientation. For super-resolution imaging the sectioning thickness was set to approximately 10 µm. The section was gently teased as a cutting motion was applied with a fine tipped paintbrush and collected onto a pre-cleaned and 0.05% poly-L-lysine pre-treated coverslip as described in *2.1* and *2.3* respectively. Coverslips complete with centralised sectioned tissue were then stored at -20 °C until required for immunohistochemistry.

2.16. Immunohistochemistry for cardiac tissue

Sectioned cardiac tissue, on number 1.5 coverslips, was affixed to imaging chambers as described in *2.2*. Tissue sections were briefly hydrated, 2-5 minutes, with PBS. This was then replaced by a single droplet from a bottle of Image-iT™ FX Signal Enhancer (I36933, ThermoFisher Scientific, Loughborough, UK) and incubated in a hydration chamber for 1 hour at RT. Anti-SERCA2 ATPase (Ab2861, Abcam, Cambridge, UK) mouse monoclonal [2A7-A1] IgG2a primary antibody, see Table 2.1 for a full list of antibodies used, was diluted (1:200) in an

incubation solution containing 2% BSA (w/v), 0.05% sodium azide (NaN_3) made up into PBS and incubated overnight at 4°C in the hydration chamber. The following day samples were washed thoroughly, 3-4 times with excess PBS for 15-30 minute durations. The tissue was then incubated with goat anti-mouse IgG (H+L) highly cross-adsorbed polyclonal secondary antibody Alex Fluor 660 (A-21055, ThermoFisher Scientific, Loughborough, UK), diluted (1:200) in incubation solution for 2 hours at RT and subsequently washed in PBS, 3-4 times as above.

2.17. Immuno-labelling for attached isolated myocytes

Isolated, fixed, and attached, via laminin pre-treated coverslips described in 2.9, cardiomyocytes were briefly permeabilised with 0.1 % Triton™ X-100 (T9284, Sigma Aldrich Co, Gillingham, UK) (v/v) in PBS for 10 minutes. Samples were then blocked with PBS containing 10% normal goat serum for 1 hour at RT. The primary antibody, see Table 2.1, was diluted in incubation solution (as 2.15) and applied overnight at 4 °C. Washing and secondary antibody incubation steps were the same as described in 2.16.

The mouse monoclonal anti-ryanodine receptor-2 IgG from Clone C3-33 (MA3-916, ThermoFisher Scientific, Loughborough, UK) was used for labelling the ryanodine receptors in the fixed cardiomyocytes. This antibody is well characterised for its high specificity of binding[78] and has been established as one of the consistently reliable probes for diffraction-limited[77,79] and super-resolution microscopies[62,74] of RyR2. The epitope is not known as the antibody was raised against the full size protein and as the protein is a homo-tetramer it may have up to 4 binding sites. As a qualitative comparison, a monoclonal pan RyR antibody of clone 34C (MA3-925, ThermoFisher Scientific, Loughborough, UK) was used to obtain independent DNA-PAINT images of peripheral RyR2 distributions in the myocytes. For staining Caveolin-3, a mouse monoclonal antibody from BD Biosciences (610421, BD Biosciences, Wokingham, UK) was used while a custom-made rabbit polyclonal antibody described previously[80] was used against Juctophilin-2 (JPH2).

Name	Species	Isotype	Company	Product	Epitope recognition
Ryanodine Receptor (C3-33)	Mouse	IgG1	ThermoFisher Scientific	MA3-916	
Anti-RyR2	Rabbit		Sigma Aldrich	HPA016697	
RyR1 (34C)	Mouse	IgG1	ThermoFisher Scientific	MA3-925	
Purified Anti-Caveolin 3	Mouse	IgG1	BD Transduction	610421	
Anti-SERCA2 ATPase [2A7-A1]	Mouse	IgG2a	Abcam	Ab2861	Amino acids 386-396
Na^{+}-$Ca2^{+}$ exchanger protein	Mouse	IgG1	Swant	R3F1	
Anti-beta Tubulin [1E1-E8-H4	Mouse	IgG1	Abcam	Ab131205	
Alexa Fluor 647	Goat anti-Mouse	IgG (H+L)	ThermoFisher Scientific	A-21236	
Alexa Fluor 660	Goat anti-Mouse	IgG (H+L)	ThermoFisher Scientific	A-21055	
Alexa Fluor 680	Goat anti-Mouse	IgG (H+L)	ThermoFisher Scientific	A-21058	
Alexa Fluor 680	Goat anti-Rabbit	IgG (H+L)	ThermoFisher Scientific	A-21109	
Alexa Fluor 750	Goat anti-Mouse	IgG (H+L)	ThermoFisher Scientific	A-21037	
Alexa Fluor 750	Goat anti-Rabbit	IgG (H+L)	ThermoFisher Scientific	A-21039	
Unconjugated secondary	Goat anti-Rabbit	IgG (H+L)	Jackon ImmunoResearch Laboratories	115-005-003	
Unconjugated secondary	Goat anti-Rabbit	IgG (H+L)	Jackon ImmunoResearch Laboratories	111-005-003	

Table 2.1. List of primary and secondary antibodies used throughout this thesis.

2.18. Immuno-labelling for cultured cells

Cultured COS-7 cells, derived from monkey kidney tissue, were seeded on number 1.5 coverslips and grown overnight in Dulbecco's Modified Eagle's Medium (DMEM) at 37 °C with 5 % carbon dioxide. The cells were fixed after removal of the medium in ice-cold methanol for 15 minutes at -20 °C and washed three times in PBS with 5-10 minute intervals.

(The culturing steps above were taken by Rikke Morrish before handing the cells over for labelling).

Coverslips with cultured cells had their perimeter dried with filter paper prior to attaching them to imaging chambers, as described in *2.2*. Cells were blocked with 1% BSA (w/v) in PBS for 10 minutes at RT. Samples were then incubated with anti-beta tubulin antibody [1E1-E8-H4] (Ab131205, Abcam, Cambridge, UK) at 1:500 dilution in incubation solution and stored in a hydration chamber for 1 hour at RT. Samples were washed 3-4 times in PBS for 5-15 minute intervals. Secondary goat anti-mouse IgG (H+L) antibodies Alexa Fluor, 647, 660, 680, 750 (A-21236, A-21055, A-21058, A-21037, ThermoFisher Scientific, Loughborough, UK), Figure 2.3, were applied at 1:200 dilution in incubation solution for 1 hour at RT. A further 3-4 PBS washes of intervals 5-15 minutes were conducted prior to imaging.

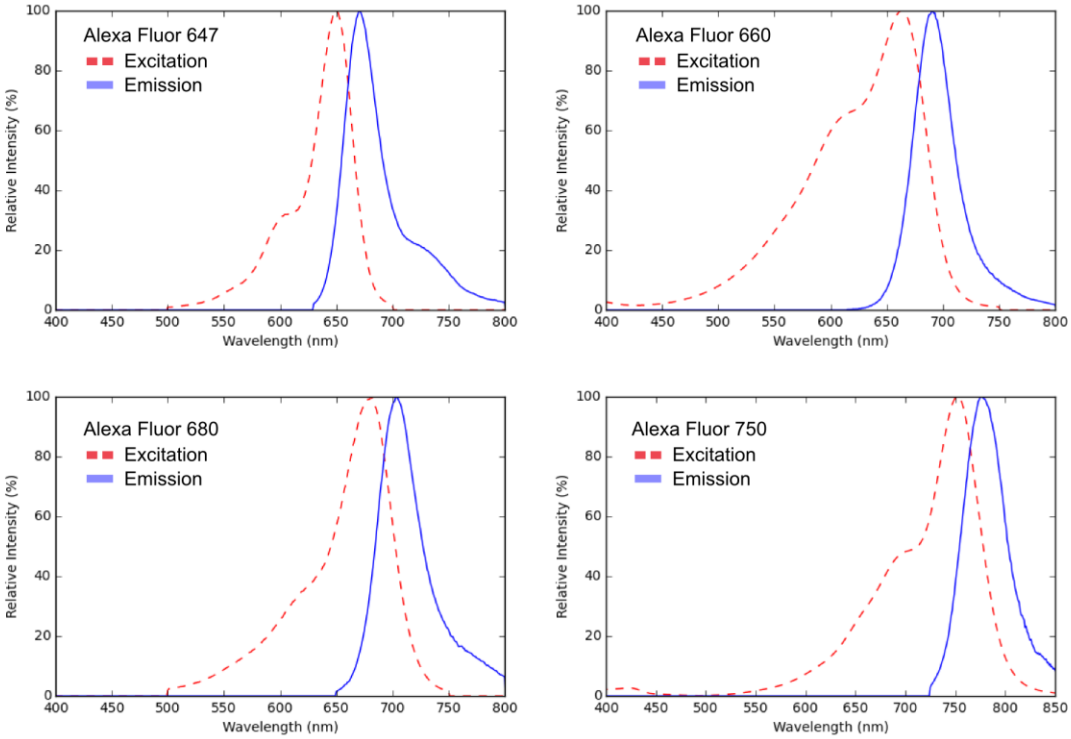

Figure 2.3. *The excitation and emission spectra for Alexa Fluor secondary antibodies (647, 660, 680, 750) used for photoswitching dSTORM experiments.*

2.19. dSTORM glycerol mounting medium

2-Mercaptoethylamine (MEA) (M9768, Sigma Aldrich, Gillingham, UK) previously made to 2 M with 10x PBS (Gibco 70011-036, ThermoFisher Scientific, Loughborough, UK) and kept in aliquots at -20 °C were freshly defrosted prior to dSTORM experiments. dSTORM buffers based on glycerol consisted of 90 % glycerol (G5516, Sigma Aldrich, Gillingham, UK) (v/v), 10% (v/v) 10x PBS and one of 5, 10, 50, 100 mM MEA depending on experiment. The pH of the switching buffer was checked to be between 8-9 using pH strips (Sigma Aldrich, Gillingham, UK) prior to adding to the sample.

2.20. Oxygen scavenging dSTORM mounting mediums

For oxygen scavenging achieved with the use of enzymes, 5-25% glucose (w/v) was first added to either PBS or 90% glycerol. Glucose oxidase from Aspergillus

(G2133, Sigma Aldrich, Gillingham, UK) and catalase from bovine liver (C40, Sigma Aldrich, Gillingham, UK) was added at 5-10 mg/mL and 0.05-0.10 mg/mL respectively. For sodium sulphite oxygen removal experiments a final 10 mM Na_2SO_3 (S0505, Sigma Aldrich, Gillingham, UK) concentration was made in either PBS or 90% glycerol.

2.21. Oxygen concentration measurements

Oxygen concentrations were measured with a NeoFox-Kit-Probe oxygen monitoring sensor (Ocean Optics, Oxford, UK). The sensor has a thin film containing ruthenium and its fluorescence is quenched by the presence of molecular oxygen. The probe was calibrated with a zero-oxygen solution made up of dH2O and excess Na_2SO_3 prior to each set of experiments. All test solutions were measured directly after being mixed, apart from any experiment involving dated sodium sulphite buffers. Measurements were taken in open top containers to mimic dSTORM experimental imaging conditions.

2.22. Thiol test solution for Ellman's reagent and spectrophotometry

In 1958 George L Ellman discovered that bis(*p*-nitrophenyl) di-sulphide (I) reacts with aliphatic thiol compounds to produce one mole of *p*-nitrothiophenol anion per mole of thiol. This anion is yellow coloured[81] and can be used as an indication of thiol activity.

A UV-vis spectrophotometer can be used to quantify this reaction, Figure 2.4.

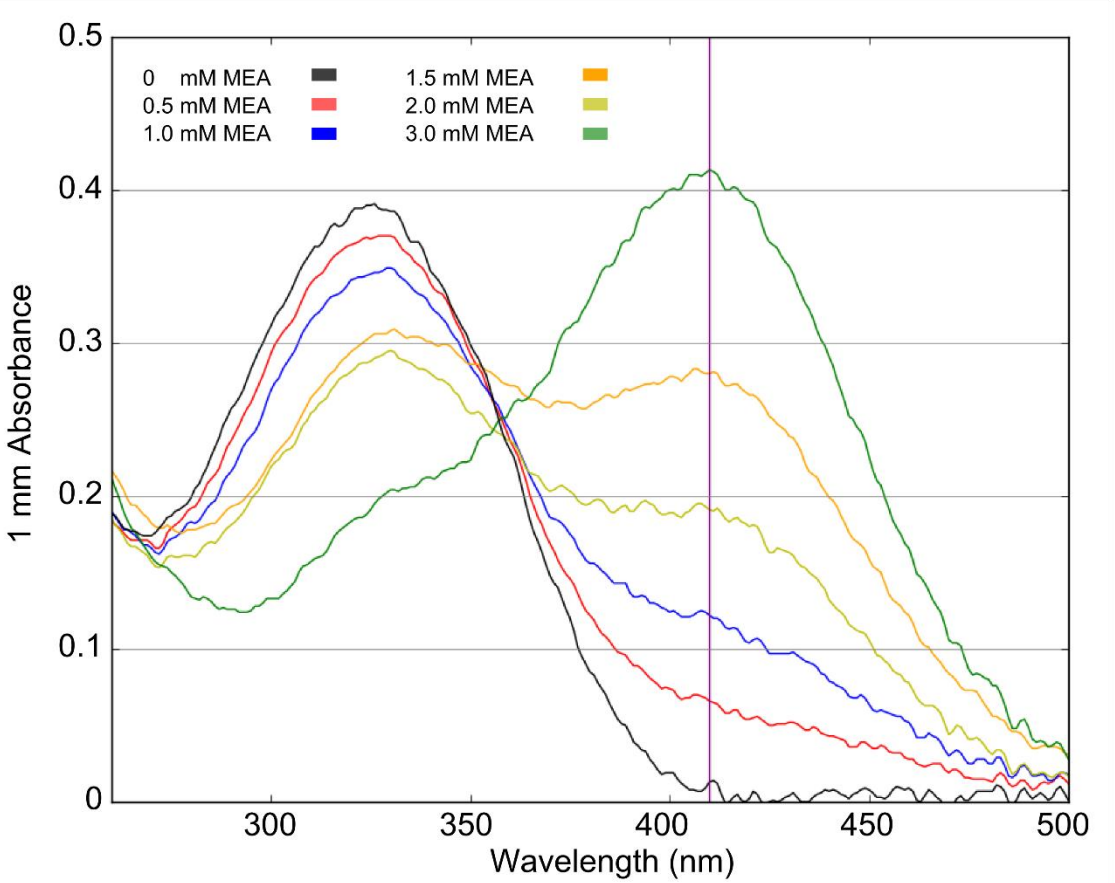

Figure 2.4. *The absorbance spectra for increasing thiol concentrations measured in Ellman's reagent. An increase in absorbance at 410 nm is observed as test solutions containing higher concentrations of MEA are measured.*

There is a linear relationship between the 410 nm peak absorbance values when plotted against the MEA concentration of the test solution, as is expected from equation 2.1, Figure 2.5.

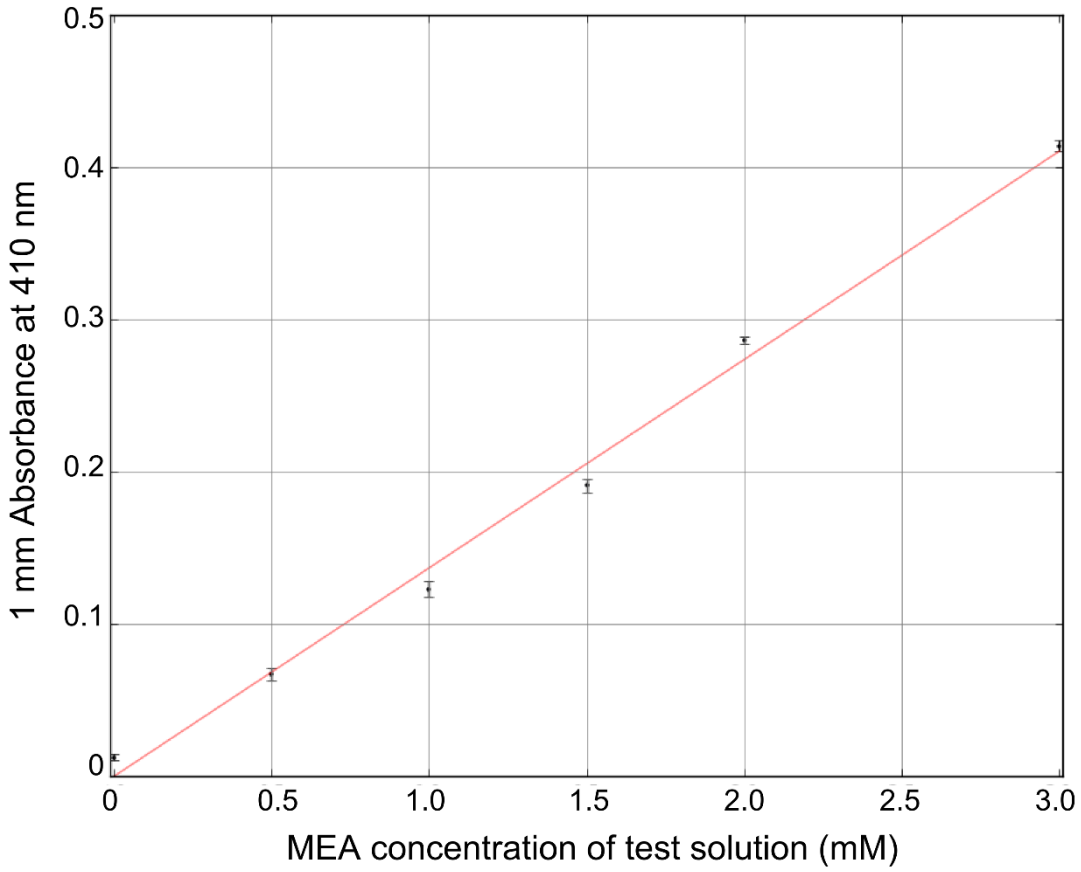

Figure 2.5. *Plotting the absorbance at 410 nm against the MEA concentration of test solutions used in the dilution series, Figure 2.4, yields a linear relationship.*

2M MEA stock solution were diluted in PBS to desired experimental concentrations. 5 µL [0.1M] Ellman's reagent was added to 250 µL 1x PBS. To this, 25 µL of the MEA test solution was added and thoroughly mixed. Rapid colour change was observed upon addition of the thiol. These visual tests were conducted for each thiol switching buffer. Approximately 1.5 µL of this solution was added to a pre-blanked NanoDrop™2000 (ThermoFisher Scientific, Loughborough, UK) and its absorbance at 410 nm measured and recorded.

The concentration of MEA stock solutions were confirmed through the use of Beer-Lambert Law, equation 2.1.

$$c = \frac{A}{b\epsilon} \tag{2.1}$$

where *A* is the absorbance, *b* the path length, and *E* the molar absorptivity coefficient of 14173 $M^{-1}cm^{-1}$, from[82], at 410 nm.

2.23. DNA-PAINT probe production

Oligonucleotide synthesis, the “docking”, “imager” and “quencher” strands (nucleotide sequence and terminal modifications detailed in Appendix 1 & 2) were commercially synthesised and HPLC purified using the custom DNA oligo services by Eurofins (Eurofins Genomics, Wolverhampton, UK) and IDT (Integrated DNA Technologies, Leuven, Belgium). The two nucleotide designs of the P1 and P3 sequences were obtained from Jungmann et al[32]. Rather than using a biotin-streptavidin linker (which is large and can give rise to undesirable non-specific labelling with endogenous biotins in the myocytes) as done in the original DNA-PAINT study[32], a direct thiolation which links a 5’ C6 amine of the docking strands and cysteines of the antibody was used. In addition, the conjugated docking strands contained a 3’ fluorophore which had the advantage that the conjugated antibody markers carry a fluorochrome, enabling positive staining to be confirmed. This fluorophore does not interfere with later DNA-PAINT imaging since generally the 3’-fluorophore was selected spectrally distinct from the imager fluorophore. In rare cases where there was overlap between the docking strand fluorophore and imager fluorophore emissions a period of intense illumination, from a 642 nm laser (~9mW at the sample), was used to remove any background from docking strand fluorophores by permanent photobleaching before commencing DNA-PAINT acquisition. Respective docking strands were conjugated to either a goat anti-mouse IgG(H+L) or a goat anti-rabbit IgG(H+L) secondary antibody (affinity purified, azide-free form (115-005-003 and 111-005-003, Stratech, Ely, UK) using a Thunder-Link® kit (Expedeon, Cambridge, UK). The docking strands were diluted to ~80 µM in PBS. 100 µL of the oligo and 100 µL 1 mg/mL primary antibody was added to the respective activation solutions in the Thunder-Link® kit for 1 hour at RT. The activated suspensions were desalted in a gravity driven column and combined. In some experiments a primary antibody against RyR2, clone C3-33, was conjugated directly to DNA-PAINT docking strands. The conjugated antibody was purified from unconjugated docking strands by use of a Thunder-Link® kit-based precipitation step and centrifugation at 13,000g. The relative concentration of the antibody and the docking strand (by the 3’-fluorophore) in the conjugate were determined with the use of a NanoDrop 2000 spectrophotometer. Only antibody

samples with an oligo:antibody conjugation ratio ≥ 1:1 were used for sample labelling. Aliquots of conjugated docking strands were stored at -20°C until ready for use and upon thawing stored at 4°C for short-term.

2.24. Fixed origami structures

The GATTA-PAINT HiRes 40R DNA-origami sample slide (GATTAquant DNA Nanotechnologies, Braunschweig, Germany) containing two different structures was used as an ideal candidate for a quantitative PAINT test product. The sample largely consists of trimer-nanorulers, with linear spacing 40 nm centre to centre, testing the localisation precision of experimental setups and a sparsely distributed larger fiducial marker intended to allow tracking of drift from the sample/slide. Both origami constructions have docking sites that hybridise with the same complimentary imaging strand, free in solution, allowing for a quantitative comparison between the two to be drawn. In my experiments an ATTO655 imager strand version was used, Figure 2.6.

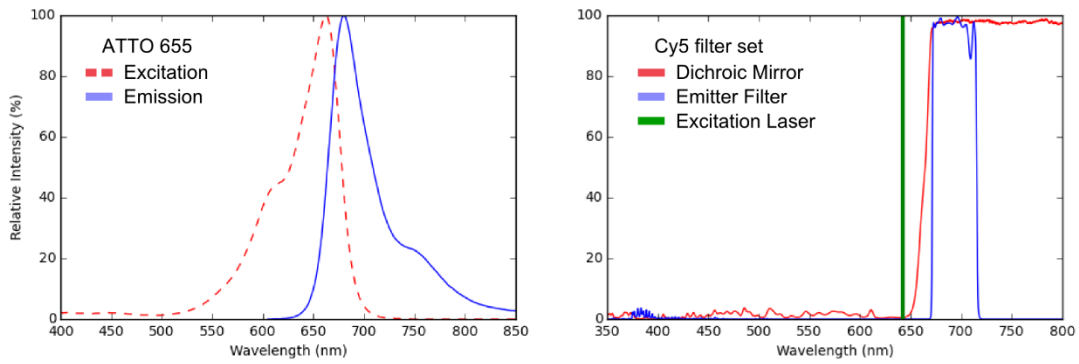

Figure 2.6. *The excitation and emission spectra for ATTO 655 used in DNA-PAINT experiments as the modified oligonucleotide imager strand. A Cy5 filter set was used for these experiments. Dichroic mirror (FF660-Di02, Semrock, Cambridgeshire UK) and emitter filter (692/40, Semrock, Cambridgeshire UK).*

2.25. DNA-PAINT imaging buffer, Buffer C

1x PBS was adjusted to contain 500 mM NaCl. This solution was made to contain 1 mM EDTA and the pH was adjusted to 8.0. This buffer, originally termed 'Buffer

C'[32], was used for washing DNA-PAINT samples, diluting and applying the imager strand. DNA-PAINT sequences were recorded using an integration time of 100 ms and at least 10,000 frames were acquired for each target structure imaged. The overall image resolution for SMLM is largely controlled by localisation precision and sampling density[83]. Depending on experimental conditions the total number of frames required will have to be adjusted and oversampling is preferred.

2.26. Imaging apparatus

Single molecule images from DNA-PAINT and dSTORM experiments were acquired with a modified Nikon Ti-E inverted fluorescence microscope (Nikon, Kingston-upon-Thames, UK) and fully-adjustable custom-built optical illumination and detection paths, see also Figure 2.7.

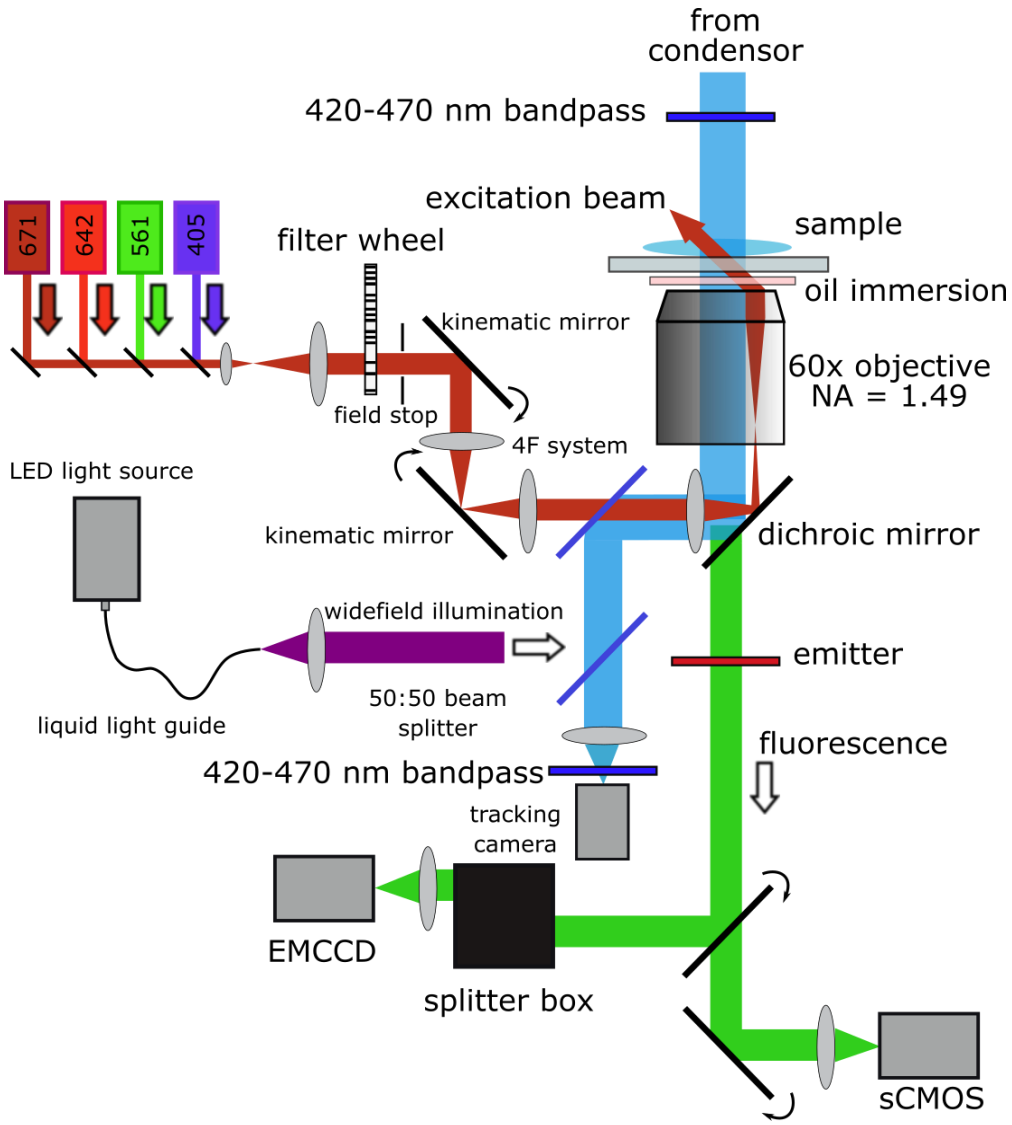

Figure 2.7. *Imaging setup, sample tracking mechanism and performance.* ***(A)*** *Schematic of the custom-built dSTORM/PAINT microscope system. Laser beams* ***(red)*** *from different modules are coupled and propagate through a 4F system before entering the microscope. The 4F system consists of two kinematic mirrors which can be rotated in conjugate image and Fourier planes, respectively, allowing the angle and position of the illumination beam to be adjusted. Fluorescence* ***(green)*** *is collected by a high NA 60x objective and detected by either an EMCCD or a sCMOS camera. Transmitted light* ***(blue)*** *for tracking information is recorded by a tracking camera. Prior to imaging, samples can be examined by a widefield multi-spectral LED light source* ***(purple)****.*

A 200 mW 561 nm (Jive-200, Cobalt, Solna, Sweden) laser or a 140 mW 642 nm (Omicron) laser, or 671 nm (Viasho VA-I-N-671, Beijing, China) were used. The laser excitation intensity was controlled with a computer driven neutral density filter wheel (Thorlabs, Exeter, UK) and accousto-optic modulators built into the laser modules. These custom-optics allowed the lasers, to be conveniently focused into the sample in an angle either exceeding the critical angle, θ_c, (for TIRF imaging) in DNA-PAINT experiments or at a shallower angle for oblique illumination[10] for dSTORM experiments. From equation 1.2 the critical angle for our setup was found to be 61°. Adjusting the angle of incidence directly altered the penetration depth of the evanescent field by equation 1.4, as seen in Figure 2.8 depicting an idealised case. An ~20 μm wide illumination spot was sufficiently large enough to observe the single molecule events (DNA-PAINT or dSTORM) from peripheral couplons near the surface of the cell which was in contact with the coverslip, as performed previously[62]. The laser was focused into the sample with a 1.49NA 60x oil immersion objective fixed onto a piezo focus z-drive (P-725 Physik Instrumente, Bedford, UK) which was mounted rigidly within a custom-made aluminium bracket to minimise any thermal drift of the focal plane.

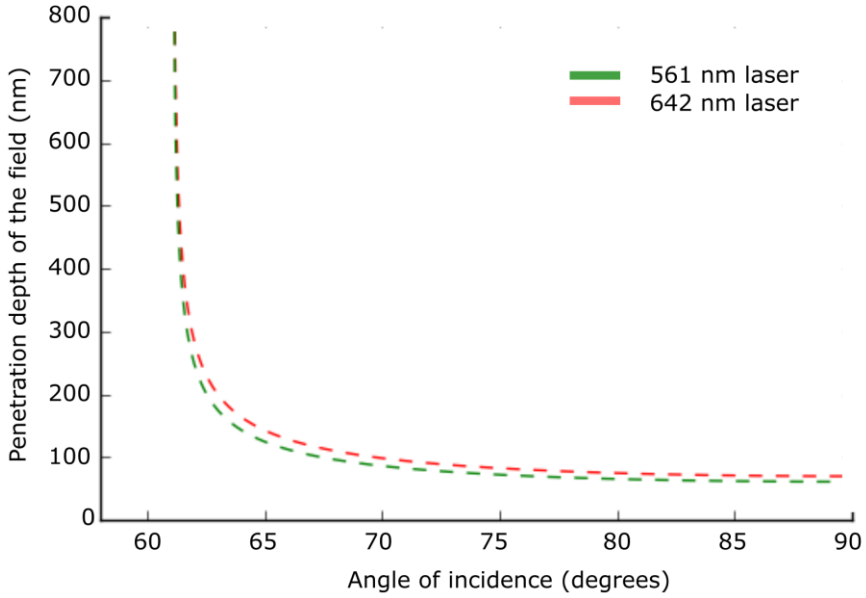

Figure 2.8. *Increasing the angle of incidence past the critical angle decreases the penetration depth of the evanescent field. Plotted here is the approximate penetration depth achieved in an aqueous chamber (n = 1.33) with coverslip attached (n = 1.52) for a 561 nm and 642 nm laser as calculated from the theoretical expression equation 1.4.*

Prior to super-resolution imaging, the presence of the primary and secondary antibodies was confirmed by the fluorescence of the docking-strand fluorophores (Cy3 or FITC, Figure 2.9) in the case of DNA-PAINT or Alexa Fluor dye with the use of a multi-spectral epi-fluorescence exciter (CoolLED, Andover, UK).

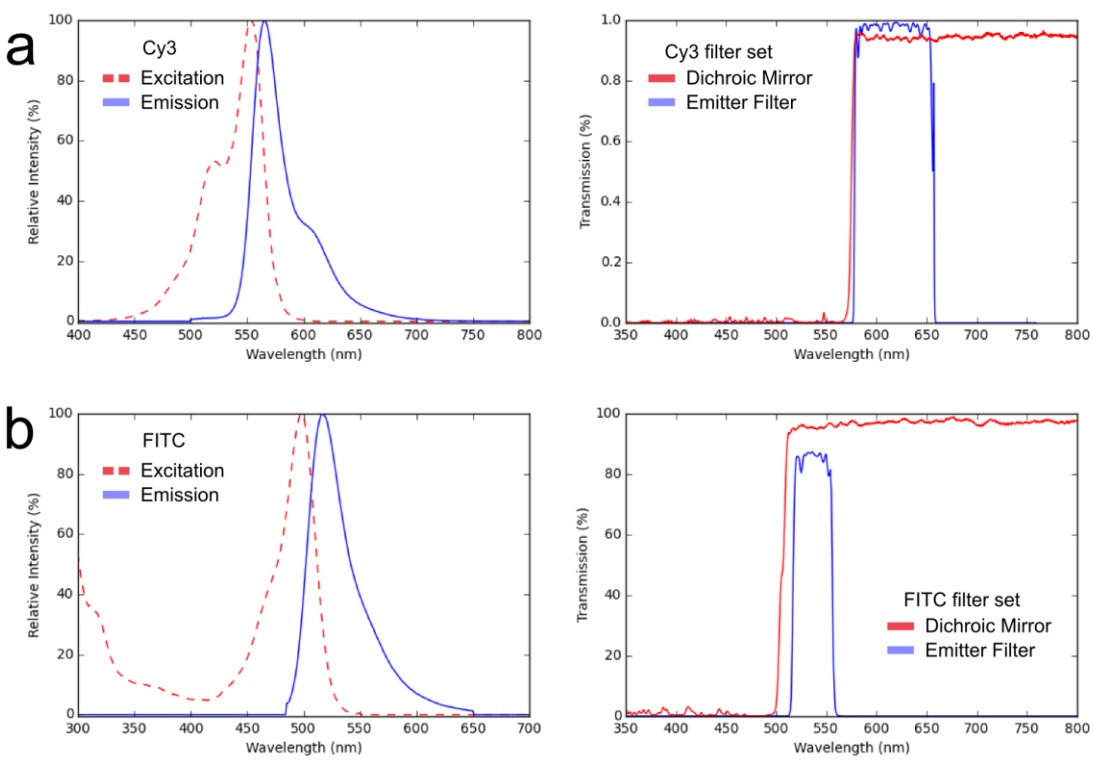

Figure 2.9. *The excitation and emission spectra and filter sets for Cy3* ***(a)*** *and FITC* ***(b)*** *present on modified oligonucleotide docking strands used for confirmation of labelling. Cy3 dichroic mirror (Di02-R561-25x36, Semrock, Cambridgeshire UK), Cy3 emitter filter (617/73-25, Semrock, Cambridgeshire UK), FITC dichroic mirror (DM505) and FITC emitter filter (D535/40M 230459, Chroma, Germany).*

Single molecule images were acquired with a scientific-CMOS camera (Zyla 4.2, Andor, Belfast, UK) operated with integration times of either 100 ms (DNA-PAINT experiments) or 25 ms (dSTORM). The system readout rate was 560 MHz with a 16-Bit depth (low noise - high well capacity) gain setting. The image data was acquired and analysed in real-time by a quad-core PC using the open source custom-written Python Microscopy Environment (PYME) software (http://python-microscopy.org/). Analysis of localisation data from the sCMOS camera was performed with algorithms that correct for non-uniform sCMOS pixel properties which are implemented in PYME as described recently[33].

2.27. Tracking calibration and drift correction

Transmitted light, which was passed through a blue filter (FF02-447/60, Semrock, Huntingdon, UK), was independent from the excitation and emission of the fluorophores used for SMLM, Figure 2.10. Prior to single molecule acquisition a calibration z-series was taken using a separate camera (DCC3240N, Thorlabs, Exeter, UK), see Figure 2.7.

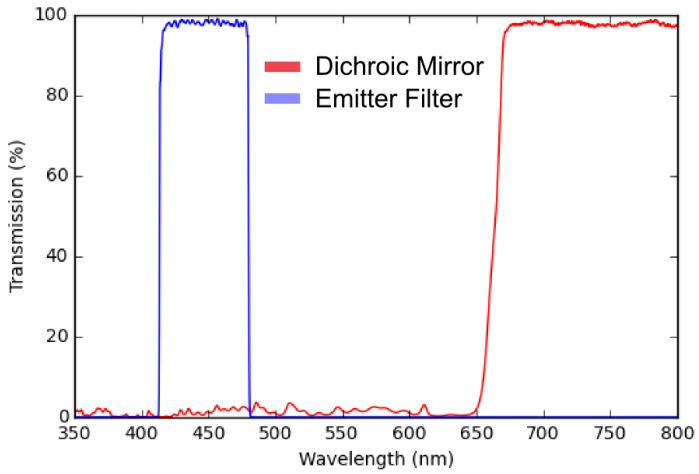

Figure 2.10. *White light illumination was passed through a FF02-447/60 emitter filter and reflected back through the microscope by an FF660-Di02 dichroic mirror. This blue light was used to track drift.*

Ten reference frames were taken, above and below the focal plane, in 200 µm steps in order to monitor and later correct for residual thermal drift in x and y whilst actively maintaining a stable z-position, Figure 2.11.

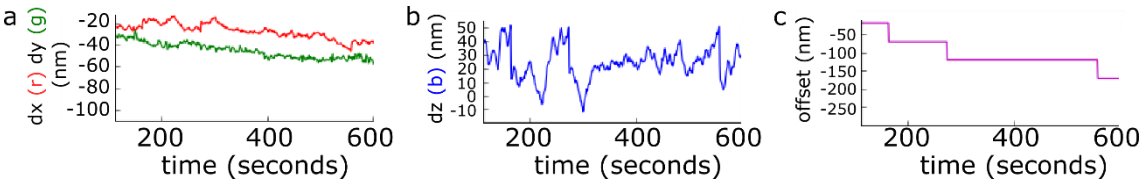

Figure 2.11. *Typical traces generated by the tracking system. Lateral drift trajectories* ***(a)*** *were logged during imaging and applied during the data analysis process to remove x-y drift. A focus lock mechanism was implemented where the axial drift* ***(b)*** *was monitored in a digital feedback loop and corrected in real-time. All autonomous corrections were recorded* ***(c)*** *by way of the axial offset profile.*

This calibration stack was then compared every second to the current transmitted light image. Via cross-correlation analysis, similar to a method described in[84], focal plane shifts were corrected, with a tolerance of ~30 nm, by communication with the PiFoc. The per second update frequency is sufficient as, for instance, drift over 10 nm occurs on the scale of tenth of seconds. Similarly, a 30 nm focus track tolerance is small as compared to the z-resolution of 2D SMLM which has approximately confocal z-resolution, i.e. >300 nm in biological samples. Lateral sample movement was digitally removed during analysis by subtracting the recorded lateral drift time course, Figure 2.12.

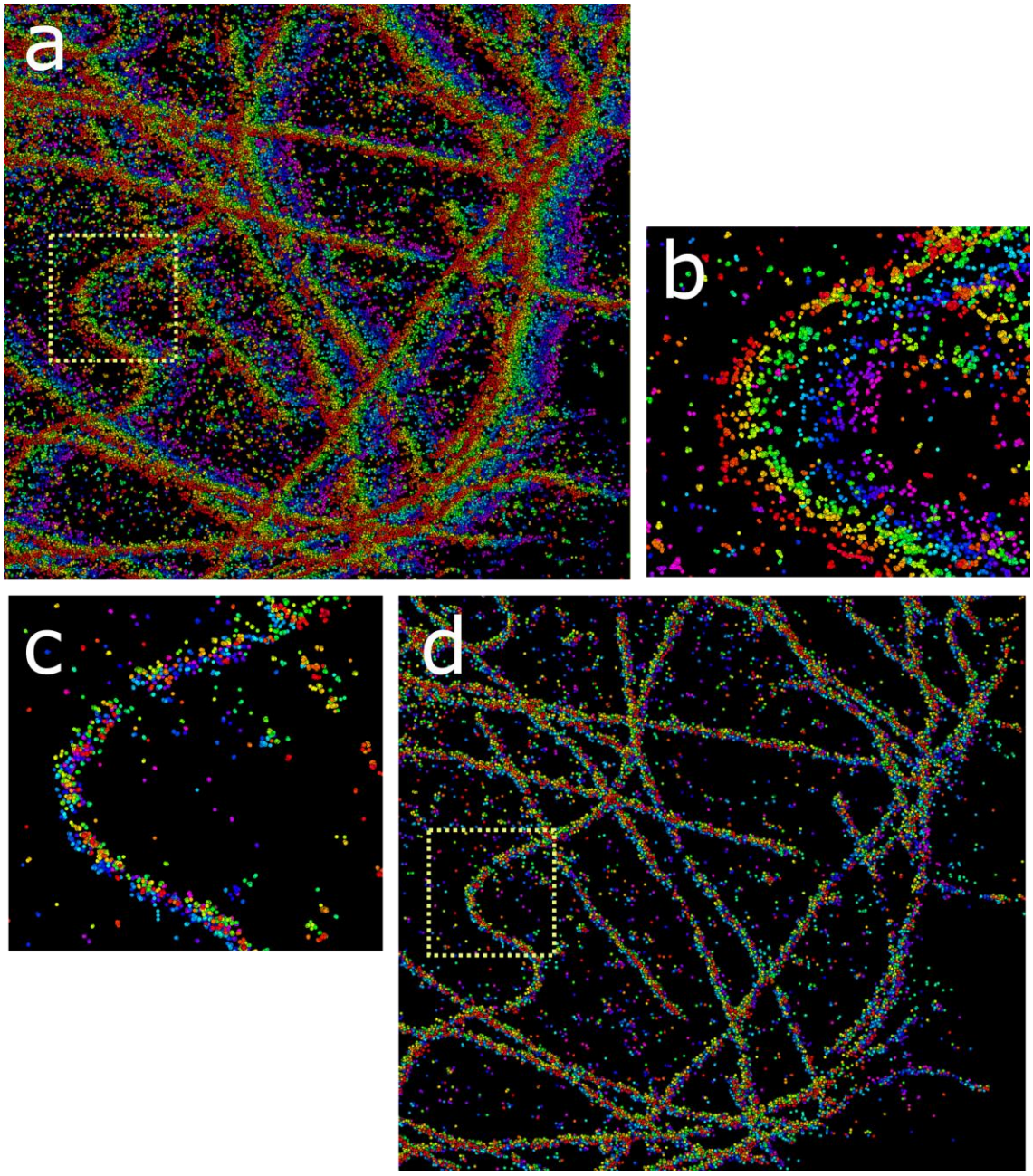

Figure 2.12. *A pseudo-colour applied to the detected localisation events* ***(a)*** *displays events according to relative acquisition time (red being the earliest). With a small ROI selected* ***(b)*** *the recorded lateral drift time courses were applied to correct for drift* ***(c)****. This corrected drift across the entire sample* ***(d)****.*

2.28. Ratiometric dSTORM imaging

For dual-colour dSTORM a dichroic mirror (Q680LP, Chroma Technology, Olching, Germany) and emission filter (XF3104-690ALP-17430, Laser components, Chelmsford, UK) was used to collect fluorescence emission, Figure 2.13.

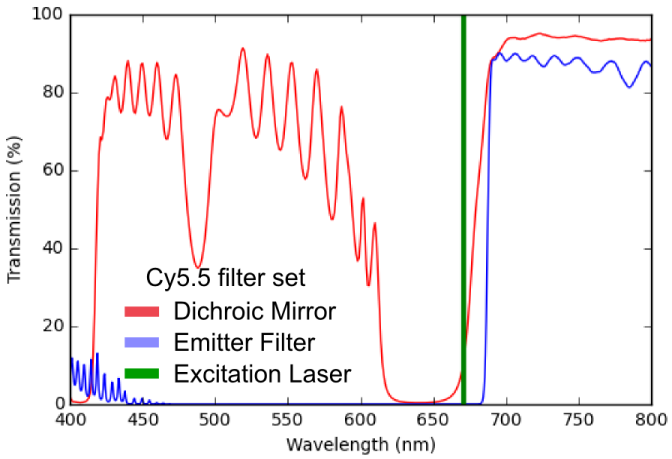

Figure 2.13. *The filter set used for dual colour dSTORM with Alexa Fluor 680 and 750. Dichroic mirror (Q680LP, Chroma Technology, Olching, Germany) and emitter filter (XF3104-690ALP-17430, Laser components, Chelmsford, UK)*

A splitter device (OptoSplit II, Cairn research, Faversham, UK), Figure 2.14, containing a dichroic mirror (t740lpxr, Chroma Technology, Germany) which allows the transmission of wavelengths longer than 741 nm, separates the Alexa Fluor 680 and Alexa Fluor 750 emission spectra.

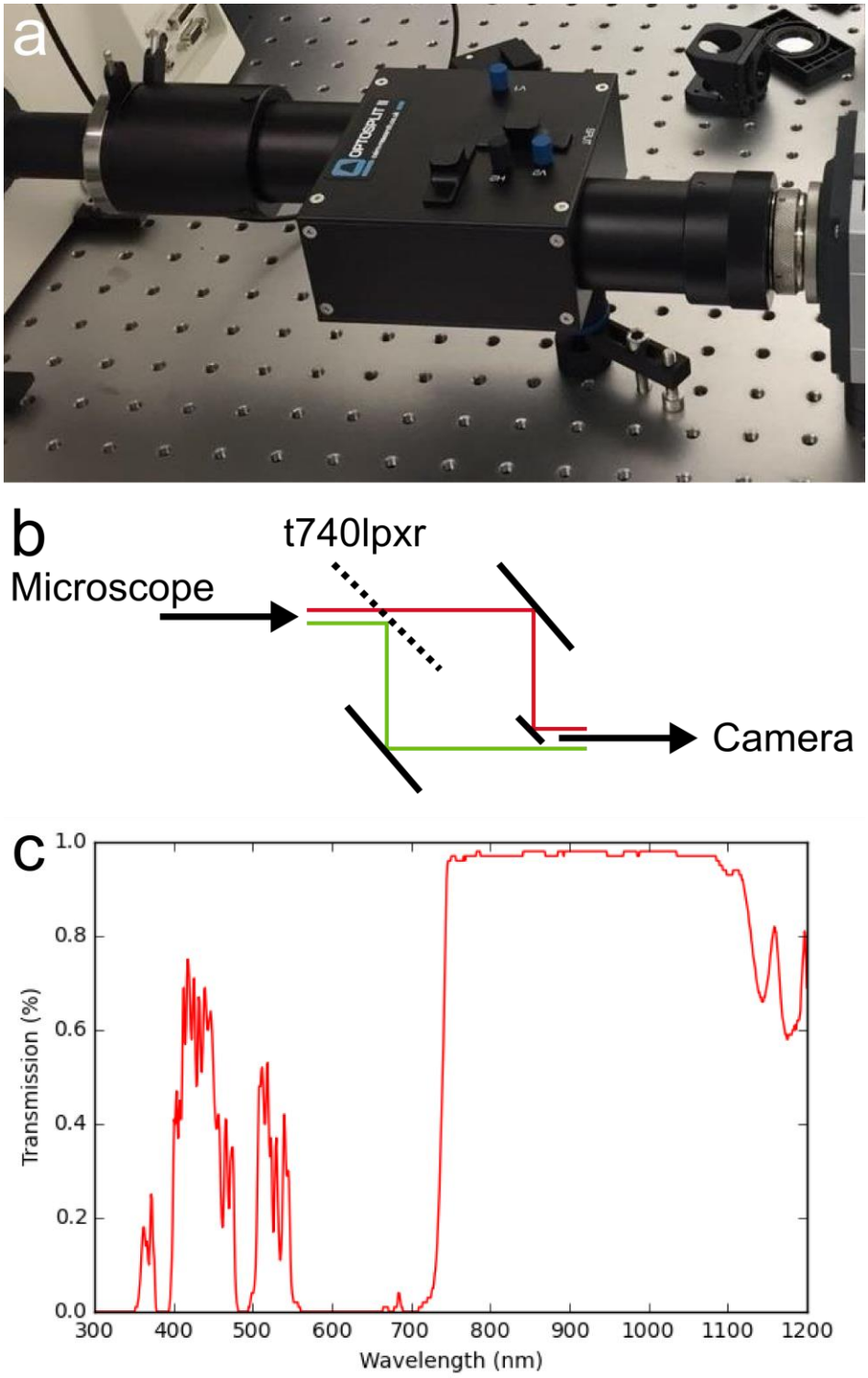

Figure 2.14. *A picture of the OptoSplit II splitter device used* ***(a)****. Schematic drawing of the passage of short and longer wavelengths through a t740lpxr (Chroma, Olching, Germany) dichroic mirror* ***(b)****. The transmission spectra for the t740lpxr dichroic mirror* ***(c)*** *which splits the emission of Alexa Fluor 680 and 750.*

Each of the two images are focussed onto separate halves of an electron multiplying charge-coupled device (iXon Ultra – EMCCD DU-897U, Andor, Belfast, UK) camera[85]. The use of adjustable mirrors allows for alignment between the two channels, Figure 2.15.

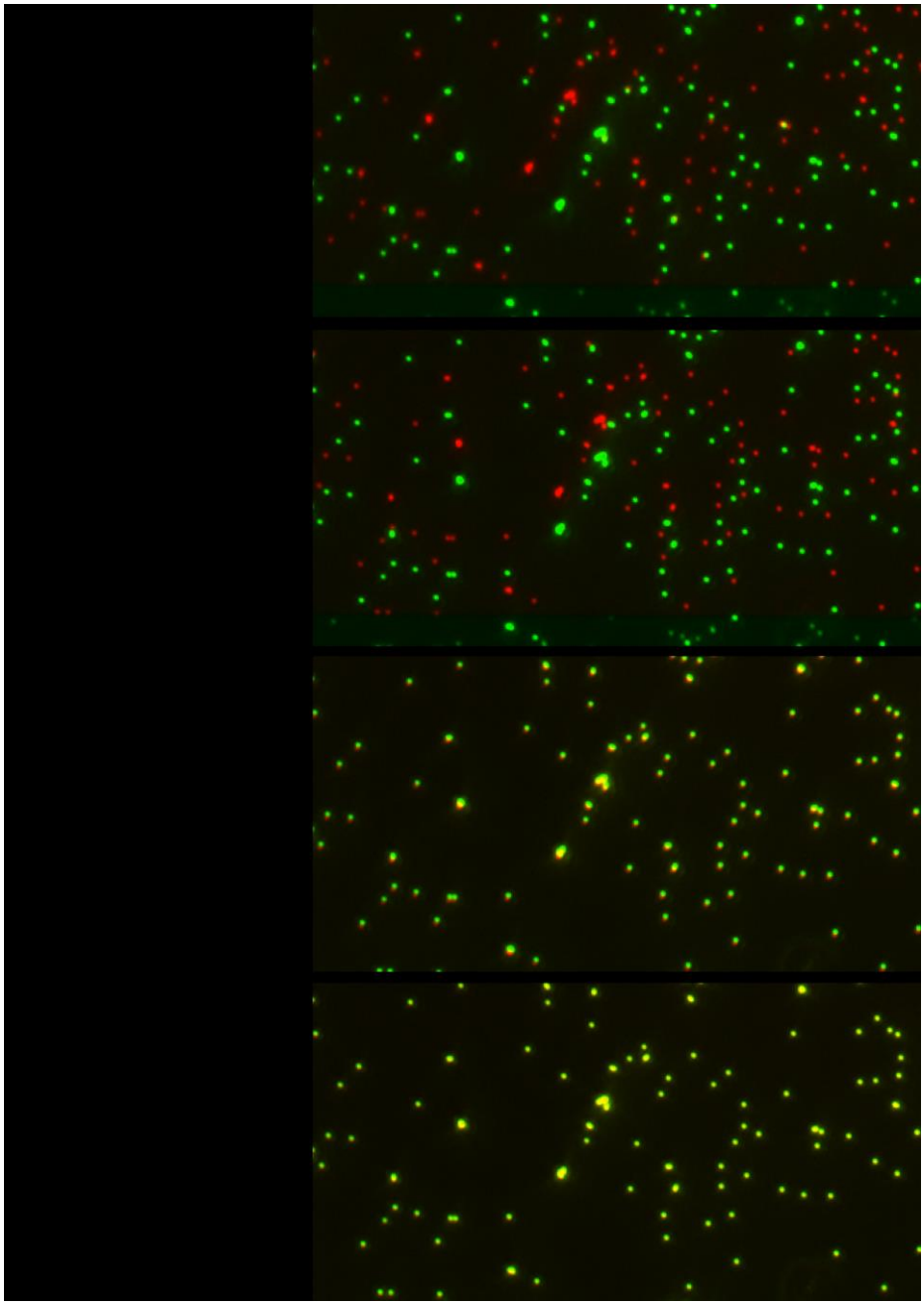

Figure 2.15. *Widefield images of the short (green) and long (red) channels. Clearly some spatial alignment required so that the two images overlap. Manual adjustments were made by tuning the mirrors until strong correlation could be seen.*

The remaining chromatic aberrations were corrected by obtaining a shiftfield sequence which calculated the vector difference between the same structure as viewed through each channel. An interspersed sample containing 0.21 µm dark red fluorescent beads (FluoSpheres™ carboxylate-modified dark red (660/680), F8807, ThermoFisher Scientific, Loughborough, UK) was moved a total of 60 µm in the x-direction in a series of 15 steps. A movement of 4 µm was then made in the y-direction and the process repeated until 60 µm had been covered in both axes, Figure 2.16.

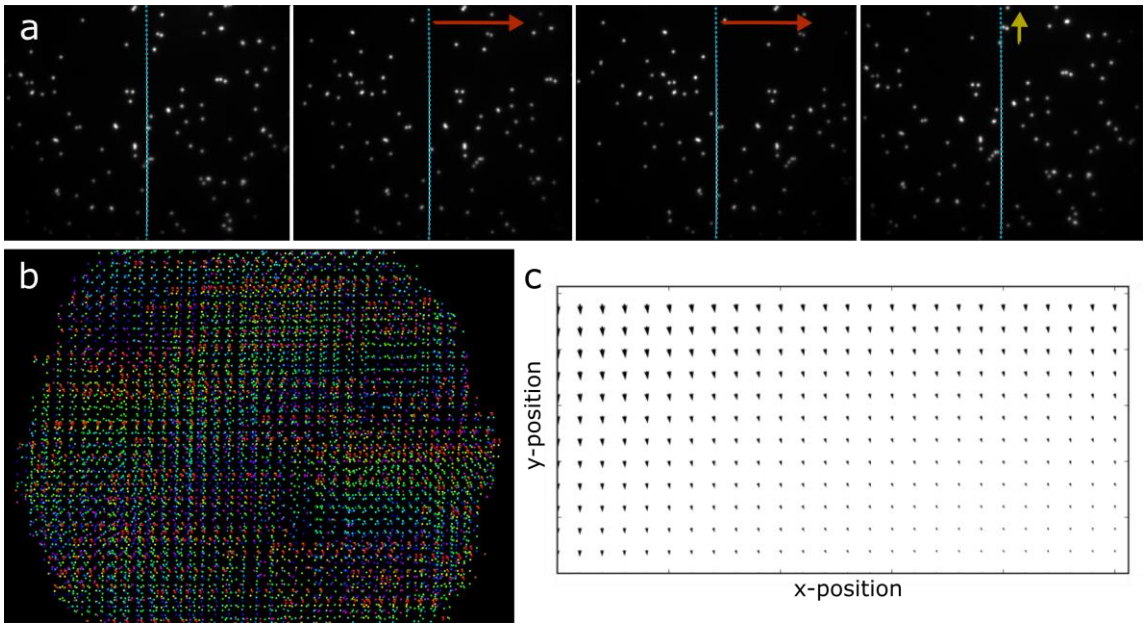

***Figure 2.16**. A shiftfield was obtained to calibrate the splitter prior to dual-colour dSTORM experiments. A fluorescent bead sample **(a)** was moved in a series of steps in both x and y directions, at each step an image was recorded, with a 500 ms integration time, and the position of the beads in both channels recorded **(b)**. The vectors were then extracted across the entire field of view **(c)** and saved.*

This vector map was then applied in the PYME software and close attention was paid to the correction via the appearance of the fluorescent beads, Figure 2.17.

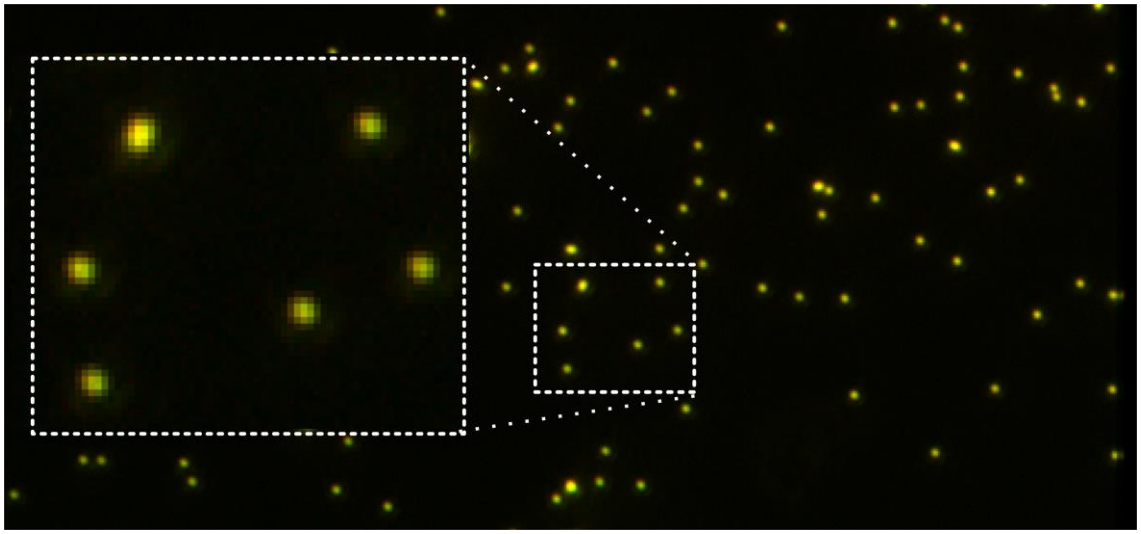

Figure 2.17. *Once a shiftfield has been completed and vectors extracted and applied the fluorescent beads should appear as one structure (**inset:** a magnified view of the visual registration shows residual sub-pixel shifts between the short and long splitter channels, however these shifts are correctly taken into account in the fitting routines).*

The overlap of the emission spectra from Alexa Fluor 680 and 750 after the splitter dichroic mirror results, Figure 2.18a, in single molecule events from these dyes being observed in both channels. The ratio of the pixel intensity from the two channels was used to determine which fluorophore the signal belonged to, Figure 2.18b.

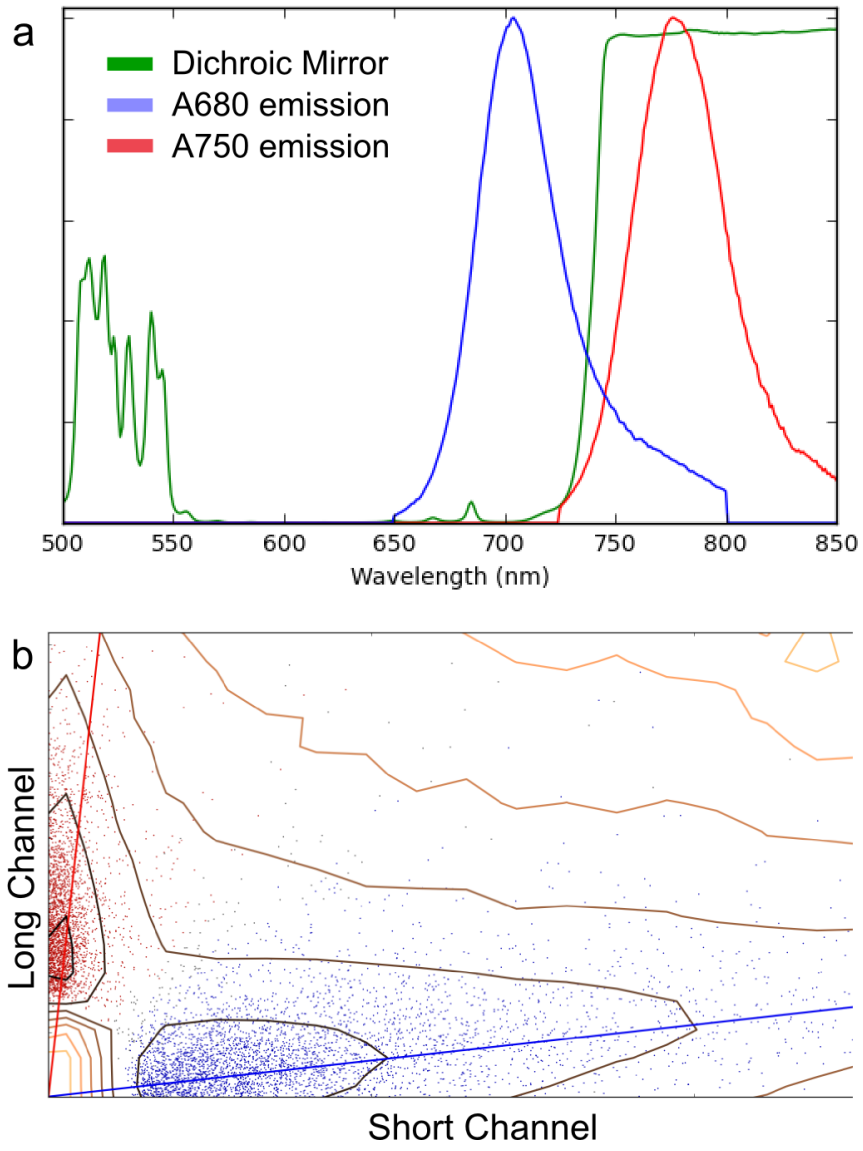

Figure 2.18. *The overlapping emission spectra* ***(a)*** *of Alexa Fluor 680 and Alexa Fluor 750, even after the splitter dichroic mirror (t740lpxr, Chroma Technology, Olching, Germany), results in signal from the fluorophores being present on both halves of the EMCCD. Events detected during dual-colour dSTORM acquisition and their apparent detection ratio shows a high degree of separation between the two clouds. Linear fits over the point clouds from pixel intensities* ***(b)****, from the two channels was used to assign events to the correct chromophore.*

2.29. Laser power measurements

Illumination intensities were controlled by adjusting the laser output power via the appropriate interface, i.e. power supply controls or digital command interface, and/or with the use of neutral density filters in the laser path. Power measurements were taken at the focal plane with a microscope slide photodiode power sensor (S170C, Thorlab, Exeter, UK) with a ±3% uncertainty.

2.30. SMLM acquisition

A region of interest (ROI), ~20 x 20 µm, was selected for each dSTORM or DNA-PAINT experiment and image acquisition started using the PYME software. The detection algorithms were executed in the open software PYME as implemented by David Baddeley and were fully analysed by him, as well as tested in a quantitative evaluation of software packages for SMLM by Sage et al[86]. Further detail can be found in the PYME software distribution and the cited publication. Detected events were displayed effectively in real time with the caveat that the event viewer was updated with a frequency of once per two seconds to reduce processing overheads and ensure responsiveness of the GUI interface. Single molecule event duration from 9bp imagers were tuned with the adjustment of neutral density filters to achieve a power, with the 642 nm laser, of 1-3 mW at the focal plane. This was suitable to achieve high signal to noise for individual events whilst utilising the average duration the imager strand was bound to the docking strand (~300ms) without prematurely photobleaching. The initial frames were used to determine a suitable detection threshold, Figure 2.19. Testing an individual frame allows a visual inspection of the results of the threshold and enables the user to adjust the stringency for detection, Figure 2.19b & c.

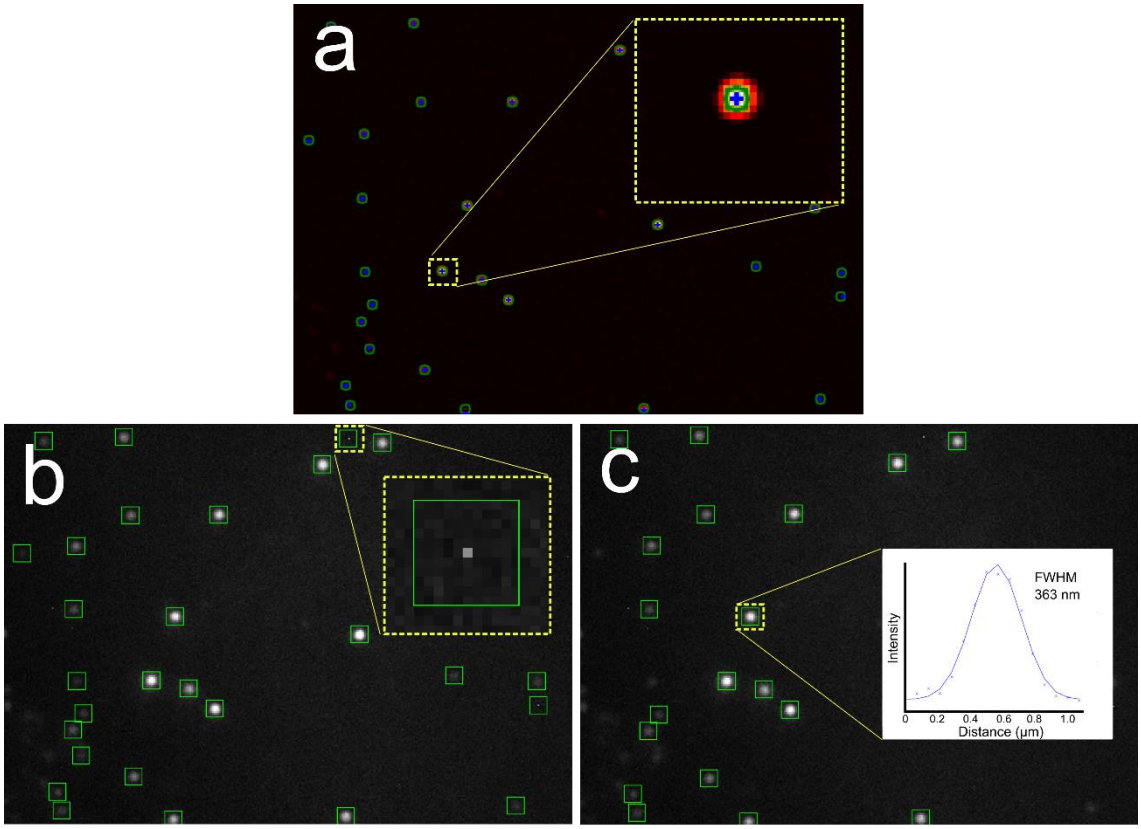

Figure 2.19 *Testing the detection threshold on an individual single molecule acquired frame* ***(a)****. Inset shows a magnified view of one of these single events producing co-ordinates for the centroid of the event. Green squares around events signify detected single molecule events whose centroid would be mapped* ***(b)****. At low detection thresholds overlapping, out of focus, and hot pixels* ***(inset)*** *are detected as events. Increasing the threshold rejects poor event data* ***(c)****. An intensity profile across a detected event yields a FWHM of 363 nm.*

2.31. Photon count estimates

An estimate for the number of photons per event, Figure 2.20, was calculated via equation 2.2.

$$N = \frac{2\pi A\sigma^2}{v_p^2} \times \frac{c_{e^-}}{G_{EM}} \tag{2.2}$$

where *N* is the number of photons per event, v_p is the voxel pixel size, *A* and σ are the amplitude and width respectively of the best Gaussian fit of the form $Ae^{\frac{-(x-x_0)^2-(y-y_0)^2}{2\sigma^2}}$, c_{e^-} is the conversion from electron to count in units electron per count, and G_{EM} is the EM Gain.

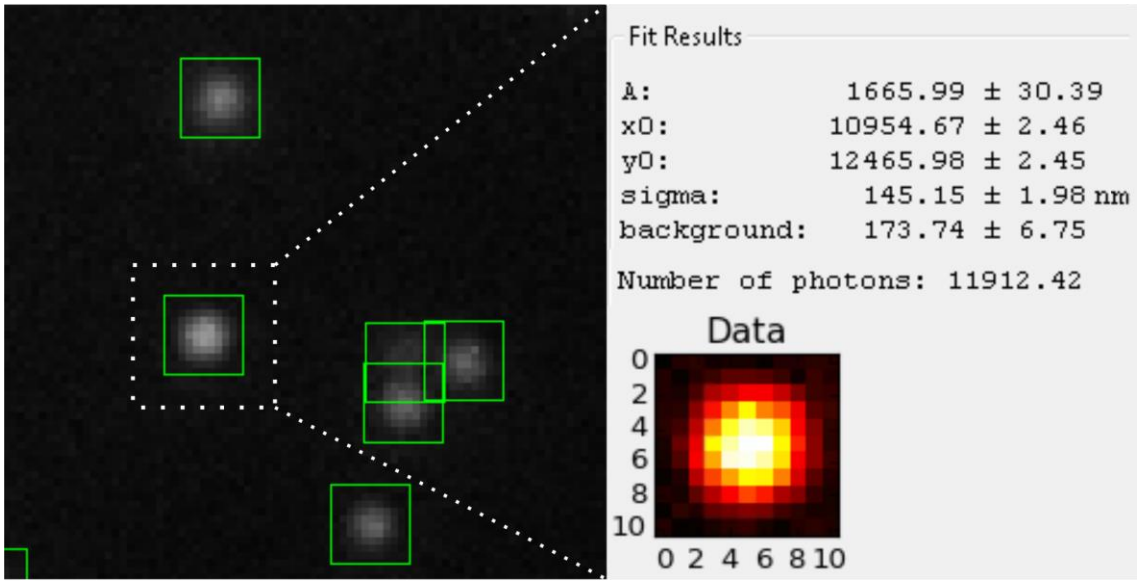

Figure 2.20. *A raw image frame from a single molecule experiment taken with an Andor Zyla 4.2 with an electron per count of 0.28 and voxel size 72 nm. Applying equation 2.1 yields an estimate for the number of detected photons.*

2.32. Localisation error estimates

The localisation error, whose derivation is very complex, was estimated using equation 2.3 from[34].

$$\sigma_{loc} = \frac{\sigma_a}{\sqrt{N}}\sqrt{\frac{16}{9} + \frac{8\pi\sigma_a^2 N_B}{Na^2}} \tag{2.3}$$

where N_B is the background photons, *a* the pixel size and σ_a the pixel-corrected event sigma where;

$$\sigma_a^2 = \sigma^2 + \frac{a^2}{12} \tag{2.4}$$

2.33. dSTORM dye photorecovery

A 405 nm laser (MLD™, Cobolt, Solna, Sweden), whose excitation was aligned with the other lasers, was used in brief 0.1-1 mW ON/OFF bursts, for UV recovery experiments.

2.34. dSTORM vs DNA-PAINT experiments

Secondary antibodies with custom oligonucleotides, Appendix 1, capable of conducting both DNA-PAINT and dSTORM experiments were incubated, as described above, for cultured COS-7 cells. The complimentary fixed imager strands, conjugated with Alexa Fluor 647, were added at 10 nM to a PBS solution. After labelling was confirmed by visual inspection, the sample wash thoroughly in a 10 mM MEA glucose oxidase (5 mg/mL) and catalase (0.05 mg/mL) 10% glucose (w/v) PBS solution. After the sample was completely photobleached, a transiently binding ATTO 655 imager sequence was introduced, at 0.3 nM, in order to conduct DNA-PAINT experiments. In DNA-PAINT experiments imager binding times were approximately 0.1 s and therefore the frame times were increased to this ON-time (from 25 ms to 100 ms) for proper temporal sampling.

2.35. Imaging probes, reagents and DNA-PAINT protocol

In DNA-PAINT imaging, the sample was immersed in ‘Buffer C’, containing typically 0.2 nM of the imager strand complementary to the respective docking strand which is linked to the secondary antibody that was intended to be imaged. The imager strands reversibly bind to the sequence-complementary docking strands and under TIRF illumination, the fluorophores of hybridized imager strands are imaged while transiently immobilised and appear in the image as transient events to produce short-lived fluorescent spots, Figure 2.21. whose shape matches the PSF of the microscope in its focal plane. These events are recorded as a series of image frames.

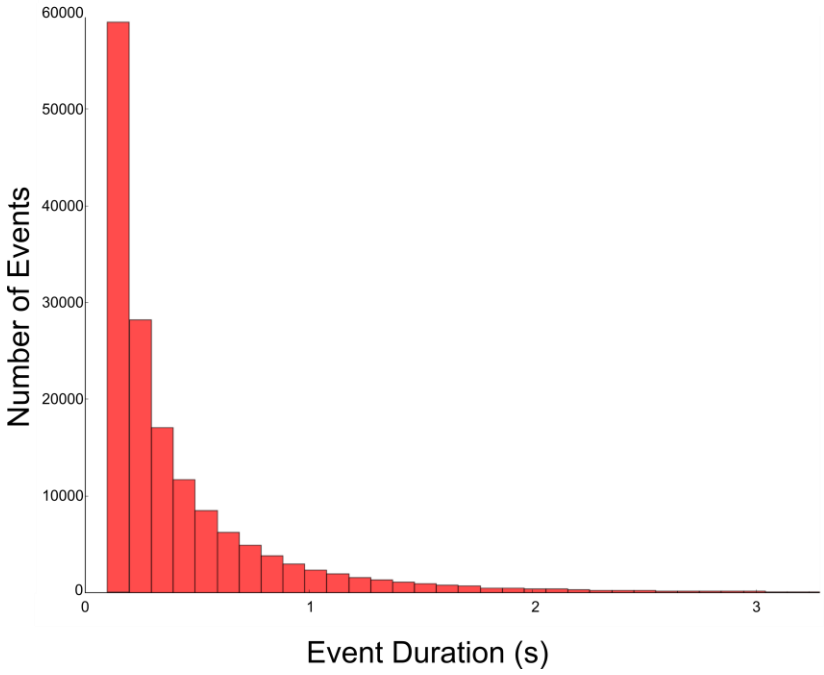

Figure 2.21. *A histogram depicting the duration of transient hybridisation between imager and docking strand in a normal DNA-PAINT acquisition. The duration of each 9bp P1 imager event, in Buffer C, varies with a mean 'ON' time of 392 ms.*

For DNA-PAINT imaging with the 642 nm laser and a secondary antibody with a P1 docking strand, a P1 imager strand with an ATTO 655 fluorophore was used in conjunction with a Cy5 dichroic and emission filter set (see Table 2.2 for details of each configuration). Each acquisition took between 15-25 minutes to acquire. Alexa Fluor 647-linked Goat anti-mouse IgG (ThermoFisher Scientific, Loughborough, UK) was used as a secondary antibody against the RyR2 primary antibodies in dSTORM experiments that were conducted for comparison.

2.36. Exchange-PAINT

For exchange-PAINT experiments (see protocol[32]), the P1 imager strand was either (i) replaced with another P1 imager with a different fluorophore (in experiments to test fluorophore- or excitation-specific variation in the image), (ii) after washout of the original P1 imager strand the same P1 imager strand was washed in again to test puncta reproducibility and robustness, or (iii) with a P3 imager strand with the same fluorophore that targets a second population of

secondary antibodies linked to a P3 docking strand. Exchange-PAINT experiments took twice as long as normal DNA-PAINT but with the addition of a 5-15 minute washing intermediate step.

2.37. Quencher-Exchange-PAINT

Experiments were conducted as in Exchange PAINT (2.36) apart from the washing step. After imaging the first target of interest, for example with a P1+ imager (see Appendix 2), a complementary strand was introduced at a concentration an order of magnitude greater than P1, which had a 5' lowablack modification. This quencher strand competes with the docking strand and binds irreversibly to the P1+ imagers. Quencher-Exchange-PAINT experiments removed the washing step in Exchange-PAINT and made the transition stage approximately 5 minutes whilst also reducing the risk of introducing sample drift with extended washes. At the end of an acquisition all imagers and quenchers were washed out and fresh imager introduced at the start of a new experiment.

2.38. Simulation of synthetic data

An algorithm implemented in the PYME software was used to generate synthetic single molecule localisation data as performed previously[87]. As a first step, model images of punctate RyR labelling densities placed in either (a) a gridded organisation at a fixed spacing, or (b) randomly placed and at a variable spacing to the next nearest neighbour as described by a random sample from a normal distribution with a specified σ. The centroids of the puncta were then convolved with a 2D Gaussian model with a σ of 5 nm (i.e. with a full width at half maximum of 12 nm) to smooth the mask. The model was then used as a starting template in the PYME software which generated single molecule events within the labelled regions to match the imaging parameters (length of acquisition, event rates, localisation error) observed in the dSTORM and DNA-PAINT experimental data for simulation of dSTORM and DNA-PAINT imaging, respectively. The parameters used for the synthetic data simulation are summarised in Table 2. 2. The generated point data were rendered into 2D greyscale data and subjected to

the centroid computation algorithm identically to the experimental analysis protocol described above to closely mimic the processing of the experimental data.

These simulations were conducted by Dr. I.D. Jayasinghe.

Image Analysis

2.39. Basic analysis and greyscale rendering

The frame data of DNA-PAINT single molecule events were analysed in real-time (during acquisition) using the freely-available PYME (http://python-microscopy.org/) developed by Dr David Baddeley in collaboration with our laboratory[85]. The analysis included the detection of single molecule events and least-squares fitting of a 2D Gaussian to localise their sub-pixel scale centroid. It also included the removal of the effect of sCMOS chip pixel non-uniformities, in terms of offset, read-noise, and fixed pattern noise, by the use of camera-maps. These non-uniform sensor properties were characterised in a separate study[33] and mention all details as to how the camera maps were recorded and the information incorporated for localisation is covered in the cited publication . The point data of the localised marker positions from a sub-series of 10,000 frames were selected for further analysis and events lasting more than one frame (tracked in consecutive frames to be within the localisation precision) were coalesced to minimise localisation errors, with the exception of qPAINT analysis. For qPAINT analysis, described in more detail below, un-coalesced single frame events where used. The event positions were then rendered into a 16-bit greyscale TIFF image with a pixel scaling of 1 nm/pixel using an algorithm based on Delaunay triangularisation[88] called “jittered triangulation”. In these images, the pixel intensity was linearly proportional to the local density of localised markers, i.e. similar in its information content to a typical greyscale fluorescence micrograph albeit at higher spatial resolution.

2.40. Analysis of punctate nanoscale densities

The punctate RyR labelling densities in the rendered images were detected using a custom-written analysis algorithm implemented in PYME. This involved a smoothing of the images (kernel size of 3.0 pixels) and a multi-threshold detection of labelled regions. In a second round, an automatically-defined region of interest (ROI) capturing each of the punctate densities was least-squares fitted with an adaptive two-dimensional (2D) Gaussian model to determine the sub-pixel coordinates of the 2D centroid of each punctum. These centroids were used to count the number of observable RyRs within each cluster and to calculate the neighbour distances through a Delaunay triangulation implemented with custom-written programs in the IDL programming language similar to previously described analyses[74]. The centroids from RyR images were also used to construct Euclidean distance maps which were the basis for the distance-based density analysis of JPH2 labelling.

2.41. Area-based analysis of DNA-PAINT images

The greyscale rendered DNA-PAINT images were also subjected to threshold-based analysis of RyR cluster areas similar to previous studies[62,89]. Using custom-written programs implemented in IDL, a global threshold which encapsulated 80% of the total labelling fraction above background was adopted to generate a mask of the RyR labelled area. By filling in all dark 'holes' in connected mask regions that were smaller than 5000 nm^2, a 2D mask of the overall RyR cluster area was robustly obtained. These 2D masks were used for computing the 2D area of RyR clusters and for performing a co-localisation analysis on the overlap between JPH2 and RyR in two-colour DNA-PAINT data based on an algorithm detailed previously in the supporting material from Baddeley et al[62].

2.42. Quantification of DNA-PAINT data using qPAINT

qPAINT analysis was used as a second approach to estimate the number of receptors underlying the recorded DNA-PAINT signals by statistical analysis of the fluorescence time series data as described recently[90]. Temporal fluorescence time courses were reconstructed from the localised event data, Figure 2.22, after segmenting events based on clustering. The qPAINT analysis code package, developed by the Soeller laboratory, is available as a supplementary PYME package and can be downloaded at:
http://bitbucket.org/christian_soeller/pyme-extra.

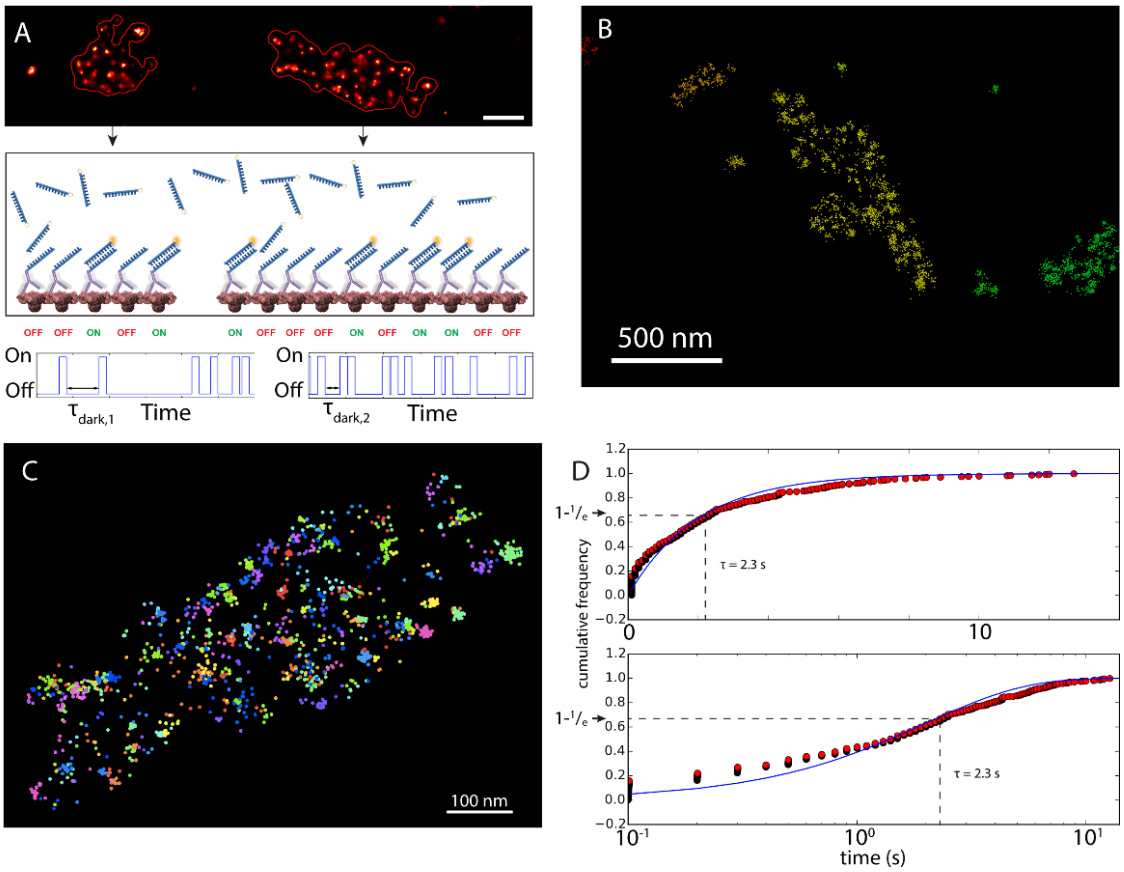

Figure 2.22. *Methodology of qPAINT analysis to verify RyR cluster size. qPAINT is a procedure described by Jungmann et al*[90] *which allows the estimation of the number of DNA-PAINT binding sites within a given nanodomain. This method, of quantitative imaging to estimate the number of RyRs per cluster, was used independently of the morphological analysis of the punctate labelling densities.* ***(A)*** *Principle of DNA-PAINT. qPAINT analyses the temporal properties of single molecule event detections recorded at a given cluster. Two clusters are shown, one larger than the other. The rate at which imagers bind to receptors in a cluster is proportional to the number of receptors in the cluster. In qPAINT the average dark time between detected binding events is measured (lower panels) which shortens as more labelled receptors provide binding sites for imagers in solution. The receptor numbers are proportional to the inverse of the dark time but to obtain absolute numbers a calibration must be performed to determine the constant of proportionality (which depends on imager on rates and concentration).* ***(B)****. A view of detected events* ***(dots)*** *in a small section of a DNA-PAINT data set. Events are segmented and coloured according to the cluster they belong to. Segmentation was conducted based on local event density.* ***(C)****. A single cluster is shown where all events belonging to this cluster are coloured according to the time at which they were detected.* ***(D)*** *From the events belonging to a cluster and their time stamps (frame number) a cumulative histogram of dark times is reconstructed* ***(red dots)*** *which is fit with the theoretically expected distribution for a first order binding reaction. The average dark time is located at the 1-1/e point of the curve, here τ = 2.3 s.* ***Top panel:*** *linear time scale;* ***bottom panel:*** *logarithmic time scale.*

qPAINT analysis of DNA-PAINT data is based on the idea that the temporal statistics of imager binding contains information about the number of binding sites (docking strands) given that the transient binding between individual imaging and docking strands follows first order binding kinetics. Specifically, the measured dark time, τ_D, is related to the number of binding sites, N_B, via

$$N_B = \frac{1}{k_{on} c_i \tau_D} \tag{2.5}$$

where k_{on} is the on-rate of imager to docking strand binding and c_i is the imager concentration. When using a marker, such as an antibody, that holds α docking sites and the number of antibodies, β, bind on average to a single receptor the number of receptors N_R is also proportional to ${\tau_D}^{-1}$.

$$N_R = \frac{N_B}{\alpha\beta} = \frac{1}{\alpha\beta k_{on} c_i} \frac{1}{\tau_D} = c' q_i \tag{2.6}$$

where all constants have been grouped into the constant *c'* and termed the inverse of the dark time the "qPAINT index" $q_i = {\tau_D}^{-1}$. N_R can be obtained from the uncalibrated qPAINT index q_i if the calibration value q_{i1} can be measured, where q_{i1} is the qPAINT index value for a single receptor. Inspection of the formulae then yields

$$N_R = \frac{q_i}{q_{i1}} \tag{2.7}$$

I pursued the calibration strategy as derived above to obtain receptor number estimates. The *in-situ* calibration was performed for each DNA-PAINT series since it is difficult to control the imager concentration, c_i, accurately between experiments. Care was taken to only analyse DNA-PAINT sequences that exhibit a constant event rate over the time window that was analysed for qPAINT quantification.

2.43. Measurement of dark times and qPAINT indices

Cluster event segmentation was performed based on cluster segmentation of rendered images. Cluster masks were obtained from rendered images as described in the section “area-based analysis of DNA-PAINT images” above. Events located within the cluster mask of a given cluster were grouped into the event group belonging to that cluster. The event group of a cluster and the associated event time stamps were used to reconstruct the sequence of dark times as contiguous frame times that did not contain an event. All dark times from a cluster were pooled to obtain a normalised cumulative histogram of dark times for the cluster. The resulting dark time histogram was fit with an exponential expression 1-exp(-t/τ_D) to estimate the dark time constant, τ_D. The inverse of the dark time, ${\tau_D}^{-1}$, was calculated for each cluster and stored as the qPAINT index q_i of the cluster.

2.44. Calibration of qPAINT data

To obtain estimates of receptor numbers, N_R, for each cluster, a calibration was performed for each DNA-PAINT series. This was achieved by calculating a histogram of cluster qPAINT indices for very small clusters as identified by a cluster area < 10,000 nm^2. Visually these corresponded to clusters containing one or few puncta. The calibration histogram generally exhibited a prominent peak at a small qPAINT index value q_{i1} and secondary peaks at multiples of this value. The calibration value was determined by a multi-exponential histogram fit with peaks at multiples of the fitting parameter q_{i1}. qPAINT indices of all clusters were combined with the calibration value q_{i1} to obtain absolute receptor number estimates N_R as the ratio q_i / q_{i1}.

2.45. Measurement of receptor ratios in DNA exchange-PAINT series by qPAINT analysis

To obtain an estimate of the ratio between the number of RyRs, N_R, and N_J of JPH receptors for each cluster qPAINT analysis was conducted as described above for the RyR and JPH channels of DNA exchange-PAINT series, respectively. This included per channel calibrations of the RyR and JPH signals, respectively. The analysis was limited to larger RyR clusters (> 15 RyRs) which consistently contain JPH2[91] and the RyR cluster mask was used for both the segmentation of the RyR and JPH event data. The ratio $r_{J\text{-}R} = N_R / N_J$ was then calculated for each large cluster in this way.

Parameter	dSTORM	DNA-PAINT
Events per pixel	1.0	1.0
Event intensity (photons)	1000	8000
Event background (photons)	200	600
Event duration (frames)	3	6
Events per marker	2	5
Number of frames	30000	10000
Rendering localisation error filter threshold	30 nm	10 nm

Table 2.2. *The parameters adopted for generating synthetic localisation data in Python Microscopy Environment software.*

Chapter 3

Observations of the variables associated with single molecule imaging

The aim of this chapter was to investigate the sensitivity of dSTORM imaging to certain experimental parameters. Four Alexa Fluor photoswitchable probes were used to examine the effects of adjusting specific imaging parameters, including laser excitation and mounting buffer ingredients. Reducing agents, commonly used in dSTORM switching buffers, have a limited shelf-life. Here I quantify thiol activity through spectrophotometry of its reaction with Ellman's reagent. I examine an alternative oxygen depletion method that uses sulphite, prolonging the activity of thiol buffers, enabling a readymade solution to be stored for quick use over a period of one month. Secondary, blue-shifted excitation of the photoswitching molecular probes was investigated to determine its benefit, and it was found to reduce localisation error and substantially increase event numbers. The Alexa Fluor 660 dye was found to have excellent photoswitching capabilities and exhibited an improved quantum yield upon excitation with a 561 nm laser. A custom-designed oligonucleotide allowed for a direct comparison between the dSTORM and DNA-PAINT approaches.

3.1. Introduction

dSTORM is dependent on the ability of a fluorescent dye to be able to photoswitch. Only a small number of existing fluorophores have the required characteristics that make a good single molecule dye[18,29,34,92]. These important parameters include:

1. Photon yield: The number of photons emitted (and detected), per switching cycle, must be high to precisely locate the position of the fluorescent label. This follows from the approximate inverse square root dependence of the localisation precision (Δx) on the number of detected photons[92], equation (3.1).

$$\Delta x = {}^{\sigma}/_{\sqrt{N}} \tag{3.1}$$

   Where Δx is the localisation error when the background contributions are negligible, σ the standard deviation of the PSF, and N the number of detected photons.

2. Duty cycle: This is the measure of how fast the molecule switches between an on and an off state. The duration needs to be long enough for each event, in order to emit a sufficient number of photons and therefore obtain strong signal to noise. However, the longer the duty cycle the greater the probability of observing overlapping events.

3. Survivability: A measure of how well a fluorophore endures photoswitching, and to what extent they can return to a fluorescing state before succumbing to permanent photobleaching.

The photoswitching abilities of these single molecule fluorophores can themselves be directly altered by adjusting a number of imaging variables. Photon numbers, and duty cycles, can be boosted by adjusting the excitation

laser power. The duty cycle can be further manipulated, along with the fluorophore's resistance to photobleaching, by varying the composition of a super-resolution mounting buffer. For single molecule photoswitching experiments all of these variables need to be considered, and optimised, in order to obtain good localisation precision. Here I further investigate and discuss the most important parameters; including medium composition, oxygen concentration and secondary blue-shifted excitation on a selection of organic fluorophores for use in dSTORM imaging.

3.2. Mounting medium

Conventional imaging solutions, or switching buffers, for super-resolution experiments tend to be either aqueous[93] or glycerol-based[94]. Aqueous mixtures have a lower refractive index (~1.33), resulting in poorer contrast and resolution, due to refractive index mismatching[95,96] with the glass coverslip (~1.52). Glycerol's refractive index (~1.47), being closer to glass, reduces the amount of spherical aberration observed with increasing depth, improving the resolution when imaging optically thick samples. The original STORM publication[16] used an oxygen scavenging system and thiol reducing agent within an aqueous solution. This buffer enabled the switching of Cy5, a structurally similar fluorophore to the Alexa Fluor dye 647. There have been at least five other, substantially different photoswitching cocktails for use with dSTORM, that have been reported in the literature. These buffers have been attempted to improve photon yields, or photoswitching, or longevity and include; modifying redox chemistry with ascorbic acid[97] or PCA/PCD and Trolox[98], reduction with tris 2-carboxyethly phosphine (TCEP)[99], strong reduction into a long-lived non-fluorescing form using sodium borohydride ($NaBH_4$) and subsequent photoactivation with a blue-shifted laser excitation[100], and a buffer with unknown additives in the form of a commercial product called Vectashield[101].

3.3. Oxygen concentration

Fluorophores that have entered into a triplet state, required for photoswitching[27], can become permanently photobleached by reactions with molecular oxygen. Reducing oxygen concentrations in dSTORM mounting buffers is key to maintaining photoswitching for the extended durations necessary for imaging. It is possible to reduce or completely remove oxygen from switching buffers through the use of oxygen scavenging enzymes, Figure 3.1, or other chemical processes. In aqueous buffers, such as PBS, one can use the oxygen scavenging enzymes glucose oxidase and catalase to remove oxygen.

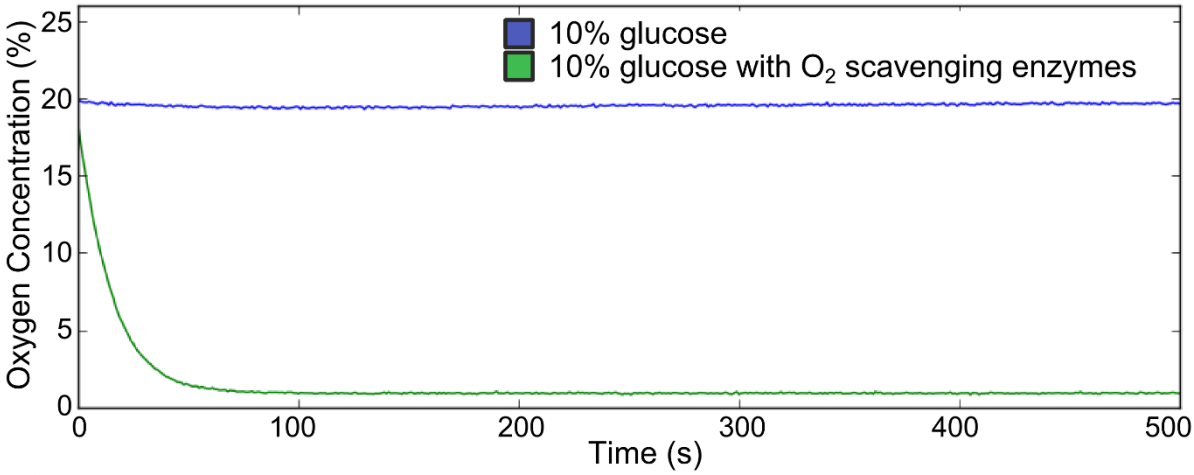

Figure 3.1. *Oxidation concentration readings, taken with a NeoFox-Kit-Probe oxygen monitoring sensor (Ocean Optics, Oxford, UK), of PBS containing 10% (w/v) glucose. Upon introduction of 0.5 mg/mL glucose oxidase and 0.05 mg/mL catalase, free oxygen is rapidly scavenged over the course of one minute.*

The diffusivity in liquid is given by the Stokes-Einstein equation (3.2).

$$D = {}^{kT}/_{6\pi\mu r} \tag{3.2}$$

where *k* is the Boltzmann constant, *T* is the temperature, *μ* is the viscosity, and *r* is the radius of the diffusing particle.

In glycerol, which has higher viscosity and therefore a lower diffusivity coefficient, the rate at which the enzymes are able to remove oxygen is greatly diminished. Increasing constituent glucose concentration increased the rate at which the oxygen could be scavenged, but oxygen was never consistently reduced to background levels, Figure 3.2.

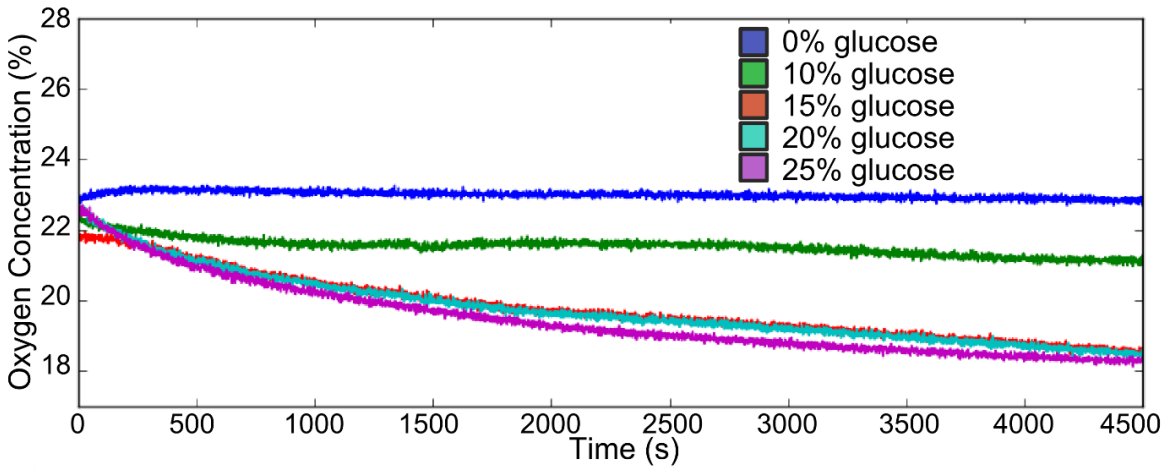

Figure 3.2. *With the same enzyme concentration used in PBS mountants, the oxygen concentration was measured for glycerol buffer containing increasing percentages of glucose (w/v). At levels between 15-25% glucose (w/v) oxygen removal rates appeared to saturate.*

The imaging chambers used for super-resolution experiments are open topped, exposing solutions to the ~21% atmospheric oxygen. Competition therefore exists between the chemical oxygen scavengers and the oxygen transfer occurring at the surface. As long as the ability to scavenge oxygen outcompetes this process, atmospheric oxygen is not an issue.

Doubling the starting concentration of both the enzymes appeared to resolve this, depleting the oxygen levels in higher glucose concentrations (w/v) to near zero, Figure 3.3.

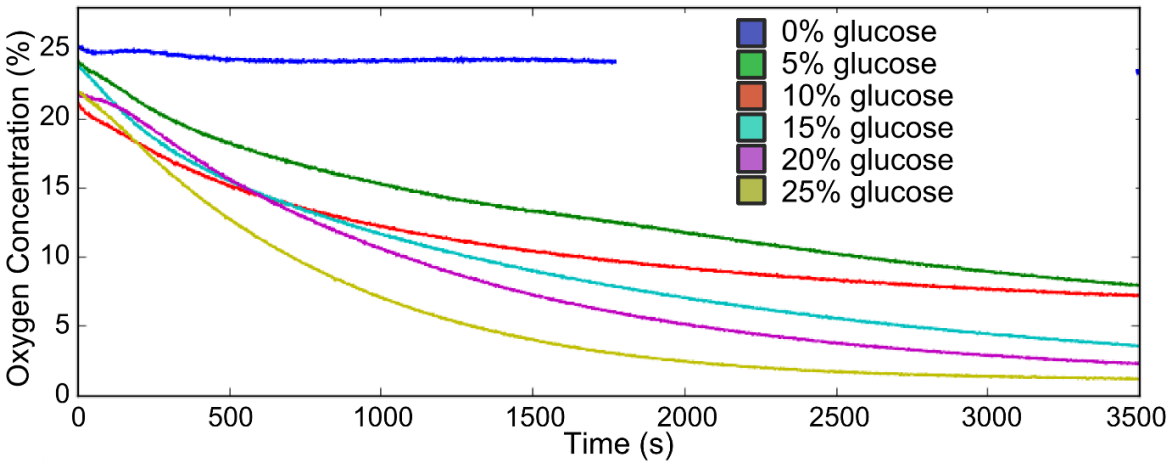

Figure 3.3. *The oxygen concentration of glycerol containing 1.0 mg/mL glucose oxidase and 0.1 mg/mL catalase with increasing glucose (w/v). Even at 5% glucose (w/v) oxygen concentration begins to deplete. Between 15-25% glucose (w/v) oxygen levels are all significantly reduced within one hour.*

The glucose oxidase (GOD) catalyses the reaction of glucose and oxygen to D-glucono- 1, 5-lactone and hydrogen peroxide, equation 3.3.

$$C_6H_{12}O_6 + O_2 \xrightarrow{GOD} D\text{-}glucono\text{-}1{,}5\text{-}lactone + H_2O_2 \tag{3.3}$$

D-glucono-1,5-lactone spontaneously hydrolyses to gluconic acid, which over time increases the pH, equation 3.4.

$$C_6H_{10}O_6 + H_2O \leftrightarrow C_6H_{12}O_7 \tag{3.4}$$

The glucose catalase (CAT) catalyses the decomposition of hydrogen peroxide to water and oxygen, equation 3.5.

$$2H_2O_2 \xrightarrow{CAT} 2H_2O + O_2 \tag{3.5}$$

Not only can acidification be problematic for biological tissues, especially when attempting live dSTORM super-resolution, but acidity also affects the photo-physical properties of the fluorescent probes[102].

Alternatively, reducing agents such as the thiol β-Mercaptoethylamine (MEA) which have a carbon-bonded sulfhydryl (R-SH) group, also reacts with oxygen and can themselves be used to remove oxygen, Figure 3.4 via equation (3.6) and (3.7).

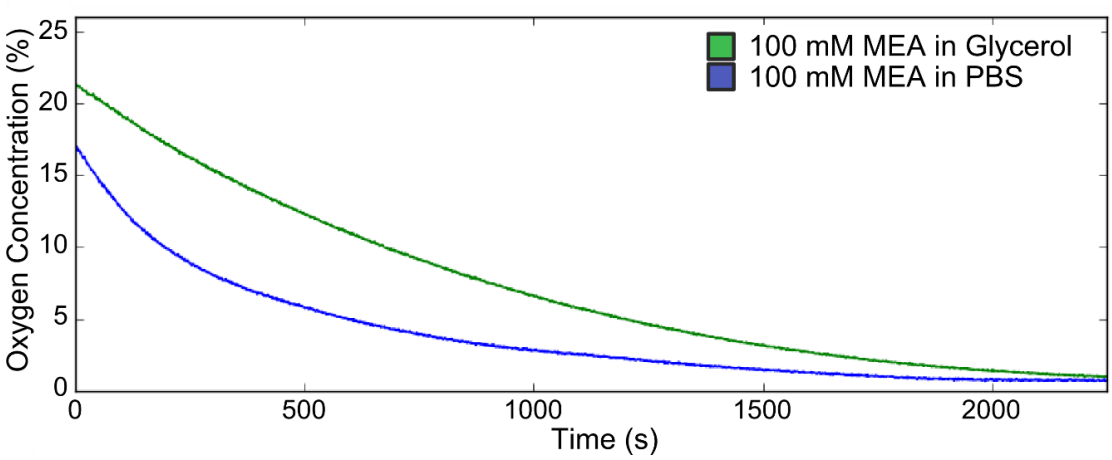

Figure 3.4. *The ability of a thiol reducing agent, MEA, to remove oxygen from both an aqueous, PBS containing, and glycerol based switching buffer without the use of alternative oxygen scavengers. Again, the rate at which the oxygen is removed in glycerol is slower.*

$$2\,RSH + O_2 \rightarrow RSSR + H_2O_2 \tag{3.6}$$

$$4\,RSH + O_2 \rightarrow 2\,RSSR + 2H_2O \tag{3.7}$$

3.4. Buffer stability

A constraint on the majority of photo-switching buffers, in current use for super-resolution imaging, is their limited shelf-life. Reducing agents, by their very nature, degrade over time. As a result, the reproducibility in buffer performance from day to day experiments is often unpredictable, and good practice requires fresh buffer to be made before every experiment.

The water-soluble Ellman's reagent, Bis(3-carboxy-4- nitrophenyl) disulphide or DTNB)[103] is used prior to dSTORM experiments to provide a simple visual inspection, to confirm adequate thiol activity. With the use of a UV-vis spectrophotometer, see Chapter 2.22, estimates for thiol activity were made.

Measuring the reactivity of dated MEA 2M stock solutions displays the degradation over time, Figure 3.5. After ten weeks the stock solution was found to have <50% thiol activity.

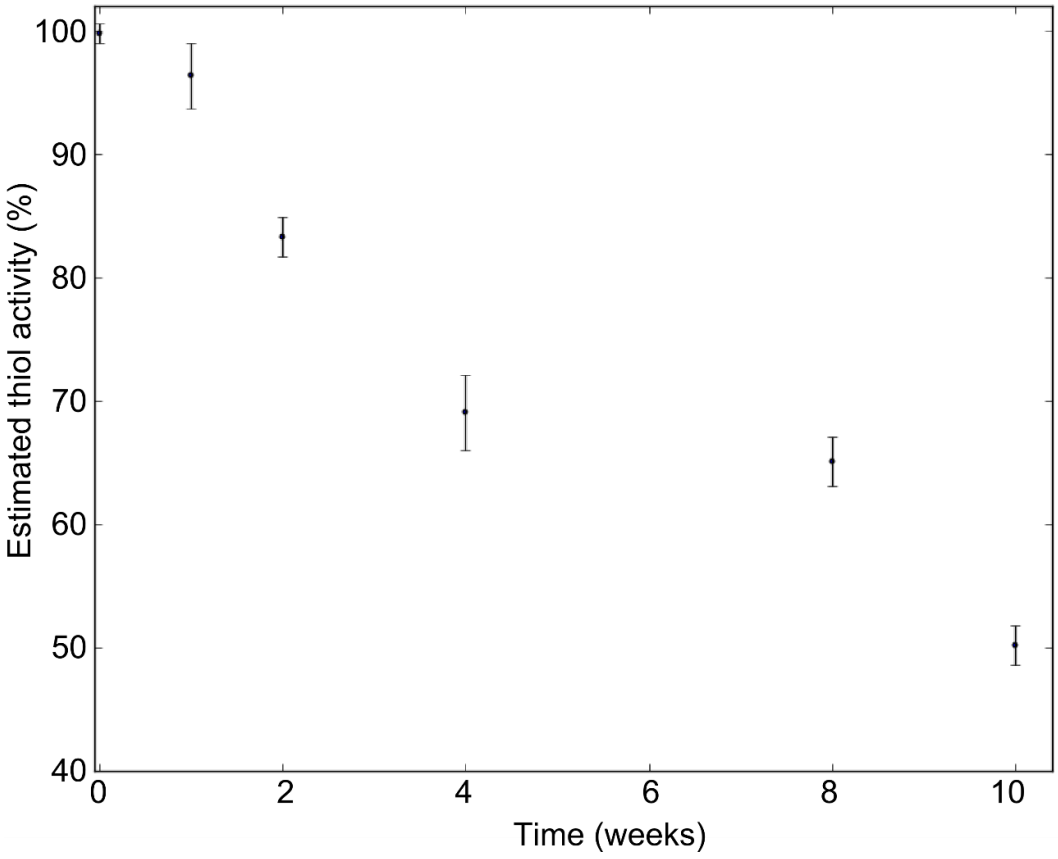

Figure 3.5. *Measuring the absorbance at 410 nm of aged MEA solutions and comparing this to the expected, shows a decrease in the active concentration over time.*

The ability to ascertain the active thiol component, see Chapter 2.22, in dSTORM switching buffers enables the experimenter to adjust their buffer in a quantitative

manner prior to experimentation. This has the potential to save time by reducing failed experiments caused by thiol degradation.

However it would be ideal if the stability of MEA solutions could be improved, perhaps by reducing the oxygen concentration. The effects of adding sodium sulphite (Na_2SO_3), Figure 3.6, as an oxygen scavenger, using the reaction (3.8) was investigated in an attempt to address this.

$$2Na_2SO_3 + O_2 \rightarrow 2Na_2SO_4 \tag{3.8}$$

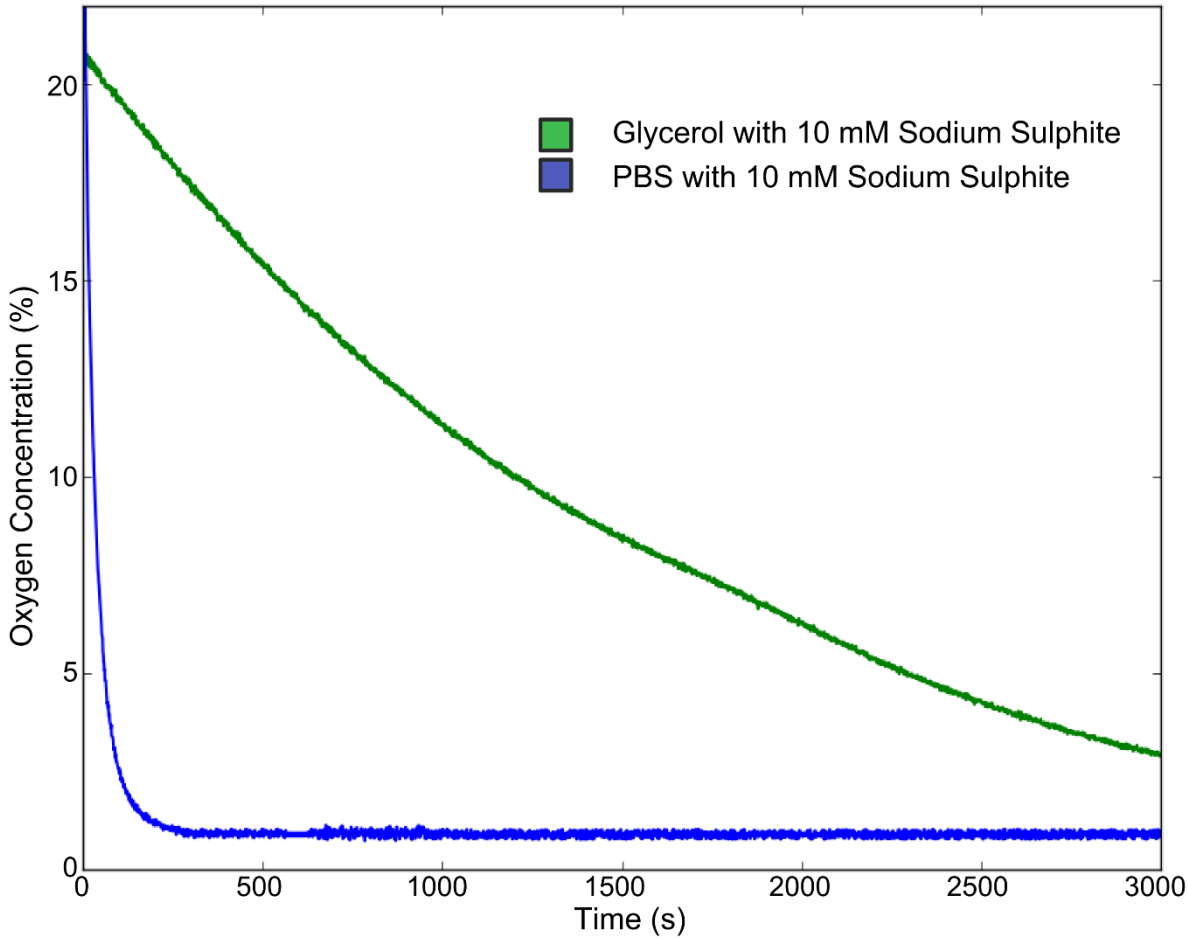

Figure 3.6. *10 mM sodium sulphite rapidly removes oxygen from aqueous solutions. The process takes close to an hour in glycerol.*

In comparison to a freshly made, (including 30 minute mixing time), 10 mM MEA solution, there was a slight, approximate 10%, reduction in photon collection per

event, Figure 3.7. However, the 10 mM Na_2SO_3 protected the mountant for an extended duration with only a slight degradation to the quality of photoswitching in comparison to its first use. The use of Na_2SO_3 enabled the same buffer to be used for up to one week.

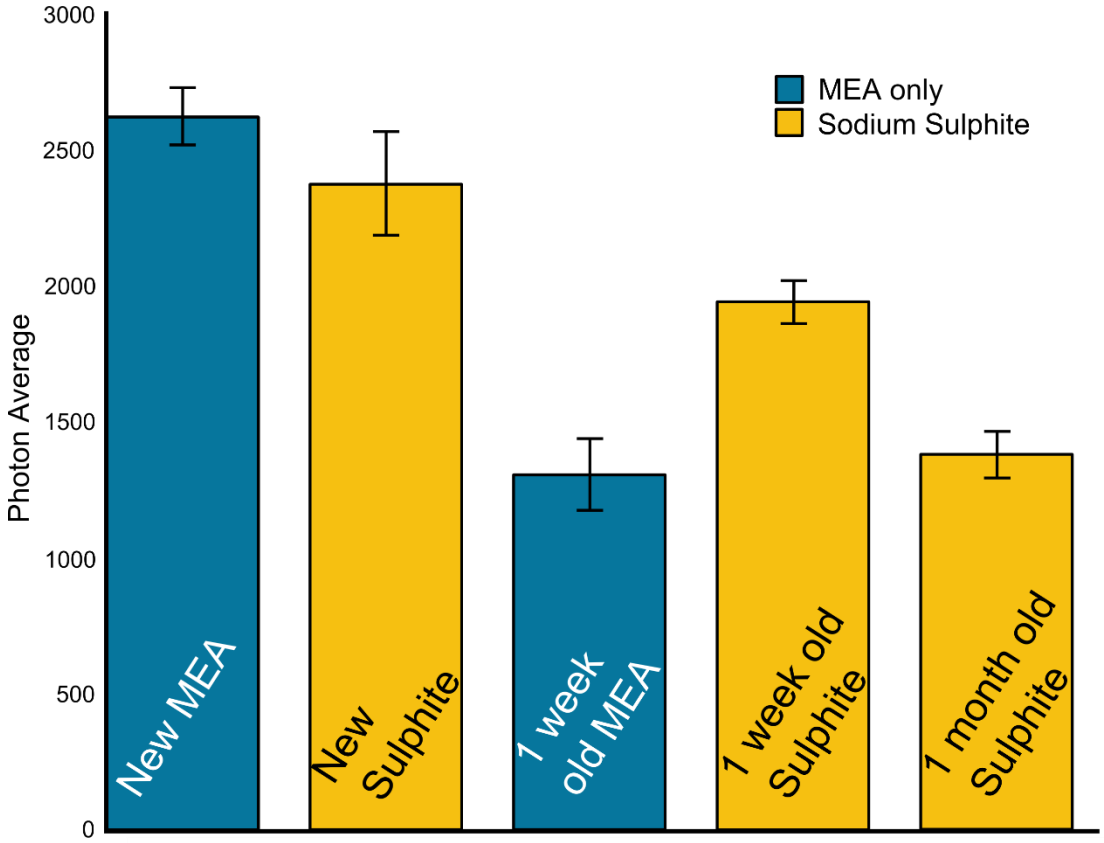

Figure 3.7. *Average photon counts during dSTORM experiments, using 10 mM MEA glycerol based switching buffers, both with 10 mM sodium sulphite* ***(yellow)*** *or without* ***(blue)****. A 10% decrease in the number of photon detected per event was observed with the use of Na_2SO_3 in comparison to using fresh MEA of the same concentration. At one week the buffer containing only MEA became less reactive, obtaining ~50% photon yield in comparison to MEA with sulphite ~85% maintained photon collection. After the period of one month a dSTORM image was unobtainable with the MEA only solution whilst the Na_2SO_3 still produced ~60%, in comparison to its starting ability.*

Sulphite is also capable of reacting with Ellman's reagent[104] and so a quantitative measurement of the protection Na_2SO_3 offered the MEA was not possible.

The reactivity of the thiol was found to be dependent on the medium in which it was stored. For instance the 2M stock solution in 10x PBS, that fresh buffers were typically made from, remained approximately 80-90% reactive for 2 weeks at 4°C. A 10 mM MEA switching mountant in glycerol, made to test its extended use, exhibited in comparison a sharp decline in activity, Figure 3.8.

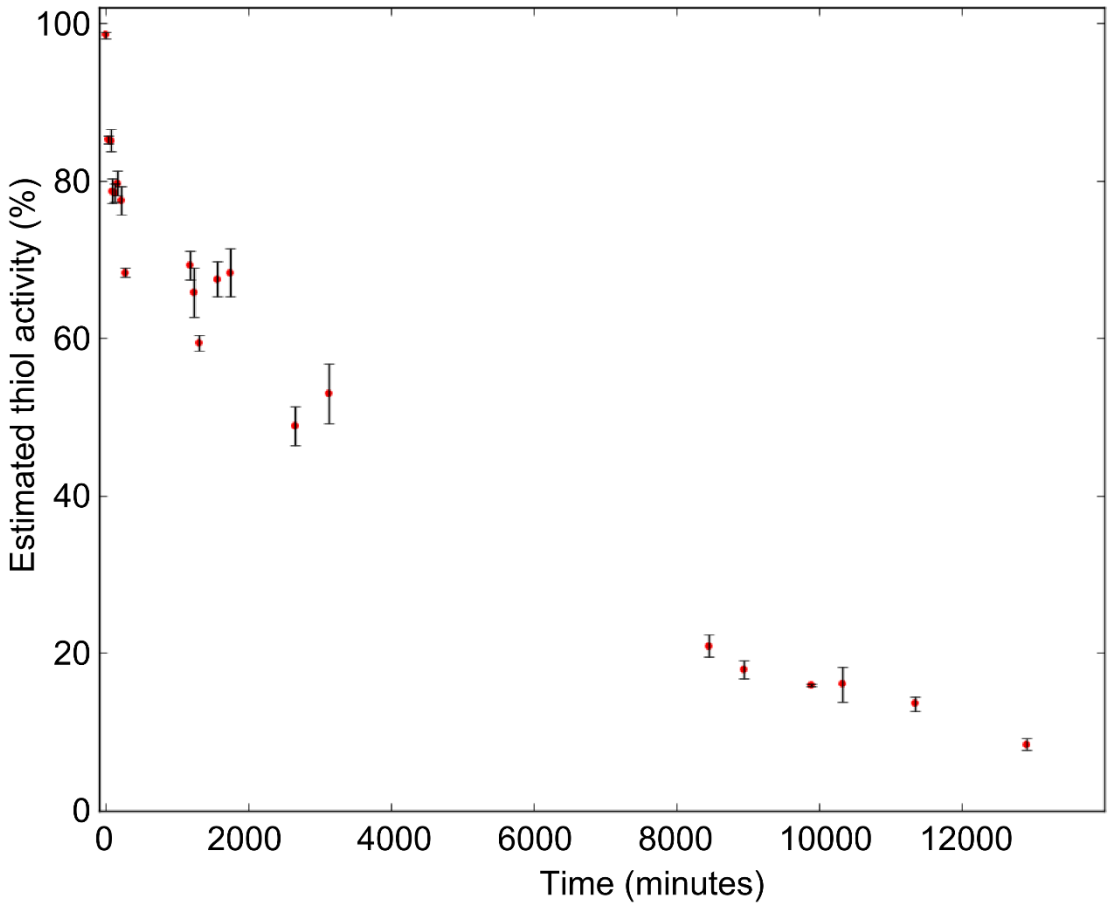

Figure 3.8. *A 10 mM MEA switching buffer, made in glycerol, stored at RT for an extended duration and tested for thiol activity using the Ellman's reagent (DTNB). The estimated activity calculated from the 410 nm absorbance peak showed rapid degradation during the first few hours.*

3.5. MEA concentration

An important practical consideration is the concentration of MEA to be used. A range of commercial organic fluorophores behave differently to one another when using the same switching buffers. The readily available molecular probes in the Alexa Fluor family, whose names are suffixed by the dye's emission peak, include

several bright fluorophores that can be photoswitched. To optimise a probe for dSTORM imaging, an assortment of buffer compositions should be tested for each chromophore used. Cultured cells offer ideal conditions to examine these variables and the important parameters that make a good SMLM dye, Figure 3.9. They are relatively homogeneous, thin (~few microns), and easily grown. COS-7 cells display long, continuous microtubules whose intertwining is diffraction limited and present a suitable target for labelling.

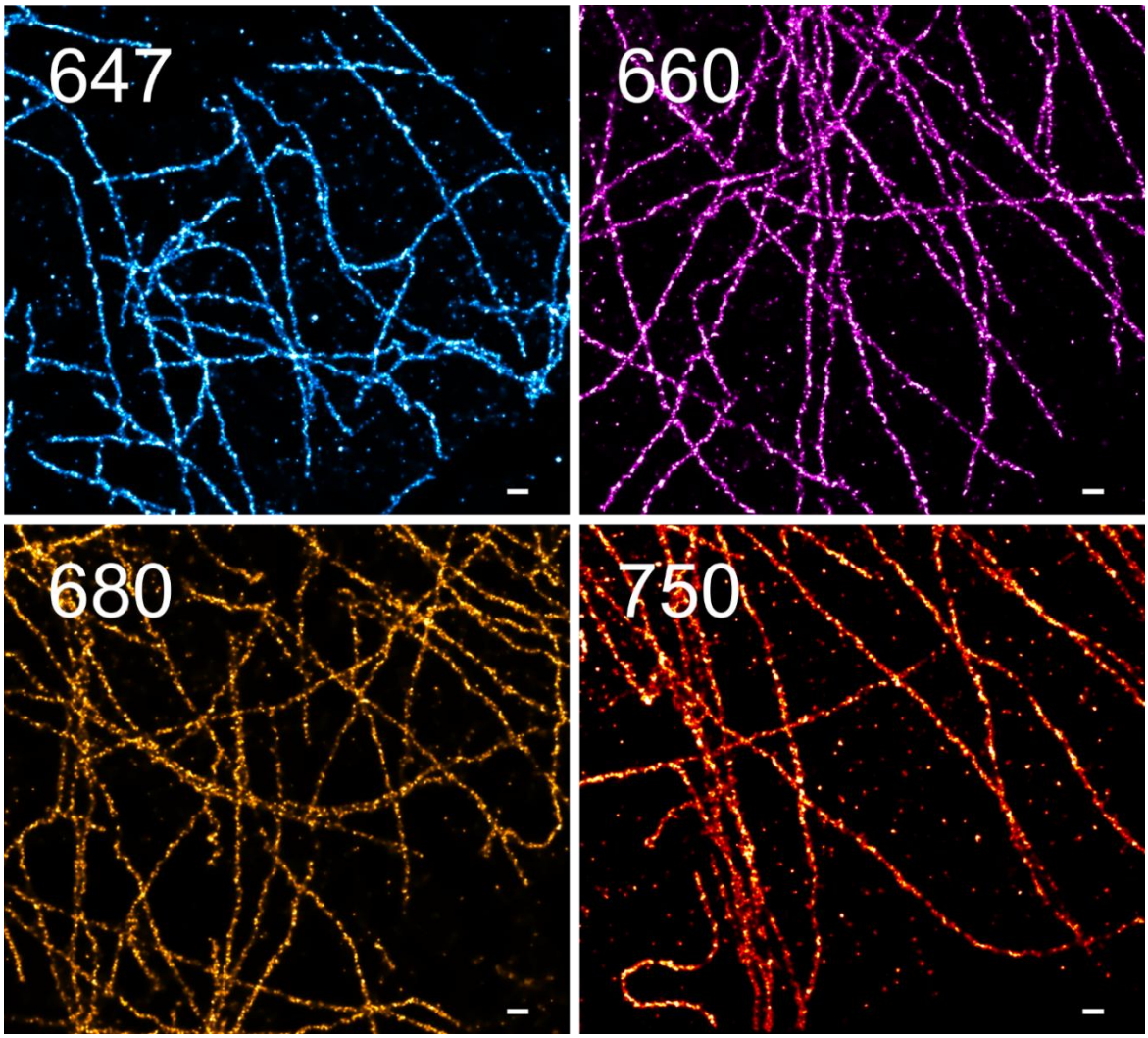

Figure 3.9. *Microtubules from COS-7 cultured cells, labelled with four different Alexa Fluor dyes,* ***(numbers represent emission peak wavelength)****. Each of these molecular probes is photoswitchable with illumination from a 671 nm excitation laser, enabling dSTORM imaging.* ***Scale bar:*** *250 nm.*

A 671 nm laser (VA-I-N-671, Viasho, Beijing, China) was used to excite a range of photoswitchable Alexa Fluor dyes; 647, 660, 680, and 750. These dyes were tested in a range of thiol concentrations at differing excitation powers, Figure 3.10. Alexa Fluor 750 was the poorest performer in terms of photon yields and robustness with permanent photobleaching occurring rapidly at MEA concentrations exceeding 10 mM. Although the other dyes could photoswitch, for a prolonged period at higher MEA concentrations (50 – 100 mM) a reduction in mean photon counts was observed.

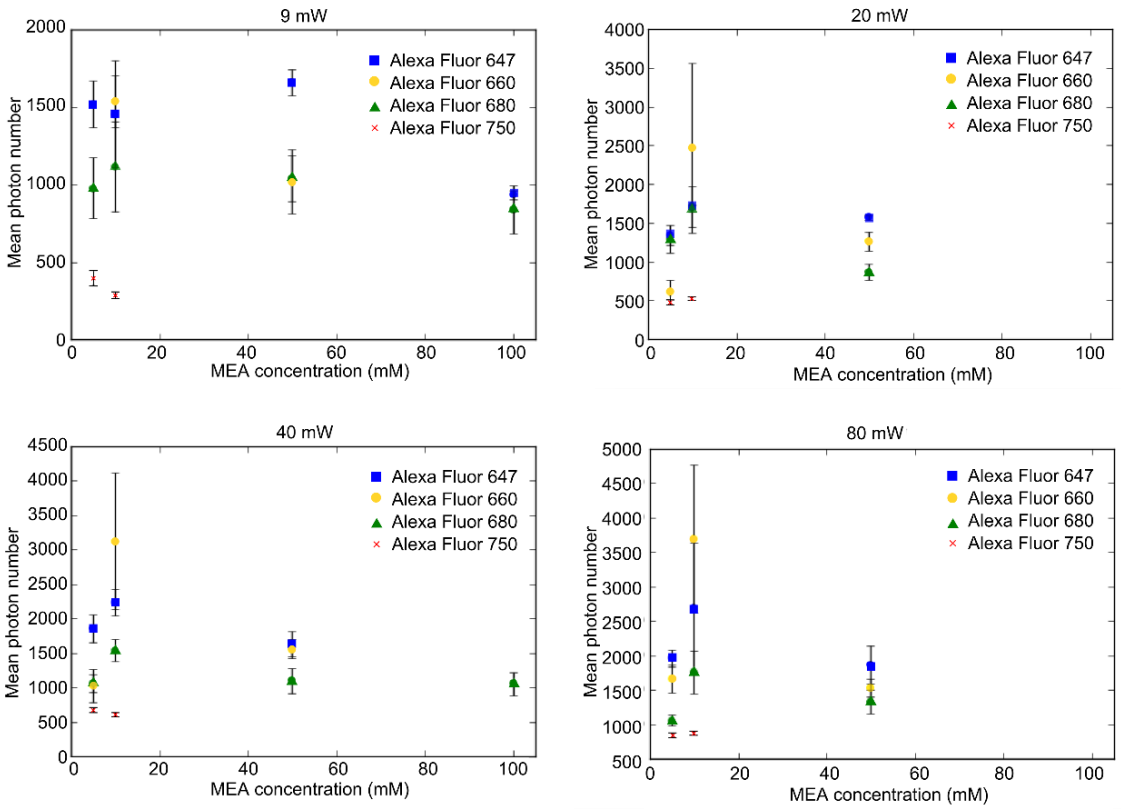

Figure 3.10. *Mean photon yields acquired from dSTORM experiments when using a range of Alexa Fluor dyes at varying concentrations of MEA and measured at different laser powers. The molecular probes were excited in glycerol buffers containing 5-100 mM MEA with a 671 nm laser achieving approximately 9, 20, 40, or 80 mW power at the focal plane.*

The on-state lifetimes were reduced at higher excitation laser powers, as has been reported elsewhere[97], resulting in only marginal gains in the mean number of detected photons when operating between 20 – 80 mW. Switching times were

also decreased at larger excitation powers and/or at higher MEA concentrations, Figure 3.11.

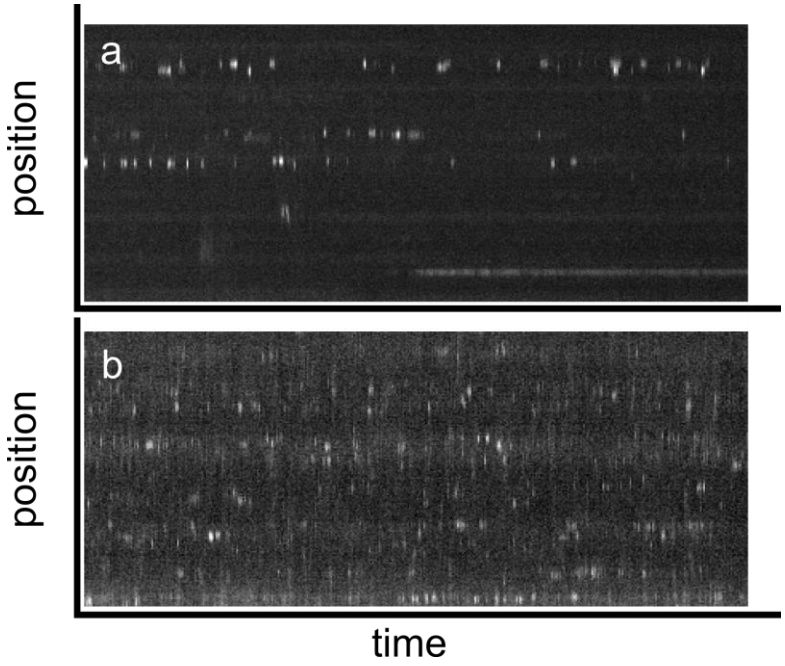

Figure 3.11. *Time course plots of single molecule events during dSTORM experiments. At low thiol (10 mM) concentrations and excitation power the events are prolonged and the time between events are well spaced* ***(a)****. As the switching buffer is exposed to both greater (100 mM) MEA concentrations and illumination power the events are faster, as their duty time is decreased, and the switching cycles increase* ***(b)****.*

Alexa Fluor 660 achieved the highest photon yields, at a relatively low, 10 mM MEA concentration across a range of 671 nm excitation powers. Interestingly, in my setup, Alexa Fluor 660 behaved as well, if not better in some circumstances, when excited using a 561 nm laser in comparison to the 671 nm laser. This unexpected behaviour was also observed in biological tissue sections, taken from the left ventricle of a horse heart, Figure 3.12.

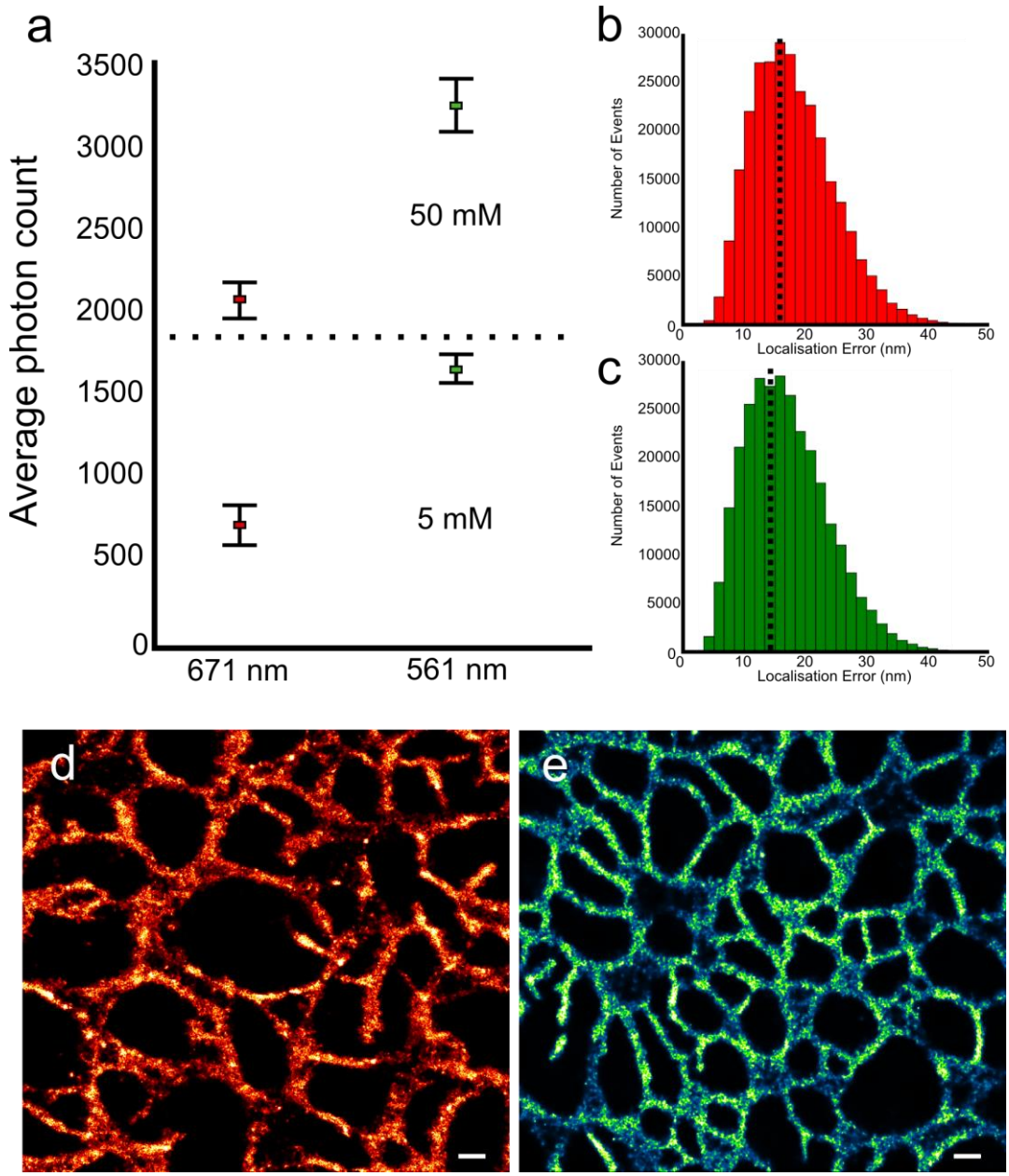

Figure 3.12. *dSTORM measurements taken in ~10 µm sections of horse ventricular tissue. The average photon count detected in tissue samples* ***(a)*** *excited with 671 nm or 561 nm lasers and tested in buffers containing either 5 or 50 mM MEA. The histograms of the localisation errors, see* ***Chapter 2.32****, obtained using 671 nm* ***(b)*** *and 561 nm* ***(c)*** *excitation sources. The 561 nm localisation error shows a slight shift to the left, indicating more precise event detections, as a result of the greater photon numbers collected. Tissue sections labelled for SERCA2 ATPase to show the sarcoplasmic reticulum (****d & e****). The molecular dye Alexa Fluor 660 was photoswitched using 671 nm* ***(d)*** *and 561 nm* ***(e)*** *excitation laser sources.* ***Scale bar:*** *500 nm.*

3.6. Ultraviolet secondary excitation

Occasionally an experimenter may not be able to replace an exhausted switching buffer for one which is freshly mixed, for example a sample mounted between coverslip and slide. In these circumstances, the use of an additional blue-shifted excitation laser can tremendously boost event rates in some molecular dyes[29]. Under illumination, with a suitably matched excitation laser, and in the presence of a thiol, organic dyes can transition to a non-fluorescent state, where the thiol is bound to the dye. Further illumination with ultraviolet (UV) or violet light can cleave the thiol from the dye[105], immediately reverting it back to its ground state and into a fluorescent state. Such a situation is shown in Figure 3.13, where a 405 nm excitation is used to revive switching. This procedure can yield a super-resolution image from an experiment that would otherwise have failed.

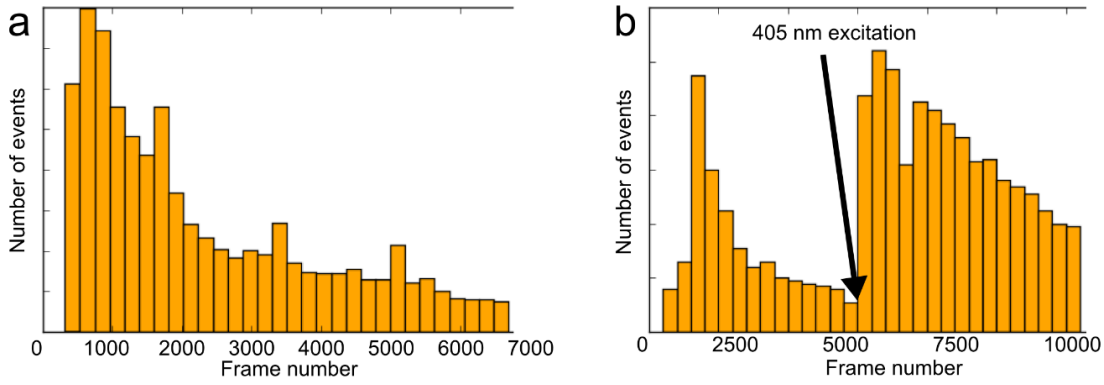

Figure 3.13. *The number of events detected over the course of an experiment, in a sample whose mountant has failed. When the mounting buffer is no longer able to maintain fluorescent switching the events rapidly decay* ***(a)****. Brief exposure to a 405 nm laser with 0.1 mW power at the sample, the fluorophores can be forced to blink* ***(b)****.*

The 405 nm excitation can boost event rates to greater than the number of events originally detected per frame as shown in Figure 3.14. This often has superior resolution, obtained in far fewer frames, when compared to the initial data.

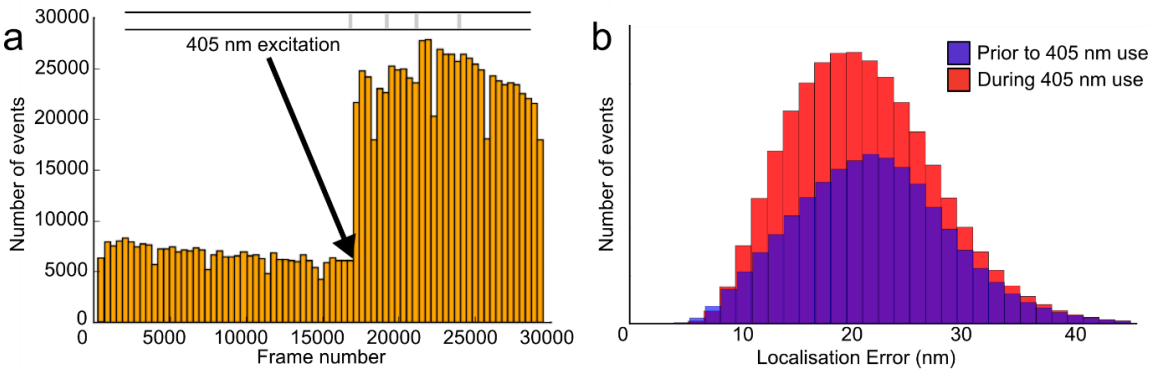

Figure 3.14. *The event rate of a stable mounting buffer which has the 405 nm excitation laser turned on part way through acquisition* ***(a)****. The number of events increase to values greater than the initial experiment. A comparison of the localisation precision obtained for both halves of the experiment* ***(b)****, shows that the initial resolution is marginally improved with the addition of the 405 nm laser. Grey bar above event rate indicates short ON/OFF <1 s exposure to a 405 nm secondary excitation laser with 0.1 mW power.*

Gradually increasing the excitation laser power of the 405 nm laser also led to moderate, “stepping” behaviour, increasing the number of events detected, Figure 3.15.

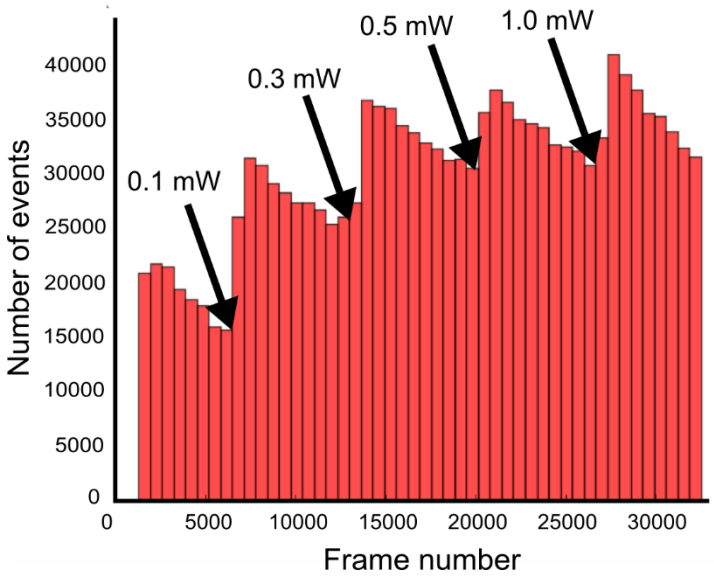

Figure 3.15. *With a stable switching mountant the number of events were boosted with an initial ON/OFF 0.1 mW secondary excitation exposure with a 405 nm laser. Steadily increasing the illumination power of the violet light-source further raised the number of detected events.*

It is critical not to dose the sample with too much of the 405 nm excitation, as most cell types are intrinsically fluorescent upon UV exposure[106]. This is especially true of cardiac cells, Figure 3.16, and tissue which contains large numbers of mitochondria, that house endogenous fluorophores, such as nicotinamide adenine dinucleotide (NADH) and flavin coenzymes[107].

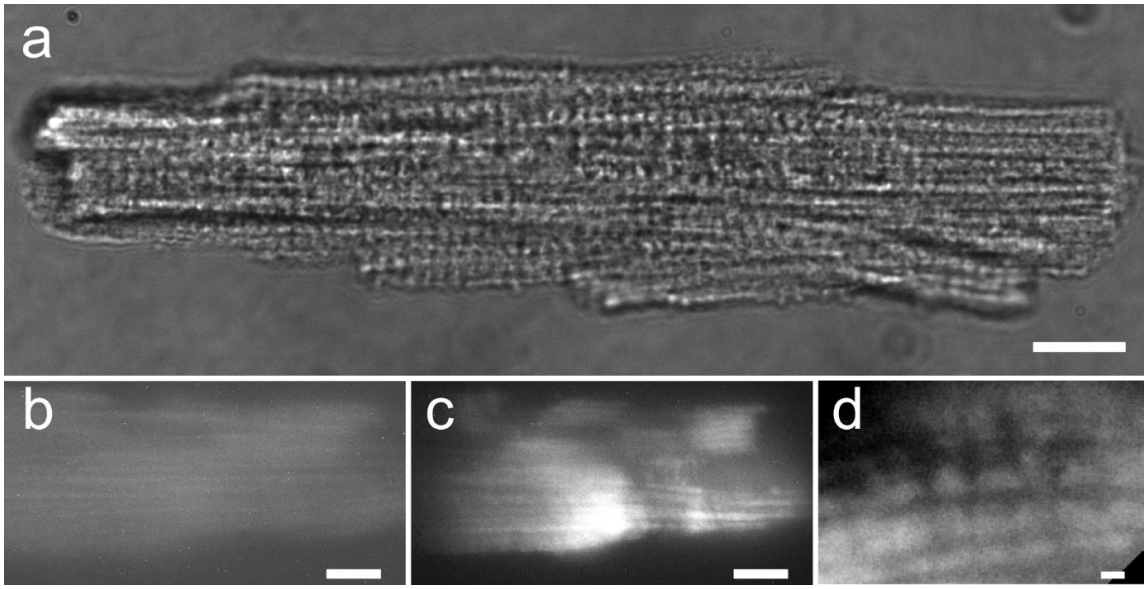

Figure 3.16. *An unlabelled, isolated rat ventricular cardiomyocyte* ***(a)*** *viewed through transmitted light. Illumination with a 671 nm laser source* ***(b)*** *shows a slight auto-fluorescence present within the cell. Secondary excitation of the cell using a 405 nm source* ***(c)*** *emphasizes the intrinsic auto-fluorescence that emanates from the mitochondria allowing them to be clearly visualised* ***(d)****.* ***Scale bars: (a-c)*** *10 µm,* ***(d)*** *1 µm.*

The 405 nm excitation is a useful tool for improving or recovering dSTORM experiments, however it does not work on all fluorescent dyes, Table 3.1. Whilst all fluorescent probes tested showed a sudden increase in event rates, when briefly illuminated with a secondary violet laser source, the lifetime of the near infra-red (NIR) Alexa Fluor 750 rapidly diminished, ending the experiment with no possibility for recovery.

Dye	A647	A660	A680	A750
UV excitable	✓	✓	✓	✓
Survivability	✓	✓	✓	✗

Table 3.1. *A summary of the Alexa Fluor dyes tested. All probes were susceptible to secondary excitation with a violet light source, bringing dark-state fluorophores back into a fluorescing state. Photoswitching was prolonged in A647, A660 and A680, in contrast A750 underwent irreversible photobleaching upon 405 nm illumination.*

3.7. Non-photoswitching single molecule localisation microscopy

A new technique termed DNA-PAINT[32], removes much of the complexity associated with dSTORM switching buffers. The method, which relies on the predictable nature of DNA interactions, uses oligonucleotides situated at desired marker locations and their complementary sequences, conjugated to a photostable fluorophore. These 'imager' strands are free to transiently bind to 'docking' sites and yield a highly effective alternative approach to stochastic blinking. The events occur naturally, without the need to use large laser powers nor to introduce reducing agents or additional chemicals to aid photoswitching. There is limited photobleaching of the imager strands due to their sporadic interaction with the excitation laser, and their continual diffusion in the bulk solution provides 'new' imager strands at the imaging plane. There is additionally no change to the conditions of the imaging buffer over the course of experiments. These features mean that, once an equilibrium has been reached within the sample, the detected events occur at near continuous rates, endlessly, Figure 3.17.

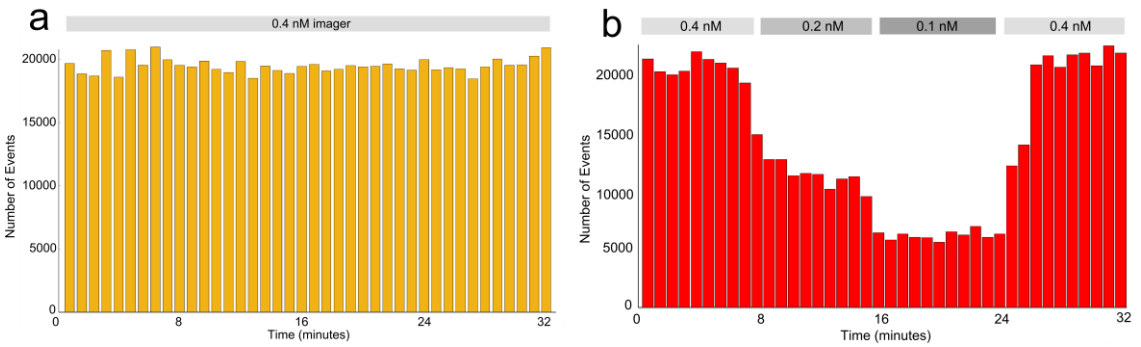

Figure 3.17. *Time traces of the number events over the course of an experiment. In a DNA-PAINT experiment the number of events remain relatively constant for the duration of the acquisition* ***(a)****. The rate, which is largely dependent on the concentration of the imager strand, can be controlled approximately proportionately with dilution of the imaging buffer or reintroduction of the imager* ***(b)****. Over the course of imaging the imager concentration is halved twice seeing a proportional drop in the number of events. Reintroducing the starting concentration results in similar event numbers.*

3.8. dSTORM vs DNA-PAINT

A custom docking oligonucleotide that has the capability to perform both dSTORM and DNA-PAINT experiments was designed and tested. The sequence, Appendix 1, enabled a direct comparison between the two techniques by imaging the same secondary antibody, Figure 3.18.

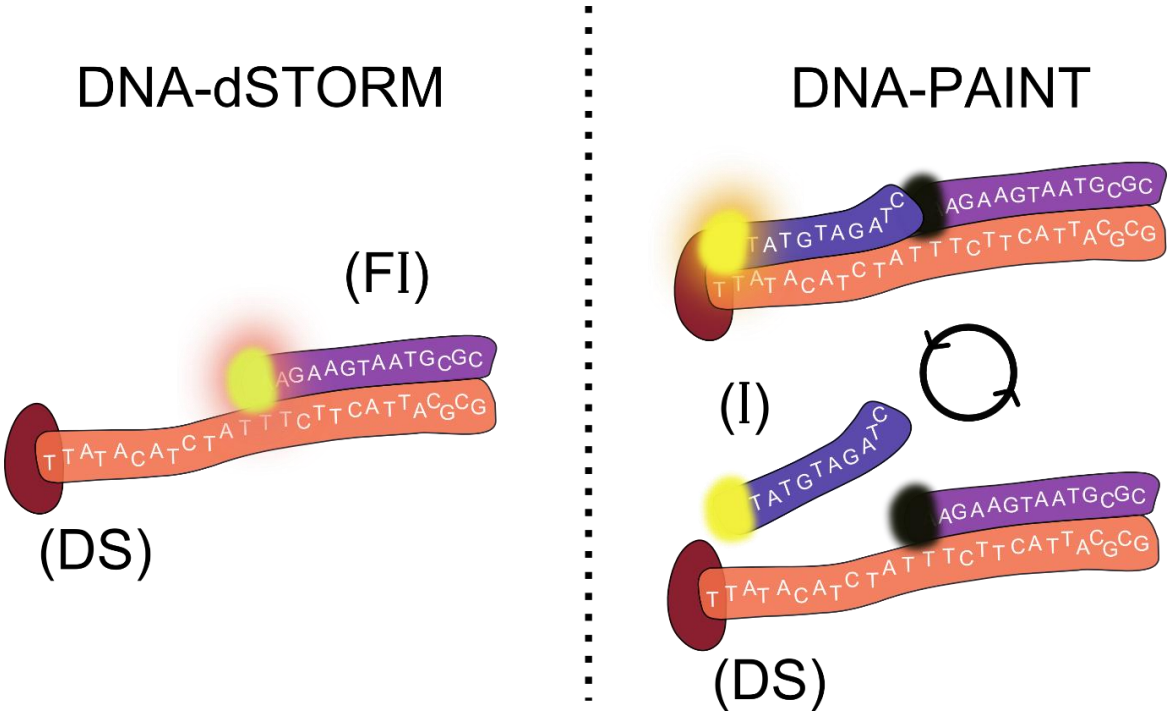

Figure 3.18. *The concept of conducting dSTORM and DNA-PAINT on the same target. A fixed imager* ***(FI)*** *sequence, with a photoswitchable dye, binds permanently to the oligonucleotide docking strand* ***(DS)*** *and is first used as an initial confirmation of successful labelling. dSTORM is performed with the fixed imager* ***(FI)*** *until the dye is photobleached. The transiently binding imager* ***(I)*** *sequence is then introduced and DNA-PAINT is conducted on the same target.*

From the available fluorophores, eligible for conjugation to an oligonucleotide, the photoswitchable dye Alexa Fluor 647 was chosen for the fixed imager. ATTO 647N was originally tested, due to its similar excitation and emission spectrum, as the chosen comparison transiently binding imager strand. However, the ATTO 647N dye, which has a net electrical charge of +1, had a propensity to become stuck to other objects, producing imaging artefacts. ATTO 655, the photostable oxazine dye, has a net electrical charge of 0 and is also excitable with a 642 nm laser. Experiments involving the dSTORM-DNA-PAINT docking strand showed strong agreement after channel realignment between the two techniques, Figure 3.19. The DNA-PAINT localisation precision was found to be 3-4 times greater than the dSTORM measurements of the same target.

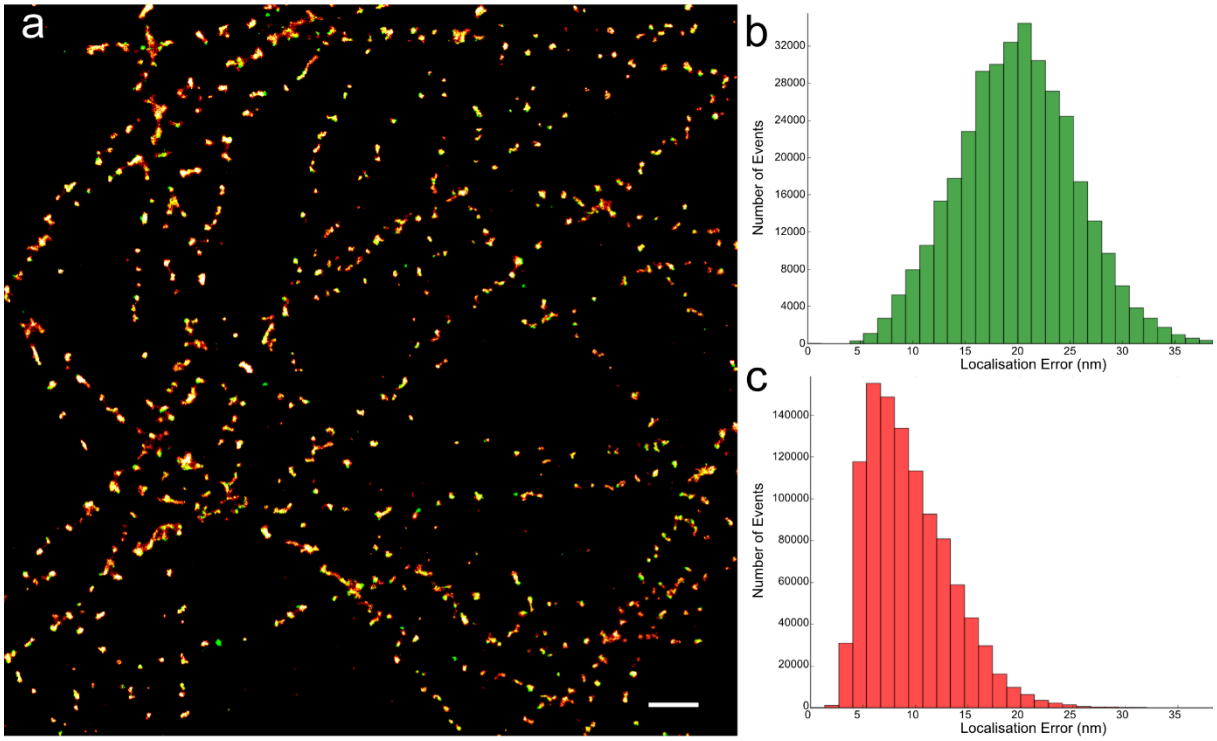

Figure 3.19. *A COS-7 microtubules image, labelled using a docking strand capable of both dSTORM and DNA-PAINT experiments* ***(a)****. First dSTORM (green) is conducted on an Alexa Fluor 647 fixed imager sequence. Once the sample area is completely bleached the transient imager strand with ATTO 655 is introduced (red). The localisation error histogram plots for dSTORM* ***(b)****, and DNA-PAINT* ***(c)*** *demonstrate the improvement obtainable with the new technique.* ***Scale bar:*** *200 nm*

3.9. Conclusion

There are many variables in dSTORM imaging including the choice of fluorescent probe, the composition of the mounting buffer, and the experimental operating parameters and there is no consensus on the “best” choices. Several of these critical parameters involved in single molecule localisation microscopy buffer preparation and image acquisition have been examined.

A method to quantify the colourific Ellman’s test[103] for use with dSTORM buffers was developed to provide an indicator of thiol activity through spectrophotometry, see Figure 2.4. This process helps to clear any ambiguity in the human visual

inspection of the Ellman's reagent and enables the experimenter to adjust their buffer accordingly.

A chemical approach was introduced to remove oxygen and prolong thiol activity with the use of sodium sulphite. This buffer, made in glycerol, takes much longer to run down and does not result in the production of carboxylic acids over time, as glucose oxidase mountants do. Approaches to prolong the lifetime of imaging buffers has been achieved previously with the use of oxygen tight chambers (OTC)[108] keeping sample and MEA buffer together. However, this method is limited by dissociation of the antibodies/dyes from the epitopes by keeping the thiol present. With the sodium sulphite glycerol buffer the MEA at nominal millimolar concentrations maintained its reductive ability for extended periods of time. This created a buffer that was more reliable than other thiol based cocktails, as it dependably delivered desirable photoswitching capabilities. The price of this consistency was a slight reduction, ~10%, in the number of photons collected when compared to a freshly made thiol buffer of the same concentration. The sulphite buffer could be used immediately and repeatedly, over the course of one month with only a fraction of the reduced thiol activity observed in comparison to dated MEA switching mountants, Figure 3.7.

I found that illuminating the Alexa Fluor probes 647, 660, 680 and 750 with higher laser powers had only a marginal effect on photon yields. This was in agreement with a recent study[109] that tested Alexa Fluor 647 only, in a thiol based buffer. They determined that high intensities increased the speed of imaging, by increasing the dye duty cycle, but the benefits were counteracted by the rate of photobleaching. However, the conclusions cannot be directly transferred to other combinations of fluorescent dyes and buffer compositions since photophysical properties can be significantly different[29,98].

A range of MEA concentrations were also tested on a selection of photoswitchable Alexa Fluor dyes. The Alexa Fluor 750 was the weakest performing single molecule probe with both a low photon yield and poor survivability. At MEA concentrations greater than 10 mM the dye rapidly photobleached and could not be used for SMLM experiments. An extensive report on 26 organic dyes[29] also concluded that Alexa Fluor 750, in an aqueous MEA buffer, was the worst performer but did also show photon yields could be

approximately doubled when using an alternative thiol, BME. Not all fluorophores are photoswitchable and this severely limits the possible choices for multi-colour dSTORM. Despite its poor performance, Alexa Fluor 750 can be paired with Alexa Fluor 680 for dual colour experiments[85] as conducted in **Chapter 6** of this thesis.

The Alexa Fluor 660 dye, relatively untested for single molecule imaging, performed strongly in comparison to the other Alexa Fluor dyes tested. Increased photon counts were also observed upon sole-excitation of a 561 nm laser, producing improved super-resolution images, Figure 3.12.

Photoactivated (PA) or caged fluorophores are typically non-fluorescent at the beginning of an experiment and are activated by irradiation with a 405 nm laser. These probes are often used in the super-resolution approach called photoactivated light microscopy (PALM)[5,15] and can result in strong photon yields[100]. In dSTORM, photoswitchable Alexa Fluor dyes are photoreduced in the presence of electron donors, like thiols, forming dye radical anions[26]. All radical anions have a strong absorbance at approximately 400 nm and recovery of the dye to a fluorescent state can be facilitated by illumination using a 405 nm laser[26,110]. The results obtained in this Chapter agree with previous observations of the photorecoverable nature of the Alexa Fluor 647 dye[29] and in addition Alexa Fluor 660 and 680 also benefitted from secondary excitation using a 405 nm laser source. Fluorescence recovery of the Cy5 dye has previously been shown in experiments with irradiation cycles of secondary 405 nm laser illumination at constant power[93]. By gradually increasing the 405 nm power, over the course of an experiment, it was shown that this approach could lead to a surge in the number of detectable events and result in more precise localisation in fewer frames, Figure 3.14.

With the advent of DNA-PAINT, the desired characteristics of fluorophores is reverting back to conventional qualities. High photon counts and resistance to photobleaching are still desired, but for DNA-PAINT the fluorophore needs to be photostable. This changes the pool of fluorophores DNA-PAINT experiments should be conducted with. The lessons learnt and approaches taken to improve qualities for dSTORM experiments may also be beneficial to enhancing dye

photostability in DNA-PAINT investigations[111]. A direct comparison of the two techniques, using my custom designed oligonucleotide sequences, Figure 3.18, exhibited the improved localisation precision obtainable with DNA-PAINT and it is likely that the majority of SMLM investigators, where possible, will adopt some form of DNA-nanotechnology in the near future. The utility of DNA-PAINT as an alternative to dSTORM is explored further in subsequent Chapters.

Chapter 4

True molecular scale visualisation of variable clustering properties of the cardiac ryanodine receptor

Localisation microscopy allows observation of protein organisation at previously unattained resolution and sensitivity. Limited brightness, and hence precision, of switchable dyes has however made resolving and quantifying individual proteins clustered within cellular signalling nanodomains challenging. Of considerable interest are intracellular calcium release nanodomains in cardiomyocytes and the RyRs which cluster therein. In this Chapter, by harnessing the high localisation precision of DNA-PAINT (~10 nm), punctate labelling was visualised, confirmed as single RyRs. Analysis of RyR positions within sub-plasmalemmal nanodomains suggested that RyRs commonly cluster through random assembly into irregular arrays containing significant gaps. These gaps were occupied by other proteins, including the inhibitory protein JPH2 whose stoichiometry with RyRs varied from cluster to cluster (0.5-3.5), revealing a new level of complexity in the regulation of RyRs. The data underscores how improved precision in localisation microscopy can reveal intimate protein organisation within signalling nanodomains and observe molecular cluster regulation *in situ*.

4.1. Introduction/Background

Recent improvements in the application of localisation microscopy have come about through protocols for improved fluorophore photoswitching properties[29], combination of light-sheet[112] or 4-pi microscopies with single molecule detection[113] to achieve resolutions of 5-10 nm. Another approach, DNA-PAINT, utilises the specificity and predictability of DNA hybridisation to localise molecular targets which can be tagged with synthetic single stranded DNA oligonucleotides[32] at a similar resolution.

In this study, DNA-PAINT was applied to resolving individual RyR molecules within tightly organised junctional nanodomains to understand the *in situ* molecular interactions of RyR and other junctional molecules, for detailed methods see **Chapter 2**.

The unlimited replenishment of imaging probes in DNA-PAINT, the compatibility with multi-colour imaging and the quantitative nature of the transient DNA-hybridisation interaction which provides an encoding of the underlying protein density were all exploited. The data has made it possible to examine how RyR clusters separated by mere hundreds of nanometres appear to adopt different densities of the JPH2 accessory protein in relation to RyRs. Benefiting from the improved spatial resolution, these images go on to distinguish protein subpopulations which are likely to interact physically, e.g. by direct binding, from those which are separated by tens of nanometres. These populations were previously indistinguishable with methods such as dSTORM[74,91]. The new image data reveal complexities in protein distribution and physical interactions which allow a biological interpretation of the significance of protein co-localisation. The image-based *in situ* protein counting method used here to detect nanodomain specific variations in the co-clustering of such proteins provides a novel nanoscale analytical tool that directly complements immuno-co-precipitation.

Results
4.2. Improved visualisation of RyRs within clusters

To visualise the immuno-labelling of RyRs in peripheral clusters (or “couplons”) of rat ventricular myocytes, cells adhered to coverslips were studied in TIRF mode, Figure 4.1.

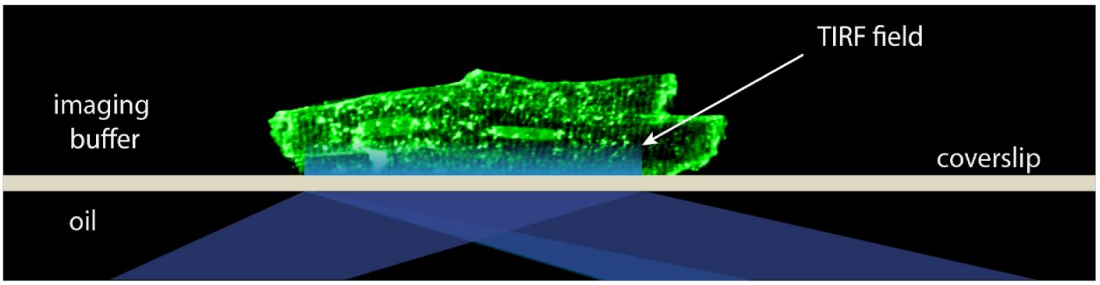

Figure 4.1. *Schematic diagram illustrates the adaptation of total internal reflection fluorescence (TIRF) for imaging the peripheral RyRs adjacent to the coverslip.*

dSTORM images of surface membrane areas attached to the coverslip revealed clusters of RyR labelling loosely organised in a transversely striated pattern, Figure 4.2, as seen before[62]. To acquire DNA-PAINT images of RyRs, adhered cells were labelled with a primary RyR antibody, recognised by a secondary antibody which was covalently linked to short ‘docking strand’ oligonucleotides.

In the imaging buffer, a low concentration (~0.2 nM) of complementary ‘imager strands’ was delivered that transiently and stochastically bind to the ‘docking strands’ localised at RyR markers. When illuminated within the thin TIRF field, transiently immobilised imager strands give rise to sparse and transient fluorescent spots which were recorded in a series of greyscale images. The positions of the imagers were localised from these data and rendered into a greyscale marker density map which showed an organisation of RyR clusters across the cell, Figure 4.2B. This pattern reflects the periodic arrangement of sarcomeres with most RyRs close to the z-lines[62], similar to the distribution seen with dSTORM. At closer inspection, however, the DNA-PAINT images reveal very distinctive puncta within the cluster area, which were not observed in the dSTORM images, Figure 4.2C&D. It was hypothesised that these puncta reveal

individual RyRs within the essentially flat 2D peripheral clusters[114] which dSTORM data could not resolve.

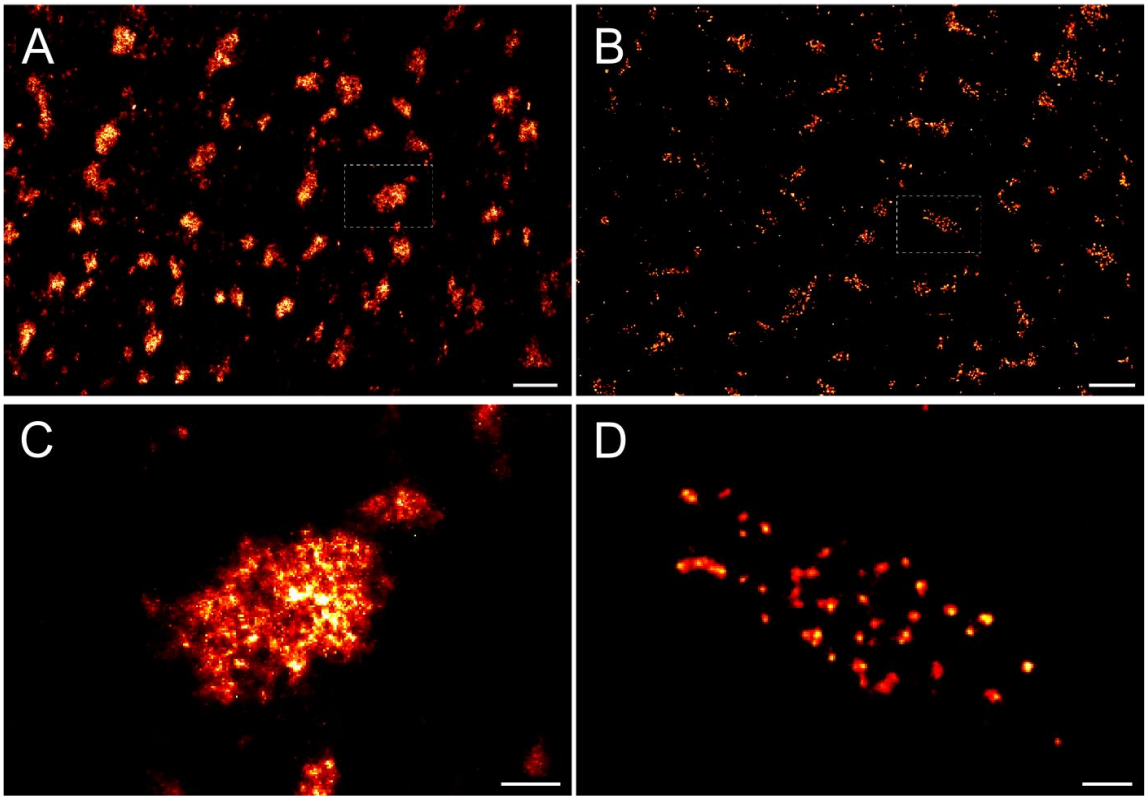

Figure 4.2. *Images of immunofluorescence labelling of RyRs in peripheral couplons of rat ventricular myocytes.* ***(A)*** *STORM imaging typically reports RyR clusters organised loosely in a transverse striated pattern facing the surface plasmalemma (parallel to image plane), each with a unique shape, size and high density of labelling.* ***(B)*** *The DNA-PAINT image of similar regions in another cell illustrates a similar cluster distribution near the cell surface. Magnified views of clusters from these images* ***(****boxed regions in* ***A*** *and* ***B)*** *show the unresolved cluster sub structure in dSTORM data* ***(C)*** *which contrasts with resolved punctate densities in the clusters mapped with DNA-PAINT* ***(D)****.* ***Scale bars: (A&B)*** *1 μm,* ***(C&D)*** *100 nm.*

Further analysis of these puncta was conducted with a detection algorithm to reliably determine the puncta centroids. The point data, Figure 4.3, shows direct evidence of the groupings of the single molecule events localised into distinct puncta.

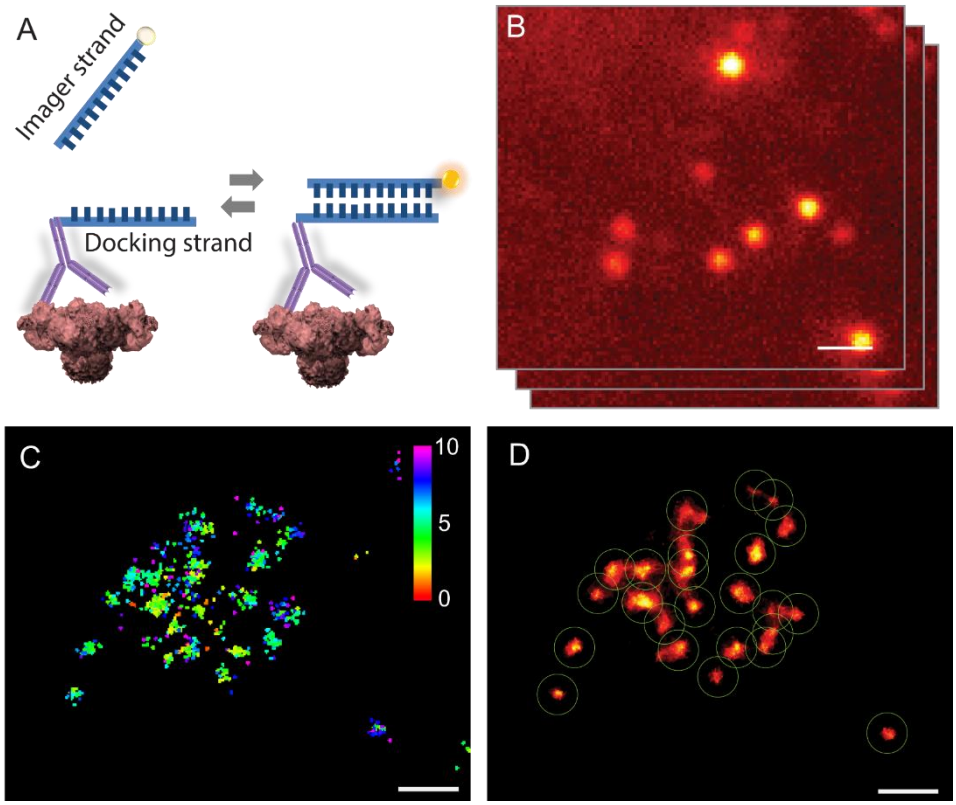

Figure 4.3. *DNA-PAINT implementation for RyR imaging and analysis.* ***(A)*** *The DNA-PAINT principle works by the thermally-driven stochastic and transient hybridisation of the imager strand oligonucleotide carrying the excitable fluorophore to the docking strand oligonucleotide marking the target RyR within the TIRF excitation field.* ***(B)*** *Binding events were visualised in fast series of TIRF images as bright fluorescent spots (single molecule events) which match the two-dimensional approximately Gaussian lateral shape of the point spread function.* ***(C)*** *These events were used for localising the marker positions into a series of points whose spatial patterns were characteristic of nanometre-scale punctate structures (localisation error shown in colour-coded bar; scale in nm).* ***(D)*** *The point data were rendered into a 2D greyscale 32-bit image which shows the punctate morphology. To discretise these punctate densities, the centroids of each punctum were calculated with an automated puncta detection algorithm. Each detected event is indicated with centred circles of 50 nm radii.* ***Scale bars:*** ***(B)*** *500 nm,* ***(C&D)*** *50 nm.*

Examination of the reason for this improved resolution of RyR markers revealed that a higher photon yield, likely resulting from the binding duration of each event and the photo-stability of the dye species, were a key difference between DNA-PAINT and dSTORM data, Figure 4.4. In addition, backgrounds were reduced in the TIRF configuration. Analysis of these data in terms of estimated localisation error, yielded a left-shifted distribution of estimated event localisation error with an ~6 fold improvement of the localisation error mode as the primary cause of the improved resolution.

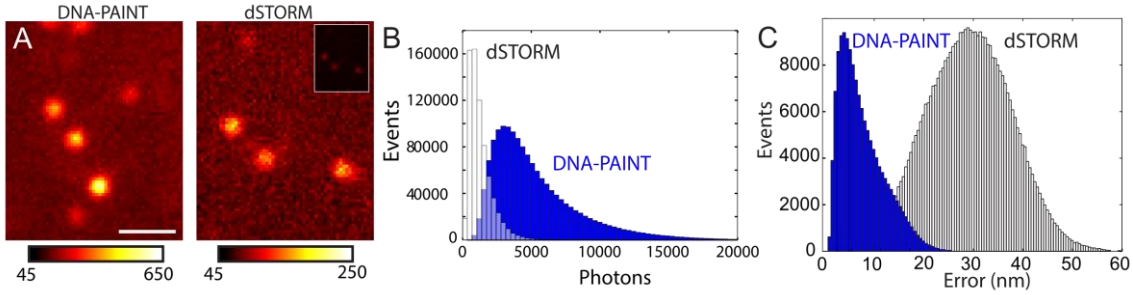

Figure 4.4. *DNA-PAINT image data and improvement beyond the dSTORM resolution. To illustrate the mechanistic similarity between the two methods and the attributes of DNA-PAINT data which guarantees superior resolution, raw image data and their properties between DNA-PAINT and dSTORM were compared.* ***(A)*** *Typical single frames from both DNA-PAINT* ***(left)*** *and dSTORM* ***(right)*** *experiments illustrate the similarity in the nature of the single molecule events, in their stereotypic shapes and frequencies. Noting the distinct scales in the two example data sets, a higher intensity (calibrated in detected photons per pixel) was observed in DNA-PAINT events compared to dSTORM. For comparison, a facsimile of the dSTORM frame is shown in the inset with the same colour-scaling as the DNA-PAINT image.* ***(B)*** *A frequency histogram analysis of typical DNA-PAINT and dSTORM datasets revealed a 3-10 fold higher mode in the estimated total photons collected per event in DNA-PAINT.* ***(C)*** *This higher event intensity contributed to a reduced event localisation error in DNA-PAINT events as shown in the frequency histogram from a corresponding image series.* ***Scale bar:*** *1 μm.*

Due to the relatively large size of RyRs (~30 nm) similar results were obtained with directly labelled primary ABs against RyRs as with the secondary labelling system Figure 4.5. The secondary system was therefore adopted for most experiments.

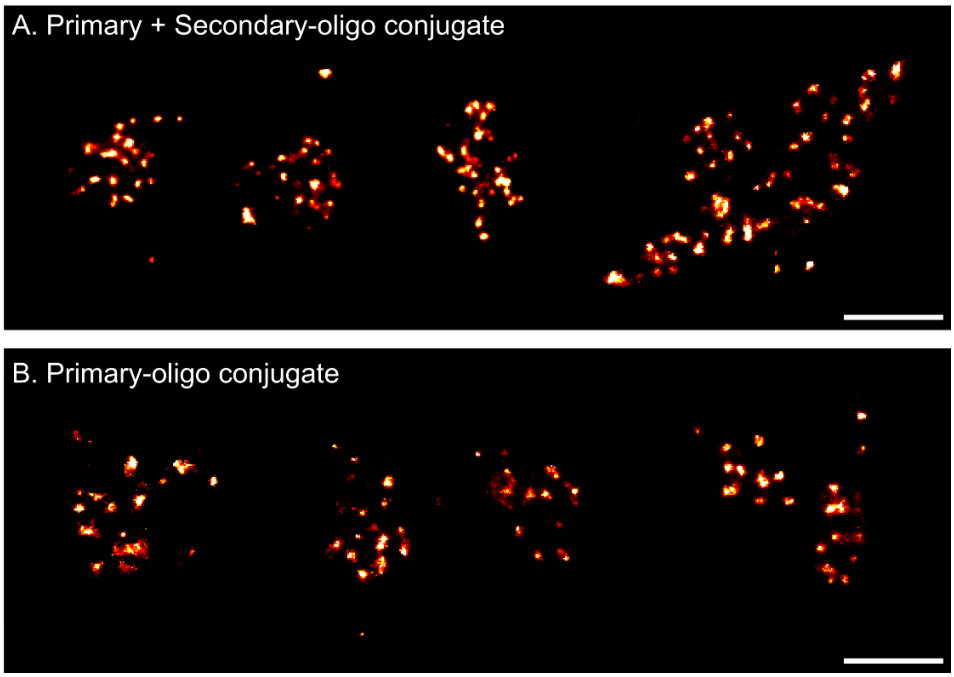

Figure 4.5. *Evaluation of the reproducibility of the RyR cluster morphologies between a direct primary versus secondary antibody labelling approach. DNA-PAINT images of RyRs shown and analysed in this study were generally acquired with a primary and secondary antibody labelling method. To verify whether the morphology of the RyR cluster can be reproduced independently of the nature of the marker of the target protein (i.e. whether the morphology was dependent on the primary and secondary antibody interaction), a comparison was made between two labelling methods:* ***(A)*** *A gallery of RyR clusters resolved with DNA-PAINT where the receptors were labelled with a monoclonal anti-RyR IgG primary antibody and then an anti-IgG secondary antibody conjugate of the docking strand.* ***(B)*** *A similar series of images of RyR clusters where the receptors were labelled with the anti-RyR primary antibody which was directly conjugated to the docking strand revealed a similar punctate morphology. This confirmed that the punctate labelling densities related to the sites of primary antibody localises a RyR and were essentially independent of the interaction between the primary and secondary antibody complexes.* ***Scale bar:*** *200 nm.*

4.3. Reproducibility of receptor localisation with DNA-PAINT

The punctate patterns of RyR labelling within clusters were visually suggestive of single RyRs. A series of experiments were conducted to reconcile this morphology with the previously observed dSTORM images of the same structures as well as experiments to confirm that the morphology observed in the DNA-PAINT data is robust. Correlative imaging was performed to assess the consistency between DNA-PAINT reported RyR clusters and dSTORM cluster data. A correlative imaging experiment where DNA-PAINT and dSTORM was performed using a mouse monoclonal anti-RyR2 and a rabbit polyclonal anti-RyR2 (previously shown with dSTORM to report >70% spatial agreement[74]), respectively. The correlative dSTORM and DNA-PAINT images revealed strong spatial agreement of the cluster positions and the shapes. It also confirmed that the punctate RyR labelling in DNA-PAINT images were essentially confined to the cluster area resolved with dSTORM. The effectively "photobleaching free" properties of DNA-PAINT was taken advantage off to test the reproducibility of the punctate labelling pattern of RyRs. Correlative DNA-PAINT images were acquired sequentially of the same RyR clusters by washing imager strands, matching the RyR secondary antibodies, repeatedly in and out again as done in Exchange-PAINT[32], Figure 4.6. These experiments established that the locations and the morphology of the puncta were robustly reproduced with a median error (displacement of a given punctum in a pairwise comparison of images) of 0.94 nm (47 clusters; 5 cells). 94.2 ± 0.9% (mean ± SEM, 5 cells) of puncta locations were reproduced within 10 nm (80.9% within a stringency of 5 nm) across sets of Exchange-PAINT images. An example of this reproducibility is illustrated in Figure 4.6C where the localised and detected puncta positions from three independent Exchange-PAINT repetitions (shown as red, blue and green dots) confirm strong alignment and reproducibility.

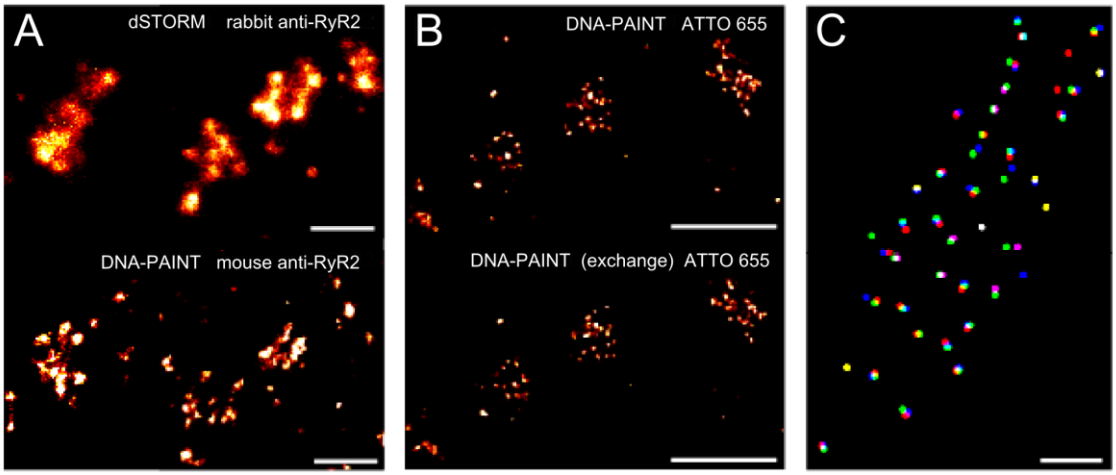

Figure 4.6. *Evaluating the reproducibility of RyR cluster nanostructure with DNA-PAINT imaging.* ***(A)*** *dSTORM images of RyR clusters* ***(upper)*** *in rat ventricular peripheral junctions showed clear visual agreement with correlative DNA-PAINT images of the same RyR clusters* ***(lower)****.* ***(B)*** *Sequential images acquired of RyR clusters using an Exchange-PAINT protocol confirm the high reproducibility of both the cluster shape and punctate morphology.* ***(C)*** *Analysis of the centroids of each RyR punctum in three independently acquired DNA-PAINT images of the same cell (one cluster and three colours shown in example) revealed that 94.2 ± 0.9% of the puncta were detected within the corresponding punctum.* ***Scale bars: (A)*** *250 nm,* ***(B)*** *500 nm,* ***(C)*** *250 nm.*

These results show that the puncta are a robust feature of the DNA-PAINT RyR data. Individual puncta represent locations of single RyRs, as given the localisation precision (5-10 nm) it is unlikely that markers bound to the same RyR can be resolved into distinguishable puncta. As a consistency check, a simulation, Figure 4.7, was performed to test the hypothesis that individual RyRs within a cluster can be directly resolved and distinguished from adjacent RyRs with a technique such as DNA-PAINT, given the localisation properties of DNA-PAINT. At a localisation precision matching that of the experimental data, it was found that individual RyRs within a regular array, spaced at centre-to-centre distances as close as 30 nm, can be resolved and detected at event densities similar to those shown in the data.

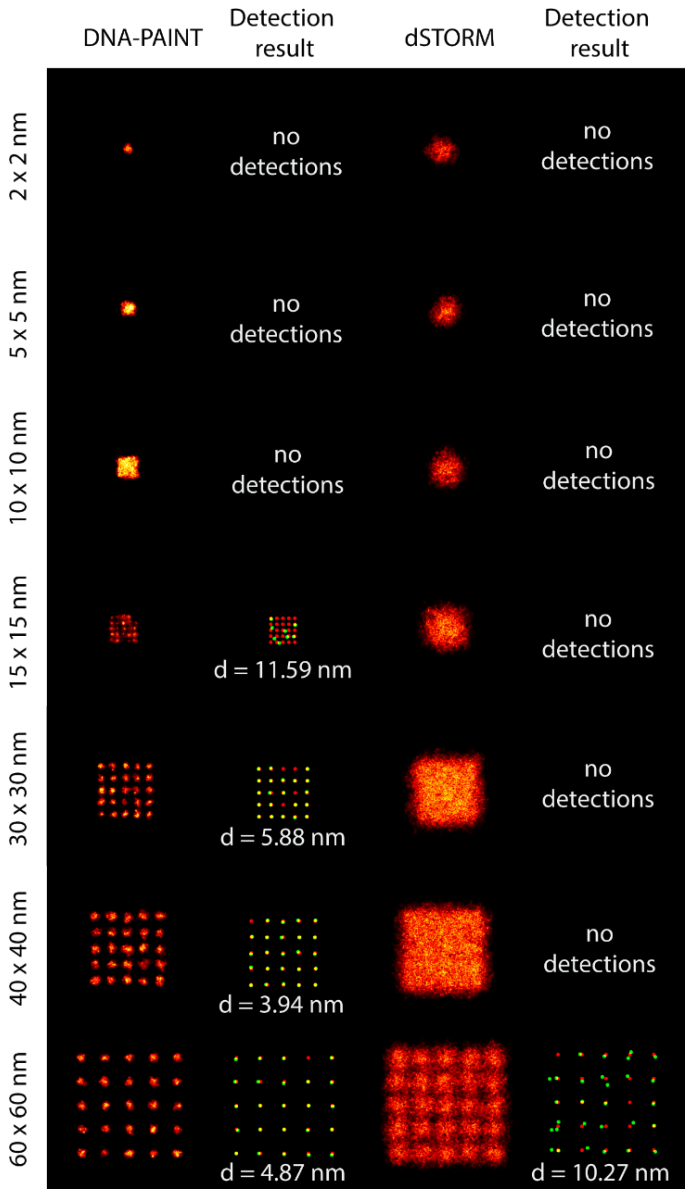

Figure 4.7. *The ability to resolve target spacing with DNA-PAINT versus dSTORM. Here simulated data was used to investigate the ability to resolve the protein distribution in clusters as a function of the localisation precision and associated imaging parameters. Simulated super-resolution DNA-PAINT* ***(first column)*** *and dSTORM* ***(third)*** *images of a cluster with receptors on a square grid containing targets at regular spacing, specified on the left, were simulated using imaging parameters specified in* ***Table 2.2****. Note that the square outline of the cluster is faithfully reported when the target spacing is >5x5 nm for DNA-PAINT like parameters and >30x30 nm for dSTORM like imaging parameters. The centroids of the any punctate marker densities were determined* ***(green circles)*** *and overlayed with the original centroids of the targets used for the simulation* ***(red)****,* ***second*** *and* ***fourth columns****. Note that the markers are only resolvable when the marker spacing is >10x10 nm for DNA-PAINT and reliably detectable at an efficiency of ~84% when the spacing is >15x15 nm. In dSTORM data, markers within the cluster are not resolvable until spacing is ~60x60 nm and may yet include errors in the centroid detection. The mean distance* ***d*** *between the original target centroid and the detected marker centroid is stated below each panel. This simulation was carried out by Dr. I.D. Jayasinghe.*

This is also broadly consistent with DNA-PAINT imaging of a test sample made from DNA origami on our system that clearly resolved 40 nm distant puncta using localisation data with a similar precision as in the RyR data, Figure 4.8. In summary, the analyses showed that marker positions were robustly reproduced over several DNA-PAINT imaging repetitions and puncta occurred at a spacing compatible with detection based on the high localisation precision data.

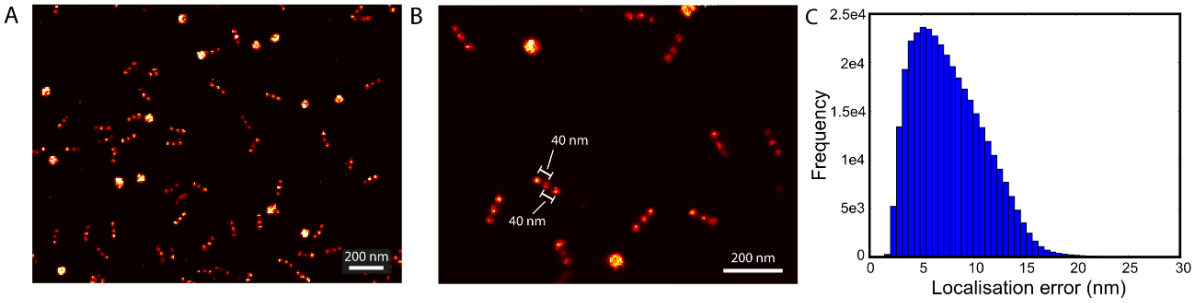

Figure 4.8. *Resolving 40 nm distant labelling puncta using a DNA origami test sample. (**A**) An overview image of reconstructed 40 nm distant puncta on DNA origami molecular rulers in a GATTAquant-PAINT HiRes 40R slide. The larger, round objects are additional, structurally different DNA-origami fiducial markers provided for drift correction. These structures were not employed for drift correction, instead drift was correct using transmitted light described in Chapter 2. **(B)** A detailed view shows 40 nm puncta were clearly separated. **(C)** The estimated localisation errors of the events, in the frame data used to generate these images, were similar in magnitude to those in the experimental data of RyR distribution in myocytes.*

4.4. RyR clustering and quantitative analysis by in-situ calibrated qPAINT

The reproducibility and the static positions of the punctate event densities, observed in DNA-PAINT data, is strong evidence that they reflect the positions of RyRs within the underlying cluster. The clustering of RyRs and the density at which RyRs aggregated within clusters was investigated, using the DNA-PAINT

data, because the precise clustering and density of RyRs critically determines their cross-signalling via calcium[66]. Cluster segmentation was performed by normalised thresholding of DNA-PAINT event densities as illustrated in Figure 4.9A. Receptor numbers within clusters were estimated from puncta counts over 2062 clusters (17 cells) which revealed a frequency histogram of cluster size with an approximately exponential distribution. This distribution, in shape, was similar to that constructed previously with dSTORM data[62], however, with a smaller average size of 8.8 ± 0.86 RyRs per cluster (n=17 cells). Considering clusters which contained two or more RyRs, the nearest neighbour centre-to-centre distance for each RyR punctum was measured. Analysis of data from 21 cells revealed a near-Gaussian distribution with a mean of 40.1 ± 0.9 nm and a mode at ~40 nm, similar to the mean itself. The average of the distance to the 4 nearest surrounding RyRs (for clusters with >= 5 RyRs) as a measure of a typical calcium diffusion distance to the immediately surrounding group of receptors was also determined and had a mean of 58.9 ± 0.9 nm and a mode at ~47 nm (n = 1691 clusters and 21 cells). The larger distances exhibited (as compared to the single nearest neighbour distance) reflect the variable distances of RyRs within the cluster.

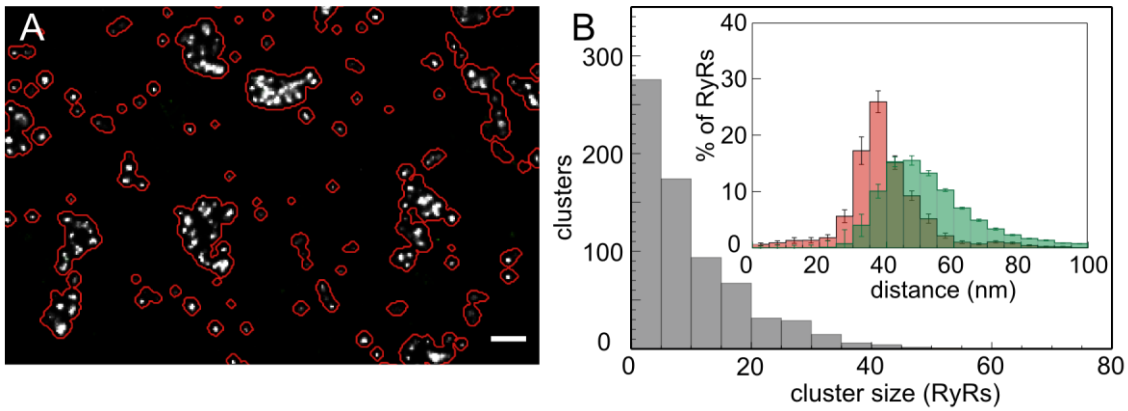

Figure 4.9. *Quantitative analysis of RyR cluster properties.* ***(A)*** *Clusters were segmented using an algorithm that contours the image based on local event density* ***(red lines)****.* ***(B)*** *A frequency histogram of RyR puncta counted within segmented RyR clusters revealed that peripheral clusters in rat ventricular myocytes typically consisted of fewer than* 40 RyRs (Mean ± SD = 8.81 ± 3.56 RyR/cluster; n=17 cells, 10 animals*). Analysis of the nearest neighbour puncta distances in clusters with 5 or more receptors* ***(see inset; red)*** revealed mean inter-RyR centroid-centroid distances of 40 nm (40.1 ± 0.9 nm; mean ± SEM; n=1802 clusters, 8 animals). *The average of the 4 nearest neighbour distances* ***(green)*** *followed a wider and right-shifted distribution, with a mean of* 58.9 ± 0.9 nm (mean ± SEM) *consistent with an irregular arrangement of RyRs within the clusters.* ***Scale bar:*** *200 nm.*

Recently, a powerful way to quantify protein numbers from DNA-PAINT data has been introduced by Jungmann et al[32] called quantitative PAINT, qPAINT. The RyR data was subjected to qPAINT analysis as a second, largely independent analysis from the puncta counting approach. qPAINT is based on the idea that the binding and unbinding of imager strands to docking strands in the sample (schematically shown in Figure 4.10A) can be analysed through time to obtain a measure that is proportional to the number of docking sites, i.e. the number of markers, within a chosen region of the sample. By providing a suitable calibration measurement this proportionality measure can be turned into an absolute count of docking sites, or, if a calibration from single receptors is available, into a direct count of receptors[90]. qPAINT analysis was conducted on a per-cluster basis. By analysing all frame times at which a binding event was observed, cumulative

histograms of the dark time durations for the cluster were obtained and were used to estimate the mean dark time between binding events. Due to the first order binding kinetics between imager strands and docking strands the inverse of the measured mean dark time, which we term the “qPAINT index”, provides a measure directly proportional to the number of docking strands in the cluster region. Figure 4.10B shows a histogram of the qPAINT index of small clusters which were selected based on their measured geometrical area and visually contain only one or a small number of puncta when rendered. The qPAINT index histogram of these small clusters exhibits a number of peaks that are a hallmark of “quantal” behaviour representing one, two, three etc, units characteristic of single RyRs. The mean qPAINT index for single receptors obtained in this way, e.g. 0.14 in Figure 4.10B, was used to calibrate the cluster qPAINT indices in the corresponding image and turn them into absolute receptor number estimates. Figure 4.10C illustrates receptor number estimates for 3 larger clusters.

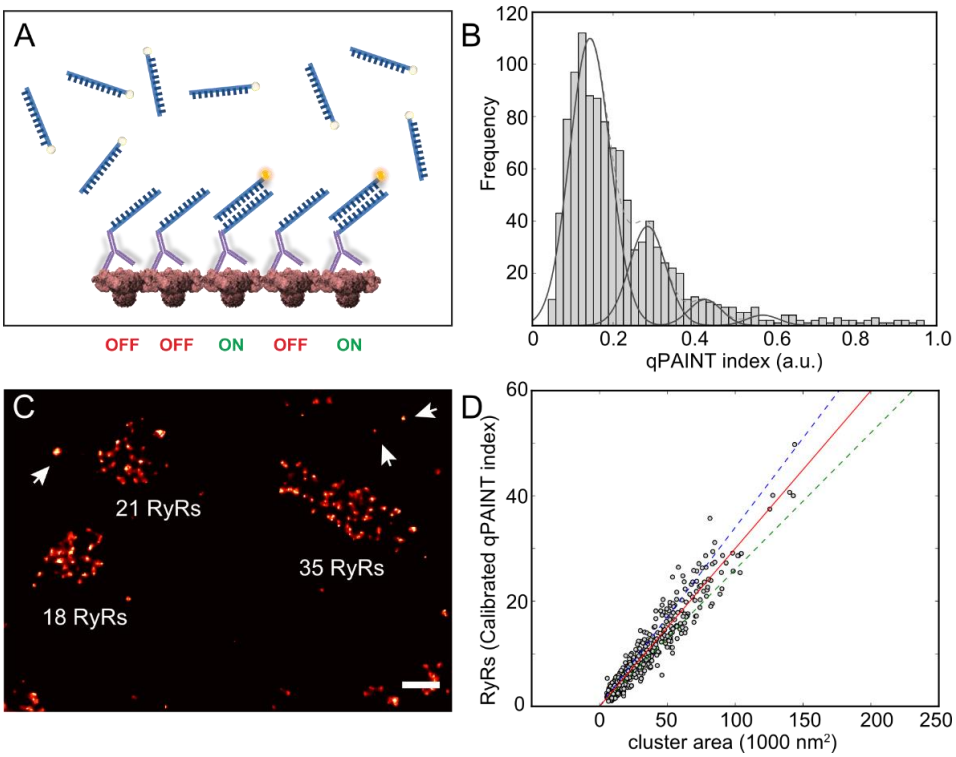

Figure 4.10. (A) *The schematic illustrates the principle of qPAINT which analyses the temporal occupancy of docking sites in a cluster by transiently binding imagers. Due to first order binding kinetics, the inverse of the mean time between imagers binding to a cluster, which we term the 'qPAINT index', is proportional to the number of binding sites.* ***(B)*** *The qPAINT indices of small clusters which contain only one or a few puncta provided a calibration to "count RyRs". The qPAINT index histogram exhibits equidistant peaks, characteristic of a quantal increments in imager strand binding sites, with a primary maximum of 0.14 qPAINT index units, equivalent to a single receptor. By dividing the qPAINT index of larger RyR clusters by this calibration value, the calibrated qPAINT index provides an estimate of the number of receptors in a cluster.* ***(C)*** *Examples of the RyR counts made through calibrated qPAINT are shown for three nearby large clusters.* ***(D)*** *Scatter plot of cluster area versus qPAINT estimated RyR counts. A linear regression* ***(solid line)*** *of the scattergram provides an estimate of the two-dimensional area of packing as 1 RyR per 3300 nm² for this dataset from one cell (391 clusters). The dashed lines indicate 15% variation from the linear regression slope.* ***Scale bar:*** *200 nm.*

The estimated RyR numbers closely agree with the counted number of puncta in these clusters, as shown in Figure 4.11C, further supporting the hypothesis that puncta correspond to individual RyRs.

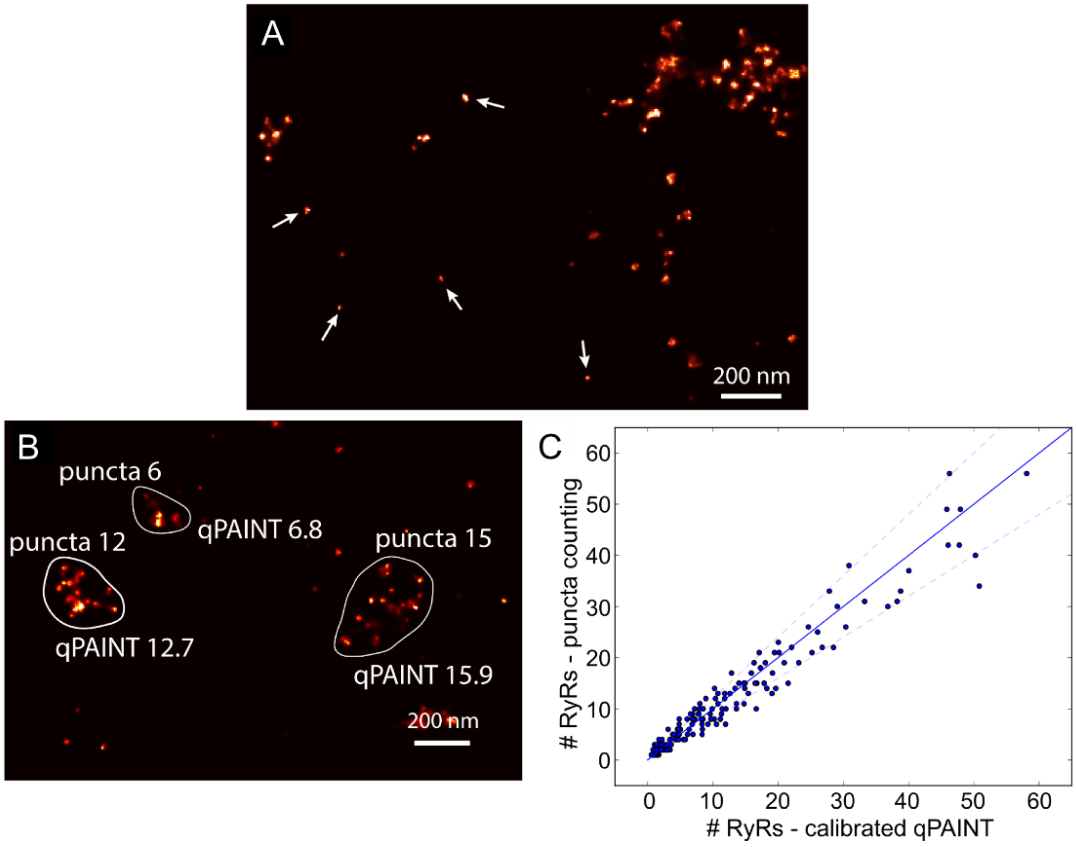

Figure 4.11. *qPAINT calibration with single receptor signals and comparison with puncta quantification.* ***(A)*** *Small clusters, visually containing only one or very few puncta* ***(arrows)****, were identified by apparent cluster area (cluster area < 10,000 nm^2) and their dark times and qPAINT indices were determined.* ***(B)*** *The qPAINT index was calculated for these clusters as the inverse of the measured mean dark time. The obtained histogram of qPAINT indices exhibited peaks at multiples of a qPAINT index of 0.14, see* ***Figure 4.10B****. It was visually confirmed that the clusters corresponding to qPAINT indices around 0.14 corresponded to clusters containing a single punctum. The calibration value was used to calibrate the corresponding data set and obtain estimated receptor numbers for each cluster as the ratio of the original qPAINT index q_i and the calibration value q_{i1}. Similar calibrations were conducted for each data set using an in-situ calibration.* ***(B)*** *This small section of a DNA-PAINT image of RyR labelling shows three clusters and the comparison of RyR number estimates obtained by puncta counting and calibrated qPAINT analysis indicates good agreement.* ***(C)*** *The correlation between RyR cluster sizes determined by puncta counting and qPAINT analysis is relatively tight. The solid line is the line of identity, the dashed lines show ratios of 1.2 and 0.8 between estimates, respectively. Each data point represents a single cluster.*

When the estimated receptor numbers of each cluster are plotted against the geometrical area of clusters (Figure 4.11D) a linear relationship was obtained that was used to estimate the apparent RyR density within clusters. The slope of this relationship was 0.32 ± 0.05 RyR / 1000 nm^2, (mean ± SEM, 1507 clusters, 6 cells from 3 animals) equivalent to a linear distance between receptors of ~56 nm, similar to the distance obtained above as the average of the 4 nearest neighbour puncta distances (~59 nm).

The quantitative analysis concluded that from the high-quality DNA-PAINT data, markers identifying the location of individual RyRs could be seen. It also confirmed that RyRs occur at a density within clusters that is lower than would be expected based on a close packed arrangement of RyRs which has a limiting density[115] of ~1 RyR / 1000 nm^2. In addition, the distances between receptors is variable and therefore the cluster properties were investigated in further detail as RyR distances are expected to strongly affect the gating properties of clusters[116].

4.5. Analysis of the organisation of RyRs within clusters

The organisation of RyRs into clusters is thought to be an important aspect of the calcium signalling of cardiac muscle cells. The size of RyR clusters and the precise spatial arrangement of RyRs within clusters determine how “excitable” a cluster is[66] because open RyRs can directly increase the open probability of surrounding RyRs via the local calcium increase they cause. This is due to the diffusion of Ca^{2+} to these surrounding receptors, notably the local Ca^{2+} concentrations decrease steeply with distance from open RyRs. The ability to directly visualise RyRs and their molecular positions in situ should therefore allow unprecedented insight into the biophysical control of Ca^{2+} within cells. While the quantitative analysis of the new DNA-PAINT data of RyRs suggests this is now possible for the first time from high contrast fluorescence data, some factors could affect the data analysis. For example, the binding of antibodies to RyRs may be incomplete, which could affect the interpretation of the data.

Figure 4.12A shows several typical clusters in which receptors are arranged apparently irregularly. These cluster patterns could be closely mimicked by assembling simulated clusters according to a rule that constructed clusters by placing new RyRs in a random direction and with a distance that varied slightly around a mean distance of 40 nm according to a Gaussian distribution with a sigma of 7.4 nm (Figure 4.12B), a distribution that closely matches the observed distance distribution in mean and width. This self-assembly process led to the appearance of some larger “gaps” in the clusters similar to those observed in the data as highlighted in distance maps between RyRs in experimentally observed clusters as shown in Figure 4.12C.

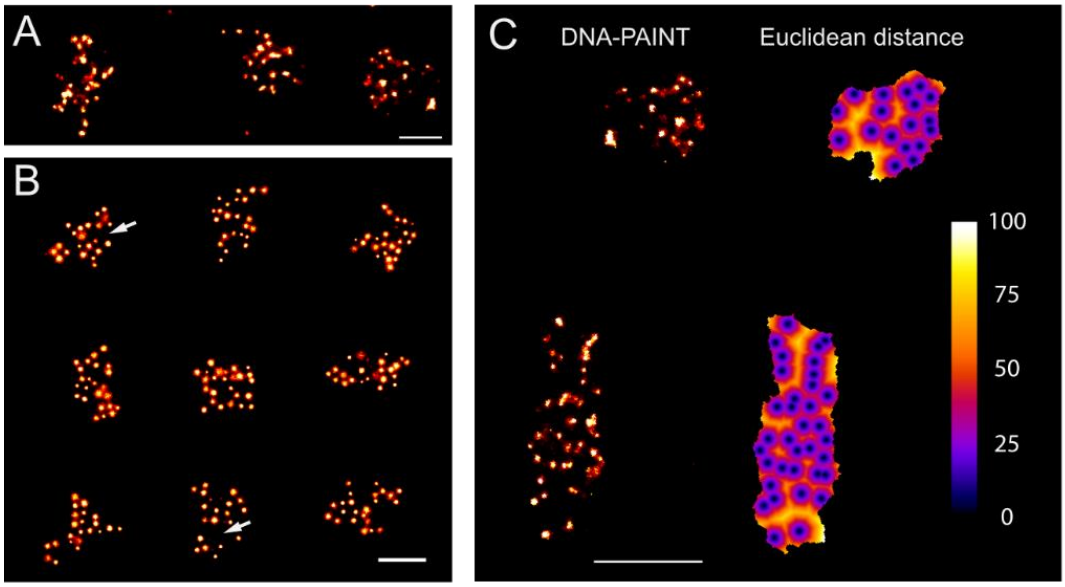

Figure 4.12. *Morphology of RyR organisation within clusters.* ***(A)*** *Example of rendered DNA-PAINT event densities within three adjacent peripheral RyR clusters reported irregular cluster shapes and amorphously arranged punctate event densities of labelled RyRs.* ***(B)*** *Simulated super-resolution images with similar morphology were reproduced in an in silico Monte Carlo simulation of directionally unconstrained RyR cluster self-assembly. 25 receptors were sequentially assembled at variable nearest neighbour distances based on a random Gaussian distribution with* μ= 40.0 nm and σ=7.4 nm. *Note the gaps* ***(arrows)*** *within the arrays which naturally appeared within the cluster as a result of the random self-assembly process.* ***(C)*** *Experimental data showing this amorphous RyR distribution* ***(left)*** *was further analysed for the Euclidean distances (colour maps in nanometres) between the centroids of RyR labelling densities. Regions coloured in yellow-white revealed sub-nanodomain boundaries within the RyR cluster where the gaps between adjacent RyRs exceeded 100 nm.* ***Scale bar: (A&B)*** *200 nm,* ***(C)*** *400nm. The simulation in (B) was carried out by Dr. I.D. Jayasinghe.*

In an additional simulation, the effect of detecting varying fractions of the receptors in a cluster was investigated. Comparison of simulations based on clusters generated with the random direction cluster model and assuming detection levels of 100%, 90% and 60% are shown in Figure 4.13. Increasingly lower detection fractions shift the average of local distances to longer values and

especially give rise to a marked tail in the average distance to the 4 nearest neighbours (N4ND) distribution. By contrast, the nearest neighbour distance (NND) stays approximately constant. Comparison suggests that the observations are consistent with a model where >80% of all RyRs are detected because otherwise gaps and 4 nearest-neighbour distances would markedly increase.

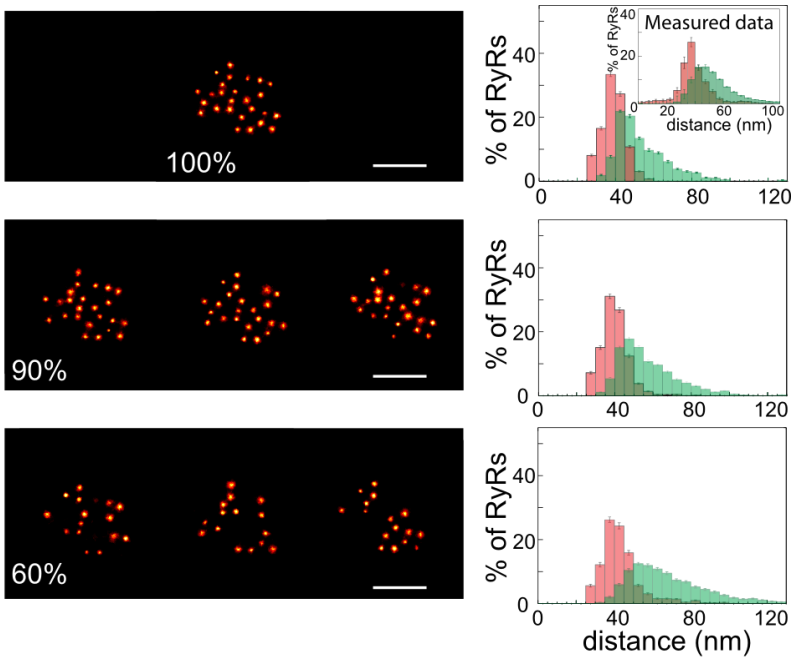

Figure 4.13. *Simulation of effect of binding analysis. For this simulation, clusters were generated, as in* ***Figure 4.12B****, and then a fraction of RyRs were randomly omitted from the generated clusters, with the retained fraction from* ***top*** *to* ***bottom*** *panel 100, 90 and 60%, respectively. On the* ***right****, nearest neighbour* ***(red)*** *and average of 4 nearest neighbour distance* ***(green)*** *histograms calculated from an ensemble of simulated clusters with varying detection fraction are shown, fractions as given in* ***left*** *panel.* ***Scale bar:*** *200 nm. This simulation was carried out by Dr. I.D. Jayasinghe.*

The ability to distinguish between a model of more closely spaced RyRs (30 nm) with lower detection efficiency (50%) versus the 40-nm spacing observed, Figure 4.14, was also tested.

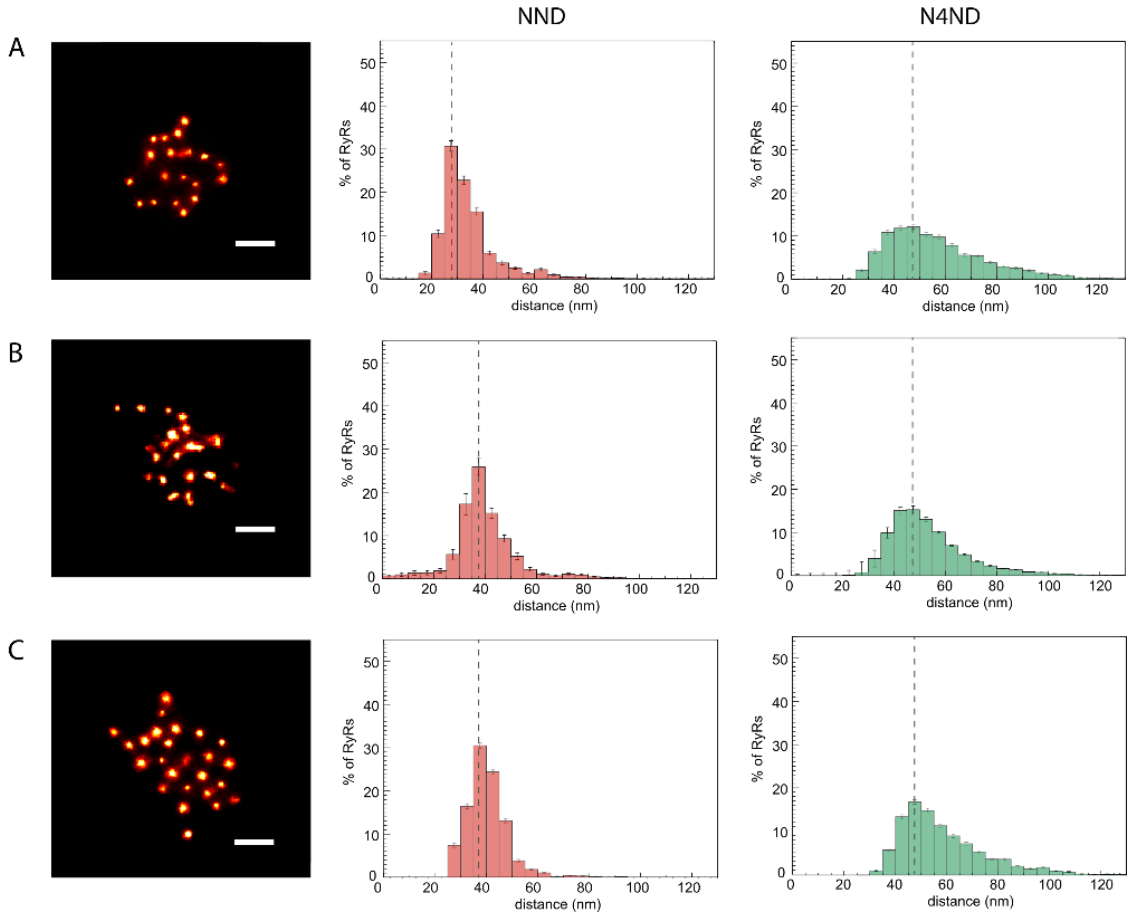

Figure 4.14. *Distinguishing narrow receptor spacing and low labelling efficiency from wider spacing with high labelling efficiency.* ***(A)*** *A simulated cluster* ***(left panel)*** *from an ensemble generated with a mean receptor spacing of 30 nm and a detection efficiency of 50 %. The NND distribution* ***(middle panel)*** *is only weakly affected by the missed receptors, the mode is still at ~30 nm. The N4ND distance measure is more sensitive and right-shifted.* ***(B)*** *By contrast, the measurements of actual clusters exhibit a NND mode at ~40 nm, and N4ND mode at ~50 nm.* ***(C)*** *The experimental observations are consistent with a cluster model that has a mean distance between nearest receptors of 40 nm* ***(middle panel)****, an example cluster is shown in the* ***left panel****. The N4ND* ***(right panel)*** *agrees well with experimental observations when a large detection efficiency >0.8 is assumed.* ***Scale bar:*** *100 nm. The simulations were carried out by Dr. I.D Jayasinghe.*

These simulations strongly suggest that a scenario of much more closely arranged receptors, i.e. 30 nm, can been ruled out based on the data. In a separate experiment, it was confirmed that the density of markers observed in RyR clusters was not a limiting density of the detection system used. The membrane protein caveolin-3 was imaged in coverslip attached membrane areas using equivalent staining protocols and DNA-PAINT imaging as for RyR detection and at least three-fold higher puncta densities was observed, Figure 4.15.

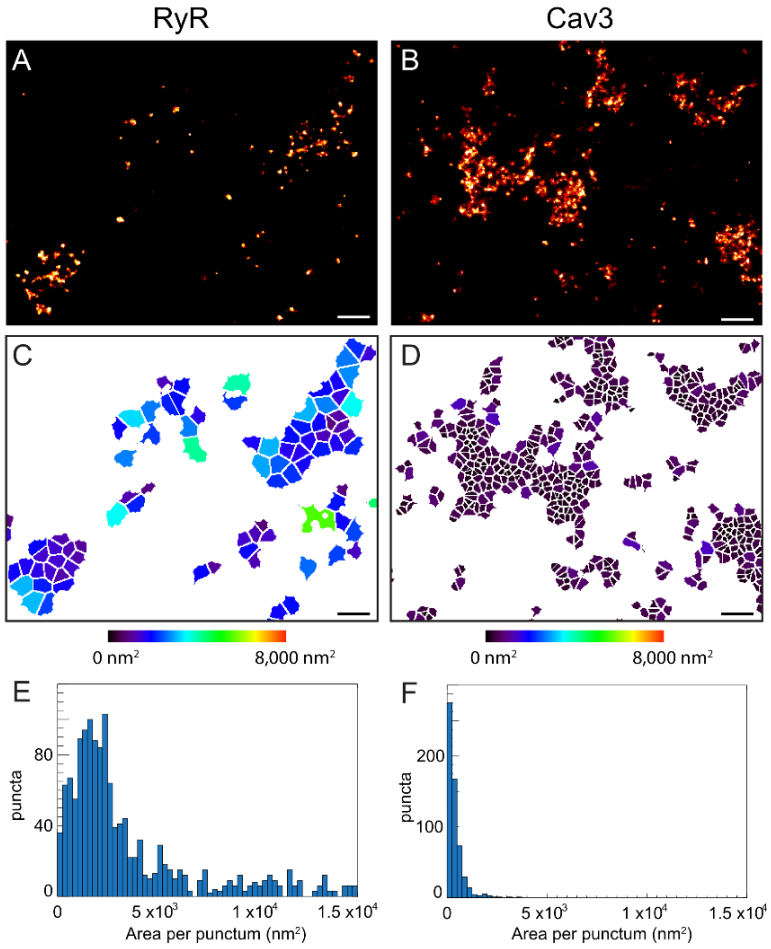

Figure 4.15. *The packing distances of antibody labelling densities are not limited by the labelling system. To examine whether the apparent marker binding density or the resolvable marker spacing were limited to these distances, DNA-PAINT data acquired from TIRF micrographs of rat ventricular myocytes labelled similarly against the densely-organised plasma membrane protein Caveolin-3 was examined.* ***(A)*** *Typical DNA-PAINT images of peripheral cluster labelling of mouse monoclonal anti-RyR2 antibodies.* ***(B)*** *DNA-PAINT images of mouse monoclonal anti-Caveolin-3 antibodies in similar regions. Note the punctate labelling morphology in both label distributions. To quantify the proximity of packing, the centroids of the punctate densities were computed and subjected to Voronoi partitions to visualise the "areas" per punctum for both the* ***(C)*** *RyR and* ***(D)*** *Caveolin-3 label distribution. Each of the Voronoi partitions is coloured according to the size of the area around a punctum. The frequency distributions of the Voronoi partition areas for* ***(E)*** *RyR antibodies and* ***(F)*** *Caveolin-3 antibodies quantify the smaller partitions in Caveolin-3 images compared to RyR. This observation confirmed that the methodology was able to detect higher punctate labelling densities than observed with RyR markers and that the observed RyR morphology or distance measurements are unlikely to be limited by marker access to the target or the resolution of the DNA-PAINT images. Average densities of puncta in RyR data was one per 4314.87 ± 1332.47 nm² while that in caveolin-3 was one per 1466.95 ± 455.5 nm².* ***Scale bar:*** *50 nm.*

4.6. Investigation of RyR-JPH co-clusters with Exchange-PAINT

Previous work has shown that RyRs are co-clustered with other Ca^{2+} handling proteins, regulator molecules, as well as structural proteins that may modulate their localisation and packing within the cluster microdomain[91]. The apparent irregular organisation of RyRs within clusters prompted an investigation into the distribution of another protein JPH2 in relation to RyRs. JPH2, an intrinsic SR protein, has been implicated in forming and maintaining the close apposition of SR and cell surface membranes where RyRs are preferentially located[117]. Previous work suggested that JPH2 can bind to and appears to stabilise RyRs, i.e. shift RyR opening to higher Ca^{2+} concentrations[118]. Applying Exchange-PAINT (i.e. sequential imaging of two populations of docking-strand markers)[32] revealed JPH2 within the same nanodomains as RyR clusters, in co-clustered regions of JPH2 labelling. Overlay of the two images confirmed intimate tessellation of both RyR and JPH2 labelling densities, Figure 4.16. Quantitative analysis of a large ensemble of clusters exhibited a high density of JPH2 labelling within just 50 nm of the centroids of RyR puncta.

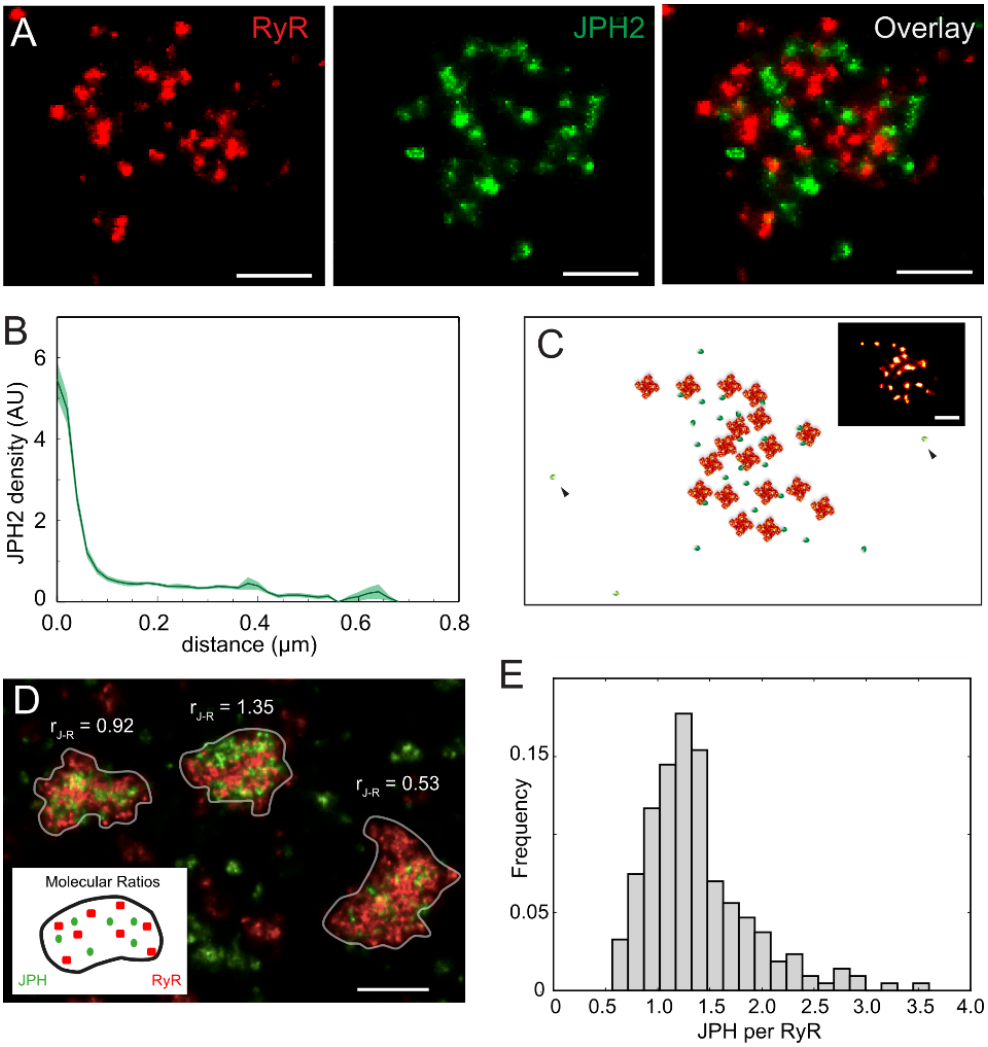

Figure 4.16. Exchange-PAINT dual-colour nanoscale analysis of JPH2 interaction with RyR in peripheral clusters. **(A)** An example of sequentially-acquired DNA-PAINT images of RyR **(red)** and JPH2 **(green)** within a peripheral cluster allowed a direct examination of their spatial relationship at sub 10 nm distances, illustrated in overlay. **(B)** Analysis of the JPH2 DNA-PAINT labelling density as a function of the distance from the centroids of the single RyR puncta illustrates a high density of JPH2 markers within 50 nm of the RyRs. At distances >100 nm, this density was maintained at ~ 10-20% of that seen near the RyRs. **(C)** A schematic reconstruction of protein arrangements compatible with the DNA-PAINT data: an irregular RyR array **(orange)**, populations of densely co-localised or bound JPH2 **(dark green)** and sparsely distributed extra-junctional JPH2 **(light green)** similar to actually observed experimental DNA-PAINT data **(inset)**. **(D)** Molecular ratios by Exchange-qPAINT of RyR and JPH2 determined from calibrated qPAINT data of RyR-JPH2 co-clusters **(inset shows schematic)**, shown in three adjacent clusters exhibiting ratios between 0.53 and 1.35 JPH2/RyR. **(E)** Histogram of JPH2 to RyR ratios. The distribution of ratios has a mean of *1.38 JPH per RyR, a mode at 1.25 and a width of 0.5 (standard deviation), n = 250 clusters (containing ≥ 15 RyRs) from 3 cells, 2 animals*. **Scale bars: (A)** 200 nm, **(C)** 100 nm, **(D)** 250 nm.

A distance-based co-localisation was applied (as in Jayasinghe et al)[91] to quantify the nature of co-localisation between RyR and JPH, Figure 4.17A. To verify whether the observed JPH2 localisation distribution showed preferential co-clustering with RyR, a DNA-PAINT image of a randomly distributed marker population of JPH2 was also simulated whose 2D position was assigned based on a random uniform distribution. The Euclidean distance map constructed from the centroids of the RyR puncta (0.1 nm and 0.3 nm contours) were overlaid with the DNA-PAINT images. This showed that both RyR (Figure 4.17A, left panel) and experimental JPH2 distributions (Figure 4.17A, middle panel) were intimately co-clustered within the 100 nm distance bands, whilst the simulated JPH2 data (Figure 4.17A, right panel) showed this to a lesser extent.

Histogram analysis of the density of JPH2 labelling as a function of the distance from the centroids of the single RyR puncta showed a high density of JPH2 markers within 50 nm of the RyRs, Figure 4.17B. At distances beyond 100 nm, this density was approximately uniform, but 5-10 times lower. Replacing the experimental JPH2 image with the simulated JPH2 image where JPH molecules were randomly placed exhibited essentially a uniform density distribution, Figure 4.17C, as expected. These results confirmed that this increased density of JPH2 in the immediate regions adjacent to RyRs reflects a preferential (non-random) co-clustering behaviour.

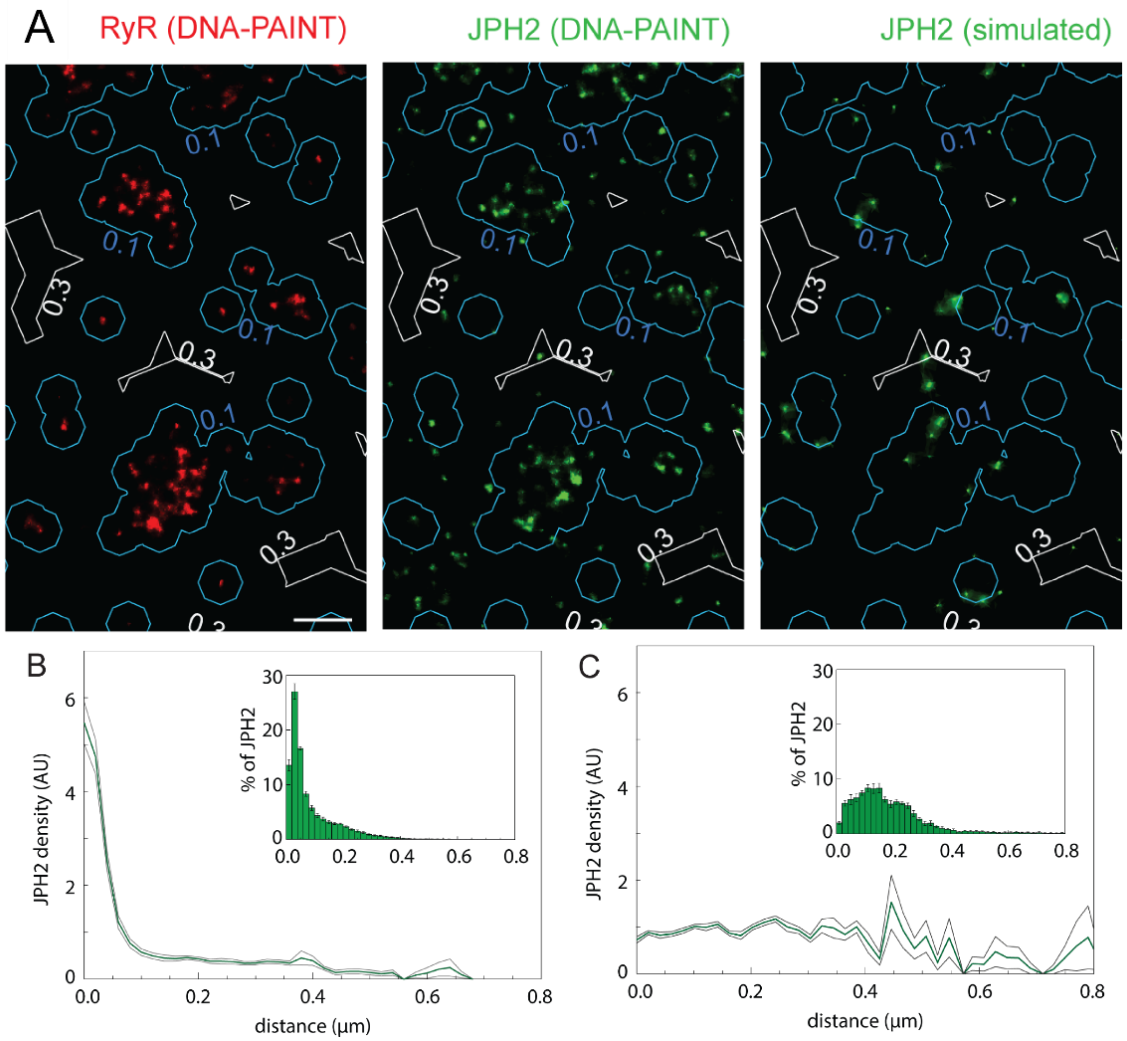

Figure 4.17. (A) *DNA-PAINT images overlaid with the Euclidean distance map constructed from the centroids of the RyR puncta (0.1 µm and 0.3 µm contours) showed that both RyR* ***(left panel)*** *and experimental JPH2 distributions* ***(middle panel)*** *co-clustered within the 100 nm distance bands. A simulated JPH2 random uniform distribution* ***(right panel)*** *showed less co-clustering.* ***(B)*** *A high density of JPH2 markers within 50 nm of the RyRs were shown in a histogram analysis of the density of JPH2 labelling as a function of the distance from the centroids of the single RyR puncta. Analysis of the percentage of the integrated labelling density as a function of this distance scale* ***(inset)*** *showed that >86% of all the JPH2 events were localised within 200 nm of the RyR puncta.* ***(C)*** *JPH2 with a simulated random placement diminished the high percentage of JPH2 organised closely to RyR (only ~ 58% of the JPH2 labelling localised within 200 nm) confirming that the experimentally observed JPH2 distribution is not compatible with random placement relative to RyRs.* ***Scale bars:*** *200 nm. Dr. I.D. Jayasinghe provided the simulated JPH2 DNA-PAINT data.*

The RyR and JPH2 protein arrays in DNA-PAINT were resolved as punctate densities, in contrast to dSTORM data of identical cells which only resolves cluster outlines and contained extended stochastic labelling densities due to the lower localisation precision of the dSTORM data, Figure 4.18. When investigated within cluster boundaries, as expected, dSTORM and Exchange-PAINT data reported arrangements between RyR and JPH2 that were quantitatively consistent. The mean percentage of JPH2 overlapping within the area of the RyR cluster was similar between dSTORM and DNA-PAINT images (72.0% vs 70.3%; p = 0.49 in Student's t-test). There was also no statistically significant difference between the percentages of co-localising RyR labelling in the two types of image data (57.2% vs 50.1%; p=0.39).

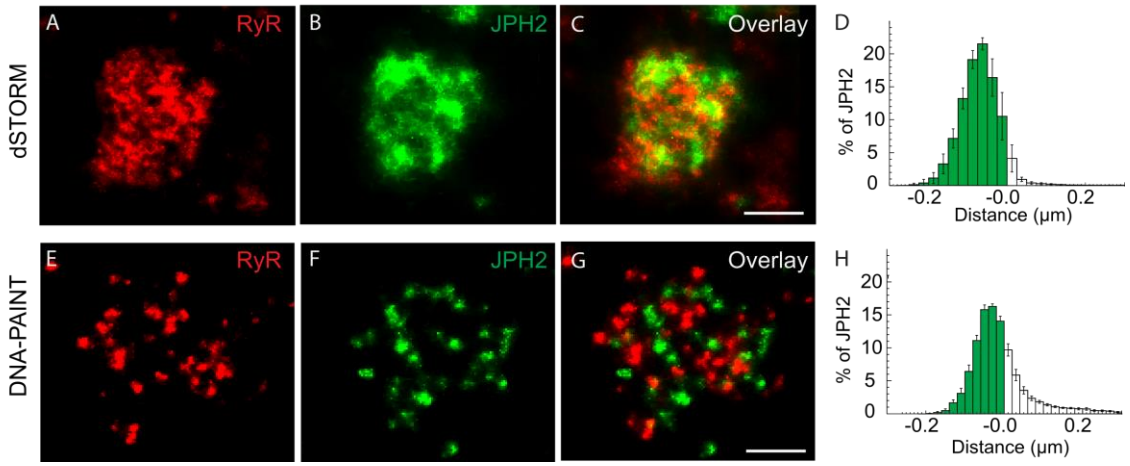

Figure 4.18. *Co-localisation of JPH2 with RyR estimated by dSTORM versus DNA-PAINT. Shown, an image of* ***(A)*** *an RyR cluster,* ***(B)*** *corresponding JPH2 labelling and* ***(C)*** *overlay from dSTORM data of a peripheral couplon in a rat ventricular myocyte.* ***(D)*** *The* ***shaded area*** *(distances <0.0) of the percentage histogram of the integrated JPH2 labelling plotted as a function of the distance from the edge of each RyR cluster reports 72.0 ± 2.5% (n=5 cells; 2 animals) of this labelling within the RyR mask (see also previous analysis by Jayasinghe et al[91]). In contrast, both* ***(E)*** *the RyR and* ***(F)*** *JPH2 followed a punctate pattern in DNA-PAINT images of identical cells.* ***(G)*** *Overlay revealed close proximity of these punctate labelling densities which was consistent with some JPH2 binding (directly or via accessory proteins) to RyRs.* ***(H)*** *The percentage histogram equivalent to above, from an analysis based on the cluster edge, revealed a smaller total fraction (~70%) of JPH2 now co-localising with RyR. This decrease is expected due to the higher resolution in the DNA-PAINT data but the dSTORM data does not detect the increase in JPH2 density close to RyRs, consistent with the lower effective resolution.* ***Scale bars:*** *200 nm.*

In addition to the high density of JPH close to RyRs (<50 nm) in the DNA-PAINT data, a non-zero JPH2 density was present at distances of >50 nm in Figure 4.16B. Given that some of these distances corresponded with gaps located within the RyR arrays, the location of JPH2 labelling in relation to similar RyR Euclidean distance maps was examined, Figure 4.19, to find that some, but not all of such regions, were occupied by puncta of JPH2 labelling. Taken together, these observations are highly suggestive of a sub-population of JPH2 molecules located within RyR clusters which are unlikely to be directly bound to RyRs (labelling at distances > 50 nm), as shown schematically in Figure 4.16C, while another sub-population is close enough to be conceivably in a molecular complex with individual RyRs.

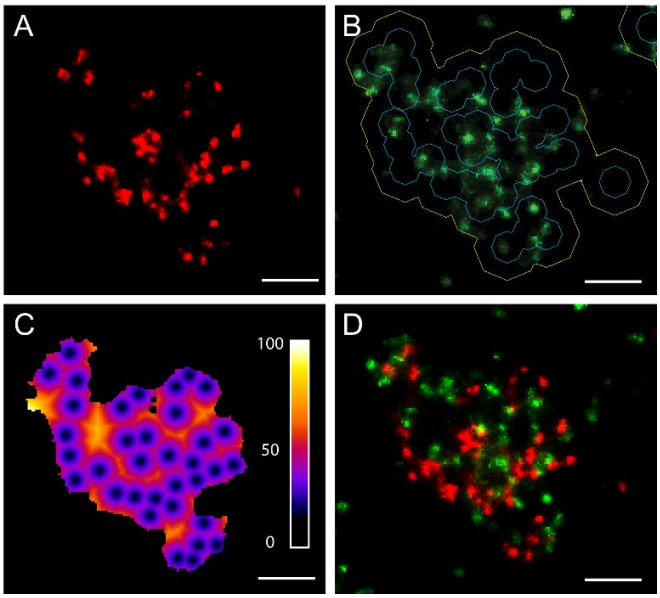

Figure 4.19. *Examination of the organisation of JPH2 within the non-uniform RyR arrays. The non-uniform arrangement of RyR led to the examination of whether any of the JPH2 densities could be localised to the regions within the RyR cluster that were devoid of receptors. Shown, Exchange-PAINT images of* ***(A)*** *RyR and* ***(B)*** *JPH2 acquired from a rat ventricular myocyte. Overlay of the JPH2 image with a contour map (50 nm in blue; 100 nm in yellow) of the Euclidean distance from the centroids of RyR puncta illustrates that a large fraction of the JPH2 are localised within the 50 nm bands (i.e. most likely bound to RyRs). A smaller fraction was observed between the* ***yellow*** *and* ***blue*** *contours signifying JPH2 which are resident to the junction, but nevertheless unlikely binding partners of RyR.* ***(C)*** *The latter population of JPH2 align strongly with the yellow regions of the Euclidean distance colour map (scale in nm) reporting continuous regions devoid of RyR.* ***(D)*** *This distinguishing of potentially specialised localisation of JPH2 is also notable in the two-colour overlay of DNA-PAINT images unlike the dSTORM images* ***(Figure 4.18)****.* ***Scale bar:*** *200 nm.*

The high degree of co-clustering motivated an additional analysis that was enabled by the quantitative nature of qPAINT. By combining calibrated qPAINT analysis with the Exchange-PAINT of RyR and JPH2 molecular ratios of JPH2 to RyRs were determined on a per cluster basis. The analysis was conducted for larger RyR clusters (containing >15 RyRs) that are likely located in larger junctions between surface and SR membranes. Figure 4.16D shows three typical

clusters which exhibited ratios r_{J-R} of JPH2 to RyR between r_{J-R} = 0.53 and r_{J-R} = 1.35. It is notable that clusters with considerably different molecular ratios are observed in close proximity. An ensemble analysis (214 large clusters, n=3 cells) revealed a distribution in which ratios varied between ~0.5 and 3.5 with a mean at 1.38 JPH2 per RyR, a mode at 1.25 and a histogram width of 0.5 (quantified by the distribution standard deviation) as shown in Figure 4.16E. To my knowledge this is the first time such a molecular ratio has been determined *in situ* using qPAINT analysis and presents a measurement that can be more directly biologically interpreted than co-localisation measures which are notoriously difficult to interpret.

The use of DNA-PAINT based super-resolution imaging enabled fully quantitative imaging of clusters of RyRs in peripheral couplings of ventricular myocytes with molecular resolution. Improved photon yields and reduced backgrounds were critical in resolving individual receptors, and revealing their molecular-scale clustering patterns within the working cell at an unprecedented level of spatial detail. The new data revealed apparently irregular arrangements of RyRs with considerable gaps within clusters and an apparent receptor density that was lower than close-packed RyR arrays observed previously in artificial membranes. The improved resolution also allowed the visualisation of RyR-JPH2 co-clusters in which a sub-population of JPH2 was in molecular proximity to RyRs, compatible with being in a complex with individual RyRs. In-situ quantification of receptors showed that per-cluster ratios of JPH2 to RyRs are variable and adjacent clusters often exhibit substantially different ratios.

4.7. Clusters of RyRs at true molecular resolution

The new data presented here show, for the first time, individually resolved RyRs and their arrangements into clusters using purely optical methods. Previous super-resolution imaging using dSTORM[62] and STED[66] had been able to resolve cluster outlines, but the lower resolution (~50-60 nm FWHM) limited determination of the density and arrangement of RyRs within individual clusters.

Using DNA-PAINT to visualise receptors, distinct puncta were observed, that suggested a rise from markers bound to individual RyRs. The puncta were highly reproducible in location and number, justifying the interpretation that individual receptors were robustly detected. Their observed distance is compatible with the expected ability of the DNA-PAINT imaging system to resolve objects ≥ 30 nm apart. With the labelling system used and because RyRs as homo-tetramers provide several binding sites for marker antibodies, individual puncta may arise from more than one marker. A single RyR, in turn, should not give rise to more than one punctum that can be spatially resolved since RyRs are less than 30 nm in diameter[69]; if markers were bound in different places of a single receptor, these would be unlikely to be resolved into several puncta. The idea of each punctum representing a single RyR is further supported by a second quantitative analysis approach which used the recently introduced qPAINT analysis method[90] to quantify the number of docking sites *in situ*. The qPAINT calibration measurements (Figure 4.10B) are compatible with a quantised distribution of groups of docking sites, and the size of the quantal groups corresponded closely with individual puncta. This suggests that puncta are stereotypic in the number of binding sites/markers that they represent, compatible with a scenario where each punctum arises from markers/binding sites complexed with a single receptor.

4.8. DNA-PAINT achieves molecular resolution with relatively low experimental complexity

Our data confirms that DNA-PAINT can provide very high spatial localisation for SMLM. It achieves this with comparatively low, optical complexity and demands on dye photo-physics, so that these precisions were routinely achieved in experiments with relatively complex biological preparations. As shown recently[32,119], the photon yields for imaging, with DNA-PAINT, are large enough for localisation better than 10 nm in precision. At this level of precision the elimination of drift during long acquisition series is vital. This was achieved with a transmitted light tracking system that did not require any fiducial markers.

Some modifications to the labelling system as described by Jungmann et al[32] were made. Notably, by adding a dye to the docking strand the successful

staining and determination of suitable imaging areas was as straightforward as with conventional immuno-fluorescence imaging. In my hands, this was important to increase throughput and success rates in the experimental processing pipeline. Due to the properties of DNA-PAINT this comes at effectively no cost for super-resolution imaging. This is because the dye can be chosen spectrally different to imager dyes or, if there is potential cross-talk, the docking dye signal can be removed by local photo-bleaching. Fresh imagers overwhelm any signal from permanently attached cross-talking dye species. In addition, the ability to control 'blinking rates', by imager concentration, enabled straightforward reduction of blinking rates to a level that avoided emitter signal overlaps and maximised spatial resolution.

Another important advantage of DNA-PAINT is the ability to quantify the number of binding sites and calibrate the number of receptors. qPAINT[90] relies on the well-characterised first-order binding between complementary DNA-strands rather than on models of dye photo-physics, which can be a source of considerable uncertainty. The theoretical exponential dark time histograms have essentially only one free parameter, the characteristic dark time, and deviations from the expected behaviour would become apparent in the qPAINT analysis. qPAINT was used as an independent counting approach for RyRs and, in combination with Exchange-PAINT, also extended it to determine protein ratios between RyRs and the accessory protein JPH2. The DNA based technology underlying this approach makes the scheme very flexible and in my hands delivered a robust, quantitative super-resolution approach that is compatible with very high localisation precision. Classical approaches to analysing protein co-clustering ratios would involve co-immunoprecipitation approaches which rely on physical tethering of the targets of interest. The quantitative ratio analysis performed here, benefiting from the resolution to accurately recognise discrete nanodomains, removed the need for homogenisation of the tissue structure. This approach was arguably more sensitive in reporting location-specific variations in the co-clustering.

4.9. RyR cluster properties

Both puncta counting and qPAINT analysis provided estimates of an average receptor density within clusters of ~0.3 RyRs/ 1000 nm^2. This is considerably lower than the dense packing that can be observed on artificial lipid membranes where receptor density was ~1 per 31.5^2 nm^2 = 1 per 992 nm^2, or about 3 times higher[115,120]. This is consistent with a larger apparent distance between RyR puncta in the data which was >40 nm, rather than ~32 nm as expected for dense packing (although this estimate may be slightly affected by marker jitter as discussed below). While it is possible that some RyRs were not detected because no markers were bound, such an effect is unlikely to explain the differences. In support of this idea it was shown that the marker system can detect proteins at considerably higher densities, as demonstrated with CAV3, which was detected at a density >3 fold higher than the apparent RyR density. Therefore, in principle, this method is capable of mapping RyRs at a packing density seen in *in vitro* conditions. In addition, several simulations were carried out that suggest that the detection efficiency is high, as discussed below in the section on cluster morphology. Consistent with the lower receptor density the average size of RyR clusters was smaller than earlier estimates (~64%), which had assumed a dense packing and used cluster outlines/areas to deduce cluster size, rather than counting receptors directly as done here. The estimated size of RyR clusters was not reduced in direct proportion to the lower density which may result from overestimates of cluster areas, due to the lower resolution in the original dSTORM data[62]. The reduced size and reduced RyR density within clusters that were revealed here has direct effects for the expected biophysical properties of RyR clusters.

4.10. RyR cluster morphology and RyR biophysics

The distance between RyRs within clusters and the general spatial arrangement of RyRs, i.e. the “cluster morphology” has been suggested to play a major role in determining the excitability of a cluster by calcium[66,67]. While EM methods can provide data with sufficient resolution, limits of contrast and throughput have

generally meant that only a small number of clusters could be studied in this way[76]. The new data provided here allows for the first time to investigate a large number of clusters and their detailed receptor arrangement with high contrast. The analysis of RyR DNA-PAINT data was performed exploiting that peripheral couplings run parallel to the surface membrane[114]. The membrane is attached to the coverslip and therefore the peripheral clusters are essentially flat in 2D[114]. To limit recordings to peripheral couplings TIRF was used, restricting the excitation to a region approximately only a couple of hundred nanometres from the coverslip interface, see Figure 2.8 & 4.1.

The distribution of puncta appeared irregular and could be mimicked using a model. In this model clusters were generated using placement of new receptors in random directions and at a distance that varied around a mean value of ~40 nm. Puncta nearest neighbour distances, which are important in determining the ability of the calcium flux through an open RyR to open adjacent RyRs[121–123], had a strong mode at ~40 nm, which is larger than the distance of ~32 nm expected for dense packing of RyRs. This is consistent with recent electron tomography data which showed that RyRs in clusters are not homogeneously densely packed.

A complication in analysing distances between RyRs could arise from marker jitter, i.e. the fact that dye molecules conjugated to antibodies are localised rather than the RyR themselves. This could lead to an offset between reported marker positions and actual RyR locations that may be between 0 and ~12.5 nm[58]. On the other hand, with the possibility of more than one primary antibody binding to a single homo-tetramer this could pull the centre of mass of the resulting punctum closer to the centre of the RyR. As a result, the marker displacement may be smaller than expected, but it is currently difficult to conclusively identify regularly packed sub-groups of receptors. It is notable that directly labelled primary antibodies do not resolve the jitter, as primary antibodies may bind to RyRs with a variable offset, depending on the location of epitopes on the large 27 x 27 nm protein. Nevertheless, nearest neighbour distances provide a robust lower limit estimate as marker jitter would be expected to reduce the measured NND as compared to the actual value.

In connection with this point, the robustness of the NND estimate (with a prominent mode at ~40 nm) would be little effected by missed receptors, as demonstrated in Figure 4.14. In addition, two lines of evidence have been provided that suggest a large fraction of all receptors are detected. First, a secondary antibody system for DNA-PAINT imaging was shown to be able to detect a membrane protein, CAV3, with >3 times higher density than the RyR density detected here. Furthermore, a simulation suggested that a large fraction of missed receptors would be expected to increase the tail of the average of 4 nearest neighbours histogram substantially, more than that observed. From that point of view, the data is consistent with a >80% RyR detection. In support of this estimate, it was confirmed that labelling conditions maximised RyR labelling, i.e. experiments with additional permeabilisation with Triton™ X-100 did not increase observed RyR density and a saturating concentration of primary ABs was chosen in the experiments.

The observations based on the new data have several consequences for RyR cluster biophysics as the principal mechanism of concerted and fast calcium release from internal stores of cardiac muscle. The density of RyRs within clusters is lower than previously assumed, at least when based on close packing. This will reduce the cross-signalling between RyRs and needs to be incorporated into models of RyR cluster behaviour during Ca^{2+} release. In addition, there are sizable gaps in RyR clusters, that may extend up to 150 nm. The phenomenological cluster assembly model showed that such gaps can arise randomly and do not require any targeted templating mechanisms. Such gaps can dramatically alter the diffusion patterns of the cytoplasmic Ca^{2+} experienced by RyRs, a variable which dictates the probability of concerted cluster activation[66,67] and self-regulating termination of local Ca^{2+} release[124]. Walker et al[66] have already predicted that the excitability of clusters may be lowered in clusters containing gaps of ~ 50% of their internal area. New mathematical models need to be refined to capture the effect of such gaps on cluster excitability using the data provided here. These models should not be based on regular RyR arrays (e.g. Figure 2 of Laver et al[124]) but rather allow for irregular placements as seen in the data. Another consequence of $\geq$ 40 nm nearest neighbour distances is that many RyRs will not be in direct molecular contact with neighbouring RyRs. This has implications for putative cross-signalling mechanisms that rely on direct

contact[125]. Nevertheless, such RyRs may be part of molecular complexes with other proteins such as JPH2 which have been shown to be able to bind to RyRs and could support complex signalling and modulation of gating in this way. Finally, it is noted that the data characterises peripheral couplings, internal couplings are often larger and in complex 3D arrangements which complicate their study with the methods employed in this study. Those differences notwithstanding, it is reasonable to expect the basic architecture to be similar in terms of packing density and irregular receptor distribution within clusters, consistent with the interior coupling data from Asghari et al[76].

4.11. Quantitative imaging of JPH2-RyR co-clusters

The ability to conduct Exchange-PAINT enabled the high-resolution imaging of the relative location of RyRs and the accessory protein JPH2. JPH2 has been shown to be important for the maintenance of the junctional membrane geometry[117], a structure in which RyR clusters are generally located. In addition, it has been proposed that JPH2 can bind to RyRs and modulate their gating in response to calcium[126]. Exchange-PAINT provided a method to image both targets with the same dye but using non-competing docking and imager pairs. This has the advantage that the effect of chromatic aberrations can be essentially eliminated. Distance based analysis of the Exchange-PAINT data showed that a distinct sub-population of JPH2 was within molecular distances to RyRs, as seen by an at least 5-fold increase in JPH2 densities in areas $\leq$ 50 nm around RyR puncta. Such an increase would not be expected if JPH2 were randomly distributed across the area of RyR clusters, as shown in Figure 4.17. In conjunction with previous immuno-precipitation studies[126] this observation is compatible with a subpopulation of JPH2 bound to RyRs, either directly or via other proteins in a local complex. Direct comparison with dSTORM data showed that this observation critically depended on the higher resolution of DNA-PAINT.

An additional observation from the JPH2-RyR data was the finding that JPH2 proteins were present in some of the larger gaps observed within RyR clusters. Detection of JPH2 in these areas show that the gaps are not merely reflecting a topological boundary of the SR membrane (which anchors both RyR and JPH2)

but are genuinely part of peripheral junctions devoid of RyRs, from the arguments above that a high detection efficiency for RyRs was achieved.

With the ability to quantify markers and proteins using in-situ calibrated qPAINT analysis, qPAINT analysis was also conducted on Exchange-PAINT data to estimate protein ratios of JPH2-RyR co-clusters. To my knowledge this is the first use of qPAINT for protein ratio analysis and a natural combination of the Exchange-PAINT and qPAINT concepts. The reported ratios suggest that there is more than one JPH2 per RyR in JPH2-RyR co-clusters. In addition, the Exchange-PAINT images show that adjacent clusters often exhibit considerably different ratios. The variable RyR:JPH2 ratios from cluster to cluster add another complexity to regulating units of calcium signalling. The observations provide a molecular basis for a mechanism in which RyR clusters can be locally regulated, by varying the abundance of adjacent structural and inhibitory proteins. This would provide a cluster level regulation for signalling in complex cells.

The estimated ratios are in principle subject to antibody efficiency, but regardless of a potential correction factor will provide a relative comparison between clusters. The relative variation between adjacent clusters is clearly visually apparent in Figure 4.16D, and is independent of antibody binding efficiency. Similarly, the shape of the histogram shown in Figure 4.16E is an invariant feature of the data regardless of corrections from JPH2 antibody binding efficiencies. In general, the estimation of local protein ratios in structures of biological interest, here co-clusters of the two proteins, lends itself more readily to biological interpretation than co-localisation values which are often difficult to relate to biological function. Specifically, the ratio of JPH2 to RyRs has been suggested to be important in stabilising RyRs which was critical in a JPH2 overexpression model in which RyR cluster sizes were greatly increased[65]. The larger size should have resulted in very excitable-RyR clusters, likely due to the higher ratio of JPH2 to RyRs which is compatible with more JPH2 directly bound to RyRs. Although not functionally observed here, with the improved methods presented it becomes possible to investigate this hypothesis directly.

4.12. Limitations

The size and binding location of markers on RyRs currently limit the precision with which the arrangement of RyRs can be judged and close packed areas can be identified unambiguously; the development of small markers binding to well characterised locations of RyRs should be assisted by recently improved 3D structures of the cardiac ryanodine receptor[69].

4.13. Conclusions

The application of refined DNA-PAINT approaches to the molecular characterisation of RyR clusters and JPH2-RyR co-clusters has demonstrated the potential for molecular resolution quantitative imaging in complex biological samples. Using solely optical methods it is now possible to obtain data that was previously thought to be limited to the realm of electron microscopy. The new quantitative data has revealed that the density of RyRs in clusters is lower than expected for dense packing. Clusters follow an irregular assembly pattern that is compatible with spontaneous self-assembly, but leave sizable gaps in clusters that will likely affect their calcium signalling. The high resolution of the DNA-PAINT data also revealed a previously undetected fraction of JPH2 in molecular proximity of RyRs and presents a super-resolution approach to in-situ biochemistry that will be useful to probe binding candidates in cells and tissues.

Chapter 5

Quantitative super-resolution imaging with qPAINT: *Implementation and object selection strategies*

In this Chapter a study was conducted using a high-grade DNA-origami sample that contained two distinctive structures. These two objects were frequented by imagers that had the same sequence. Recent updates to the PYME software allows geometrical analysis and object identification to be retained, whilst also being capable of measuring the time between detected events, required for quantitative DNA-PAINT analysis. I was able to ascertain an estimate for the multiplication factor for the number of docking sites, between two different origami structures. Further, I discuss the ability of quantitative PAINT to be used to count individual proteins and compare their relationship to co-localising proteins.

5.1. Introduction

Electron microscopy and crystallography are the methods of choice for interpreting macromolecular structures at high resolution. However, they incorporate complex sample preparations and in some cases require isolating protein complexes away from their natural environment[127]. Widefield optical microscopy techniques that use fluorescent markers are far less time consuming or invasive, but are limited to resolving structures that are ~250 nm apart due to the optical diffraction limit[1]. This distance is typically far greater than the size of protein complexes.

A relatively simple idea to image fluorescent markers one at a time, can be implemented on any widefield fluorescent setup, with suitable laser excitation, to overcome the diffraction limit of light. Since its inception over a decade ago, SMLM and pointillism approaches, such as PALM[5] and STORM[16] have seen little change in their fundamental approach. The samples are bombarded with high laser powers and in combination with special switching buffers, create a population inversion of the fluorescent markers. Here the probes stochastically recover from their dark state, resulting in only a subset ever being 'ON' at any one time. Each of these events have their central position precisely localised and plotted, constructing an image over time whose resolution is dependent on the number of photons detected and on the original labelling density achieved[92].

5.2. Quantitative imaging in general

The ability to reliably investigate complex protein compositions through quantitative fluorescence imaging is a highly desired tool for biologists. With the advent of super-resolution techniques the ability to visualise these structures, at tens of nanometres resolution, is already a reality, refer back to Chapter 3. Quantifying these measurements however can be fraught with complexity. Depending on the approach it is possible to both over and undercount the number of fluorescent markers. Overcounting occurs when fluorophores are localised more than once[128], creating the apparent effect of clustering. This is an issue for organic fluorophores, whose selection in dSTORM experiments, is primarily for

their reversible and bright switching nature. Photobleaching also plays a role in quantitative analysis[83] which is difficult to evaluate quantitatively, using SMLM approaches, as each individual fluorophore may have differing behaviours. Another possible contributor to undercounting is due to incomplete labelling of target sites and unknown stoichiometry of the fluorescent marker on the antibody[129].

5.3. DNA-PAINT & qPAINT concepts

A recent SMLM method, called DNA-PAINT[32], relies on the transient binding of small single strands of DNA to complimentary sequences. Target molecules, to be imaged, have a short, typically 9-11 base pairs, oligonucleotide sequence and act as docking stations for their complimentary counterparts. These ‘imager strands’, that typically have 9 base pairs complimentary to the docking strand, are conjugated to stable fluorescent probes and are introduced into an aqueous imaging buffer, Figure 5.1. These imagers are then free to seek out and transiently dock at the target sites, reporting their position. A steady diffusion of the imager strands ensures a near constant rate of hybridisation across the region of interest.

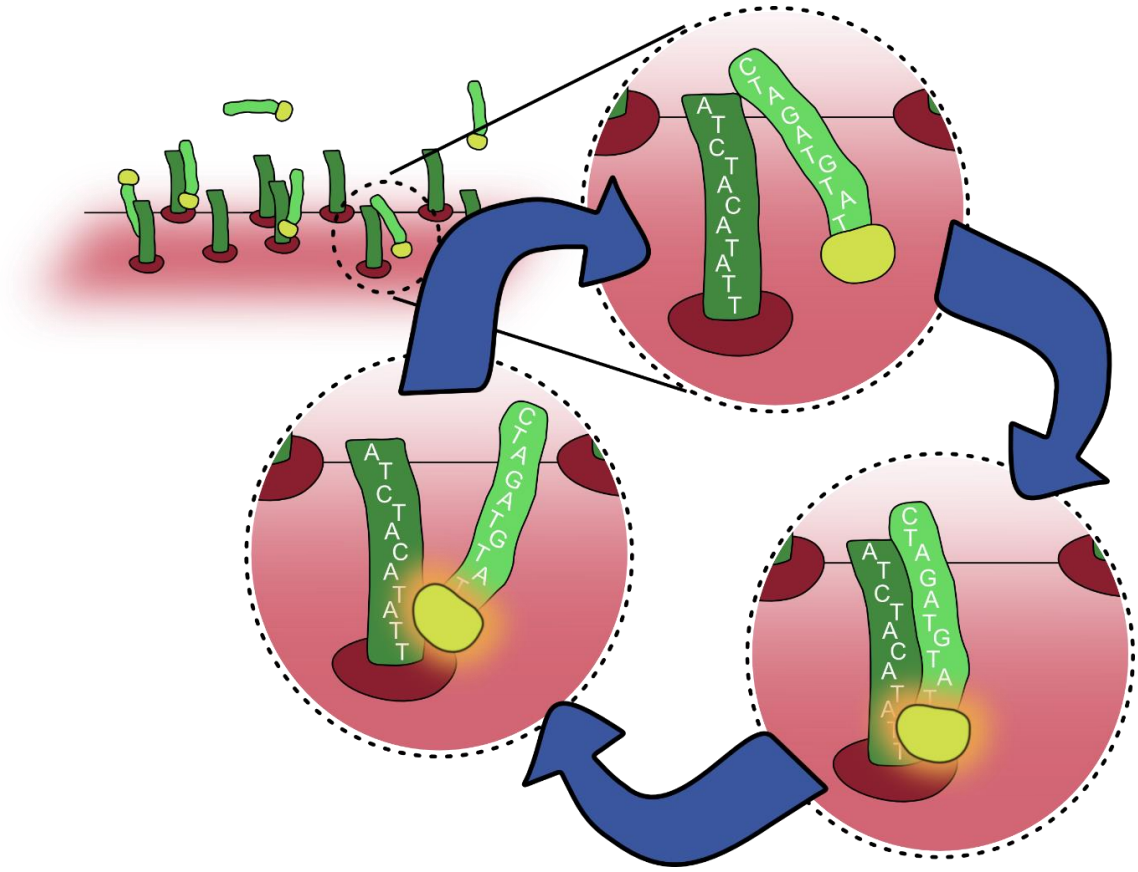

Figure 5.1. *Several immobilised docking strands are frequented by complimentary imager strands present in the bulk solution. The imagers are unrestricted in the solution and bind to these docking sites in transient interactions. Those imagers are then free to target other available docking sites in a stochastic manner.*

The mean duration of events is directly controlled by the number of complimentary base pairs between both docking and imager strands. Here the idea is not to exhaustively photobleach the fluorescent probes, with high laser power, but to find a steady state, where the maximum photon yield per hybridisation can be collected. In doing so, the predictable nature of oligo binding kinetics can be used to quantify the number of target molecules present through the analysis approach referred to as quantitative PAINT, qPAINT[90]. DNA-PAINT experiments are not limited by exhaustive bleaching of all fluorophores, as fresh imager strands are constantly replenished from the surrounding media. Looking at the time between events produces a relationship which is proportional to the number of docking sites. In its simplest form, with a fixed imager concentration,

a target area with two docking sites will have a frequency, in terms of the number of events, twice that of a target with only a single docking strand, Figure 5.2.

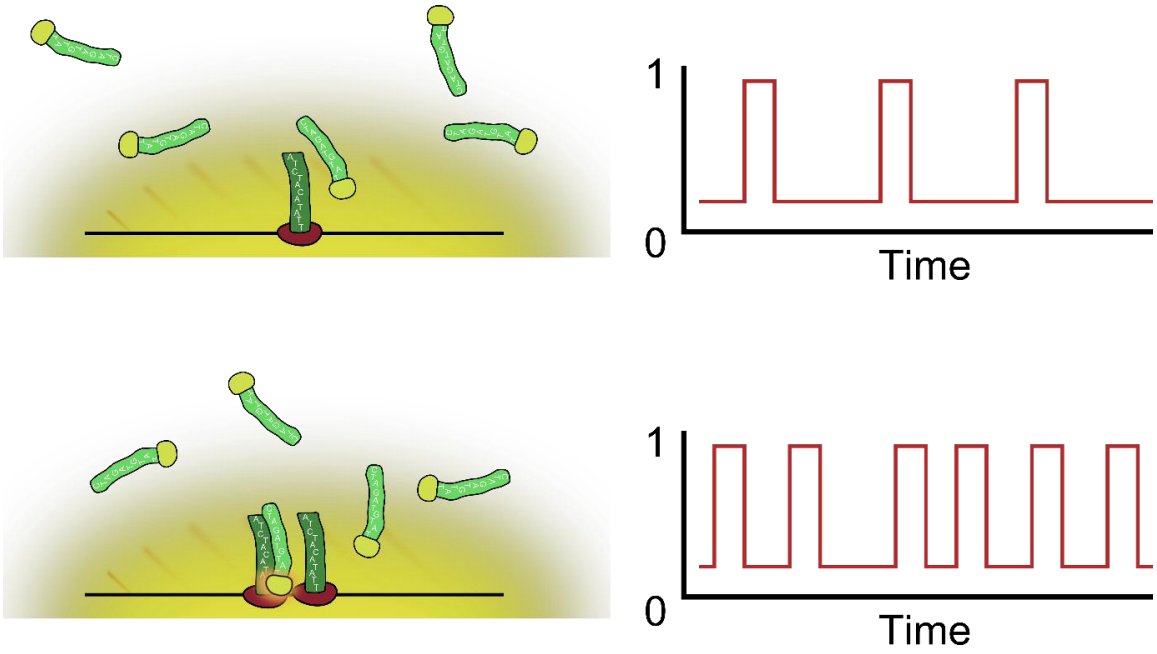

Figure 5.2. *The concept of qPAINT. Schematic diagram of docking sites and their complimentary imager strands* ***(left)*** *and the corresponding frequency of events* ***(right)****. A single docking site has sporadic interactions with imager strands dispersed in solution* ***(a)****. At the same imager concentration a target which has two docking stations will blink with a frequency of twice that of the single site in a given time* ***(b)****.*

Quantitative analysis of DNA-PAINT acquired data, qPAINT, takes advantage of the statistical predictability, inherent to the DNA hybridisation of each binding event. The mean dark time, τ_d, between detected events is proportional to the number of docking strands. By measuring a subset of structures with a known number of docking sites, such as artificial DNA-origami complexes or, based on size, targets suspected of being singular proteins, the qPAINT process can be calibrated.

Here two methods of obtaining qPAINT measurements are compared; directly from the fluorescence and by using event detection. The process was validated

with a DNA-origami test slide containing two distinguishable structures and establish the ratio of available docking sites between them both. Furthermore the idea of a qPAINT Index or qIndex, an uncalibrated qPAINT measurement is introduced and the approach applied to measuring the number of single protein receptors in a biological sample and are compared to the proportion of neighbouring co-localised proteins.

5.4. qPAINT in PYME

Information about the number of binding sites, or docking strands, can be ascertained from the temporal statistics of imager binding events. The dark time between events is linked to both the second order binding rate, k_{on}, of imager to docking strand and the imager concentration, c_i.

$$\tau_D = {}^{1}/_{k_{on}c_i}$$

(5.1)

Transient binding of imager to docking strands follow first order binding kinetics, so that the number of binding sites N_B is related to the measured dark time via, see equation 2.5. Temporal fluorescence dark time cumulative frequency plots were reconstructed from the event data and fitted with an equation of the form, equation 5.2

$$1 - exp^{\left({}^{-t}/_{\tau_d}\right)}$$

(5.2)

to estimate the mean dark time τ_d.

The qIndex values were calculated by scaling the inverse of the dark times by 100 (to obtain numbers of order unity) as:

$$qIndex = \frac{100}{\tau_d}$$

(5.3)

where all times are measured in units of acquired frames.

These qIndex values are proportional to the number of docking strands and therefore marker or receptor numbers, see also **Chapter 2.42**. *Quantification of DNA-PAINT data using qPAINT.*

5.5. Results

The GATTAquant DNA-PAINT HiRes sample slide consists of two independent structures. A trimer complex, whose point like objects are spaced at 40 nm intervals, centre to centre, in a linear arrangement are designed to test the optical capability of the imaging system. Larger, spherical objects which act as fiducial markers to aid drift correction are present at a lower density, Figure 5.3.

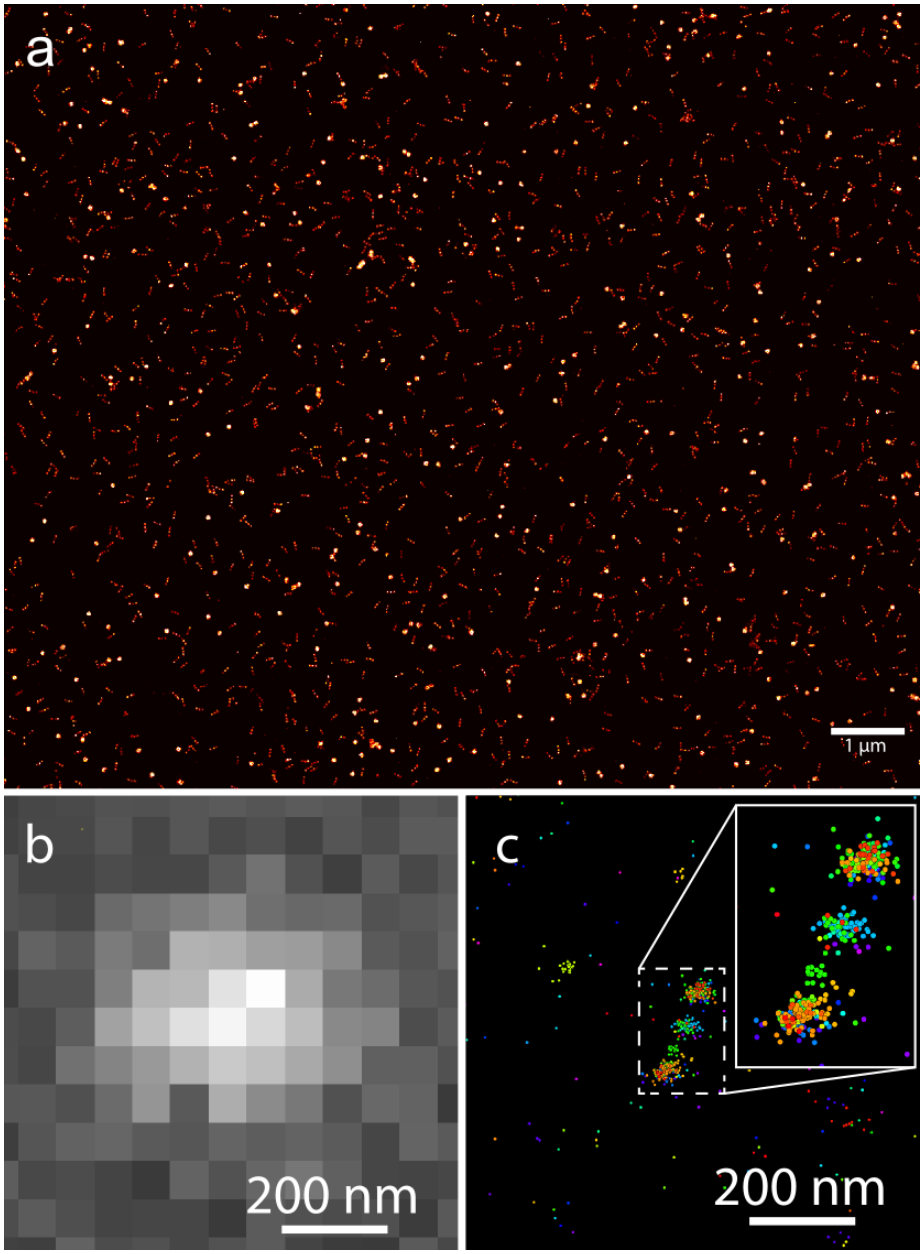

Figure 5.3. *A DNA-PAINT rendered image* ***(a)*** *of the GATTAquant HiRes test slide. The three core units, that make up the ~120 nm nanorulers are well resolved and were widely distributed throughout the sample. Large fiducial markers exist at a lower density amongst the sample. A widefield image* ***(b)*** *taken of one of the trimer nanorulers, clearly present the diffraction limited nature of the structure and demonstrates the inability to resolve it with conventional fluorescence microscopy. Localisation event clouds* ***(c)*** *of the same nanoruler, can already begin to resolve the gaps between each of the monomers, which are spaced at intervals of 40 nm (core to core).*

There are two approaches in determining the dark time values in PAINT experiments. One method is to use fluorescence thresholding and consists of looking at the intensity time traces collected during experiments, whilst this preferred procedure uses detected events information, Figure 5.4. Both techniques then plot cumulative frequency distributions to determine the mean dark time, τ_d. The advantage of using localised event data, means that any drift experienced by the sample can be corrected for prior to obtaining quantitative measurements. The issue of drift is more important in biological samples, where the proximity of docking sites cannot be easily controlled.

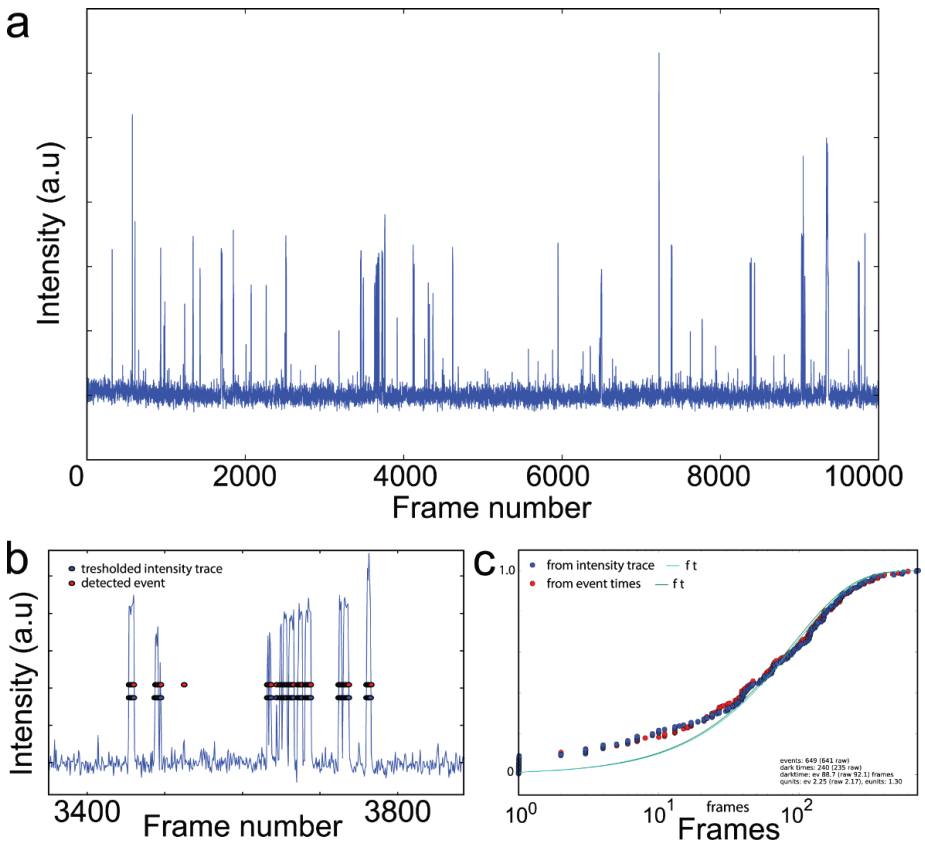

Figure 5.4. *A fluorescent intensity time trace, that examines a region of interest containing one of the trimer nanorulers* ***(a)****, obtained over the acquisition period of a typical DNA-PAINT experiment. Inspecting an area of ~400 frames, taken from this intensity time plot* ***(b)*** *exhibits the two approaches to event detection; intensity peaks that surpass a certain threshold or localisation based event detections. The latter is shown to detect an additional event, missed by the thresholding system. Cumulative frequency distribution plots of both processes show strong agreement with one another* ***(c)****. Thresholding* ***(blue circles)*** *and localised event detection* ***(red circles)****.*

Localised events obtained through DNA-PAINT experiments, using the GATTAquant HiRes sample slide, were rendered into super-resolution images as described above. These images were then analysed using the PYME software following a workflow as shown in Figure 5.5.

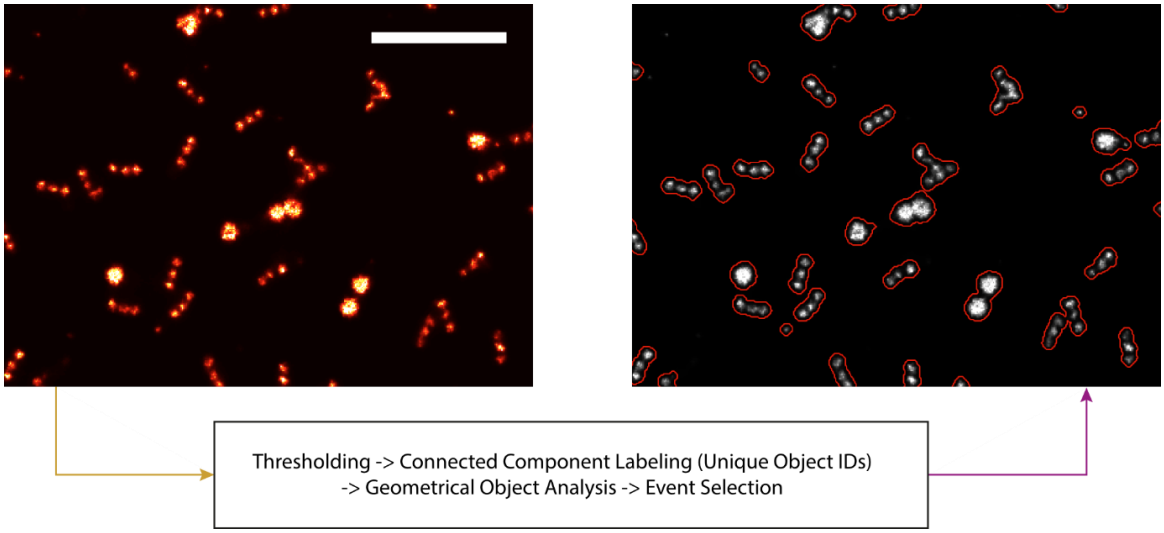

Figure 5.5. *PYME analysis workflow applied to a super-resolution image. A fractional threshold is applied that keeps 80% of the total labelling fraction, above background levels, and a 2D mask of the remaining objects created. Connected components were then assigned individual object identities and their geometrical measurements extracted. Events can now be selected based on a series of filters.* ***Scale bar:*** *500 nm.*

Once the workflow has been completed in the PYME recipe interface, the unique object categorisation can be used to select for specific filters, such as the area or the qIndex value, Figure 5.6. The filters operate simply by rejecting all events with values below a minimum threshold or above a maximum threshold that is chosen by the user. For example, a filter on the qIndex can be used to only select events with a qIndex between 2.0 and 3.4. The two distinguishable structures present in the GATTAquant slide were each isolated to examine their independent cumulative frequency distributions and calculate from these the mean darktime and subsequently qIndex values, see also **Chapter 2**.

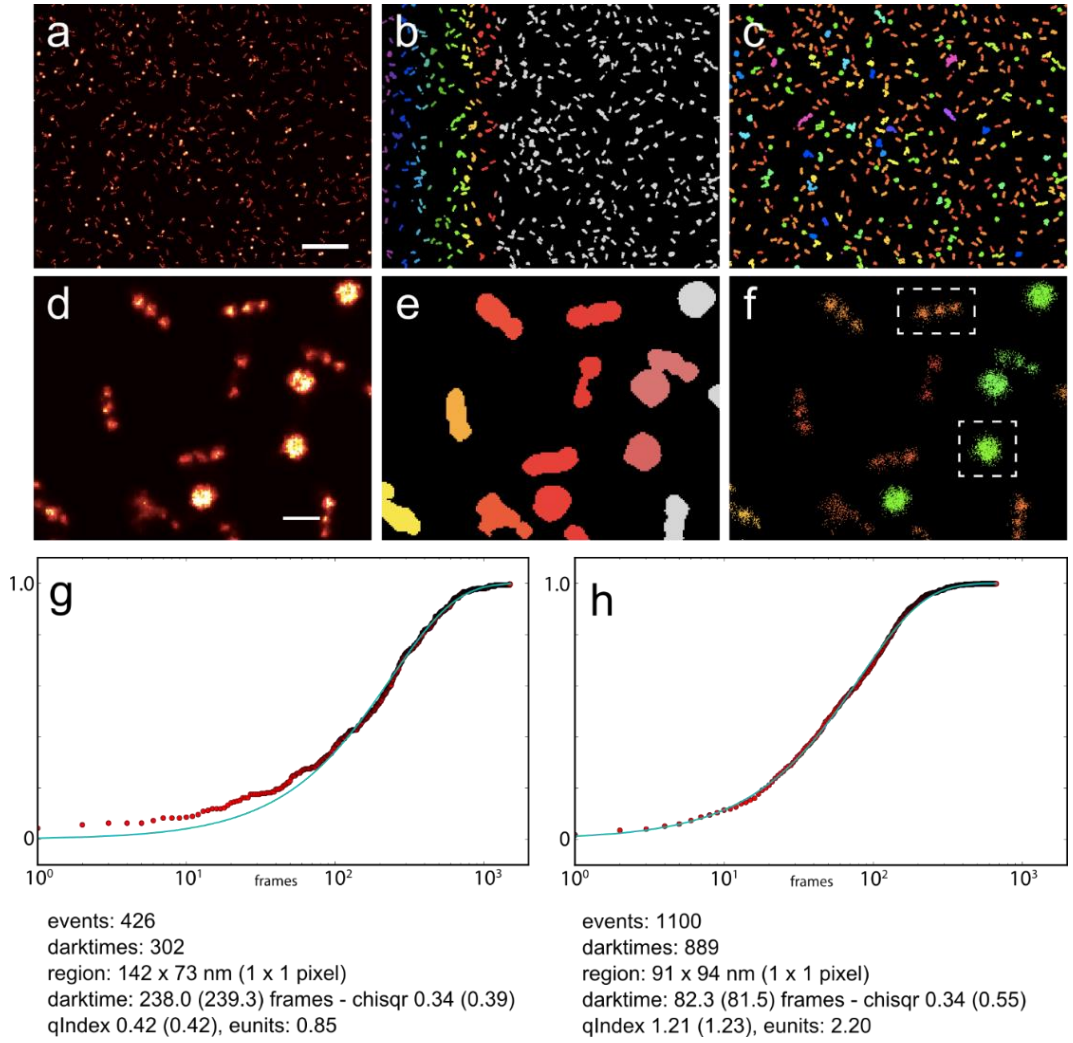

Figure 5.6. *An overview of an entire DNA-PAINT rendered image* ***(a)****, displaying both the nanorulers and fiducial markers. Using the unique object identities, post processing, enables the labels to be displayed via a colourmap* ***(b)****. These labels maintain the object's geometrical measurements and therefore allow them to be colour-coded based on size* ***(c)****. A small region of interest from* ***(a)****, that resolves the trimer nanonrulers and fiducial markers in its rendered image* ***(d)****, displays the label identities* ***(e)****, and subsequently filtered based on area* ***(f)****. Note that a nanoruler and fiducial marker which were close together have been assigned as being a single object* ***(e-f)****. Cumulative frequency distribution plots of the boxed region found in* ***(f)*** *for the trimer nanoruler and the fiducial marker* ***(g & h)*** *respectively. These plots yield the mean* τ_d*, and subsequently, it's inverse, the qIndex.* ***Scale bars: (a-c)*** *1 µm,* ***(d-f)*** *100 nm.*

Using the calculated qIndices and their corresponding geometrical measurements, maintained in the PYME analysis process, the minor to major axis ratio of all objects was plotted against their individual qIndex values. This produced two main point clouds that correspond to the two structures. The majority of outlier points, away from these clouds, were the result of poorly resolved, or overlapping structures. A qIndex value, in solutions containing a constant imager concentration, is proportional to the number of docking sites that imagers can bind to on that target. It therefore makes sense that the larger an object, the greater the qIndex value, Figure 5.7.

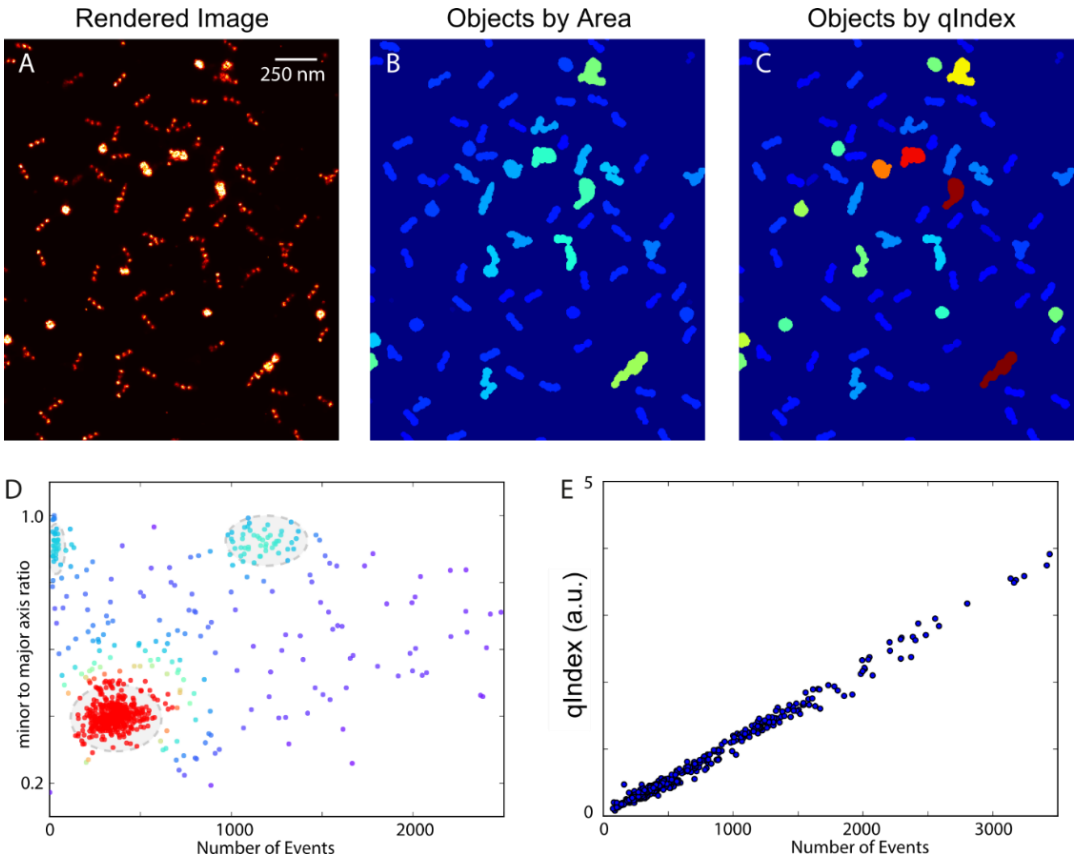

Figure 5.7. *A small region of a rendered super-resolution DNA-PAINT image of a GATTAquant HiRes 40R slide* ***(a)****, containing both trimer nanorulers and fiducial marker structures. Connected component labelling of these structures allows them to be filtered by area* ***(b)****, clearly revealing overlapping structures. Filtering for qIndex* ***(c)****, highlights the same overlapping structures, but importantly distinguishes between the nanoruler and fiducial markers. Plotting the minor to major axis measurements against qIndex* ***(d)****, for each uniquely identified object produces two dense event clouds. The large number of nanorulers are present in the red cloud, whilst a cluster of the more spherical, fiducial markers are in the second dense cloud. The qIndex, proportional to the number of binding sites, was, as expected linearly proportional to the number of detected events* ***(e)****.* ***Scale bar:*** *250 nm.*

The two structures present in the GATTAquant test slide had their events separated, based on area, to independently analyse both structures. Measurement of the qIndex values for both the trimer nanoruler and fiducial markers yielded histograms that, upon applying a Gaussian fit, produced peak

values of ~0.42 and ~1.21 respectively, Figure 5.8. The imager strand used in the GATTAquant slide was the same for both docking targets, meaning that one can infer proportionally how many more docking sites are present on the fiducial marker in comparison to the nanorule. From the qIndex calibration values, obtained for each, the ratio between them suggests ~2.9 times more docking sites are present on the fiducial bead.

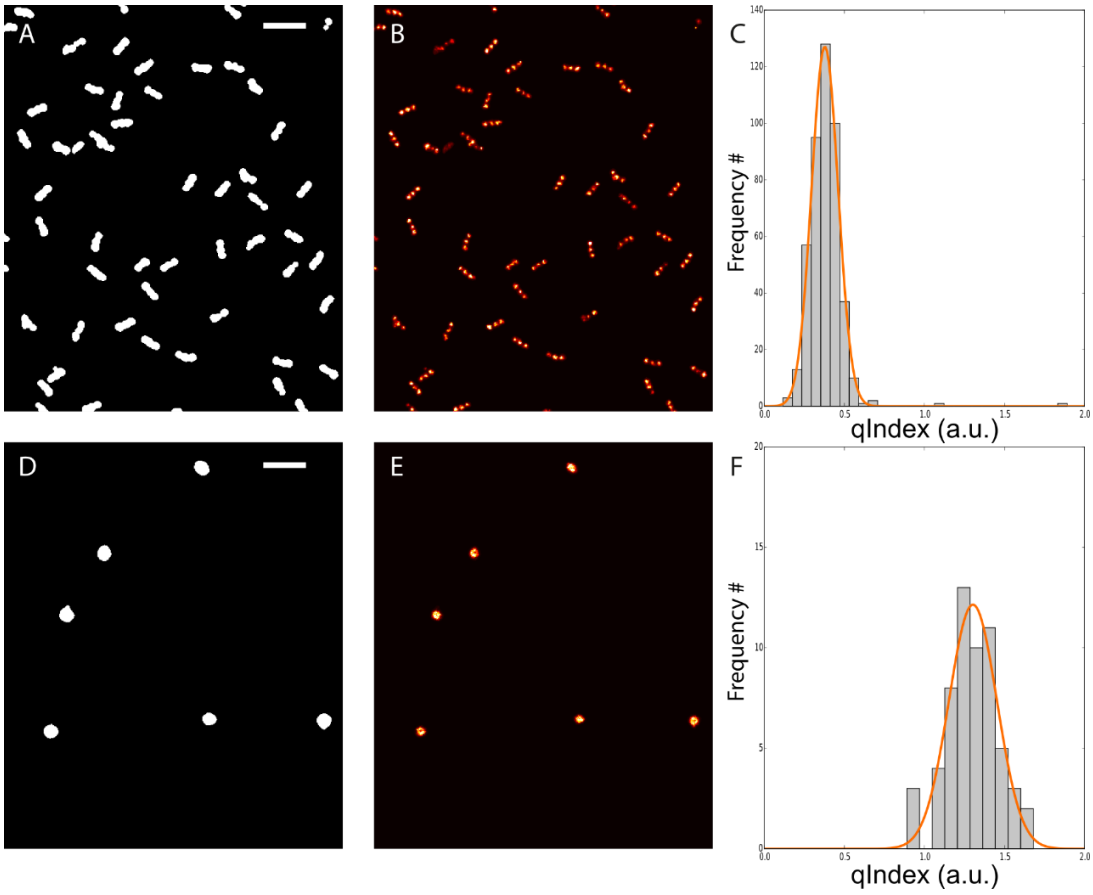

Figure 5.8. *The same region, displayed in* ***Figure 5.7****, filtered to display only the trimer structures* ***(a)****. Subsequently the DNA-PAINT events can be re-rendered to produce a super-resolution image containing only trimer nanorulers* ***(b)*** *and then measured in the same manner described previously. Measuring the qIndex of these trimers returned a single peak* ***(c)****, at ~0.42. Repeating the steps for the fiducial markers* ***(d-f)*** *produced a histogram peak at ~1.21. The ratio between these two values suggested an approximate 2.9 times as many docking sites are available on the fiducial marker as there are present on the nanoruler.* ***Scale bar:*** *250 nm.*

Estimations of protein ratios was possible with the PYME software. Exchange PAINT, explained further in Chapter 5, was used to image two co-localising proteins, the ryanodine receptors and junctophilin, in isolated cardiomyocytes. Selecting clusters with fewer than ~200 events and plotting a histogram of qIndex values exhibited a number of peaks that are characteristic of quantal behaviour. The mean qIndex of these small clusters, represent single receptor/protein and were used to calibrate larger clusters containing both target proteins, Figure 5.9, turning them into absolute number estimates.

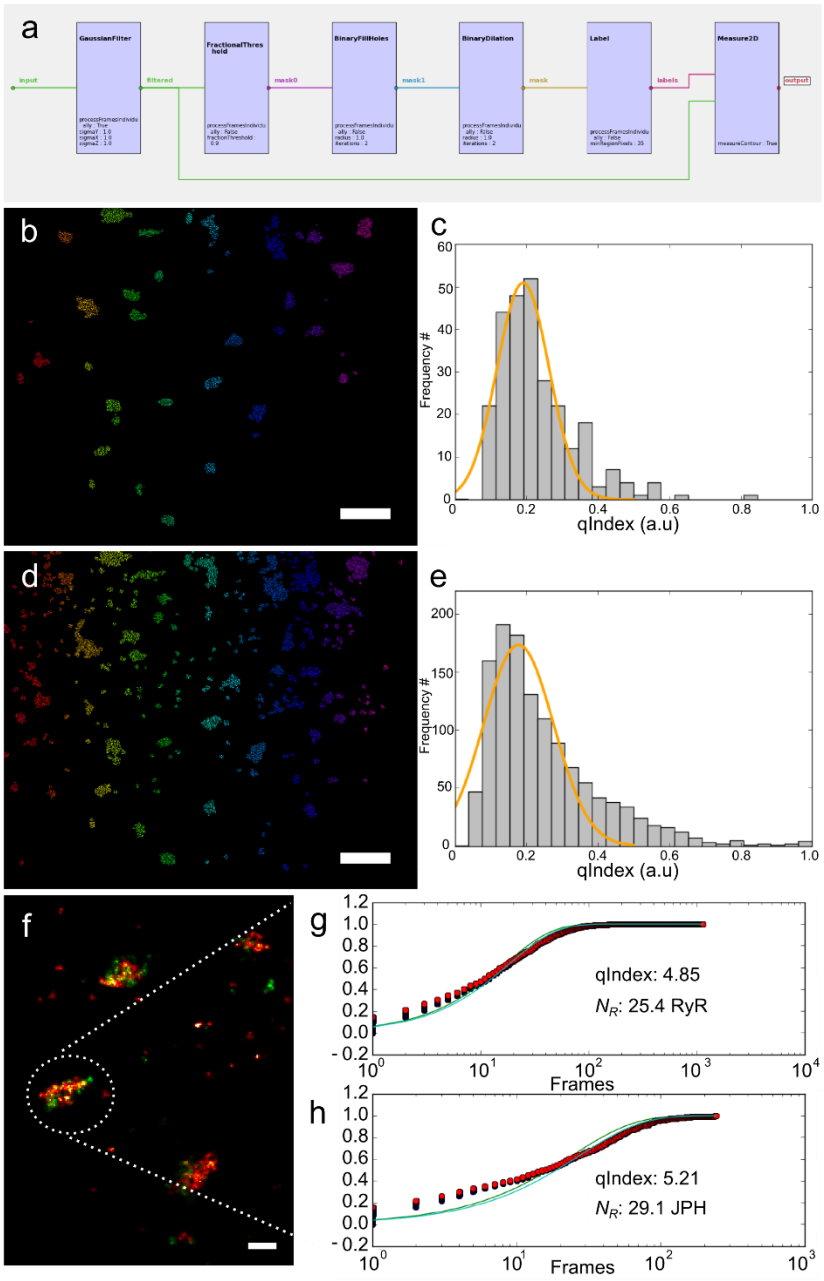

Figure 5.9. *An example of PYME's inbuilt analysis capability* ***(a)****. A series of modules, compiled together, make a simple recipe that can select, measure, and uniquely identify objects in rendered super-resolution images. The unique labels assigned to RyR* ***(b)*** *and JPH clusters* ***(d)*** *in an exchange PAINT experiment. Calibration of the qIndex value by evaluation of smaller objects for both RyR* ***(c)*** *and JPH* ***(e)*** *data. A rendered, composite image of RyR* ***(red)*** *and JPH* ***(green)*** *clusters* ***(f)*** *whose relationship can be probed to new levels using qPAINT. The cumulative frequency distribution plots from the cluster in* ***(f)*** *for both RyR* ***(g)*** *and JPH* ***(h)****.* ***Scale bars: (b&d)*** *1 µm and* ***(f)*** *250 nm.*

5.6. Conclusion

A powerful concept to quantify fluorescent marker binding sites from DNA-PAINT data has been introduced by Jungmann et al, called qPAINT[90]. Largely dependent on maintaining a constant imager concentration and first order binding kinetics, the dark time between events is related to the number of docking strands. The PYME software, with recent updates, is not only capable of maintaining geometrical object information, but also calculating dark times and subsequently qIndex values. This provides a powerful analytical tool.

The tests on the GATTAquant HiRes 40R slide concluded that the fiducial markers had approximately 2.9 times as many docking sites as the trimer structure, or ~9 times as many as each monomer making up the nanoruler.

Exchange PAINT experiments were conducted on isolated cardiomyocytes, to image the diffraction limited proteins RyR2 and JPH2. Following a suitable calibration measurement, from single receptors, an estimate for the number of receptors was possible. Further, due to functionalities in the PYME software, a direct ratio measurement between the two protein species was possible.

Chapter 6

dSTORM and DNA-PAINT in optically thick cardiac tissue

Single molecule light microscopy offers a near ten times resolution improvement on conventional fluorescence microscopy. dSTORM relies on the stochastic switching of organic probes, a process that can be influenced with the aid of special ‘switching buffers’. Further advancement has been made most recently with the application of oligonucleotides conjugated to conventional antibodies in the imaging process called DNA-PAINT microscopy. The highly accurate, reproducible nature of this method has led to 2-5 fold localisation error improvements in comparison to dSTORM in the optically thick samples that I generally use. Imaging under these conditions has introduced further

complexities to sample preparation, optical setups, and the process of analysing datasets. Tissue sections are required to be as thin as possible for pointillism approaches, without excessively causing damage to the sample, in order to improve the signal to noise ratio of events. In this Chapter the results of implementing the methodology, see **Chapter 2**, for simultaneously imaging in dual-colour the t-system and RyRs in cardiac muscle tissue using both dSTORM and DNA-PAINT is discussed.

6.1. Introduction

Both dSTORM and DNA-PAINT imaging presents several caveats to achieving, the now routinely expected, high quality super-resolution images. There are three key processes that determine the end result; sample preparation, optical setup and imaging and analysis. As with all imaging techniques sample preparation is paramount. It begins with preserving tissue in the most ideal manner and realising that protocols, which worked well for diffraction limited imaging, may not be suited for SMLM and could present previously unseen artifacts[130]. The fixation protocol used on tissue and the standard to which it is implemented is important to ensuring that artefacts are not created and that a high labelling density can be achieved. The now conventional, confocal microscopy approach is routinely used to image optically thick samples, due to its ability to reject out of focus fluorescence, and to achieve diffraction-limited resolutions. In order to attain super-resolution in tissue using pointillism approaches the tissue sections need to be as thin as possible without causing damage to the tissue. Sectioning, in general, results in damage to both the top and bottom surfaces of the tissue and therefore sections must be thicker than this mechanical damage, to avoid imaging artefacts. Typically, formaldehyde fixed muscle tissue can be sectioned reliably between ~10-15 µm thickness[87], providing at least 5 µm of undamaged usable tissue. Sections cut larger than this result in high backgrounds, aberrations, and lower labelling densities, resulting in poor final image resolution.

Beam angle, laser power and camera speed all play a role in determining the level of obtainable resolution. The use of an inclined illumination angle of the laser, as it travels through the sample, reduces the excitation volume and helps

to reduce out-of-focus fluorescence. Determining the correct amount of power to apply to the sample is largely dependent on the fluorescent probe used and should be optimised for each new dye. Higher powers may result in increased levels of detected photons but is often accompanied by a fine trade-off between the total number of events that occur and over what period of time. For DNA-PAINT laser intensity choices are guided by different considerations; here photoswitching is not the goal, rather high photon fluxes during binding while the time to photobleaching should be longer than the mean binding time of imagers. By adjusting the beam angle, to sit slightly outside of TIRF, into a highly inclined and laminated optical sheet (HILO) position[10], enables focussing past the surface and further into the sample. At this angle, signal to background is still extremely good and laser power can be controlled to avoid photobleaching, enabling the use of DNA-PAINT on tissue sections. Exchange-PAINT[32] enables the possibility to image multiple targets, one at a time, using the same fluorescent dye, removing the risk of chromatic aberrations. However, the technique requires several washes with clean buffer and can disturb the sample. Additionally, the diffusional exchange of imager strands is slow in biological tissue sections, which are optically thick. Our approach, termed Quencher-Exchange-PAINT[131], achieves the reduction of unwanted single-stranded imager concentrations to negligible levels through the use of oligonucleotides that inhibit the imager from binding to its target docking strand. A small volume of quencher can be introduced to the bulk volume of the sample, and gently mixed, leading to a rapid decline in available imager to docking strand interactions. This facilitates the ability to then introduce the next complementary imager sequence for the new target and is highly effective, Figure 6.1.

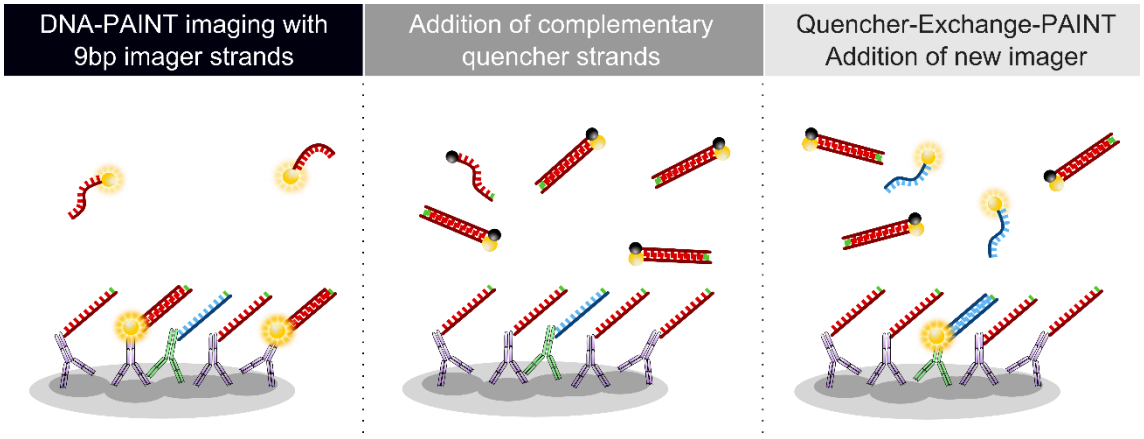

Figure 6.1. *Two different targets of interest are labelled with orthogonal oligonucleotide sequences. Conventional DNA-PAINT is conducted on the first target as normal. A complementary sequence to the original imager strand, called a quencher strand, is added at a concentration >10x the imager. Once all imager strands are quenched the complementary imager for the secondary target can be introduced and imaged as normal.*

Provided here are the results from imaging cardiac tissue using both dual colour dSTORM and Quencher-Exchange-PAINT methodologies explained previously in **Chapter 2**. The processes used here are tailored towards a combination of commercially available fluorescent probes; Alexa Fluor 680 and Alexa Fluor 750 (A680/A750) for dSTORM, and ATTO655 for DNA-PAINT. Our group have a particular interest in calcium release within the heart and so the technique was applied to image both the RyRs in rat ventricular tissue alongside the t-system network. The improvements made when implementing the methods described in this thesis are visually displayed and the reasons why they are instigated are discussed.

6.2. Representative results & discussion

Single colour dSTORM offers a near ten-fold improvement in lateral resolution compared to confocal imaging. Accomplishing the same optical improvement, whilst simultaneously imaging more than one colour in dSTORM is difficult. Challenges often arise due to the different spectral behaviours exhibited from each fluorescent probe and their specific requirement to achieve optimum blinking conditions. The emission spectra need to be sufficiently different to be

ratiometrically separable, (See Figure 2.18). However, if this separation is too far, the chromatic aberrations between the dyes may require further additional optics. These considerations results in the investigator often needing to make a compromise for one dye in order to achieve dual-colour.

The combination of the dyes, A680 and A750, require a low 5-10 mM MEA concentration, in order to facilitate the continued switching of the longer A750 dye. A750 has a low survivability in high concentrations of MEA, as reported elsewhere[29], whilst A680 is robust enough to exhibit suitable switching properties across a range of MEA concentrations.

TIRF provides excellent contrast for targets very close to the coverslip and works very well for flat samples or surface membrane targets with DNA-PAINT. However, the technique is problematic in dSTORM since it does not induce dark states efficiently in regions above the coverslip. Instead dSTORM is conducted with the beam at an inclined angle, shallower than HILO microscopy[10], producing a sheet of light around the chosen focal plane and reducing general out of focus structures, Figure 6.2.

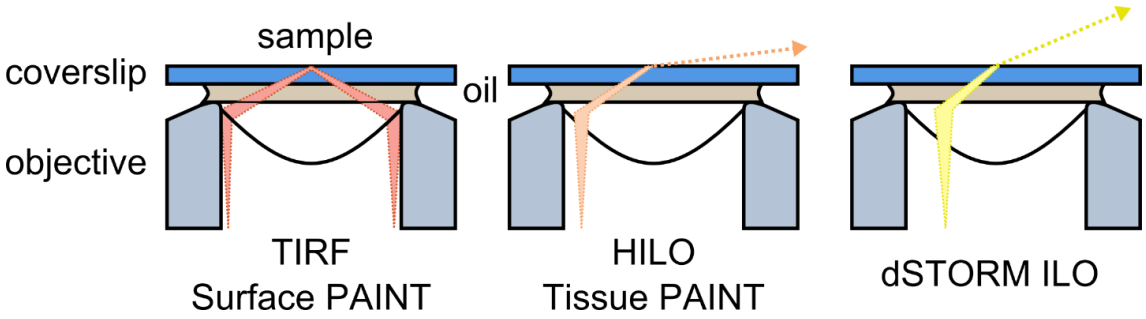

Figure 6.2. *The path of the laser as it meets the sample coverslip. With the beam angle in TIRF, a rapidly decaying evanescent wave enables the imaging of samples attached to the coverslip surface. Ideal for relatively flat samples, DNA-PAINT achieves ultra-resolution by exciting hybridised imager strands near the surface only. Fractionally adjusting the beam angle, moves the laser out of TIRF and into HILO. In this position, the beam is capable of exciting imager strands further into the sample. Signal to background drops marginally, in comparison to TIRF imaging* ***(see Figure 6.3)****. As the beam is moved, so that it exits the sample at an approximate 45° angle, it can induce photoswitching efficiently in to the sample when using a suitable switching mountant.*

For DNA-PAINT this slight adjustment of the beam, to be just outside of TIRF, facilitates imaging in thicker samples away from the coverslip, e.g. cardiac myocytes or tissue, whilst keeping out of focus contributions from imagers low, Figure 6.3.

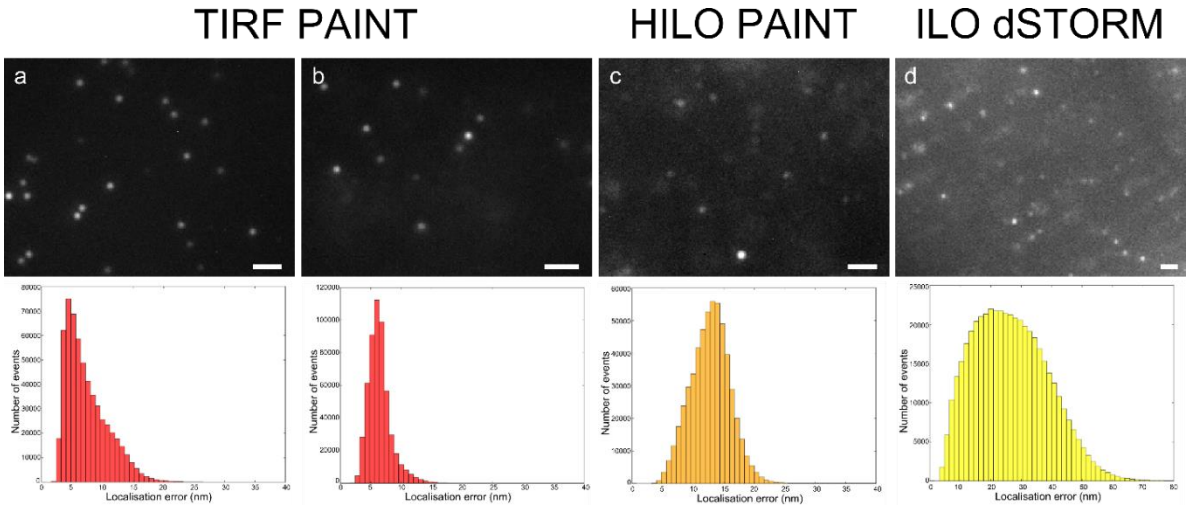

Figure 6.3. *Raw image frames taken during series acquisition* ***(top)*** *and their respective final localisation precision histograms* ***(bottom)****. TIRF DNA-PAINT experiments with cultured COS-7 cells* ***(a)*** *and surface attached cardiomyocytes* ***(b)****. The localisation error peaks at approximately 5 nm when imaging in TIRF. In HILO DNA-PAINT the signal to background is marginally deteriorated, in comparison to TIRF, and results in a shifted localisation precision peak. Dual-colour dSTORM, performed in ILO, has a larger background signal and contributes to the poorer localisation precision.* ***Scale bar:*** *1 µm.*

The nature of DNA-PAINT facilitates the ability to maintain a near constant rate of detected events, Figure 6.4. It enables the majority of localisations to be high quality events, with significant signal to background improvement upon dSTORM data. This can be attributed to a few key aspects; the steepness of the laser beam angle, reducing background fluorescence; the duration of each hybridisation, allowing for the collection of a greater number of photons; and the ability to constrain the concentration of imager strand, reducing the probability of overlapping events. The controllable use of oligonucleotides means that the addition of special quencher sequences, see Appendix 2, can be used to strongly suppress primary target imagers before the introduction of an additional imager, to acquire a secondary target, in the process we term Quencher-Exchange-PAINT[131]. While washing can be used to remove imagers this can be difficult in tissue samples and other samples with reduced diffusion, where the addition of quencher sequences enables faster and more effective suppression of imagers.

This removes the need for splitting colours as the replacement imager can have the exact same dye, removing chromatic shifts. This process, although practically taking longer to conduct, has a further benefit that it can be repeated for as many targets as the user can label.

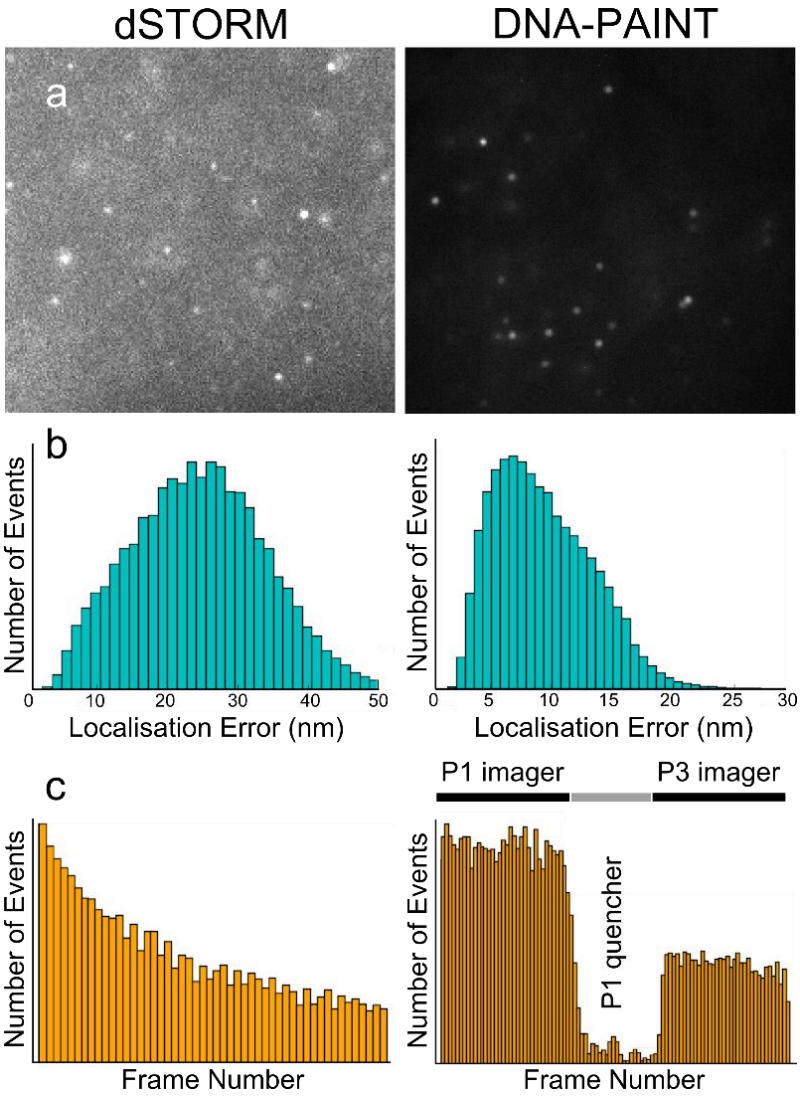

Figure 6.4. *Comparison of typical dSTORM* ***(left)*** *and DNA-PAINT* ***(right)*** *experiments. Raw frames collected during acquisition* ***(a)****, with the same colour scaling, shows the difference in signal to background achieved in both techniques. The improved contrast in DNA-PAINT, partially due to the extended camera integration time, leads to an improved localisation error* ***(b)*** *and thus final resolution. A characteristic dSTORM event rate shows the decaying nature of detected events as greater numbers of fluorophores become permanently photobleached* ***(c)****. DNA-PAINT offers prolonged, stable blink rates as target sites can be re-imaged for unlimited periods of time. The use of complimentary quencher to imager strands reduces previous imager fluorescence and events to background levels. The next complimentary imager sequence can then be added.*

With the use of custom-built Perspex imaging chambers it is possible to exchange solutions through their open tops, see Figure 2.1. This enables three independent immunohistochemistry labelling runs to be conducted on the same sample. For instance a tissue section could be labelled for widefield or confocal, dSTORM, and DNA-PAINT measurements, each of which being imaged in their own optimal media, Figure 6.5.

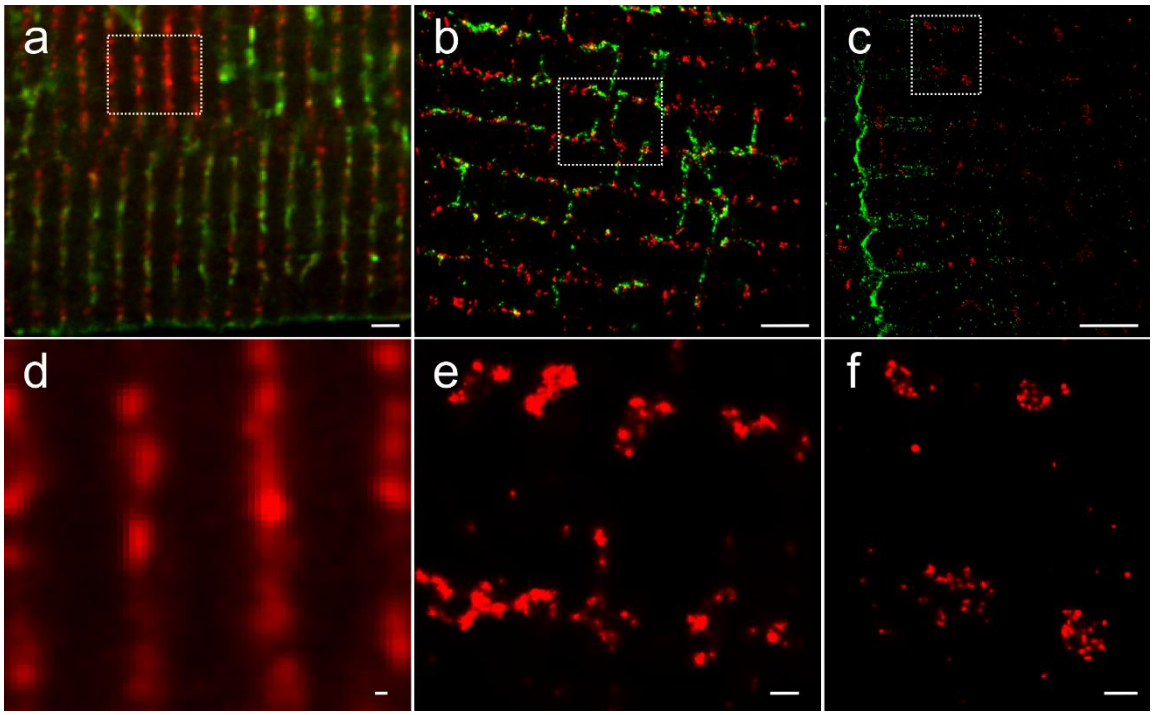

Figure 6.5. Optically thick, ~15 µm cardiac ventricular tissue measured with different optical techniques. A diffraction limited, confocal image **(a)** of the t-system **(green, Alexa Fluor 488)** and ryanodine receptors **(red, Alexa Fluor 594)** in ProlongGold. dSTORM super-resolution imaging **(b)** using the photoswitchable dyes Alexa Fluor 680 **(red, RyR)** and Alexa Fluor 750 **(green, T-system)** in 10 mM MEA 90% glycerol solution. Ultra-resolution imaging achieved through HILO-PAINT **(c)** and ATTO 655 imager strands at <1nM concentration in Buffer C. Comparison of the boxed regions in **a-c** display the differences observed across techniques for the RyRs. In diffraction limited, confocal imaging, the RyRs appear near continuous **(d)**. Using dSTORM **(e)** the RyRs are constructed of smaller clusters, that appear smooth, and vary in shape and size. At the ultra-resolution levels, achieved using HILO-PAINT, these clusters are visualised in greater detail, with clusters exhibiting punctate densities, indicative of individual markers being localised. **Scale bars: (a-c)** 2 µm, **(d-f)** 250 nm.

6.3. Conclusion

Single molecule light microscopy has been a useful tool in the biophysicists toolkit. The improved resolution allows for finer, more intricate biological structures to be resolved, giving insight into details that previously might have been missed. Sample preparation is more critical than ever, confocal microscopes can cope with tissue thicknesses approaching 50 µm but for SMLM this is simply not practical. Sections are required to be as thin as possible to reduce background fluorescence and therefore improve signal to noise ratios of single events. Individual super-resolution images take, on the order of, 20-30 minutes to acquire and over this time dSTORM mounting mediums can begin to become exhausted. This is characterised by the rapid decay, or “crash”, of event rates over a short period of time. The use of open-top chamber slides, Figure 2.1, offers the possibility to exchange these expired switching solutions for fresh medium.

DNA-PAINT imaging in TIRF has offered ultra-resolution when used to image biological samples with targets close to the coverslip, see **Chapter 3**, but the technique can also be geared towards imaging into samples. A simple, slight adjustment to the beam angle into HILO, Figure 6.2 & 6.3, enables focussing into the sample whilst maintaining strong signal to noise ratios. This method in conjunction with Quencher-Exchange-PAINT removes the unpredictable nature of photoswitching mediums required for dSTORM and allows multiple targets to be imaged, one after another, with no chromatic shift and provides superior resolution, Figure 6.5.

Concluding statements

The aim of this thesis was to optimise and compare two single molecule localisation microscopy techniques, dSTORM and DNA-PAINT, for imaging cardiac cells and tissue.

Approaches to remove oxygen, in order to improve fluorophore survivability during imaging, from glycerol based mounting buffers were examined and it was found a chemical depletion could prolong thiol activity. This produced a more reliable switching buffer that could be used immediately, over the course of several days, for dSTORM experiments. Only a minimal, ~10%, reduction in the number of detected photons was observed, as when compared to a fresh Cysteamine (MEA) buffer.

It was possible to directly compare the two pointillist approaches with the use of a set of custom oligonucleotides. These single strands of DNA enabled the transient binding of small 9-11 base pair sequences in order to conduct DNA-PAINT imaging, but also allowed for the permanent binding of a fixed imager strand. This fixed imager had a photoswitchable Alexa Fluor 647 probe pre-conjugated to it and was used to conduct dSTORM experiments. The DNA-PAINT approach achieved a localisation precision that was 3-4 times better than the dSTORM measurements conducted on the same target docking strand.

Resolution that was previously considered to be achievable only by electron microscopy was shown to be possible using optical light microscopy alone. I applied a refined DNA-PAINT approach to investigate RyR clusters and JPH2-RyR co-clusters in isolated cardiomyocytes. The images taken revealed punctate labelling, which I confirmed to be single RyRs. With the use of qPAINT I could apply a calibration multiplication to qIndex values, obtained for clusters of RyR, in order to determine the number of individual RyR present. Further, I was able to quantify the relationship between the RyRs and the inhibitory protein JPH2, whose stoichiometry I found to vary cluster to cluster.

qPAINT measurements were obtained using the PYME software package, which enables geometrical information and object identities to be retained whilst calculating qIndex values, and is a powerful analytical tool. I was able to obtain calibration qIndex values for two distinguishable DNA-origami structures and determine an estimate for the proportional difference exhibited between them of the number of available docking sites (~2.9).

By adjusting the laser beam into a HILO position and by implementing our method of Quencher-Exchange-PAINT I was able to conduct DNA-PAINT experiments in optically thick cardiac tissue samples. This approach alleviates many of the complexities associated with dual-colour dSTORM, including fluorophore selection, imaging buffer and chromatic aberration. Whilst I have only shown imaging of two targets of interest it would be feasible, although practically time-consuming, to image as many targets as one has different species of specific primary antibody.

DNA-PAINT is an incredibly powerful fluorescent microscopy super-resolution approach and this thesis has expanded upon the strong capabilities the method possesses.

References

1. Abbe E. Beiträge zur Theorie des Mikroskops und der mikroskopischen Wahrnehmung. *Arch Mikrosk Anat*. 1873;9:413-468.
2. Pawley JB. Fundamental Limits in Confocal Microscopy. In: *New York: Springer US*. New York: Springer US; 2006:20-42.
3. Binnig G, Rohrer H. Scanning tunneling microscopy - from birth to adolescence. *Rev Mod Phys*. 1987;59:615.
4. Zhou W, Wang Z. Scanning Microscopy for Nanotechnology and. In: *New York: Springer US*. New York: Springer US; 2006.
5. Betzig E, Patterson GH, Sougrat R, et al. Imaging intracellular fluorescent proteins at nanometer resolution. *Science*. 2006;313(5793):1642-1645. doi:10.1126/science.1127344.
6. Minsky M. Memoir on Inventing the Confocal Scanning Microscope. *J Scanning Microsc*. 1988;10:128-138.
7. Huff J. The Airyscan detector from ZEISS : confocal imaging with improved signal-to-noise ratio and super-resolution. *Nat Methods*. 2015;12(12):i-ii. doi:10.1038/nmeth.f.388.
8. Sheppard CJR, Mehta SB, Heintzmann R. Superresolution by image scanning microscopy using pixel reassignment. *Opt Lett*. 2013;38(15):2889-2892.
9. Axelrod D. Cell-Substrate Contacts Illuminated by Total Internal Reflection Fluorescence. *J Cell Biol*. 1981;89(9):141-145.
10. Tokunaga M, Imamoto N, Sakata-sogawa K. Highly inclined thin illumination enables clear single-molecule imaging in cells. *Nat Methods*. 2008;5(2):159-161. doi:10.1038/NMETH.1171.
11. Leung BO, Chou KC. Review of Super- Resolution Fluorescence Microscopy for Biology. *Appl Spectrosc*. 2011;65(9):967-980. doi:10.1366/11-06398.
12. Gustafsson MGL. Surpassing the lateral resolution limit by a factor of two using structured illumination microscopy. *J Microsc*. 2000;198(2):82-87.
13. Hein B, Willig KI, Hell SW. Stimulated emission depletion (STED) nanoscopy of a fluorescent protein-labeled organelle inside a living cell.

PNAS. 2008;105(38):14271–14276.

14. Hell SW, Wichmann J. Breaking the diffraction resolution limit by stimulated emission : stimulated-emission-depletion fluorescence microscopy. *Opt Lett*. 1994;19(11):780-782.
15. Hess ST, Girirajan TPK, Mason MD. Ultra-High Resolution Imaging by Fluorescence Photoactivation Localization Microscopy. *Biophys J*. 2006;91(11):4258-4272. doi:10.1529/biophysj.106.091116.
16. Rust MJ, Bates M, Zhuang XW. Sub-diffraction-limit imaging by stochastic optical reconstruction microscopy (STORM). *Nat Methods*. 2006;3(10):793-795. doi:Doi 10.1038/Nmeth929.
17. Bates M, Jones SA, Zhuang X. Stochastic Optical Reconstruction Microscopy (STORM): A Method for Superresolution Fluorescence Imaging. *Cold Spring Harb Protoc*. 2013;6:498-521. doi:10.1101/pdb.top075143.
18. Toomre D, Bewersdorf J. A new wave of cellular imaging. *Annu Rev Cell Dev Biol*. 2010;26:285-314. doi:10.1146/annurev-cellbio-100109-104048.
19. Fernández-suárez M, Ting AY. Fluorescent probes for super- resolution imaging in living cells. *Nat Rev Mol Cell Biol*. 2008;9(12):929-943. doi:10.1038/nrm2531.
20. Beljonne D, Shuai Z, Pourtois G, Bredas JL. Spin - Orbit Coupling and Intersystem Crossing in Conjugated Polymers: A Configuration Interaction Description. *J Phys Chem A*. 2001;105(15):3899-3907.
21. Henriques R, Griffiths C, Rego EH, Mhlanga MM. Review Review PALM and STORM: Unlocking Live-Cell Super-Resolution PALM and STORM: Unlocking Live-Cell Super-Resolution. *Biopolymers*. 2011;95(5):322-331. doi:10.1002/bip.21586.
22. Yuster P, Weissman S. Effects of Perturbations on Phosphorescence: Luminescence of Metal Organic Complexes. *J Chem Phys*. 1949;17(12):1182-1188.
23. Kasha BYM. Characterization of electronic tran-sitions in complex molecules. *Discuss Faraday Soc*. 1950;9:14-19.
24. Bates M, Huang B, Dempsey GT, Zhuang X. Multicolor super-resolution imaging with photo-switchable fluorescent probes. *Science (80-)*. 2007;317(September):1749-1753. doi:10.1126/science.1146598.

25. Heilemann M, Linde S Van De, Mukherjee A, Sauer M. Super-Resolution Imaging with Small Organic Fluorophores. *Angew Chemie Int Ed*. 2009;48(37):6903-6908. doi:10.1002/anie.200902073.
26. Linde S Van De, Krsti I, Prisner T, Sauer M. Photoinduced formation of reversible dye radicals and their impact on super-resolution imaging. *Photochem Photobiol Sci*. 2011;10(4):499-506. doi:10.1039/c0pp00317d.
27. Vogelsang J, Kasper R, Steinhauer C, et al. A Reducing and Oxidizing System Minimizes Photobleaching and Blinking of Fluorescent Dyes. *Angew Chemie Int Ed*. 2008;47(29):5465-5469. doi:10.1002/anie.200801518.
28. Hell S, Reiner G, Cremer C, Stelzer EHK. Aberrations in confocal fluorescence microscopy induced by mismatches in refractive index. *J Microsc*. 1992;169(3):391-405.
29. Dempsey GT, Vaughan JC, Chen KH, Bates M, Zhuang X. Evaluation of fluorophores for optimal performance in localization-based super-resolution imaging. *Nat Methods*. 2011;8(12):1027-1036. doi:10.1038/nmeth.1768.
30. Vogelsang J, Cordes T, Forthmann C, Steinhauer C, Tinnefeld P. Controlling the fluorescence of ordinary oxazine dyes for single-molecule switching and superresolution microscopy. *PNAS*. 2009;106(20):8107-8112.
31. Jungmann R, Steinhauer C, Scheible M, Kuzyk A, Tinnefeld P, Simmel FC. Single-Molecule Kinetics and Super-Resolution Microscopy by Fluorescence Imaging of Transient Binding on DNA Origami. *Nanoletters*. 2010;10:4756-4761. doi:10.1021/nl103427w.
32. Jungmann R, Avendaño MS, Woehrstein JB, Dai M, Shih WM, Yin P. Multiplexed 3D cellular super-resolution imaging with DNA-PAINT and Exchange-PAINT. *Nat Methods*. 2014;11(3):313-318. doi:10.1038/nmeth.2835.
33. Lin R, Clowsley AH, Jayasinghe IDJ, Baddeley DB, Soeller C. Algorithmic corrections for localization microscopy with sCMOS cameras - characterisation of a computationally efficient localization approach. *Opt Express*. 2017;25(10):82-87.
34. Mortensen KI, Churchman LS, Spudich JA, Flyvbjerg H. Optimized

localization analysis for single-molecule tracking and super- resolution microscopy. *Nat Methods*. 2010;7(5):377-381. doi:10.1038/nmeth.1447.

35. Lamb GD. Excitation-contraction coupling in skeletal muscle: comparisons with cardiac muscle. *Clin Exp Pharmacol Physiol*. 2000;27(3):216-224.
36. Mcnutt NS, Fawcett DONW. The ultrastructure of the cat myocardium. *J Cell Biol*. 1969;42(1):46-67.
37. Lemieux H, Hoppel C. Mitochondria in the human heart. *J Bioenerg Biomembr*. 2009;41(2):99-106.
38. Maack C, Rourke BO. Excitation-contraction coupling and mitochondrial energetics. *Basic Res Cardiol*. 2007;102:369-392. doi:10.1007/s00395-007-0666-z.
39. Cheng H, Cannell M, Lederer W. Propagation of excitation-contraction coupling into ventricular myocytes. *Pflügers Arch*. 1994;428:415-417.
40. Jorgensen A, Broderick R, Somlyo A, Somlyo A. Two structurally distinct calcium storage sites in rat cardiac sarcoplasmic reticulum: an electron microprobe analysis study. *Circ Res*. 1988;63(6):1060-1069.
41. Takeshima H, Komazaki S, Nishi M, Iino M, Kangawa K. Junctophilins : A Novel Family of Junctional Membrane Complex Proteins. *Mol Cell*. 2000;6(1):11-22.
42. Beard N, Laver D, Dulhunty A. Calsequestrin and the calcium release channel of skeletal and cardiac muscle. *Prog Biophys Mol Biol*. 2004;85(1):33-69.
43. Fleuscher S, Inui M. Biochemistry and biophysics of excitation-contraction coupling. *Annu Rev Biophys Biophys Chem*. 1989;18:333-364.
44. Akin B, Hurley T, Chen Z, Jones L. The structural basis for phospholamban inhibition of the calcium pump in sarcoplasmic reticulum. *J Biol Chem*. 2013;288(42):30181-30191.
45. Pinnell P, Turner S, Howell S. Cardiac muscle physiology. *Crit Care Pain*. 2007;7(3):85-88.
46. DiFrancesco D. Pacemaker mechanisms in cardiac tissue. *Annu Rev Physiol*. 1993;55(1):455-472.
47. Atkinson A, Inada S, Li J, et al. Anatomical and molecular mapping of the left and right ventricular His-Purkinje conduction networks. *J Mol Cell*

Cardiol. 2011;51(5):689-701.

48. Ahrens-nicklas RC, Christini DJ. Anthropomorphizing the Mouse Cardiac Action Potential via a Novel Dynamic Clamp Method. *Biophysj*. 2009;97(10):2684-2692. doi:10.1016/j.bpj.2009.09.002.
49. Rohr S. Role of gap junctions in the propagation of the cardiac action potential. *Cardiovasc Res*. 2004;62(2):309-322.
50. Kimlicka L, Van Petegem F. The structural biology of ryanodine receptors. *Sci China Life Sci*. 2011;54(8):712-724.
51. Fabiato A. Time and calcium dependence of activation and inactivation of calcium-induced release of calcium from the sarcoplasmic reticulum of a skinned canine cardiac Purkinje cell. *J Gen Physiol*. 1985;85(2):247-289.
52. Franzini-Armstrong C, Protasi F. Ryanodine receptors of striated muscles: a complex channel capable of multiple interactions. *Physiol Rev*. 1997;77(3):699-729.
53. Berridge MJ, Lipp P, Bootman MD. The versatility and universality of calcium signalling. *Nat Rev Mol Cell Biol*. 2000;1(1):11-21. doi:10.1038/35036035.
54. MacLennan D, Kranias E. Phospholamban: A crucial regulator of cardiac contractility. *Nat Rev Mol Cell Biol*. 2003;4(7):566-577.
55. Ottolia M, Torres N, Bridge JH, Philipson KD, Goldhaber JI. Na/Ca exchange and contraction of the heart. *J Mol Cell Cardiol*. 2013;61:28-33.
56. Periasamy M, Kalyanasundaram A. SERCA pump isoforms: their role in calcium transport and disease. *Muscle Nerve*. 2007;35(4):430-442.
57. Szymborsha A, de Marco A, Daigle N, Cordes V., Briggs A, Ellenberg J. Nuclear pore scaffold structure analyzed by super-resolution microscopy and particle averaging. *Science (80-)*. 2013;341(6146):655-658.
58. Mikhaylova MB, Cloin M, Finan K, et al. Resolving bundled microtubules using anti-tubulin nanobodies. *Nat Commun*. 2015;6:7933.
59. Xu K, Zhong G, Zhuang X. Actin, spectrin, and associated proteins form a periodic cytoskeletal structure in axons. *Science (80-)*. 2013;339(6118):452-456.
60. Shim S., Xia C, Zhong G, et al. Super-resolution fluorescence imaging of organelles in live cells with photoswitchable membrane probes. *Proc Natl Acad Sci USA*. 2012;109(35):13978-13983.

61. Gambin, Y., N. Ariotti, K. A. McMahon, M. Bastiani, E. Sierecki, O. Kovtun, M. E. Polinkovsky, A. Magenau, Jung W, Okano S, Zhou Y, et al. Single-molecule analysis reveals self assembly and nanoscale segregation of two distinct cavin subcomplexes on caveolae. *Elife*. 2013;3:e01434.
62. Baddeley D, Jayasinghe I., Lam L, Rossberger S, Cannell M., Soeller C. Optical single-channel resolution imaging of the ryanodine receptor distribution in rat cardiac myocytes. *Proc Natl Acad Sci USA2*. 2009;106(52):22275-22280.
63. Heilemann M, Linde S Van De, Schüttpelz M, et al. Subdiffraction-Resolution Fluorescence Imaging with Conventional Fluorescent Probes. *Angew Chemie Int Ed*. 2008;47:6172-6176. doi:10.1002/anie.200802376.
64. Crossman DJ, Ruygrok PN, Hou Y., Soeller C. Next-generation endomyocardial biopsy: the potential of confocal and super-resolution microscopy. *Hear Fail Rev*. 2015;20(2):203-214.
65. Munro M, Jayasinghe ID, Wang Q, et al. unctophilin-2 in the nanoscale organisation and functional signalling of ryanodine receptor clusters in cardiomyocytes. *J Cell Sci*. 2016;129(23):4388-4398.
66. Walker M., Williams G., Kohl T, et al. Superresolution modeling of calcium release in the heart. *Biophys J*. 2014;107(12):3018-3029.
67. Walker M., Kohl T, Lehnart S., Greenstein J., Lederer W, Winslow R. On the Adjacency Matrix of RyR2 Cluster Structures. *PLOS Comput Biol*. 2015;11(11):e1004521.
68. Yan Z, Bai C, Yan J, et al. Structure of the rabbit ryanodine receptor RyR1 at near-atomic resolution. *Nature*. 2014;517(7532):50-55.
69. Peng W, Shen H, Wu J, et al. Structural basis for the gating mechanism of the type 2 ryanodine receptor RyR2. *Science (80-)*. 2016;354(6310):aah5324.
70. Allen D., Lamb G., Westerblad H. Impaired calcium release during fatigue. *J Appl Physiol*. 1985;104(1):296-305.
71. Cannell M., Kong C. Local control in cardiac E-C coupling. *J Mol Cell Cardiol*. 2012;52(2):298-303.
72. Manita S, Ross W. Synaptic activation and membrane potential changes modulate the frequency of spontaneous elementary Ca2+ release events

in the dendrites of pyramidal neurons. *J Neurosci*. 2009;29(24):7833-7845.

73. Cannell M., Soeller C. Numerical analysis of ryanodine receptor activation by L-type channel activity in the cardiac muscle diad. *Biophys J*. 1997;73(1):112-122.
74. Hou Y, Jayasinghe I, Crossman DJ, Baddeley D, Soeller C. Nanoscale analysis of ryanodine receptor clusters in dyadic couplings of rat cardiac myocytes. *J Mol Cell Cardiol*. 2015;80:45-55. doi:10.1016/j.yjmcc.2014.12.013.
75. Loesser K., Castellani L, Franzini-Armstrong C. Dispositions of Junctional Feet in Muscles of Invertebrates. *J Muscle Res Cell Motil*. 1992;13(2):161-173.
76. Asghari P, Scriven D., Sanatani S, Gandhi S., Campbell A., Moore E. Nonuniform and variable arrangements of ryanodine receptors within mammalian ventricular couplons. *Circ Res*. 2014;115(2):252-262.
77. Jayasinghe ID, Cannell MB, Soeller C. Organization of Ryanodine Receptors , Transverse Tubules , and Sodium-Calcium Exchanger in Rat Myocytes. *Biophys J*. 2009;97(10):2664-2673. doi:10.1016/j.bpj.2009.08.036.
78. Lai FA, Liu QY, Xu L, et al. Amphibian ryanodine receptor isoforms are related to those of mammalian skeletal or cardiac muscle. *Am J Physiol*. 1992;263(2 Pt 1):C365-72.
79. Soeller C, Crossman D, Gilbert R, Cannell MB. Analysis of ryanodine receptor clusters in rat and human cardiac myocytes. *Proc Natl Acad Sci U S A*. 2007;104(38):14958-14963.
80. Landstrom AP, Kellen CA, Dixit SS, et al. Junctophilin-2 Expression Silencing Causes Cardiocyte Hypertrophy and Abnormal Intracellular Calcium-Handling. *Circ Hear Fail*. 2011;4(2):214-223. doi:10.1161/circheartfailure.110.958694.
81. Ellman GL. A colorimetric method for determining low concentrations of mercaptans. *Arch Biochem Biophys*. 1958;74(2):443-450.
82. Riddles PW, Blakeley R, Zerner B. Reassessment of Ellman's reagent. *Methods Enzym*. 1983;91:49-60.
83. Nieuwenhuizen RPJ, Lidke KA, Bates M, et al. Measuring image

resolution in optical nanoscopy. *Nat Methods*. 2013;10(6):557-562. doi:10.1038/nmeth.2448.

84. Mcgorty R, Kamiyama D, Huang B. Active microscope stabilization in three dimensions using image correlation. *Opt Nanoscopy*. 2013;2(3):1-7.
85. Baddeley D, Crossman D, Rossberger S, et al. 4D Super-Resolution Microscopy with Conventional Fluorophores and Single Wavelength Excitation in Optically Thick Cells and Tissues. *PLoS One*. 2011;6(5):1-10. doi:10.1371/journal.pone.0020645.
86. Sage D, Kirshner H, Pengo T, et al. Quantitative evaluation of software packages for single-molecule localization microscopy. *Nat Methods*. 2015;12(8):717-724. doi:10.1038/nmeth.3442.
87. Hou Y, Crossman DJ, Rajagopal V, Baddeley D, Jayasinghe I, Soeller C. Super-resolution fluorescence imaging to study cardiac biophysics : alpha - actinin distribution and Z-disk topologies in optically thick cardiac tissue slices. *Prog Biophys Mol Biol*. 2014;115(2-3):328-339. doi:10.1016/j.pbiomolbio.2014.07.003.
88. Baddeley D, Cannell MB, Soeller C. Visualization of Localization Microscopy Data. *Microsc Microanal*. 2010;16:64-72.
89. Jayasinghe ID, Clowsley AH, Munro M, Hou Y, Crossman DJ, Soeller C. Revealing t-tubules in striated muscle with new optical super- resolution microscopy techniques. *Eur J Transl Myol*. 2015;25(1):15-26.
90. Jungmann R, Avendaño MS, Dai M, et al. Quantitative super-resolution imaging with qPAINT. *Nat Methods*. 2016;13(5):439-442. doi:10.1038/nmeth.3804.
91. Jayasinghe I., Baddeley D, Kong C., Wehrens XH., Cannell M., Soeller C. Nanoscale organization of junctophilin-2 and ryanodine receptors within peripheral couplings of rat ventricular cardiomyocytes. *Biophys J*. 2012;102(5):L19-21.
92. Thompson RE, Larson DR, Webb WW. Precise Nanometer Localization Analysis for Individual Fluorescent Probes. *Biophys J*. 2002;82:2775-2783.
93. Linde S Van De, Lehmann J, Sauer M, Doose S. Methylene Blue- and Thiol-Based Oxygen Depletion for Super- Resolution Imaging. *Anal Chem*. 2013;85(6):3393-3400. doi:10.1021/ac400035k.

94. Baddeley D, Cannell MB, Soeller C. Three-Dimensional Sub-100 nm Super-Resolution Imaging of Biological Samples Using a Phase Ramp in the Objective Pupil. *Nano Res*. 2011;4(6):589-598. doi:10.1007/s12274-011-0115-z.
95. Hell S., Reiner G, Cremer C, Stelzer EH. Aberrations in confocal fluorescence microscopy induced by mismatches in refractive index. *J Microsc*. 1993;169(3):391-405.
96. Jacobsen H, Hanninen P, Soini E, Hell S. Refractiveindex-induced aberrations in two-photon confocal fluorescence microscopy. *J Microsc*. 1994;176(3):226-230.
97. Steinhauer C, Forthmann C, Vogelsang J, Tinnefeld P. Superresolution Microscopy on the Basis of Engineered Dark States. *J Am Chem Soc*. 2008;130:16840-16841.
98. Manley S, Olivier N, Keller D, Go P. Resolution Doubling in 3D-STORM Imaging through Improved Buffers. *PLoS One*. 2013;8(7):1-9. doi:10.1371/journal.pone.0069004.
99. Vaughan JC, Dempsey GT, Sun E, Zhuang X. Phosphine Quenching of Cyanine Dyes as a Versatile Tool for Fluorescence Microscopy. *J Am Chem Soc*. 2013;135(4):1197-1200. doi:10.1021/ja3105279.
100. Vaughan JC, Jia S, Zhuang X. Ultrabright photoactivatable fluorophores created by reductive caging. *Nat Methods*. 2012;9(12):1181-1184. doi:10.1038/NMETH.2214.
101. Olivier N, Keller D, Rajan VS, Pierre G, Manley S. Simple buffers for 3D STORM microscopy. *Biomed Opt Express*. 2013;4(6):885-899. doi:10.1364/BOE.4.000885.
102. Vogelsang J, Cordes T, Tinnefeld P. Single-molecule photophysics of oxazines on DNA and its application in a FRET switch. *Photochem Photobiol Sci*. 2009;8(4):486-496.
103. Ellman GL. Tissue sulfhydryl groups. *Arch Biochem Biophys*. 1959;82(1):70-77.
104. Weitzman PD. A critical reexamination of the reaction of sulfite with DTNB. *Anal Biochem*. 1975;64:628-630.
105. Chozinski TJ, Gagnon LA, Vaughan JC. Twinkle , twinkle little star : Photoswitchable fluorophores for super-resolution imaging. *FEBS Lett*.

2014;588(19):3603-3612. doi:10.1016/j.febslet.2014.06.043.
106. Schaue D, Ratikan JA, Iwamoto KS. Cellular Autofluorescence following Ionizing Radiation. *PLoS One*. 2012;7(2):1-7. doi:10.1371/journal.pone.0032062.
107. Aubin JE. Autofluorescence of Viable Cultured Mammalian Cells. *J Histochem Cytochem*. 1979;27(1):36-43.
108. Nahidiazar L, Agronskaia A V, Broertjes J, Broek B Van Den. Optimizing Imaging Conditions for Demanding Multi-Color Super Resolution Localization Microscopy. *PLoS One*. 2016;11(7):1-18. doi:10.1371/journal.pone.0158884.
109. Lin Y, Long JJ, Huang F, et al. Quantifying and Optimizing Single-Molecule Switching Nanoscopy at High Speeds. *PLoS One*. 2015;10(5):1-20. doi:10.1371/journal.pone.0128135.
110. Linde S Van De, Löschberger A, Klein T, et al. Direct stochastic optical reconstruction microscopy with standard fluorescent probes. *Nat Protoc*. 2011;6(7):34-38. doi:10.1038/nprot.2011.336.
111. Schnitzbauer J, Strauss MT, Schlichthaerle T, Schueder F, Jungmann R. Super-resolution microscopy with DNA-PAINT. *Nat Protoc*. 2017;12(6):1198-1228. doi:10.1038/nprot.2017.024.
112. Palayret M, Armes H, Basu S, et al. Virtual-'light-sheet' single-molecule localisation microscopy enables quantitative optical sectioning for super-resolution imaging. *PLoS One*. 2015;10(4):e0125438.
113. Huang F, Sirinakis G, Allgeyer E., et al. Ultra-High Resolution 3D Imaging of Whole Cells. *Cell*. 2016;166(4):1028-1040.
114. Franzini-Armstrong C, Protasi F, Ramesh V. Shape, size, and distribution of Ca(2+) release units and couplons in skeletal and cardiac muscles. *Biophys J*. 1999;77(3):1528-1539.
115. Yin C, Lai F. Intrinsic lattice formation by the ryanodine receptor calcium-release channel. *Nat Cell Biol*. 2000;2(9):669-671.
116. Chen W, Wasserstrom JA, Shiferaw Y. Role of coupled gating between cardiac ryanodine receptors in the genesis of triggered arrhythmias. *Am J Physiol Hear Circ Physiol*. 2009;297:171-180. doi:10.1152/ajpheart.00098.2009.
117. Takeshima H, Komazaki S, Nishi M, Iino M, Kangawa K. Junctophilins: a

novel family of junctional membrane complex proteins. *Mol Cell*. 2000;6(1):11-22.

118. Oort RJ Van, Garbino A, Wang W, et al. Disrupted Junctional Membrane Complexes and Hyperactive Ryanodine Receptors After Acute Junctophilin Knockdown in Mice. *Circulation*. 2011;123(9):979-988. doi:10.1161/CIRCULATIONAHA.110.006437.
119. Dai M, Jungmann R, Yin P. Optical imaging of individual biomolecules in densely packed clusters. *Nat Nanotechnol*. 2016;11(9):798-807.
120. Yin C, Han H, Wei R, Lai F. Two-dimensional crystallization of the ryanodine receptor Ca2+ release channel on lipid membranes. *J Struct Biol*. 2005;149(2):219-224.
121. Soeller C, Cannell M. Numerical simulation of local calcium movements during L-type calcium channel gating in the cardiac diad. *Biophys J*. 1997;73(1):97-111.
122. Winslow R., A T, Chen M, Greenstein J. Multiscale modeling of calcium signaling in the cardiac dyad. *Ann N Y Acad Sci*. 2006;1080:362-375.
123. Groff J., Smith G. Ryanodine receptor allosteric coupling and the dynamics of calcium sparks. *Biophys Journal2*. 2008;95(1):135-154.
124. Laver D, Kong C., Imtiaz M., Cannell M. Termination of calcium-induced calcium release by induction decay: an emergent property of stochastic channel gating and molecular scale architecture. *J Mol Cell Cardiol2*. 2013;54:98-100.
125. Marx SO, Gaburjakova J, Gaburjakova M, Henrikson C, Ondrias K, Marks A. Coupled gating between cardiac calcium release channels (ryanodine receptors). *Circ Res*. 2001;88(11):1151-1158.
126. Beavers DL, Wang W, Ather S, et al. Mutation E169K in junctophilin-2 causes atrial fibrillation due to impaired RyR2 stabilization. *J Am Coll Cardiol*. 2013;62(21):2010-2019.
127. Uzgiris, Egidijus.E; Kornberg R. Two-dimensional crystallization technique for imaging macromolecules, with application to antigen–antibody–complement complexes. *Nature*. 1983;301:125-129.
128. Annibale P, Vanni S, Scarselli M, Rothlisberger U, Radenovic A. Identification of clustering artifacts in photoactivated localization microscopy. *Nat Methods*. 2011;8(7):527-528. doi:10.1038/nmeth.1627.

129. Nieuwenhuizen RPJ, Bates M, Szymborska A, Lidke KA. Quantitative Localization Microscopy : Effects of Photophysics and Labeling Stoichiometry. *PLoS One*. 2015;10(5):1-18. doi:10.1371/journal.pone.0127989.
130. Whelan DR, Bell TDM. Image artifacts in Single Molecule Localization Microscopy : why optimization of sample preparation protocols matters. *Sci Rep*. 2015;5(7924):1-10. doi:10.1038/srep07924.
131. Lutz T, Clowsley AH, Lin R, Pagliara S, Michele L Di. Versatile multiplexed super-resolution imaging of nanostructures by Quencher-Exchange-PAINT. *Nano Res*. 2018:1-14. doi:https://doi.org/10.1007/s1227.

Appendix 1

DNA-PAINT imaging channel	Docking strand	Imager strand
561 nm excitation/ orange emission for **P1** configuration	C6-amine-5'-**TTATACATCTA**–3'-Cy5	5'– **CTAGATGTAT**-3'-ATTO 550
642 nm excitation/ far red emission for **P1** configuration	C6-amine-5'-**TTATACATCTA**–3'-Cy3.5	5'– **CTAGATGTAT**-3'-ATTO 655
561 nm excitation/ orange emission for **P3** configuration	C6-amine-5'-**TTTCTTCATTA**–3'-Cy5	5'– **GTAATGAAGA**-3'-ATTO 550
642 nm excitation/ far red emission for **P3** configuration	C6-amine-5'-**TTTCTTCATTA**–3'-Cy3	5'– **GTAATGAAGA**-3'-ATTO 655
642 nm excitation/ far red emission for **P5** configuration	C6-amine-5'-**TTTTAGGTAAA**–3'-FITC	5'- **CTTTACCTAA**-3'-ATTO655
642 nm excitation/ far red emission for **dSTORM/DNA-PAINT** configuration	C6-amine-5'-**TTATACATCTA-TTTCTTCATTACGCG**-3'	5'- **CGCGTAATGAAGA**-3'-Alexa Flour 647 AND/OR 5'- **CTAGATGTAT**-3'-ATTO 655

Appendix 1: *The nucleotide sequences and terminal modifications for the oligonucleotides used in this thesis for specific imaging configurations.*

Appendix 2

Name	Sequence
P1+ imager	5'– **GCGCTAGATGTAT** -3'- ATTO 655
P1+ quencher	5'– Iowa Black RQ – **ATACATCTAGCGC** -3'- ATTO 655

Appendix 2: *The oligonucleotide sequences used for experiments involving 'Quencher-Exchange-PAINT'. A 13 base pair version of the P1 imager strand, P1+, is fully complementary to the P1+ quencher.*